The Deformation Response of 3D Woven Composites Subjected to High Rates of Loading

by

Mark Robert Pankow

A dissertation submitted in partial fulfillment
of the requirements for the degree of
Doctor of Philosophy
(Mechanical Engineering)
in The University of Michigan
2010

Doctoral Committee:

Professor Anthony M. Waas, Chair
Professor Scott J. Hollister
Professor J. Wayne Jones
Professor Alan S. Wineman
Chian-Fong Yen, Army Research Labs

© Mark Robert Pankow

All Rights Reserved

2010

to my family

Acknowledgments

I would like to thank my advisor Professor Anthony M. Waas for his guidance, support, and encouragement throughout my Ph.D. study at the University of Michigan. A special thanks to Professor Alan S. Wineman for having lengthy discussions about teaching philosophies and life in general. Additionally I would like to thank Professor J. Wayne Jones and Scott J. Hollister for their time and effort spent on the research and on serving on the doctoral committee.

I am grateful to many colleagues, Amit Salvi, Peter Gustafson, Evan Pineda, Christian Heinrich, Pavana Prabhakar, Siva Shankar Rudraraju, Scott Stapleton, Brian Justusson, Chris Attard, Wei Ng, Eugene Kheng, Dianyun Zhang, Zach Kier, Lucas Hansen among others for their help and friendship. Additionally I want to thank many of the great friends that I have met in my time at Michigan, Neha Kaul, Pat Harrington, Devin O'Connor, Steve Walton, Paul Teini, Benjamin Reedlunn, among many others who have made me feel at home in this university and given me an outlet outside of school.

I also want to thank the administrative and technical staff of the Departments of Aerospace and Mechanical Engineering for their help support and guidance. A special thanks to Terry Larrow for his many efforts in building some of the crazy equipment that we designed for these unique tests and putting up with many last minute changes.

All these years, I owe a lot to my mountain bike, rock climbing gear and skis. They allowed me to get away from the lab and keep my sanity in some of those very difficult days. Without these hobbies and many good friends I would have left school many years earlier. Additionally the year that I spent teaching reaffirmed my motivation to finish this degree and look for an academic position.

The author would like to acknowledge the support of Textile Engineering and Manufacturing (T.E.A.M.) and the Army Research Labs, in Aberdeen Maryland. Their support and collaboration made this project possible and feasible. The direct support of Chian-Fong Yen, Seth Ghiorse and Steve Clarke has been greatly appreciated.

Table of Contents

List of Tables

Table

List of Figures

Figure

List of Appendices

Appendix

List of Symbols

a	crack length
a_i	Speed of sound in gas i
b	Specimen width
h	Specimen thickness
k	Initial Stiffness of DCZM element
n	Material parameter of the Cowper-Symonds model
r_i	pressure ratio between section i and section 1
α_{pl}	Trapezoidal shape factor
δ	Relative nodal displacement
δ_c	critical separation of displacement
ε_I	Incident strain gauge pulse
ε_T	Transmitted strain gauge pulse
ε_R	Reflected strain gauge pulse
ε_{ij}	Orthotropic strain
γ_i	ratio of specific heats for the gas in section i
ν_{ij}	Orthotropic poisson's ratio
ρ_i	Density of constitent
σ_{ic}	Cohesive strength in respective mode
σ_{ij}	Orthotropic stress
σ_{ij}^{y}	Orthotropic yield stress
τ	Engineering shear strain

A	Cross sectional area
C_o	Speed of sound in split pressure Hopkinson bar
D	Material parameter of the Cowper-Symonds model
D_{bar}	Diameter of split pressure Hopkinson bar
D_s	Diameter of specimen
E_{ij}	Orthotropic engineering moduli
F_i	Nodal force
G_{ic}	Critical energy release rate for mode i
G_{ij}	Orthotropic engineering shear moduli
L	Length
L_s	Length of Specimen
M_i	Mass of constituent
M_r	Mach number of reflected shock wave
M_s	Mach number of shock wave produced
P	Applied load
R	Cowper-Symonds yield stress ratio
R_{ij}	Orthotropic yield stress ratio
T	Temperature
V_i	Volume of constituent
Δ	Displacement

List of Acronyms

3DWC 3D Woven Composite

ARL Army Research Labs

CCM Concentric Cylinder Model

DCZM Discrete Cohesive Zone Method

DIC Digital Image Correlation

ENF End Notch Flexure

FE Finite Element

RUC Representative Unit Cell

SHPB Split Hopkinson Pressure Bar

LVI Low Velocity Impact

RTM Resin Transfer Mold

SEM Scanning Electron Microscope

T.E.A.M. Textile Engineering and Manufacturing

UMCSL University of Michigan Composites Structures Lab

VARTM Vacuum Assisted Resin Transfer Mold

VUEL User Defined Element in ABAQUS Explicit

VUSDFLD User Defined Field in ABAQUS Explicit

Abstract

The use of polymer matrix composites in structural load bearing applications is becoming more widespread, with extensive development in automotive, aerospace and recreational equipment. This increase has produced loading scenarios which are unfamiliar and not well understood by the composites community. Several applications involve impact loading, which can produce large strain rates and failure due to delamination, often rendering the component useless. However modern manufacturing methods have lead to new weave geometries that provide composites with significant damage protection. This is achieved by elimination of the delamination failure mode, and by localizing the extent of damage.

The present work is an experimental and computational study with the objective of developing a mechanism based deformation response model for structural components made of 3D woven composites, including the prediction of failure strengths, when subjected to high loading rates. Three unique experimental configurations have been developed, with new experimental methods also being produced. Along with these methods, finite element based simulations have been performed to predict the material response and failure mechanisms experimentally observed.

End Notch Flexure (ENF) tests were used to determine the effectiveness of the Z-fiber at resisting crack propagation. The crack propagation was found to have rate dependent properties, and additionally architecture based parameters that can predict the strength and resistance of the material. The computational results reinforced many of the experimental observations. A new FE implementation was used to show the effectiveness of the Z-fiber reinforcement that occurs from the Z-fiber bridging the crack that has developed in the material.

Shock impact testing was performed to simulate the effects of blast loading on the material. This test facility was a new development and new experimental measurement methods were utilized to record the deformations and strains. The out of plane deformation that occurred in the material produce matrix micro-cracking. This was the first failure mode of the material. Computational models were developed to predict the material behavior subjected to shock loading. The model incorporated a formulation for matrix micro-cracking which

predicted this mode of failure accurately. Subsequently, failed elements had a modified stiffness to reflect the failure in certain directions.

Finally, Hopkinson pressure bar testing on smaller coupon level testing was done to understand the high strain rate behavior of the material in compression in all three directions. The warp and weft directions showed an increase in strength of 100% at these elevated rates and a transition in failure mode, from kink band formation to delamination. Through the thickness testing revealed a small increase in load from rate effects and a transition from delamination to shear band formation. Computational models focused on analyzing a representative unit cell of the 3D architecture that was evaluated dynamically. The simulations were able to predict the composite material moduli, and failure loads with failure modes accurately. The results additionally showed that there was little benefit from Z-fiber in the through the thickness direction compression response.

Chapter 1
Introduction

1.1 Motivation

On December 15, 2009 we entered a whole new era of consumer use of composite materials, with the first flight of Boeing's Dreamliner 787. With this accomplishment, composites were brought from a niche market of aerospace companies, down to the average consumer and every day products that are used in transportation. Composites have long been seen as the material of the future due to their relatively large strength to weight ratios and their ability to tailor material properties to the functionality of the application. The material has filtered down from an exotic material only seen in military and aerospace applications, to that of every day common goods. In the last two decades advances in manufacturing techniques has driven down the cost of the material and also made it easier to manufacture parts, creating a larger consumer base.

In order for the consumer base to expand, details about the material behavior (deformation response) and mechanical failure need to be thoroughly understood. In typical applications, composite materials are made up of multiple layers of unidirectional material that are laminated together. These layers are essentially "glued" together, creating a weak plane between the individual layers that is only as strong as the "glue". When this "glued" joint fails it is commonly referred to as delamination. This type of failure greatly reduces the overall stiffness of a structural panel and causes widespread damage rendering the part not repairable. Longer service life or increased damage tolerance might be possible if one can localize the zone of delamination, or prevent delamination from occurring. Three delamination preventing techniques have been examined in the past: z-pins, stitching, and 3D weaving. Both z-pins and stitching suffer from mechanically inducing stress concentrations that are introduced by the insertion of the Z-pins or stitching fibers [1]. 3D weaving introduces binding fibers in the weaving process, so there is no mechanical insertion in an existing structure. The later technique is a relatively old concept since most of the weaving is done on antiquated looms dating from the industrial revolution. The 3D braided composites have

a higher energy absorption capability than unidirectional composites [2] and the architecture can be tailored to absorb even more energy if it is desired, as will be shown in this body of work. Figure 1.1 provides a schematic representation of the 3D weaving process. The weaving process works by insertion of weft fibers followed by movement of the Z-fibers moving the threads from the top to bottom and vice versa. This process is continuously repeated until the weaving is completed.

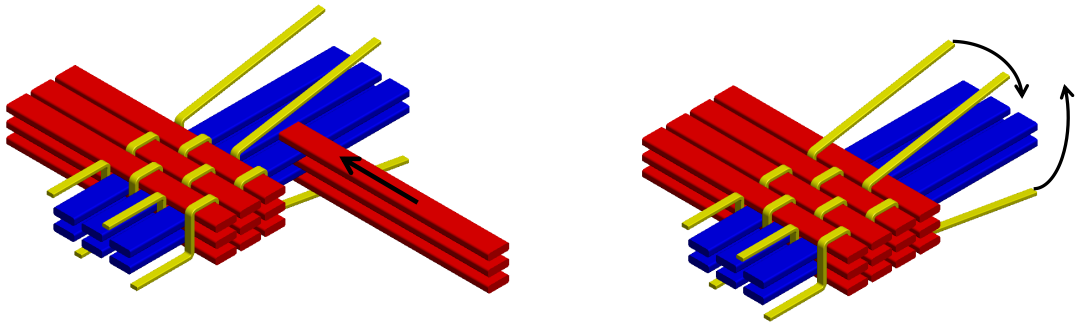

(a) Weft Insertion (Direction of Red Fibers) in weaving process

(b) Z-fiber movement in weaving process, to bind weft fibers

Figure 1.1 Schematic of how a typical 3D weaving process works. The different bundles of fibers (referred to as tows) are woven together in a pre-determined manner. The dry fabric is placed in a mold and resin is infused and cured to make a solid structural component.

1.2 3D Woven Composites (3DWC)

Although a relatively new material, there has been a significant amount of work to develop different architectures that in some cases push the limits of the loom's capability [3, 4, 5]. Here, the word architecture refers to the network of different fiber tows that are woven together to form a single interweaved unit. 3D weaving has been shown to decrease or eliminate delamination that occurs in layered materials, however there are drawbacks. Very little is known about the mechanical properties, and due to the complex textile weaves, many of the classical formulations for determining mechanical properties do not apply. Often, the end user must manufacture panels and perform tests to determine mechanical properties, which is a time consuming and costly process. Many of the current applications of 3D woven composites include boat hulls, armor plating, elimination of joints and many others as described in [4, 6, 7].

Early experimental studies of 3D woven textile composites looked at very basic test-

ing, which included tensile and compressive testing, shear tests and some 3pt. bend tests [8, 9, 10, 11, 12, 13, 14, 15, 16, 17]. Researchers typically pinpoint fiber crimp and other effects in the weaving process as initiators of premature failure mechanisms. It is also noted that the addition of z-fibers into composites degrades the in-plane performance [18]. This is typically on the order of a 5% reduction in strength, but Z-fibers also increase the out of plane and shear properties dramatically, so the trade off is beneficial overall.

Subsequent to studies of testing, researchers began to refine and extend the analytical models which were limited to unidirectional in-plane composites. Initially, the models began as analytic techniques developed on the basis of either rule of mixture or concentric cylinder model (CCM) calculations [19]. Many different analytical models have been developed which are useful for predicting in-plane engineering constants, however they are typically relegated to the linear elastic regime [9, 20, 21, 22, 23, 24]. A new derivation for more generalized geometry of a laminated beam theory can be seen in [19], however this model also suffers from limitation to the linear elastic behavior. Further, lack of fiber tow interaction, and effects of fiber crimp cannot be captured. The limitations of these analytic models were overcome with the advancements in computer based solid mechanics models. Amongst these, finite element solutions were developed to determine mechanical properties of 3D woven composites. Many different variations of finite element models exist, ranging from very simplified to quite detailed representative unit cells (RUCs) have been investigated with varying degrees of success [8, 22, 25, 26, 27, 28, 29, 30, 31, 32, 33, 34, 35, 36, 37]. Many papers comment on the limitations of the finite element models, since these methods often over-predict the stiffness, because of their assumed simplified geometry and their inability to represent fiber undulations accurately. They also do not account for non-ideal interfaces between the several constituents. These models are useful for very simple loading scenarios, however composites in use rarely see simple tension load states, rather they typically experience complex 3D load state, for example, as in transverse impact of a flat panel [38].

1.3 High Strain Rate Testing

With each new application, 3DWC see unique loading scenarios. Automobiles sometimes experience impacts through crashes, which induces high strain rate loading causing 3DWC to behave differently because their constituents are strain rate dependent. The wide spread use of 3DWC has led to many innovative solutions but has also revealed weaknesses, or unanticipated failure mechanisms. How 3DWC behave under high strain rate environments

is paramount to their successful integration into new designs.

Some previous researchers have investigated the strain rate dependence of these composites through various different standard test procedures to evaluate high strain rate effects including; Split Hopkinson Pressure Bars (SHPB), and punch shear tests [10, 39, 40, 41, 42, 43, 44, 38, 45, 46, 47, 48, 49]. Many of these studies were done to compare one 3DWC to another, by looking at the differences in the outcomes. Much of the information and conclusions were based on post-experiment optical observations. Often, it is the in-situ deformation characteristics that are believed to cause strain rate dependency.

Very few researchers have been able to validate their theories and produce accurate results with physical models showing the actual causes for these strain rate dependencies. Finite element codes have been investigated to model the high strain rate behavior of the material, often with marginal success because of assumed homogeneous material (composite) properties [50]. The results were often limited to a specific test in question with no intention to model the rate dependent behavior, rather to determine the composite properties at an elevated rate. Further, these tests are typically done on very small amounts of material often not capturing the gross composite response, which required the use of a representative volume of material. Many applications of 3DWC are slated to experience blast type loading, and this has not been studied in the past. New experimental techniques are needed to correctly capture deformation response and failure mechanisms that correspond to blast type loading scenarios.

1.4 Current Research Objectives

A detailed experimental investigation has been carried out in this work with a focus on high strain rate experimental testing. The various different tests focused on different aspects of the 3DWC, some on more of a panel level deformation response while others examined microscopic events and specific failure modes. Figure 1.2 shows a typical 3DWC panel, a repeat unit of the panel material (a unit cell) and a breakdown of the unit cell with fiber tows and matrix. Three separate high strain rate experimental facilities have been used; Drop Tower, Split Hopkinson Pressure Bar (SHPB), and Shock Tube.

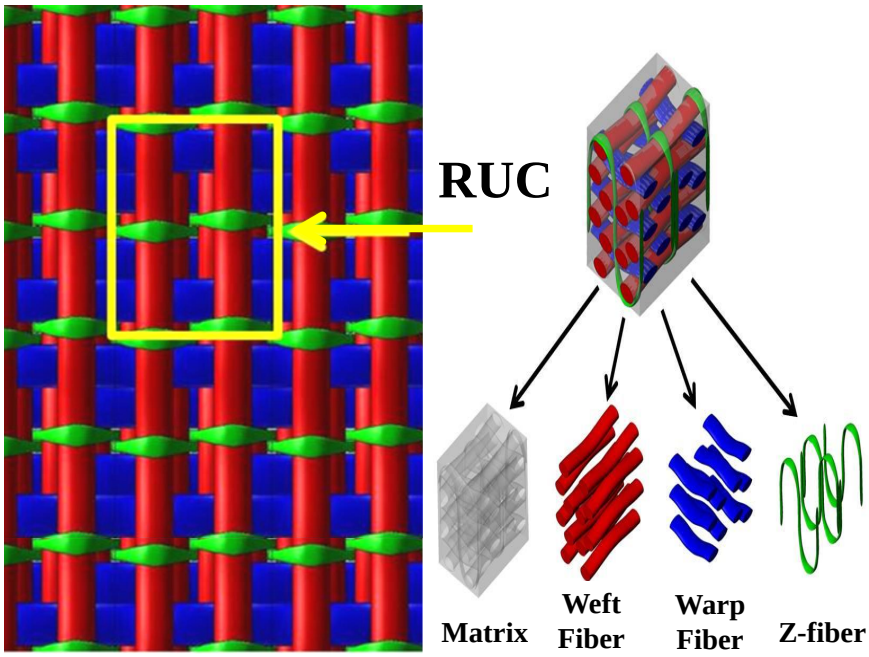

(a) 3DWC with matrix removed for visual purpose. A representative unit cell (RUC) has been identified and then broken down into its individual fiber two components.

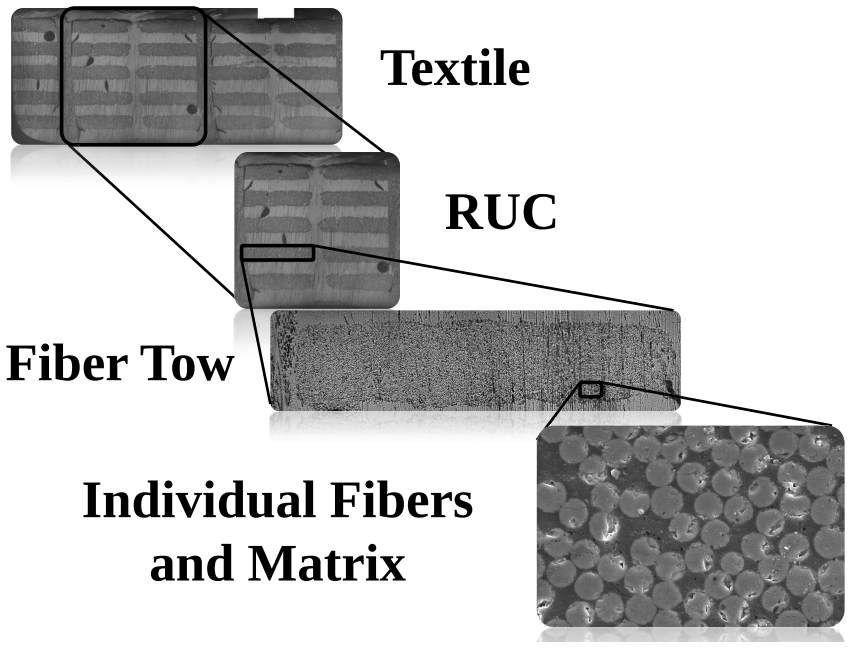

(b) 3DWC Broken down into various different components at different levels of magnification

Figure 1.2 3DWC broken down into its various different components.

The drop tower was used to subject flat 3DWC laminates to transverse impact to examine the influence of the Z-fiber on the resistance to delamination. End notch flexure (ENF) tests were used to investigate the influence of architecture on delamination resistance. High speed imaging was used to examine how a delamination crack progressed in the sample and how the loading rate affected the failure mode as it transitioned from low to high.

A shock tube was modified in order to be able to experimentally subject 3DWC panels to shock induced loading. Although this is not the first time this has been done, it is the first time one has been able to record full out of plane deformation histories and capture failure initiation. This full field information will provided complete details (on the surface) of the panel response history, which have been previously unavailable. Many different tests were done on this setup to look at the formation of matrix micro-cracking that occurred due to the out of plane loading induced by the shock impacting the 3DWC panel. Many of the observed failure mechanisms were found to be directly linked to the architecture of the 3DWC.

The SHPB was used to examine the response of the 3DWC to controlled high rate loading in different direction as sown in figure 1.3. A larger bar was developed specifically to be able to test 3DWC due to their large RUC size. Experimental investigations revealed some very interesting observations relating to the architecture. The experimental setup was further validated through the use of a digital image correlation (DIC) setup that was used to obtain full field surface strain histories of the material. This full field strain map indicated where failure would initiate and some of the very localized stress concentrations in the material based on the architecture.

One of the objectives in this research was to develop models that can accurately predict mechanical properties of 3DWC. The models are geometry based and incorporate strain rate dependent constitutive equations for the components (fibers and tows) to determine the composite properties under high rate mechanical loading. Various different finite element models have been developed to capture the complete spectrum of work that was carried out. The FE models range from RUC scale to macroscopic full panel architecture. The results provide insight on the complex deformation response of 3DWC, from the micro RUC scale to the macro, panel scale. The models developed for the different experimental tests have similar characteristics and identical properties that provide a link between all of the modeling.

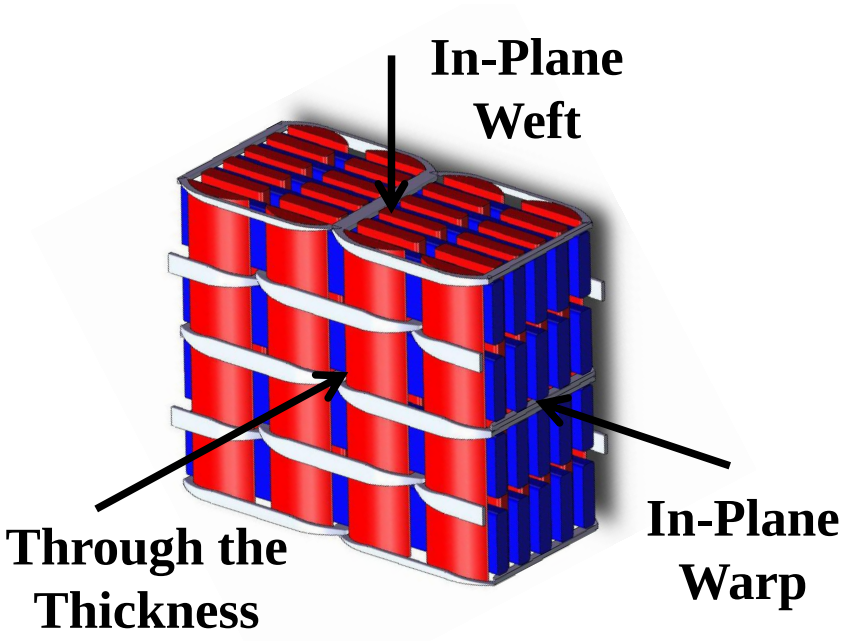

Figure 1.3 3DWC RUC showing the various different SHPB loading directions.

1.5 Thesis Outline

In the second chapter of this thesis, a detailed outline of the various geometries studied is presented. Two types of 3DWC architectures are examined; Z-fiber and layer-to-layer. A detailed study of the matrix material and its mechanical response is presented next including the effects of high strain rates on the yield point of the material.

Following the geometry characterization, a comprehensive static analysis of the in-plane and out of plane mechanical properties is presented in chapter 3. These include tension, short beam shear and laterally constrained compression test results. Preliminary conclusions about the various architectures will be drawn at this point.

A study of the 3DWC delamination resistance and associated fracture toughness is presented in chapter 4. These properties are characterized through an ENF test. Tests were carried out at both static and elevated loading rates to determine the influence of rate on delamination resistance. Computational models have been used to determine the parameters associated with the tests through an inverse modeling approach.

The fifth chapter presents the panel response of 3DWC to shock loading. These tests were performed on a modified shock tube that imposes a steeply rising pressure pulse on a sample that is three inches in diameter. The results indicate not only panel stiffness, but can also be used to characterize the first occurrence of failure through matrix cracking. This is seen both experimentally and predicted computationally.

In the sixth chapter a detailed examination of compression response of 3DWC under high rates is presented. Tests were carried out on a large SHPB, so that the effect of strain rate dependent material parameters could be determined. Both through-the-thickness and in-plane parameters are investigated and discussed. The testing revealed many architecture dependent results, and also information about SHPB testing on 3DWC specimens.

The seventh chapter includes detailed finite element models of 3DWC RUC's. The models were created in SolidWorks and then imported into ABAQUS where the model was meshed and evaluated, in many instances with user controlled subroutines. Non-linear anisotropic plasticity theory has been used on a mathematical framework to model mechanical response of the experimentally observed phenomena. Once these models were evaluated statically they were then subjected to dynamic loading that corresponds to the SHPB test. The FE results were found to compare very well against surface strain histories obtained using the DIC technique.

1.6 Unique Contributions in this Dissertation

1: A set of ENF test results at various rates to determine the rate dependent delamination resistance of 3DWC.

2: A computational investigation including discrete cohesive zone model (DCZM) elements to determine the effective G_{IIc} and σ_c values of the matrix and associated Z-fibers, that correspond to the ENF test.

3: A set of shock tube test results to determine the effective out of plane deformation response of 3DWC subjected to blast loading. The use of DIC to extract panel deformation (3D) history is unique and novel.

4: A finite element investigation to model the shock tube panel response, which included modeling of the matrix micro-cracking that occurs in the material. .

5: Development of a large SHPB to determine the various different material responses of 3DWC at high strain rates. Specifically through the thickness response and in-plane response of 3DWC were determined for the first time.

6: Development of RUC micro-mechanics models to investigate static and high rate mechanical properties, corresponding to SHPB response.

Chapter 2

Material Systems, Specimens, Test Procedures, and Microscopy Studies

This chapter provides insight into the various aspects of the composite system including some of the terminology, the two distinct types of textile architecture, the process for making specimens and material properties for each constituent of 3DWC. Details of the various different architectures are discussed and broken into individual constituents. One of the methods to achieve this is through the composite burn out process along with microscope images. The individual constituents were then analyzed to determine details. Rate dependent characterization of the matrix system is also reported.

3D weaving is not a new technique, rather the idea has been around for centuries. There are many different types of proposed architectures and these have been discussed in detail previously along with benefits and limitations [3]. Applications of the material have included boat hulls, armor, and numerous possible future implementations that are discussed in [6]. Researchers often point out that due to the Z-reinforcement and resistance to delamination, applications involving armor and bullet proofing would be ideal candidates [5, 8]. Previous studies have shown 3DWC to be more damage tolerant [46] than laminated or stitched composites.

2.1 Material Systems

3DWCs are comprised of two different components, S-2 glass fibers with SC-15 matrix. The S-2 glass fibers are the main load bearing constituents, while the SC-15 matrix provides structure to the panel. The main difference between laminated composites and woven composites is the inter-plane movement of the various fiber. These are fiber tows which bridge the multiple layers and bind the layers together. There are two main types of 3D weaving, Z-fiber and layer-to-layer.

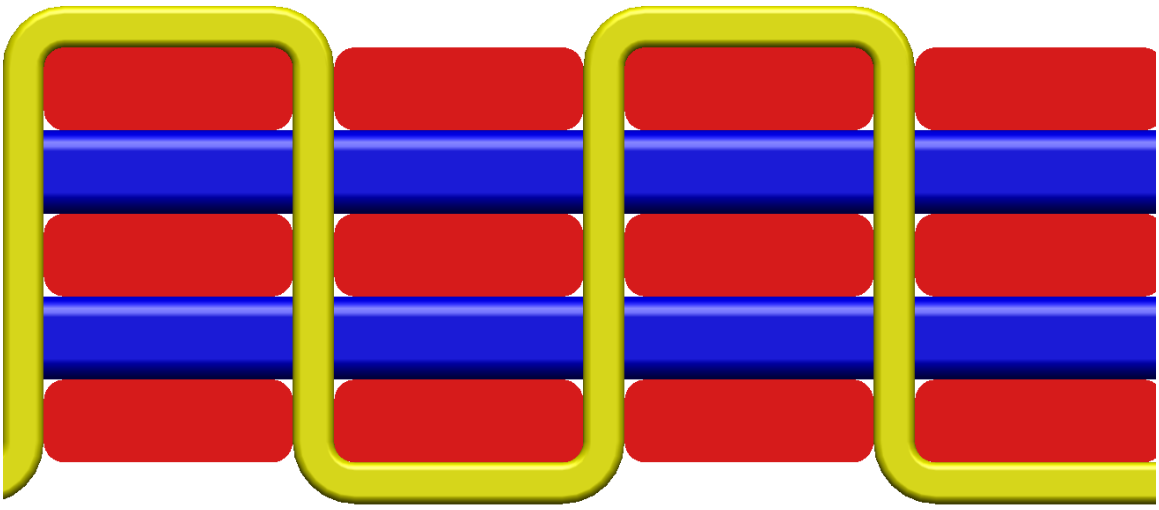

Figure 2.1 The yellow color path represents the course that the Z-fiber follows during the weaving process.

The Z-fiber architecture has a very rigid series of warp and weft fibers that are maintained in-plane through out the panel. A set of fibers running in the direction of the warp fibers is drawn from the bottom to the the top to bind all these layers together, and is usually inserted in-between the spaces of the warp fibers. Figure 2.1 shows one of the possible paths that the Z-fiber could follow in the weaving process. This path is shown in yellow, however there are multiple different paths that can be formed creating different types of architectures.

The second type of architecture is that of layer-to-layer where the Z-fibers are eliminated from the panel and the warp fibers, instead of being relatively straight, are now woven between the various layers of weft fibers. Figure 2.2 shows a possible path that the warp/Z-fiber could take in the weaving process. Notice that the warp fiber is now used to bind the layers together, however there is a much longer path that it takes in this binding process compared to the Z-fiber architecture. The layer-to-layer architecture is usually more compliant than the Z-fiber architecture.

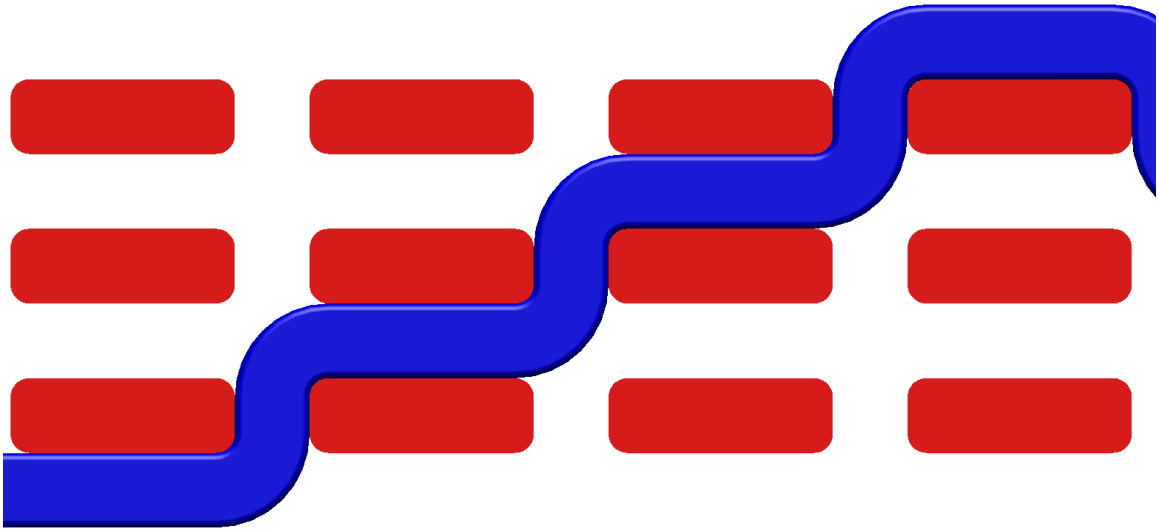

Figure 2.2 The blue color path shows a representative course that can be taken by the warp/Z-fiber as it is woven in the layer-to-layer architecture.

2.1.1 Architectures

The use of 3D weaving has broadened the spectrum of textile architectures that are now available. Ten different architectures were initially examined in this study. The first was a baseline panel that was simply a 2D plain weave layered composite. Six architectures were provided by Textile Engineering and Manufacturing (T.E.A.M.) inc., which included three Z-fiber designs and three layer-to-layer, which are shown in figure 2.3. Three architectures were provided by Albany Engineering Composites, with two being Z-fiber and the third layer-to-layer preform, as shown in figure 2.4. Most of the work reported here will focus on Z-fiber reinforced composite materials, with an emphasis on the 6% Z-fiber based on preliminary experimental studies that showed the 6% Z-fiber 3DWC to be superior to others in stiffness and strength.

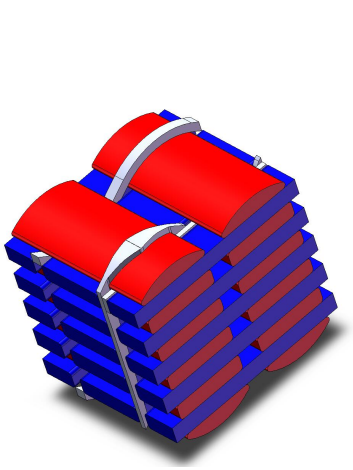

(a) 3% Z-fiber

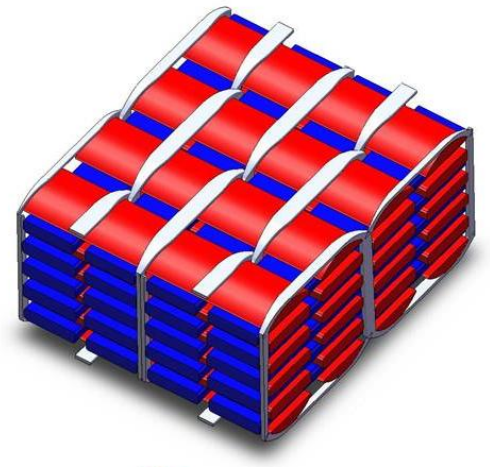

(b) 6% Z-fiber

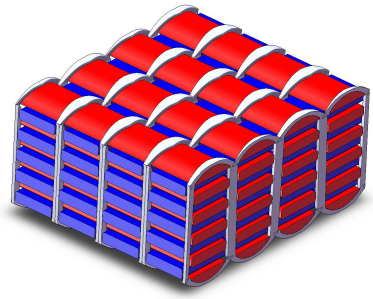

(c) 10% Z-fiber

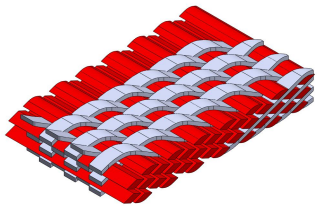

(d) 12^o Angle Interlock

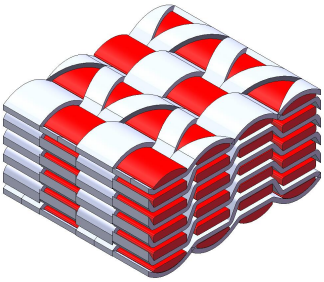

(e) 20^o Angle Interlock

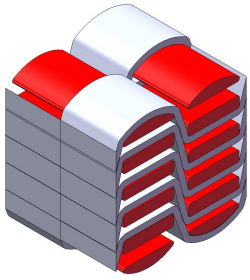

(f) 60^o Angle Interlock

Figure 2.3 Various 3D woven architectures from T.E.A.M. inc. An RUC has been shown for each of the architectures.

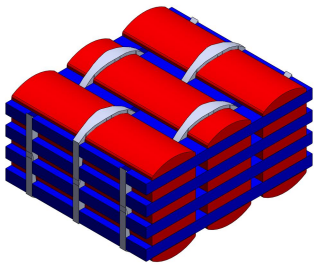

(a) Albany 1

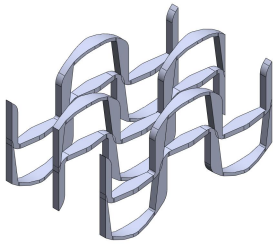

(b) Albany 1, Z-fiber Tows

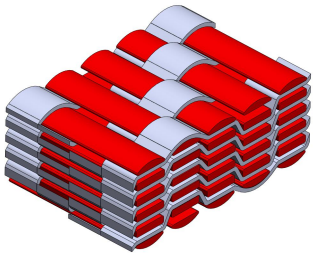

(c) Albany 2 Layer-to-Layer Orthogonal Interlock

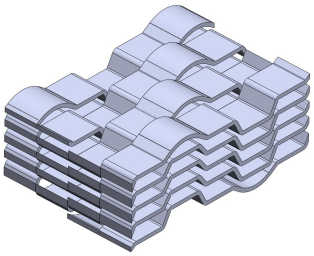

(d) Albany 2, Warp Fiber Tows

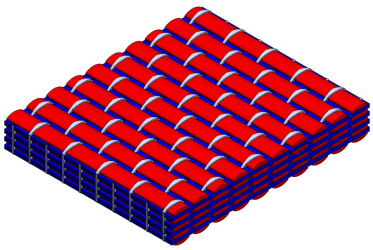

(e) Albany 7

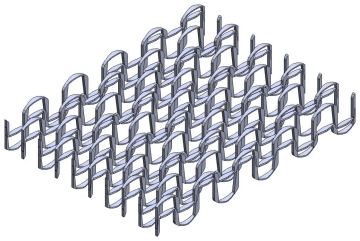

(f) Albany 7, Z-fiber Tows

Figure 2.4 Various 3D woven architectures from Albany Engineered Composites.

2.1.2 Fabrication

The panels were made using a Vacuum Assisted Resin Transfer Mold (VARTM) system. VARTM is a derived process from the Resin Transfer Mold Process (RTM). The main difference between the two is that in VARTM a vacuum bag replaces one half of the mold and the matrix is then drawn through the material to ensure proper impregnation of the fibers through the assistance of a vacuum suction on the resin flow, [51], as seen in figure 2.5. There are many benefits to this process some of which include, shorter mold time, lower tooling costs, reduced volatile emissions, lower injection pressures, and the ability to do much larger structures [52].

A typical fabrication process can be divided into five steps [52, 51]:

1: Pre-Molding, the mold surface is cleaned and a mold release agent and gel coat are sprayed onto the surface.

2: Dry fibers preforms are loaded into the mold. A flexible bag film is then used to cover the preform.

3: The mold and preform are then covered and sealed using vacuum bagging material and vacuum tapes.

4: The mold is now placed under vacuum, which draws the resin from its chamber through the preform and into a waste tank.

5: The resin is then left to cure. After curing the part is removed from the mold and is ready for use.

The VARTM process was performed at Army Research Labs (ARL) in Aberdeen, MD. It was reported by them that they experienced some problems with wetting the entire panel with matrix. The results were noticeable from both burn out and from optical measurements, both of these techniques are discussed next.

2.1.3 Burn Out Tests

In order to determine how good the wet out of the layup was, a procedure called fiber burn out was performed to determine the void content of the specimens, this procedure is based on ASTM standard D2734 [53] which used both standard D792 [54], that describes the density measurements in water, and D2584 [55], which describes how to perform matrix burn out in the furnace, the details are given in appendix A. The results of the burn out

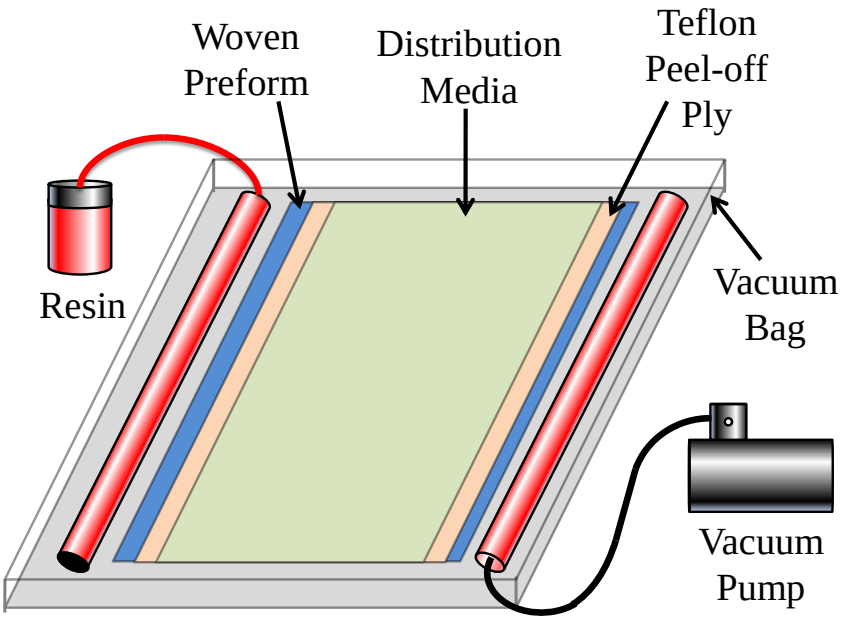

Figure 2.5 Schematic of the Vacuum Assist Resin Transfer Mold (VARTM) setup.

method can be seen in table 2.1 which shows a breakdown of the volume fractions along with the densities. According to the calculations, the void content is within the manufactures specification, however detailed imaging revealed some startling observations. Additionally post burn out photos were taken of the preform and these are shown in figure 2.6. These photos capture clearly some of the details of the architecture and the movement of the Z-fiber in the different planes.

Table 2.1 Fiber Volume Fractions

	Fiber (%)	Matrix (%)	Voids (%)	Density ($\frac{g}{cc}$)
Baseline	47.1	50.5	2.5	1.744
3%	45.2	51.8	3.0	1.713
6%	45.9	53.5	0.7	1.749
10%	45.2	52.0	2.8	1.715
20^o	40.3	58.8	0.9	1.671
60^o	39.1	57.4	3.4	1.627

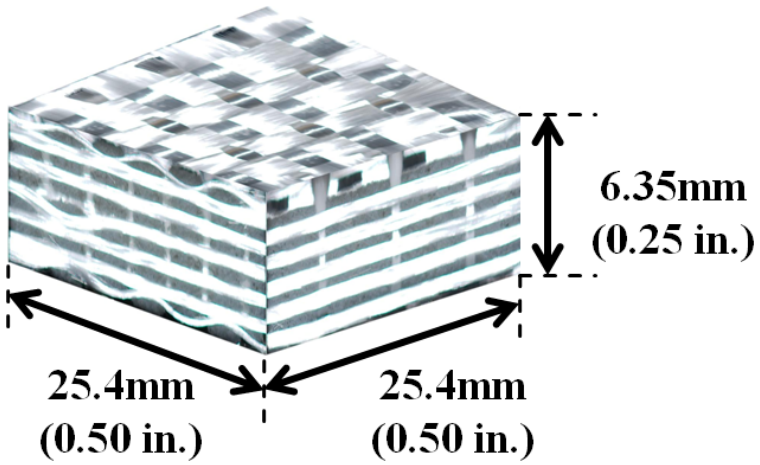

(a) 3% Z-fiber

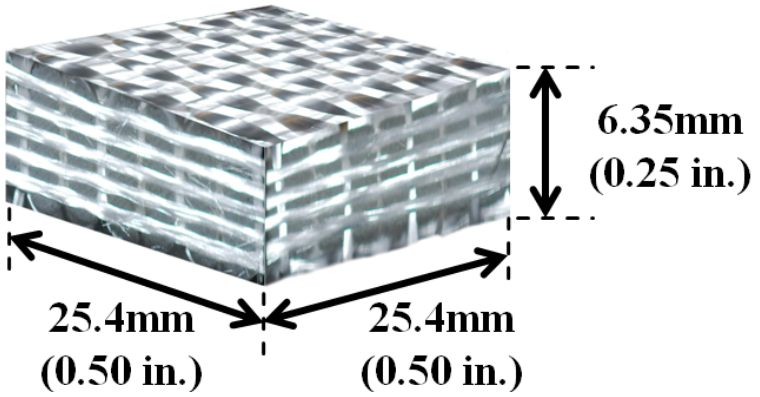

(b) 6% Z-fiber

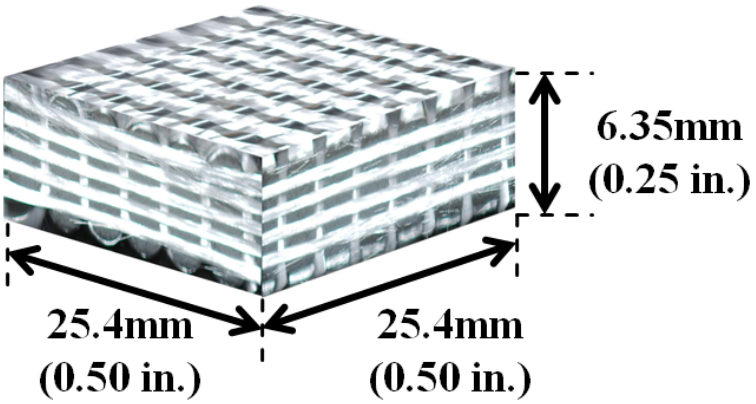

(c) 10% Z-fiber

Figure 2.6 Fiber preforms left after burnout.

2.1.4 Microscopic Imaging

Detailed imaging on the microscope using polarized light and a filter allowed us to find details of the architecture. It additionally revealed many of the voids and imperfections that were present from the manufacturing process. Some of these are very prominent and produce premature failure mechanisms, see figure 2.7. However as characterized in table 2.1, the overall void content is relatively low in comparison and meets the manufacturers specification. The macroscopic images were used to extract the as cured woven geometry and fiber volume fractions. The dimensions of each of the tows were used as inputs into finite element models that will discussed in chapter 7.

2.2 SC-15 Material

The material used as resin to infuse the panels was SC-15 epoxy a thermoset polymer. This decision was made by ARL as the panels came infused from them. SC-15 is a low-viscosity two-phased toughened epoxy resin system consisting of part A (resin mixture of diglycidylether epoxy toughener) and part B (hardener mixture of cycloaliphaic amine poluoxylalkylamine) [56]. Due to the low viscosity of the material it was a good choice for the VARTM process because it was able to flow well under vacuum to completely impregnate the material. Additionally, the long cure time allows for an adequate amount of hold to remove many of the air bubbles that exist in the material due to mixing.

2.2.1 Mechanical Properties

A set of static tensile tests were done on pure material to characterize the mechanical properties of SC-15 which can be seen in table 2.2. These values were provided by ARL through the manufacturer.

Table 2.2 SC-15 matrix static properties

E_{11} (GPa)	ν_{12}	σ_y (MPa)	ε_y (%)
2.487	0.35	110	6.4

Additional tests using a torsion testing machine were performed to determine the full stress-strain curve of the material, which can be seen in figure 2.8. This stress-strain curve will be used as a basis for mechanical properties for future computational work. The experimental results have a strong correlation to the modulus and also the failure stress.

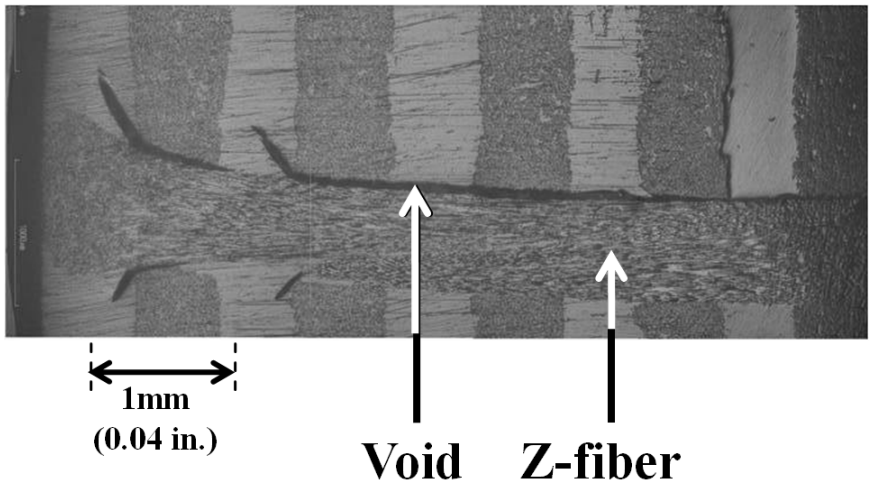

(a) Matrix void at fiber interface

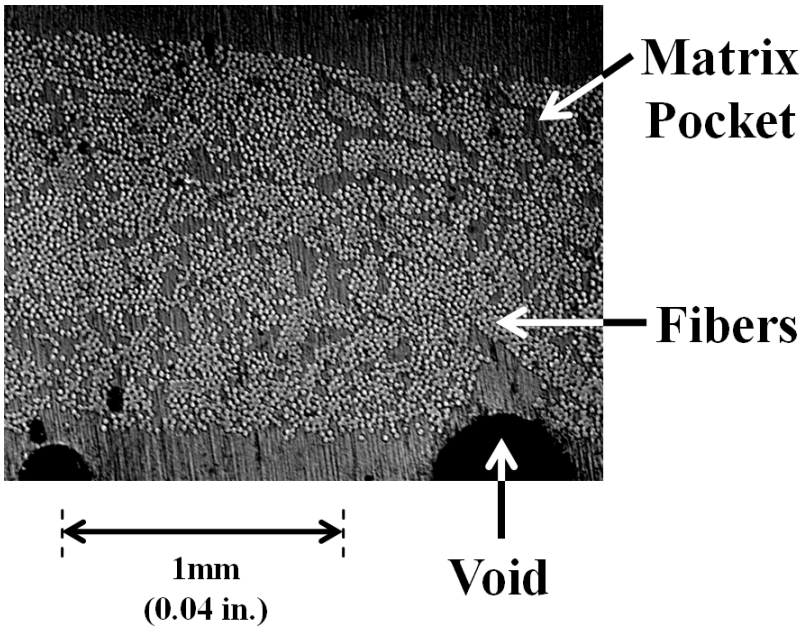

(b) Air bubble void in matrix

Figure 2.7 Various types of voids.

2.2.2 Rate Dependent Behavior

In order to better characterize the SC-15 matrix system a series of rate dependent tests were performed to expand on the previous knowledge that was obtained from ARL. As a means to determine the high strain rate behavior of the mechanical properties, a small diameter SHPB was used. The details of the SHPB procedure can be found in Pankow et. al. [57], which also describes many of the evaluation methods and also information on the selection of specimen size and shape.

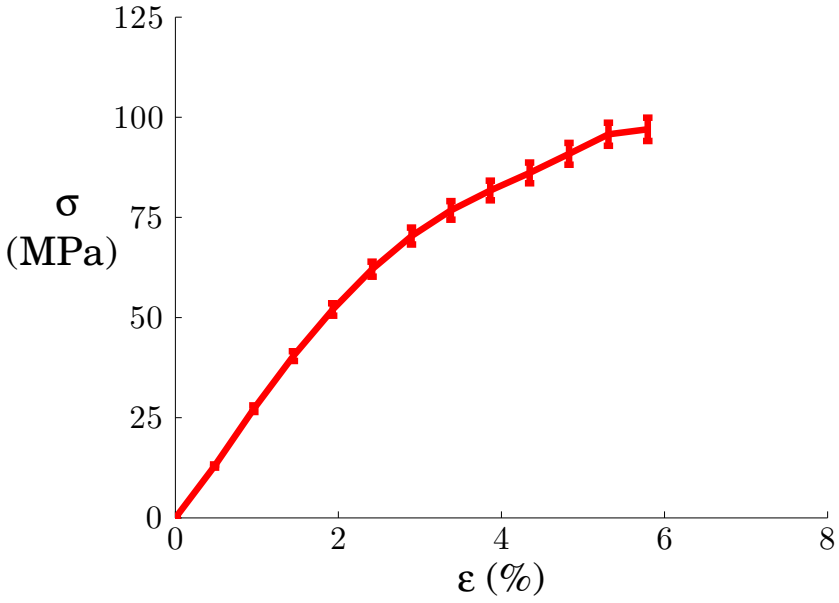

Figure 2.8 Static Stress-Strain Curve for SC-15 Matrix.

SHPB tests were performed on post cured rods of pure SC-15 matrix to understand the behavior of the material. Tests were performed on both thin and thick specimens according to Pankow et. al. [57], where the reference describes how the thick specimens are suitable for determining modulus and the thinner for yield stress. Figure 2.9 shows the results from the thick specimens and how there is very little variance of the modulus with a changing strain rate. Figure 2.10 shows how the various strain rates affects the yield of the material in thin specimens.

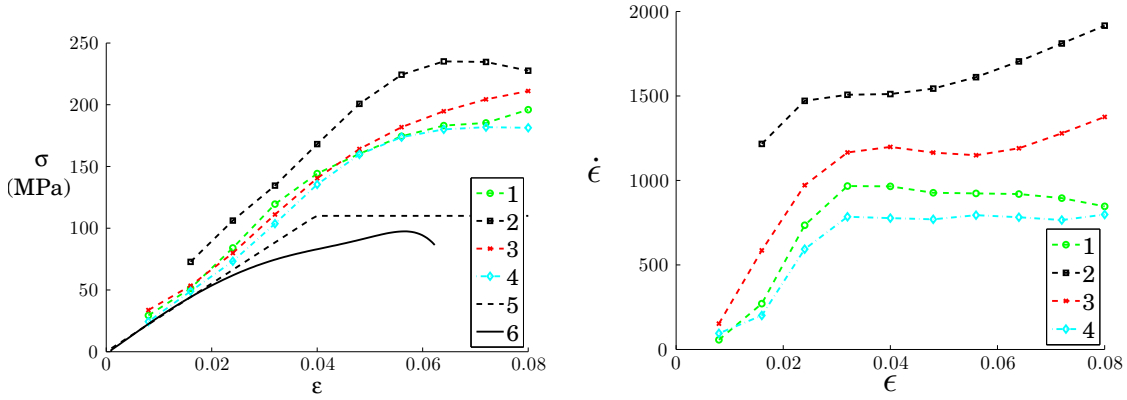

(a) 1-4 are experimental data 5 is theoretical and 6 is a static experiment

(b)

Figure 2.9 SHPB Results for thick specimens.

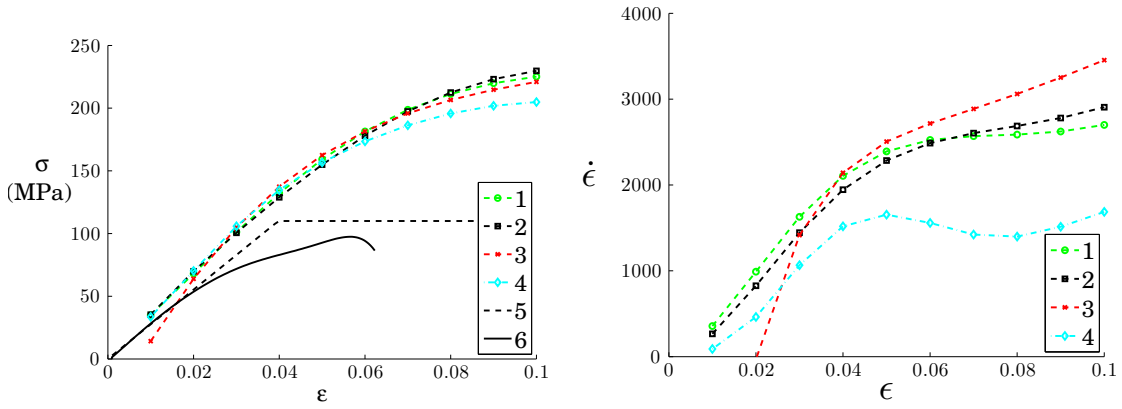

(a) 1-4 are experimental data, 5 is static theoretical and 6 is a static experiment

(b)

Figure 2.10 SHPB Results for thin specimens.

With a good understanding of the deformation response as a function of strain rate, we can develop a material model to predict material behavior. For materials which have a rate independent modulus (i.e. the modulus is constant) while only the yield stress (the point at which permanent deformation occurs) changes as a function of rate, we use the Cowper-Symonds overstress power law which has the form;

$$\dot{\varepsilon}^{pl} = D(R-1)^n \tag{2.1}$$

where D and n are material constants and R is the yield stress ratio, $\frac{\sigma}{\sigma_0}$. σ_0 is the static (or reference) yield stress and σ is the current yield stress. Using SHPB tests, we were able to determine D and n based on the compressive strain rate tests. These results are plotted in figure 2.11, where the circles represent the experimental data. The curve fit produced the parameters as shown in table 2.3. The reason for the rate dependency is the inability for the chains to slide past one another at the same rate when the rate of straining increases, thus preventing large visco-plastic strains from occurring and creating large stresses. This phenomenon eventually leads to brittle, abrupt, failure rather than ductile, elongational, failure.

Table 2.3 Cowper-Symonds Parameters for SC-15.

D	n
4880	2.883

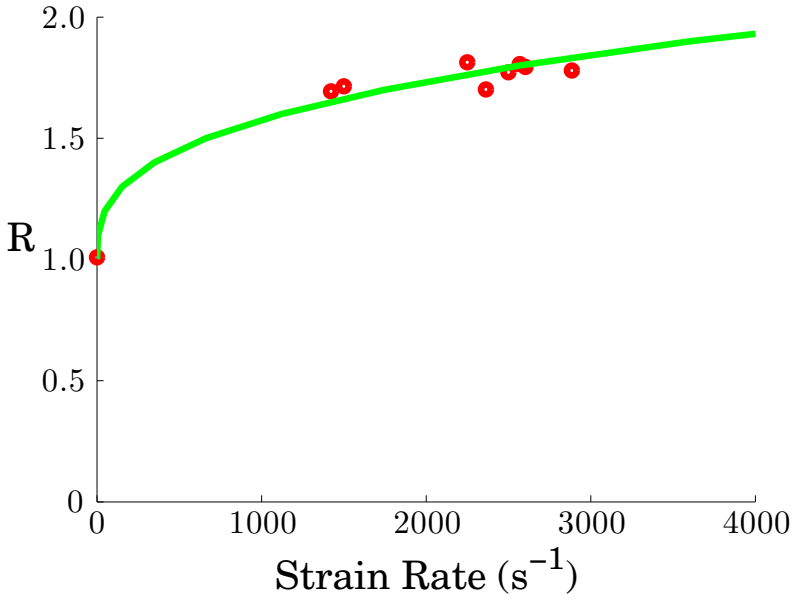

Figure 2.11 $\dot{\varepsilon}$ vs. $\frac{\sigma}{\sigma_0}$: Strain Rate Dependency of SC-15

2.3 S-2 Glass

S-2 glass was chosen as the material for the fibers, due to its high energy absorbtion ability as compared to carbon fiber. S-2 Glass was the first glass composite material that was developed exclusively for military application. The mechanical properties of S-2 glass are different compared to E-glass in that they are 30% stronger and about 15% stiffer. The fibers are made by pulling molten glass through tiny holes at the base of a furnace, [58]. They are part of the Magnesium-Alumina-Silicate glass family of fibers. The individual properties under static loading are reported in table 2.4 which is obtained from ref. [35].

Table 2.4 S-2 glass fiber properties

E_{11} (GPa)	G_{12} (GPa)	ν_{12}
114.2	46.5	0.22

It has been shown that the fibers are typically linear elastic in their response, while the matrix exhibits rate dependent behavior which is modeled through the Cowper-Symonds overstress model [59].

2.4 Conclusions

In this chapter details of the overall material system that will be investigated has been presented. The 3DWC was broken down into the various architectures and also the different constituents. The specimen manufacturing process was discussed and an experimental investigation into the mechanical properties of the individual constituents was done including the effects of strain rate on the matrix response.

Chapter 3

Static Properties of 3D woven composites

In order to establish a baseline of performance parameters for the various architectures three different static tests were performed. The tests were performed at the ARMY Research Labs (ARL) and included the following methods; Tensile, Short Beam Shear, Laterally Constrained Compression. Tables 3.1-3.5 show the representative properties obtained from each of the experimental tests. Preliminary results show that the 6% Z-fiber reinforced architecture has the best static mechanical properties with respect to both stiffness and strength. Many of these results will be carried over into dynamic simulations to provide a baseline for material properties.

3.1 Introduction

Three different static tests were performed on many of the 3DWC architectures that were designed for this project. The tests were performed at ARL and test results were sent to the author, in tabulated and graphical format. Therefore some conclusions can be drawn from this data, however concrete and detailed observations of the failure modes and architecture dependent reasoning of failure mechanisms will not be attempted. The static test results are presented here simply as a baseline, and to show trends that can be related to test results obtained by the author.

The first test performed was a simple tension test, with three different orientations being tested; $0^o, 45^o$, and 90^o. The orientations are as indicted in figure 3.1. These different orientations will tell us both the weft (0^o) and warp (90^o) in-plane moduli and also the in-plane shear component from the 45^o specimen. From these tests the failure strength was also recorded.

Historically is has been seen that weaving causes some reduction in the in-plane mechanical properties, however this is typically seen as a reduction of about 4% [15, 16, 9]. Other researchers have shown that the mechanical properties will be heavily dependent upon

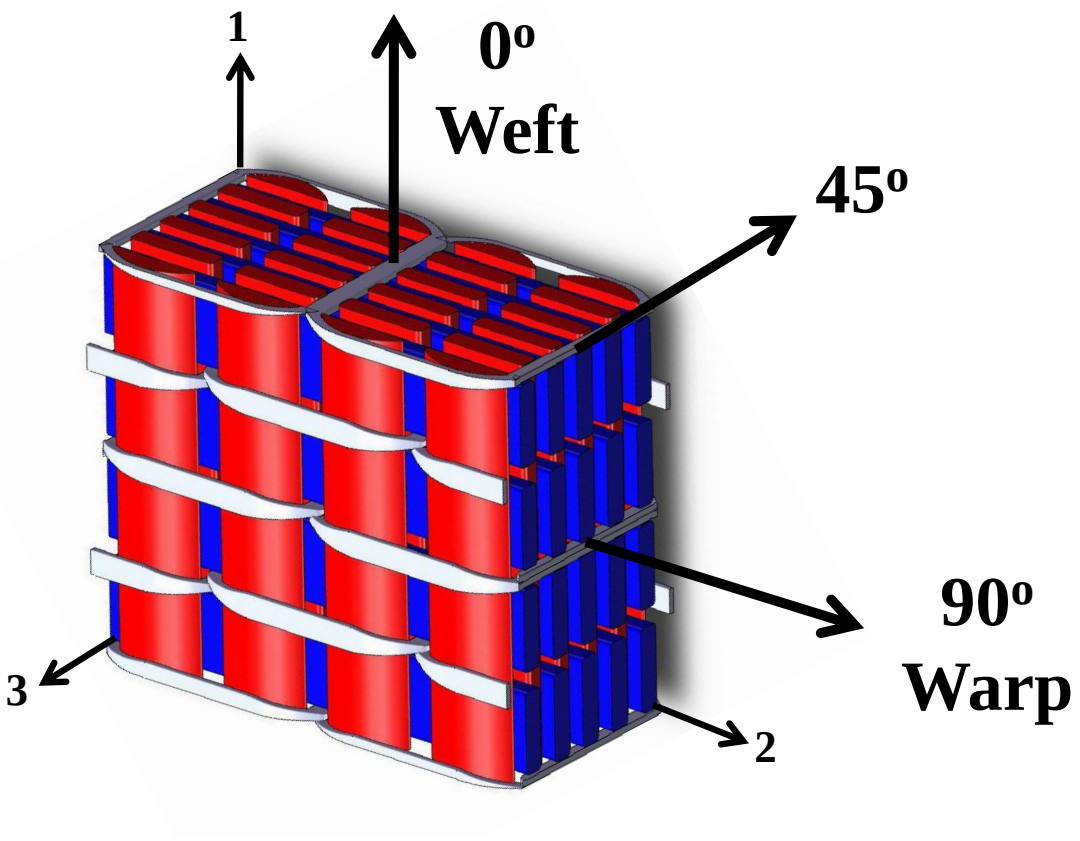

Figure 3.1 The different in-plane material orientations for mechanical testing. The overall orientation of entire specimen is also give.

the chosen architecture [11]. Some studies have specifically looked at how the Z-fiber will influence the failure path [13], showing that the Z-fiber is typically a source of failure. It has been shown that variances in weaving tensions can also affect the properties measured using tensile tests, [12].

The second test is a short beam shear test which is aimed at providing the through the thickness shear modulus, either G_{13} or G_{23}. The test was originally designed to determine the inter-laminar shear strength for layups of unidirectional composites. It will be discussed later that this may not be a good test for 3D woven specimens due to a different failure mode that occurs. Again, there were three different orientations that were tested; $0^o, 45^o$, and 90^o.

The final test that was performed was designed to determine the fiber tow shear strength. Designed by Dr. Chian-Fong Yen of ARL, the test started as a standard compression test, but after confining the sides from movement, it is possible to induce through-the-thickness shear failure in the sample. The test is only performed in though-the-thickness direction because this is the most likely failure plane to have fiber tow shear failure. Three different orientations were tested; $0^o, 45^o$, and 90^o.

3.2 Tensile Tests

The tensile tests were performed according to ASTM standard D3039, [60]. According to this specification strips of the specimen were cut and tabs were bonded to the end of the specimen to create better gripping surfaces. The test were conducted at a rate of 0.05 in/min (1 mm/min), while cross head displacement and, DIC data were collected to obtain the representative stress-strain curve for the material. The data is reduced to produce the effective Young's modulus and also the maximum strength. The results are shown in tables 3.1 and 3.2 and figures 3.2 and 3.3. It is observed from these results that the 6% Z-fiber composite has the largest tensile modulus and also one of the largest tensile strengths.

Table 3.1 Tensile Modulus (Msi)

	0^o	45^o	90^o
Baseline	3.06 ± 0.01		
6%	3.560 ± 0.206	1.084 ± 0.04	3.113 ± 0.16
10%	2.575 ± 0.04	1.145 ± 0.07	2.362 ± 0.18
12^o	2.945 ± 0.06	1.252 ± 0.07	2.297 ± 0.04
20^o	2.356 ± 0.08	0.930 ± 0.01	2.306 ± 0.02
60^o	2.195 ± 0.07	0.967 ± 0.04	2.042 ± 0.09

Table 3.2 Tensile Strengths (ksi)

	0^o	45^o	90^o
6%	67.60 ± 8.78	20.45 ± 1.22	78.79 ± 2.23
10%	78.03 ± 2.77	23.82 ± 1.07	71.55 ± 5.40
12^o	73.55 ± 3.91	12.09 ± 0.16	31.40 ± 2.39
20^o	53.01 ± 2.59	12.27 ± 0.11	30.40 ± 3.07
60^o	57.14 ± 3.64	11.10 ± 0.34	28.60 ± 1.87

3.3 Short Beam Shear Tests

Short beam shear tests were performed in accordance with ASTM standard D 2344, [61]. Specimens were cut from the quarter inch thick panels to produce relatively small specimens, due to the fact that the width and length are twice and six times the thickness of the specimen respectively. The specimens were loaded at at rate of 0.05 in/min (1.0 mm/min). The test

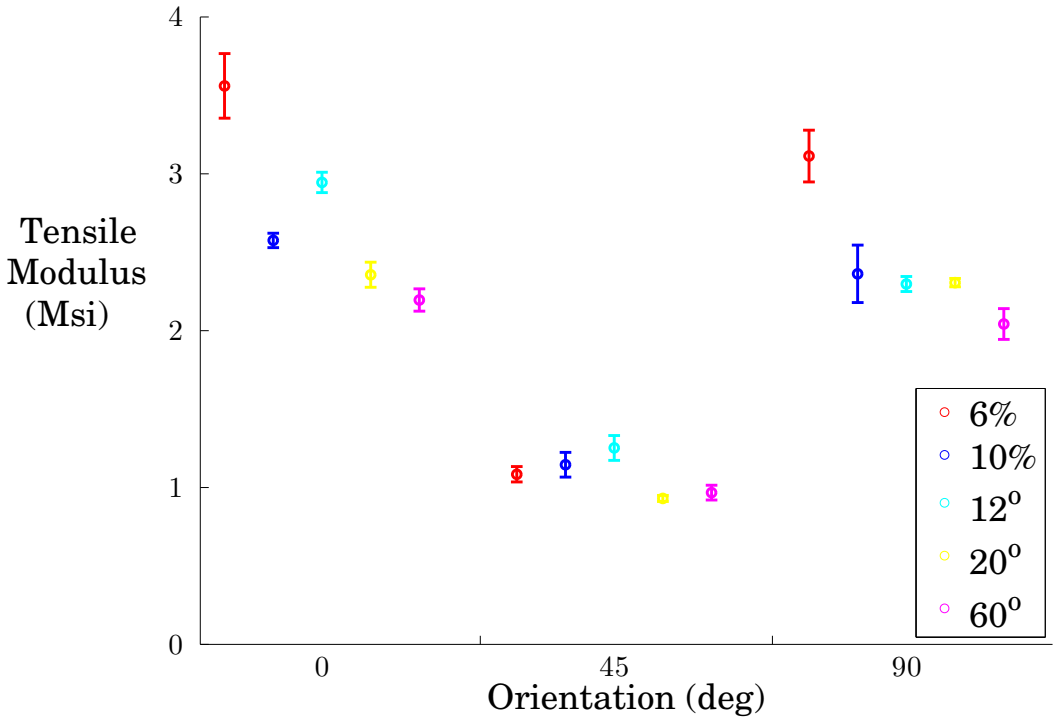

Figure 3.2 Tensile modulus vs. panel orientation for various different architectures

are not necessarily reflective of the actual properties of the material, since the test is poorly designed for reinforced materials. The standard was based on laminated composites. When Z-fibers are present in the architecture, the material may not necessarily fail by delamination. More often than not the material would fail in bending under the indenter tip either through local compression (which leads to kink band formation) or tensile failure in the matrix. However with all this being said, it is still a good test for comparison purposes, because the bending modulus will be indicative of the 3DWC stiffness and also the 3DWC resistance to shearing. Therefore we can again draw some conclusions based on the initial shear modulus, however the values calculated for shear strength may not necessarily be a good indicator of the different failure modes. Table 3.3 and figure 3.4 show a comparison of the shear moduli of the various different architectures. It is apparent that the 6% Z-fiber and the 3% Z-fiber have the highest resistance to bending. Table 3.4 and figure 3.5 show a comparison of the shear strengths of the various architectures. Although there is scatter a clear trend that appears showing that the 6% Z-fiber reinforced has the highest effective "shear strength". Although the 3% Z-fiber is relatively stiff in bending it tends to fail earlier due to matrix

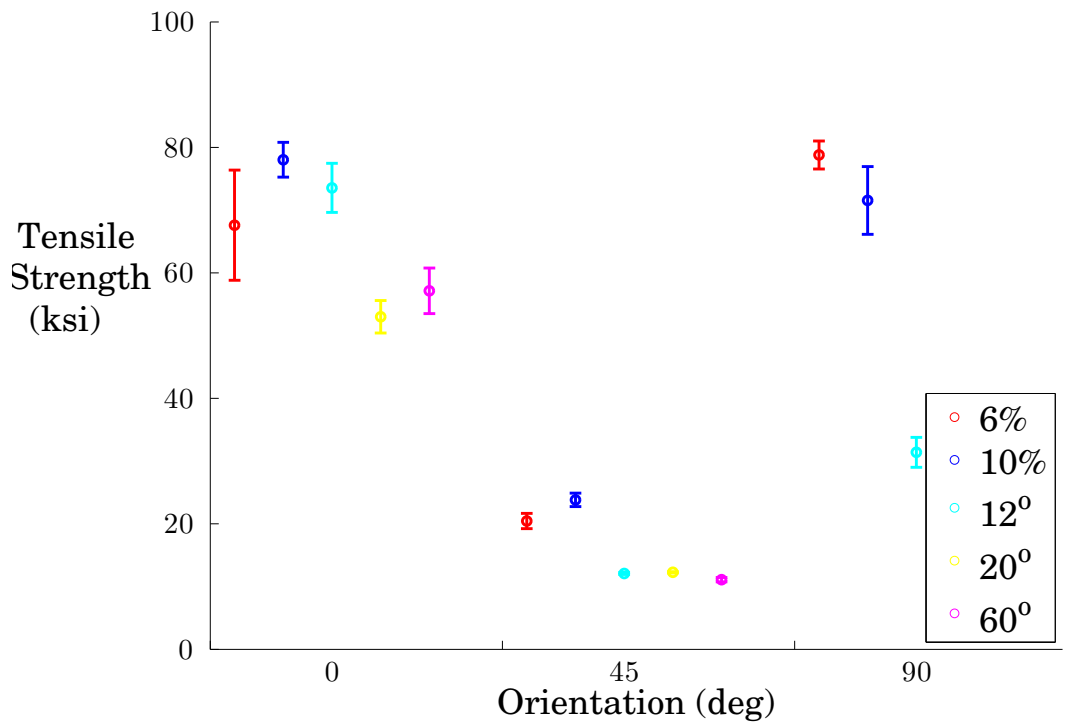

Figure 3.3 Tensile strength vs. panel orientation for various different architectures

cracking. Similar experimental results with additional details have been reported in reference [62]. It should be noted here that the shear moduli values supplied by ARL are very low. The values are about 10% Z-fiber of the shear modulus of pure SC-15 matrix, however since we do not have the raw data it was not possible to determine the error of the ARL calculations.

Table 3.3 Shear Modulus (ksi)

	0^o	45^o	90^o
3%	18.38 ± 2.32	11.13 ± 0.44	20.29 ± 1.43
6%	18.21 ± 0.57	7.94 ± 0.57	16.95 ± 1.02
10%	16.15 ± 1.31	8.15 ± 0.38	13.78 ± 0.75
20^o	13.16 ± 0.88	7.10 ± 0.14	13.46 ± 0.42
60^o	12.02 ± 2.32	7.60 ± 0.65	13.29 ± 0.30

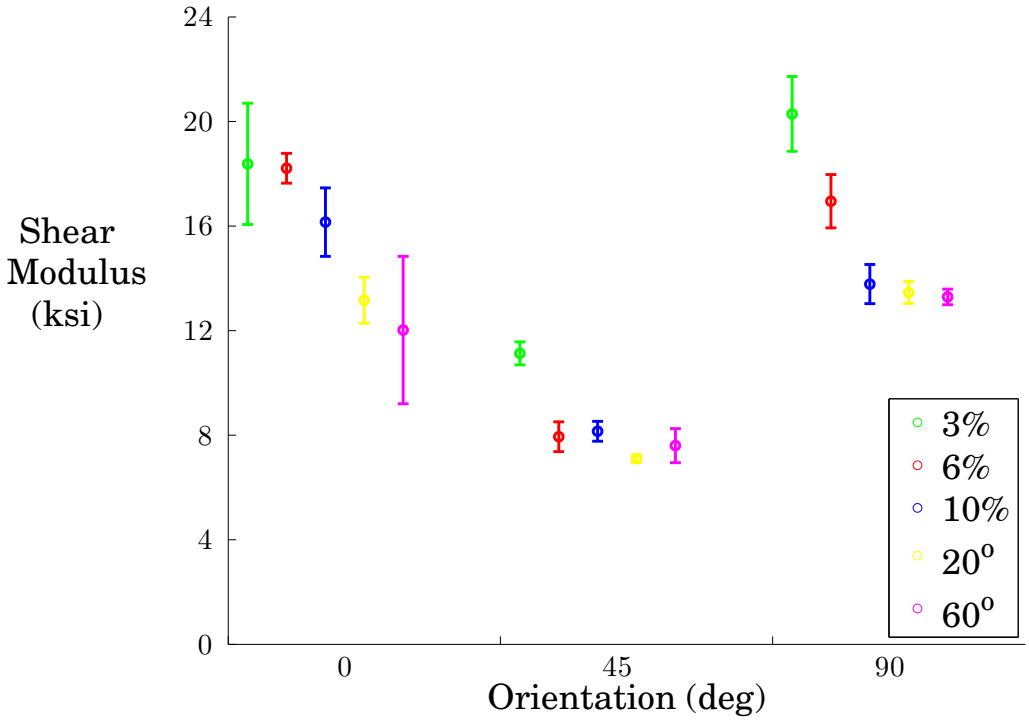

Figure 3.4 Shear modulus vs. panel orientation for various different architectures

Table 3.4 Shear Strengths (ksi)

	0^o	45^o	90^o
3%	3.59 ± 0.30	2.41 ± 0.13	3.84 ± 0.06
6%	5.30 ± 0.15	2.34 ± 0.15	4.85 ± 0.32
10%	4.75 ± 0.17	2.16 ± 0.03	3.99 ± 0.10
20^o	4.46 ± 0.12	2.56 ± 0.11	4.09 ± 0.21
60^o	4.36 ± 0.20	2.20 ± 0.11	3.40 ± 0.18

3.4 Laterally Constrained Compression Tests

The laterally constrained compression test is similar to that of a compression test through the thickness of the material however the material is prevented from expanding in the x and y directions if compressed in the z direction. The constraint essentially prevents lateral expansion due to poisson's ratio, causing higher loads and resistance to failure, often producing different types of failure not seen in a standard compression test. The material is

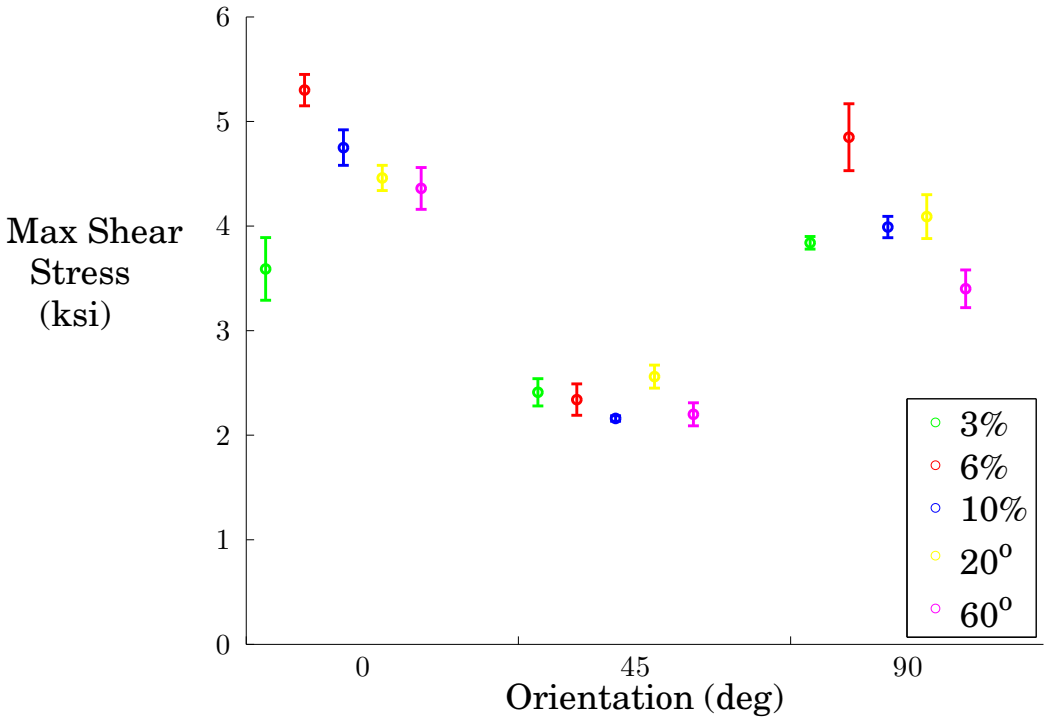

Figure 3.5 Shear strength vs. panel orientation for various different architectures

forced to fail by a shear band formation typically shearing the fibers tows. This test was designed by Dr. Chian-Fong Yen at ARL and is aimed at simulating the failure that occurs during ballistic testing. There is currently no ASTM standard for this test. The results focus on the angle of the shear band that is formed in the specimen along with the maximum load that is carried. The results are shown in table 3.5 and figure 3.6. The test should produce similar results in both the 0^o and 90^o orientations because the shear band will form in the weakest plane. There were some samples where this was not the case, however since we don't have the tested samples no conclusions can be drawn. The 6% Z-fiber sample seemed to consistently have the highest strengths in all orientations. The 10% Z-fiber sample had very similar results however the 90^o orientation was a bit lower.

Table 3.5 Compressive Strengths (ksi)

	0^o	45^o	90^o
3%	52.10 ± 1.04	55.16 ± 2.06	55.45 ± 2.80
6%	91.37 ± 7.53	89.27 ± 3.42	92.44 ± 5.58
10%	91.86 ± 4.69	93.75 ± 1.12	79.47 ± 7.73
12^o	95.44 ± 2.46	78.74 ± 2.32	73.86 ± 1.34
20^o	63.44 ± 2.87	63.70 ± 1.50	66.67 ± 2.90
60^o	70.98 ± 2.37	69.31 ± 3.16	55.62 ± 3.00

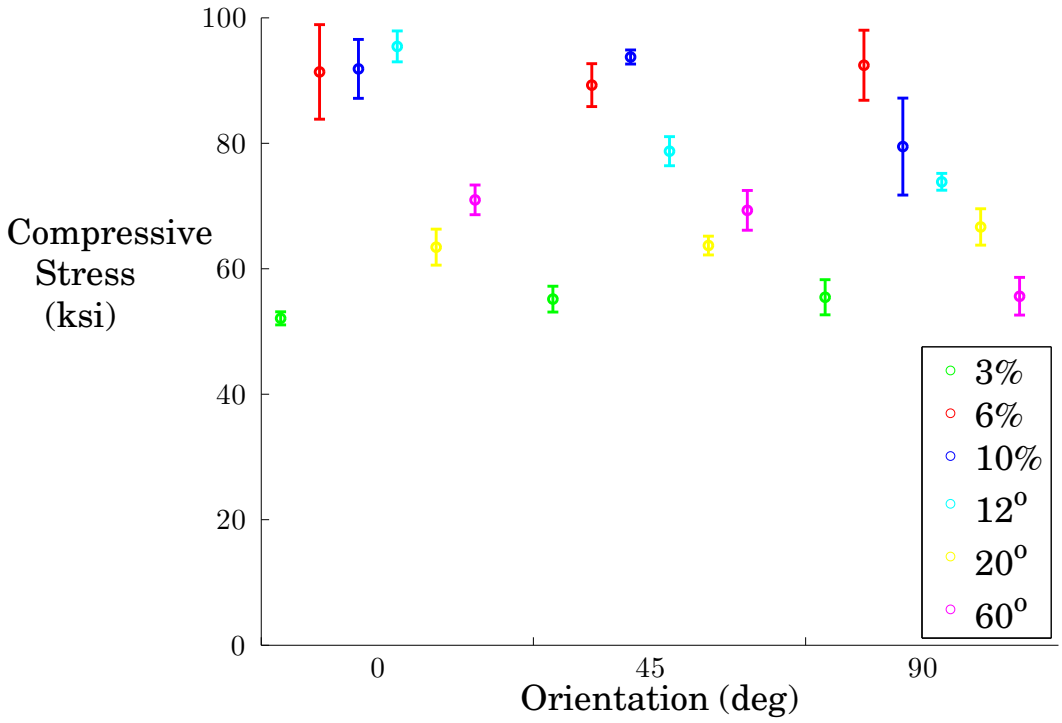

Figure 3.6 Compressive strength vs. panel orientation for various different architectures

3.5 Conclusion

Static tests were performed on each of the various different 3DWC architectures so that a comparison of mechanical properties could be made. The results showed that the 6% Z-fiber architecture may be the "best" architecture to provide both strength and stiffness, however the layer to layer architectures may be better at providing energy absorbtion under transverse

impact than the Z-fiber reinforced composites.

Chapter 4

Fracture Toughness and Shear properties.

The End Notch Flexure (ENF) tests for woven composites were performed on the various different 3DWC architectures supplied by Albany Engineered Composites. A schematic of the ENF setup can be seen in figure 4.1. The architectures were chosen for the ENF tests because the thick panel behavior is much easier to characterize through an ENF test. Two of the architectures have similar weaving patterns (Albany 1 and Albany 7) that are Z-fiber architectures described in chapter 2. Albany 2 has a different architecture which takes the warp fibers and turns them into the Z-fibers by weaving them between the weft tows. Experimental results showed that Albany 2 did not allow for crack propagation, but rather it localized the delamination failure. Albany 7 provided the best fracture strength in static testing , although Albany 1 was somewhat comparable. Three different loading rates were examined using the Albany 7 architecture and rate dependent properties were found to exist in the material.

4.1 Introduction

The problem of delamination can be improved with the technique of 3D weaving. The insertion of a Z-fiber produces reinforcement that is otherwise not present in laminated composites to prevent delamination from occurring. The fibers that run between the layers provide reinforcement to the matrix which is the only material that is holding the different layers together. The fibers will bridge the cracks that occur parallel to the layers in the matrix, reinforcing the material and allowing stable crack propagation. The layer to layer architecture is very useful because each of the fiber tows is constantly changing layers and essentially "confuses" the crack path and prevents it from propagating any further. "Confused" refers to the idea that it doesn't provide a clear pure resin layer for delamination

to propagate. The ENF test has been used to study mode II fracture behavior of laminated composites [63] and with the insertion of carbon nano-tubes for some bridging effect [64].

4.2 Static results

Experimental results related to static mode II fracture tests are presented in this section. Two tests were performed. One at a loading rate of 0.0004 in/sec (1mm/min), while a second test was performed at 2 in/sec (3 m/min) to determine the influence of elevated loading rate on fracture toughness. Figure 4.1 shows a representation of the test and some of the associated parameters. The geometry of the test specimens used are given in table 4.1. Specimens were statically loaded on a hydraulically activated MTS machine. Images of the specimens were taken during deformation using a Nikon D2X camera, which has a 12.8 MP CMOS sensor, at 2 second intervals to track the trajectory of the crack during loading. For tests performed at 2in/sec (3 m/min) a Photron SA.5 camera was used to acquire images at 2000fps. This provided more than adequate information to determine the fracture toughness.

Table 4.1 ENF Test Specimen Dimensions (refer to figure 4.1.)

		(mm)	(in)
Length		160	6.30
Width	b	25.4	1.00
Thickness	h	12.7	0.50
Length of initial crack		40	1.57
Distance between supports		120	4.73
Support Distance from end		20	0.79

The Z-fiber reinforced architecture of Albany 1 and Albany 7 is an architecture which uses Z-fiber tows to reinforce the panels, by binding the warp and weft fiber tows together. This causes distinct layers of warp and weft fiber tows held together by Z-fiber tows. Figure 4.2 shows a schematic of the load-displacement response that is characteristic of these materials. There is an initial slope where there is no crack. When the crack starts to grow, a change in slope of the load-displacement response is observed. As the crack propagates the slope remains constant at the new slope. The Z-fiber does not fail in this case providing reinforcement and additional resistance to crack propagation that will allow for the load to increase. Following the crack propagation, a drop in load is typically seen when a kink band forms in compression under the loading head, along with matrix cracking on the outer surface due to tension.

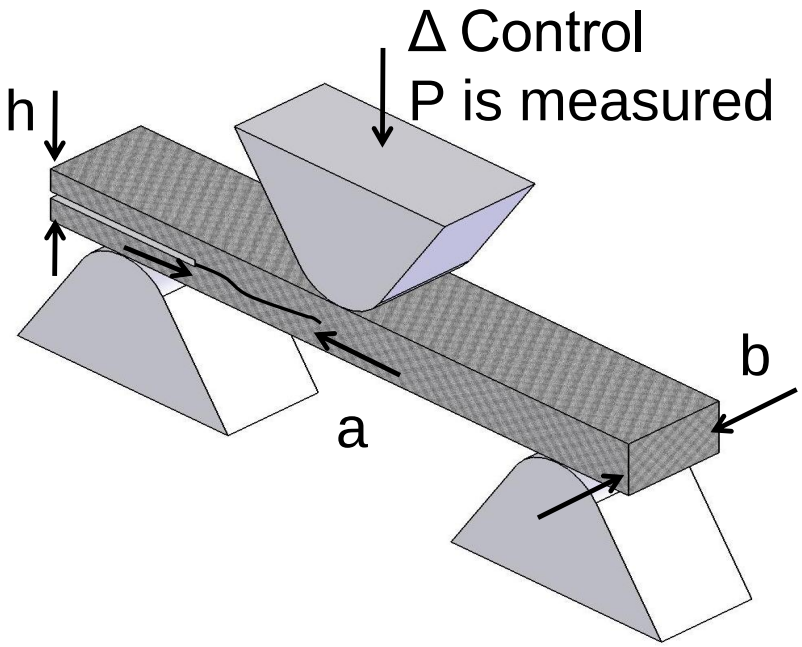

Figure 4.1 ENF test set up and determined parameters.

The layer-to-layer architecture of Albany 2 is an architecture which removes the Z-fiber tow and instead uses the warp fiber tow to weave the layers together. This architecture does not have distinct layers like Albany 1 and Albany 7. The weft fiber tows are the only tows to have a straight orientation. A typical loading curve can be seen in figure 4.3 which demonstrates a completely different failure mode. After the initial loading, small localized delaminations occur in layers near the point of the loading head. This is where the shear stress is the highest. When these micro cracks are formed, the load plateaus at a constant value while the specimen is still deforming. The main crack does not propagate from the notch end rather from localized delamination that is interrupted by the Warp/Z-fiber. These results show that the material has the ability to dissipate a lot of energy through deformation instead of a catastrophic failure. This is a prime example of where one could develop an architecture for a specific service loading environment.

Figure 4.4 shows a representative load deflection curve for each of the different architectures at each of the two separate rates. Derived parameters including slope, maximum load and other information are noted in tables 4.2 and 4.3. The Albany 1 and 7 specimen plots have a corresponding identification for the start of the crack (square indicator) and the crack growing until it reaches a point below the indenter head (circular indicator).

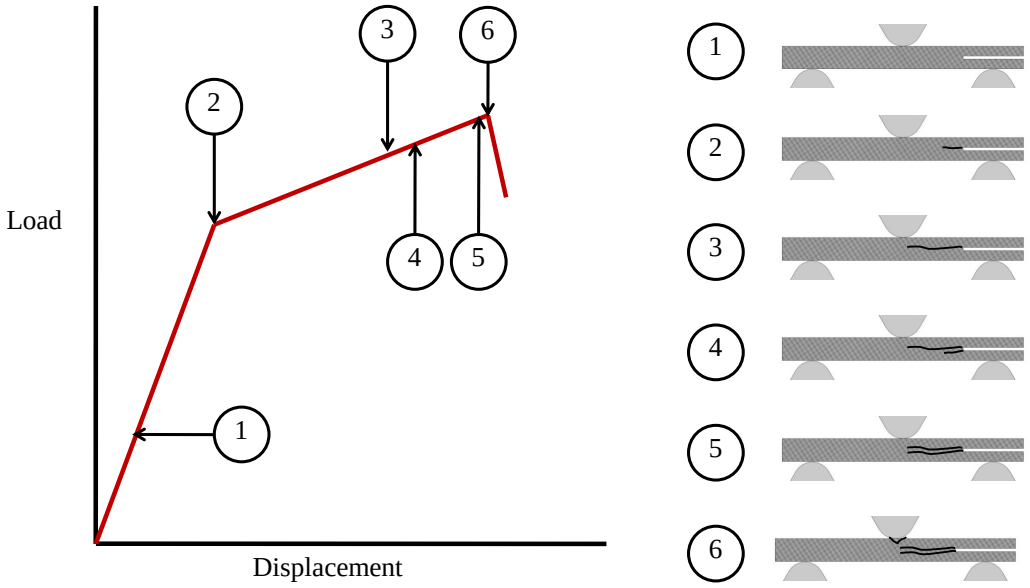

Figure 4.2 Typical Albany-1 or Albany-7 response. Crack start to grow at 2. Major crack reaches point below indicator head at 3. Secondary crack starts from initial/main crack location at 4. Secondary crack reaches point under indicator head at 5. Kink band failure occurs below indentor at 6, which corresponds to a decrease in load.

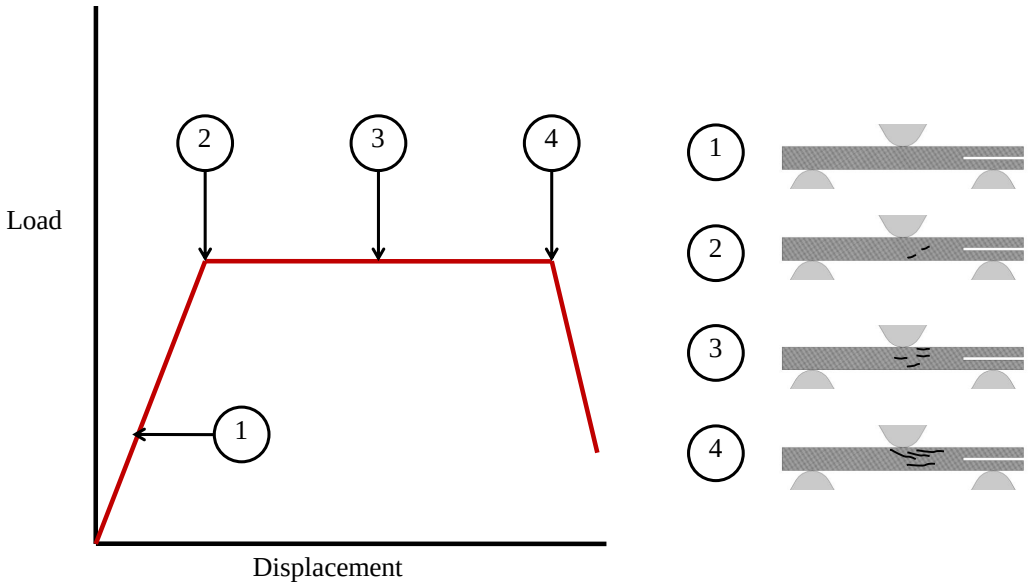

Figure 4.3 Typical Albany-2 response. Small localized delamination cracks start to form in between fiber tows at 2. The cracks propagate until they run into Z-fibers and more are formed, while the load remains constant at 3. Kink band failure occurs below indentor at 4, which corresponds to a decrease in load.

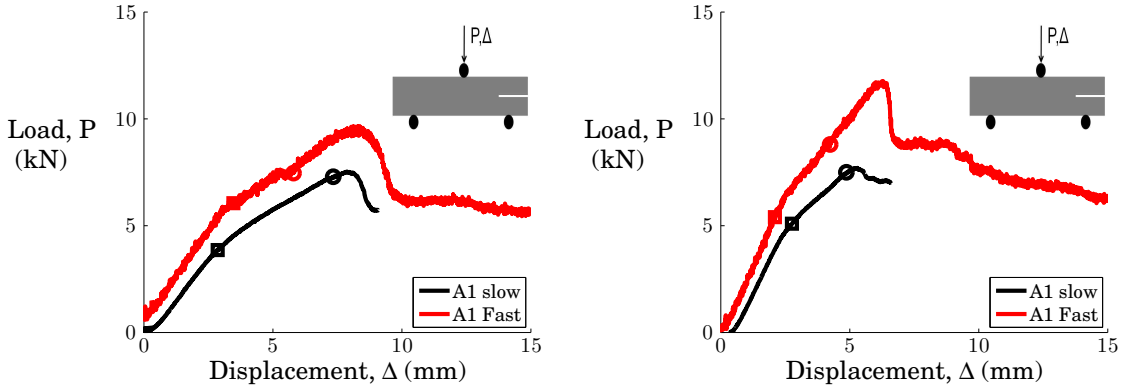

(a) Albany 1 Warp

(b) Albany 1 Weft

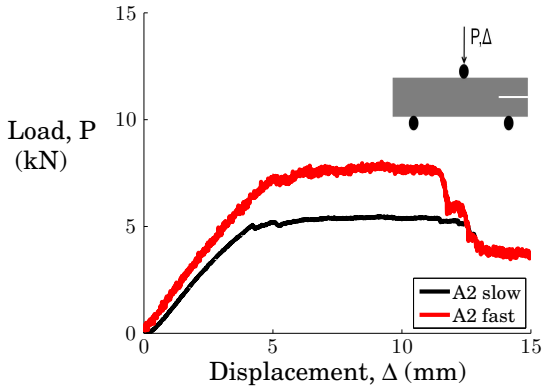

(c) Albany 2 Warp

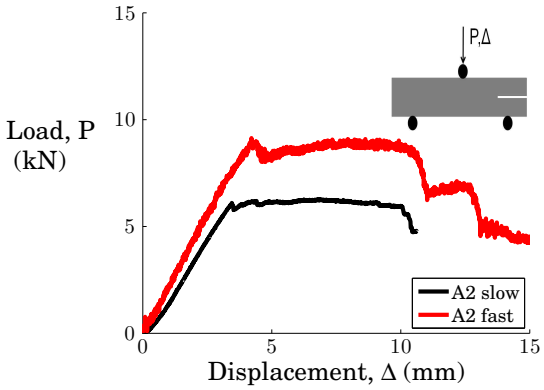

(d) Albany 2 Weft

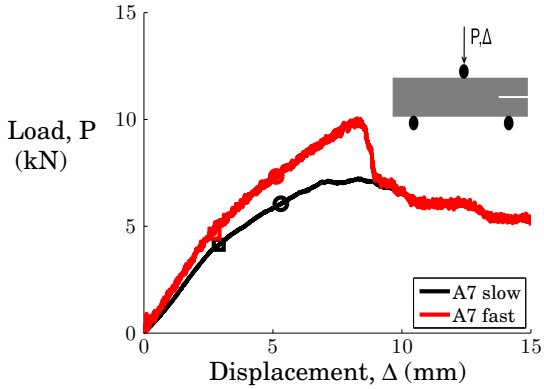

(e) Albany 7 Warp

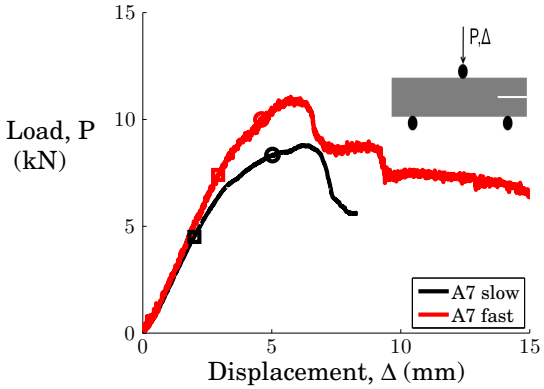

(f) Albany 7 Weft

Figure 4.4 Representative Load vs. Center point displacement for each of the 3DWC architectures at the two different loading rates. The square represents the start of the crack while the circle represents the crack reaching the center of the specimen, below the loading roller.

Table 4.2 ENF Parameters and values at a rate of 0.0004 in/sec

		$InitialSlope$ $(\frac{N}{mm})$	$SecondarySlope$ $(\frac{N}{mm})$	$MaximumLoad$ (N)
Albany 1	Warp	1585 ± 90	653 ± 15	7091 ± 388
	Weft	2492 ± 25	1121 ± 55	8070 ± 384
Albany 2	Warp	1452 ± 83	N/A	5350 ± 164
	Weft	2079 ± 30	N/A	6737 ± 471
Albany 7	Warp	1641 ± 50	670 ± 40	7502 ± 242
	Weft	2604 ± 128	1132 ± 237	9768 ± 960

Table 4.3 ENF Parameters and values at a rate of 2 in/sec

		$InitialSlope$ $(\frac{N}{mm})$	$SecondarySlope$ $(\frac{N}{mm})$	$MaximumLoad$ (N)
Albany 1	Warp	1708 ± 31	842 ± 53	9672 ± 417
	Weft	2583 ± 88	1300 ± 232	11102 ± 727
Albany 2	Warp	1534 ± 93	N/A	7439 ± 596
	Weft	2199 ± 125	N/A	8827 ± 526
Albany 7	Warp	1787 ± 18	879 ± 15	10446 ± 452
	Weft	2700 ± 75	1198 ± 31	11979 ± 1032

Figure 4.5 compares the response of the different 3DWC architectures in the warp direction. This is the orientation that the Z-fibers are woven in, therefore there should be more binding with the Z-fiber. Both the Albany 1 and Albany 7 have similar responses, with the Albany 7 having a higher crack initiation load. The Albany 2 however carries much less load, but it is able to withstand larger displacements.

Figure 4.6 compares the response of the different 3DWC architectures in the weft direction. The weft tows run perpendicular to the Z-fibers therefore less binding will be available. Both the Albany 1 and Albany 7 have similar responses, with the Albany 7 typically having a higher crack initiation load. Albany 2 again carries less load, but is still able to exhibit larger displacements.

We can further investigate the Albany 1 and 7 materials by looking at their crack propagation. By using the photographic time history we are able to track the crack as the specimen is loaded up. Figure 4.7 shows the average crack propagation distance vs. center point displacement. It is observed that the warp direction crack propagation is typically slower than that of the weft for both loading rates. Again the Z-fiber being woven in this direction will contribute to this slower movement of the crack since the fiber will inhibit its path. There was not much distinction between the two rates except for the warp direction where

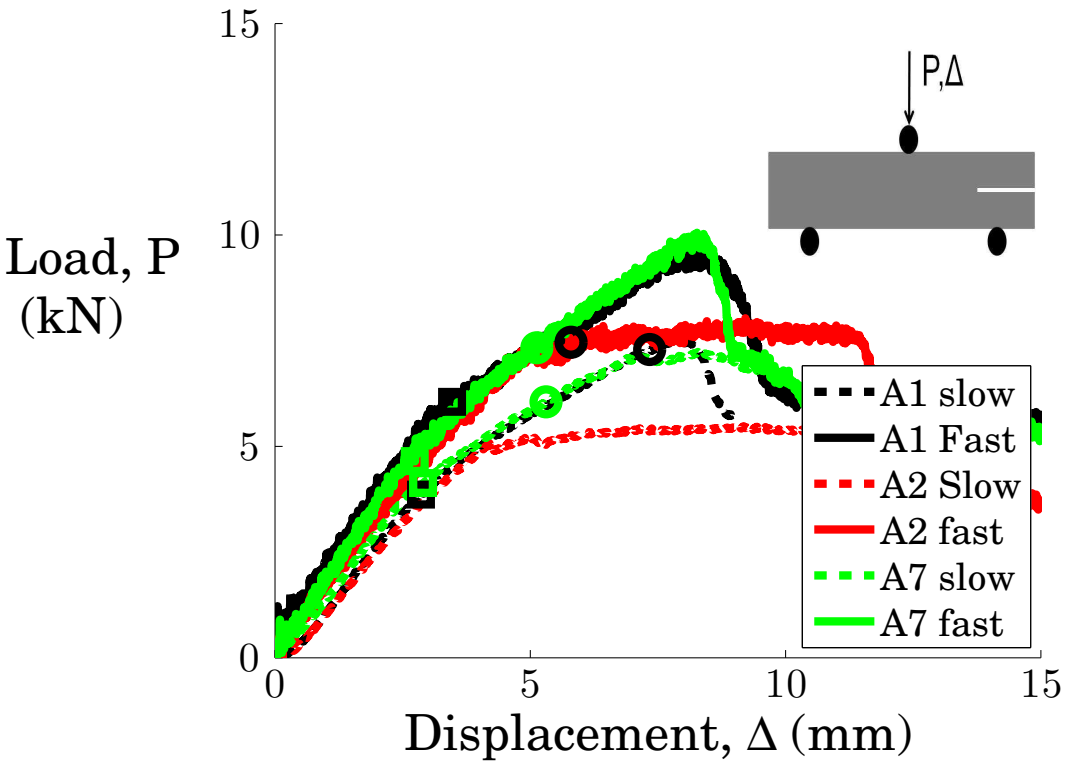

Figure 4.5 Comparison of Warp Direction Response.

the speed clearly sped up the crack propagation. However it should be noted that the crack typically started at a higher load as the loading rate was increased. It should also be noted that both specimens have stable crack growth, since the load continues to increase after the initial crack starts to propagate. This stable propagation is due to the Z-fibers bridging the crack, still transferring load across the crack faces.

Figure 4.8 shows a very similar trend to the Albany 7 architecture. Again the crack propagated at a higher deflection in the warp direction. However both directions seem to have similar propagation lengths and also showed no difference in rates, however the crack propagation load increased with the rate. Again, stable crack growth was found to occur in both orientations.

In order to get a better understanding of how the crack affects the material parameters and how progressive failure may occur in these materials, additional tests were performed.

To further investigate the materials the energy that was dissipated during failure of the materials was investigated. The energy is related to the area under the curve of the load deflection curve. Each different architecture was computed and the failure was deemed where the load dropped dramatically in the material. The associated energy was then computed for

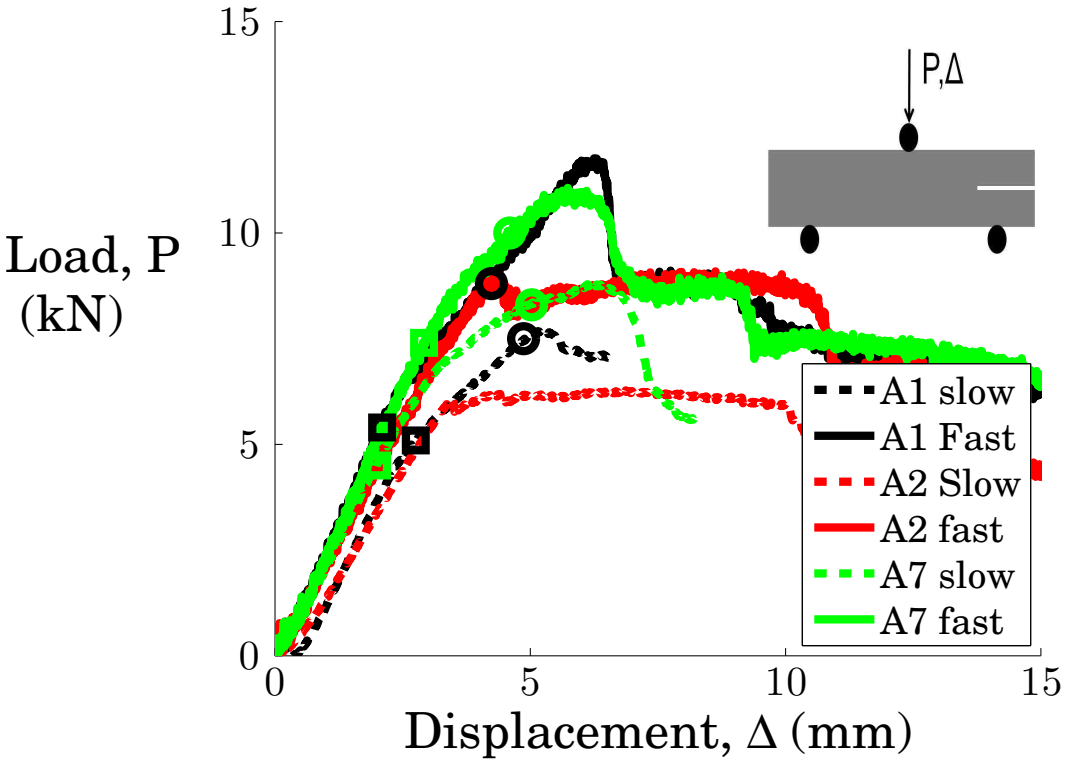

Figure 4.6 Comparison of Weft Direction Response.

each architecture and orientation. The warp orientation consistently had a higher energy dissipation than the weft direction although, a lower load was associated with failure in the warp. Additionally the Albany 2 had a much larger energy associated with failure than any of the other materials.

Table 4.4 Energy dissipation before failure of different architectures.

	Warp (kNmm)	Weft (kNmm)
Albany 1	36.6	22.8
Albany 2	54.3	50.0
Albany 7	48.9	40.4

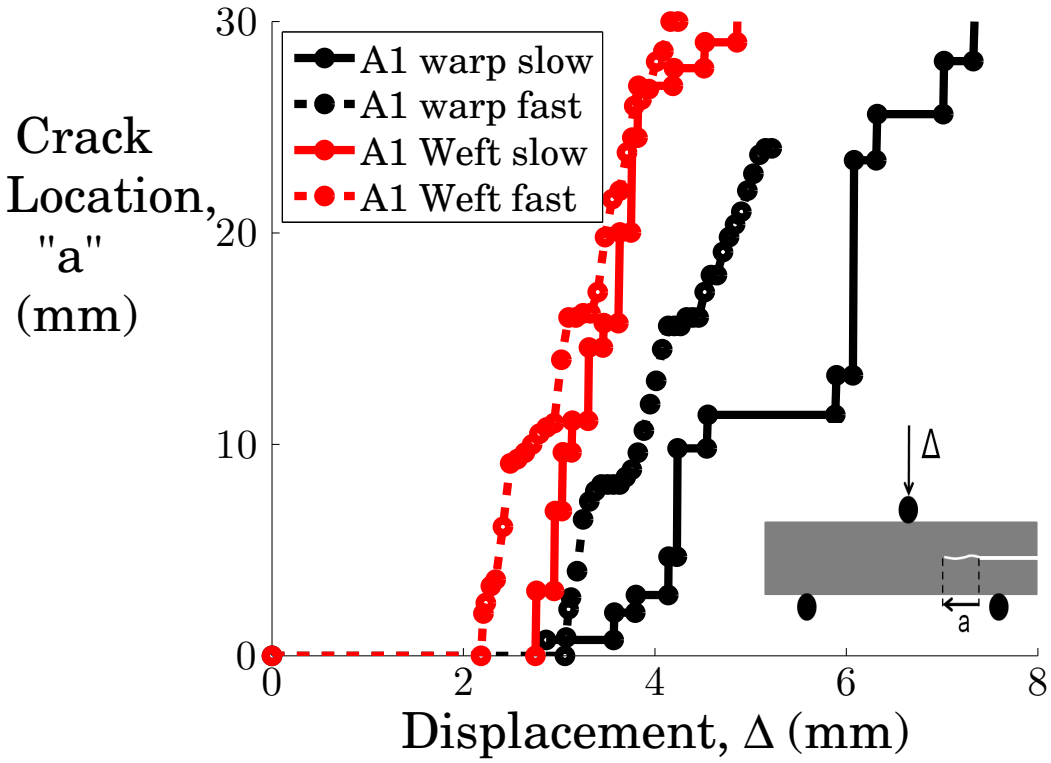

Figure 4.7 Crack propagation history for Albany 1 specimens in both directions. Crack location a, is measure as indicated in the figure legend.

4.3 Cyclic testing

Cyclic testing was performed to determine a baseline for the fracture toughness values of the different materials. The test were performed at a rate of 0.0004 in/sec (1mm/min) using displacement control. The specimens were loaded up allowing for the crack to propagate some distance, however not all the way to the center of the specimen, and then unloaded.

The cyclic loading revealed that there is very little permanent out-of-plane deformation that occurs in the material. Most of the deformation is recovered when unloaded, however the unloading path lies along a line that corresponds to a “secant” stiffness. The secant stiffness is defined as the ratio of the current load to current displacement. This shows that there is some permanent deformation in the material, however after the deformation occurs, subsequent damage does not accumulate until the material is again loaded up to the point at which the unloading took place. In terms of crack propagation, the crack will not propagate any further until the same load and deflection are reached, in a subsequent loading cycle.

One of the results that we can calculate with this cyclic loading is the fracture toughness.

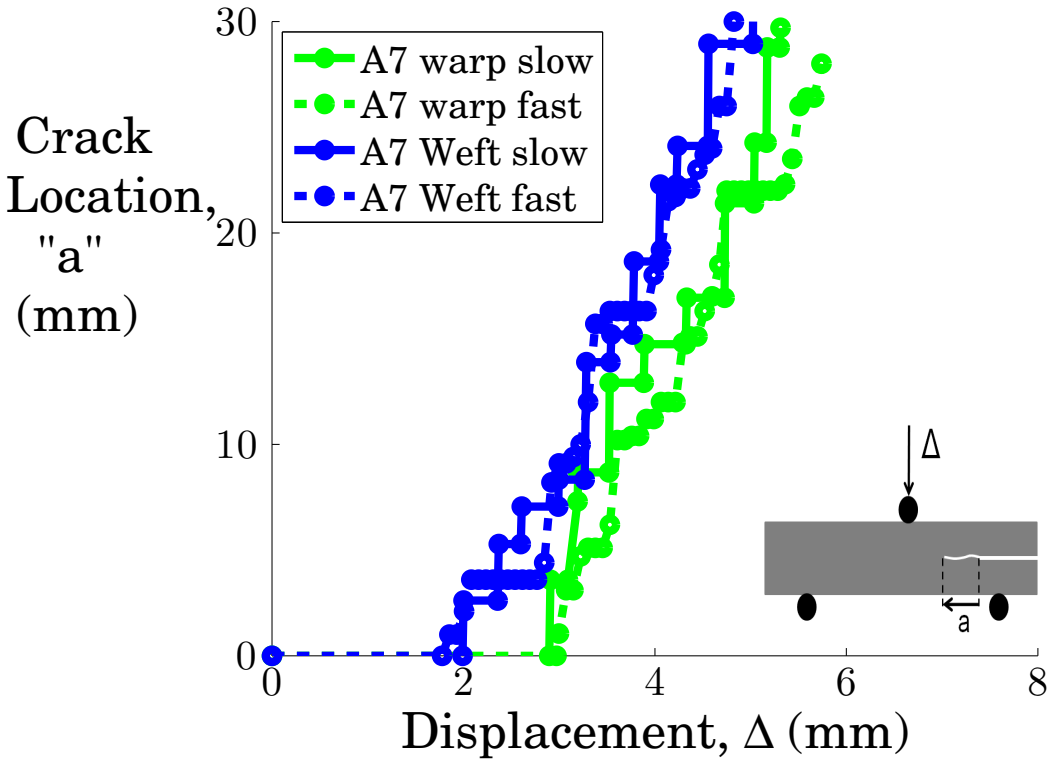

Figure 4.8 Crack propagation history for Albany 7 specimens in both directions. Crack location a, is measure as indicated in the figure legend.

The fracture toughness is related to the total area under the load and unload curve and the fracture surface areas, see figure 4.9. The relation to obtain the mode II fracture toughness is,

$$G_{IIc} = \frac{Area}{2t\Delta a} \tag{4.1}$$

where the area is the area under the first cycle of load and unload, t is the width of the specimen and Δa is the crack length. This is derived from the energy needed to open up a new crack surface. Table 4.5 shows a summary of the G_{IIc} values obtained from the cyclic loading. It should be noted that an effective value was estimated for the Albany 2 architecture, however the estimate is very rough due to the estimation of the crack surfaces. The warp direction has a higher fracture toughness as compared to that of the weft. This information will be re-examined later in the context of computational modeling.

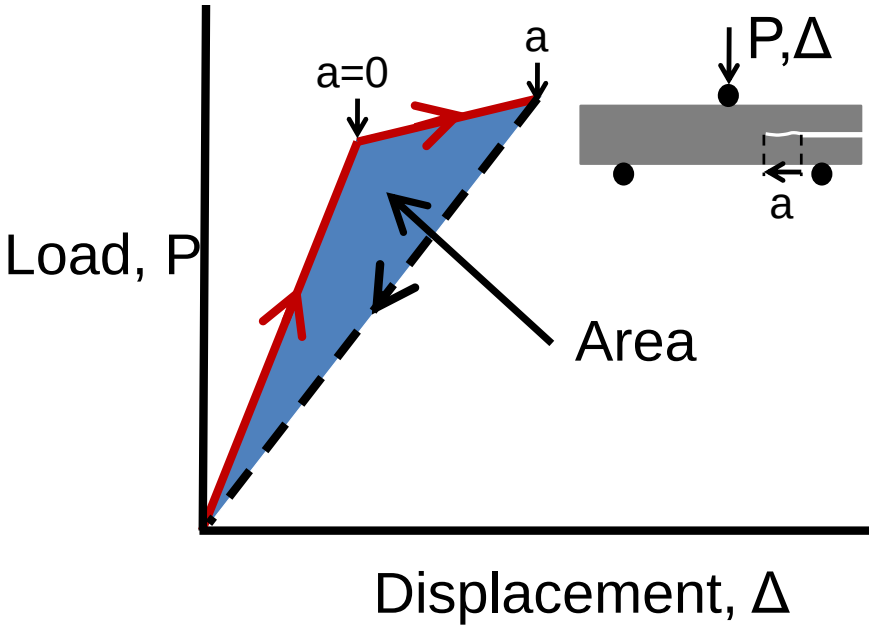

Figure 4.9 The total area under the load and unload curve. The red line represents the loading cycle while the dashed black line represents the unloading curve. The "lost" work done is converted to "fracture energy".

Table 4.5 Fracture Toughness from Cyclic Testing

		G_{IIc} $\frac{N}{mm}$
Albany 1	Warp	46.6
	Weft	33.7
Albany 7	Warp	43.3
	Weft	41.9
Albany 2	Warp	142.6
	Weft	71.9

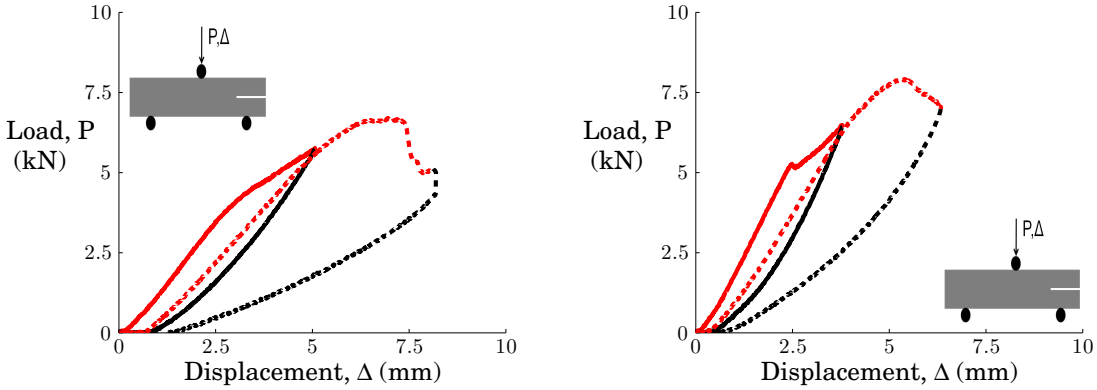

(a) Warp (b) Weft

Figure 4.10 Load vs. Center point displacement with cyclic loading for Albany 1 architecture.

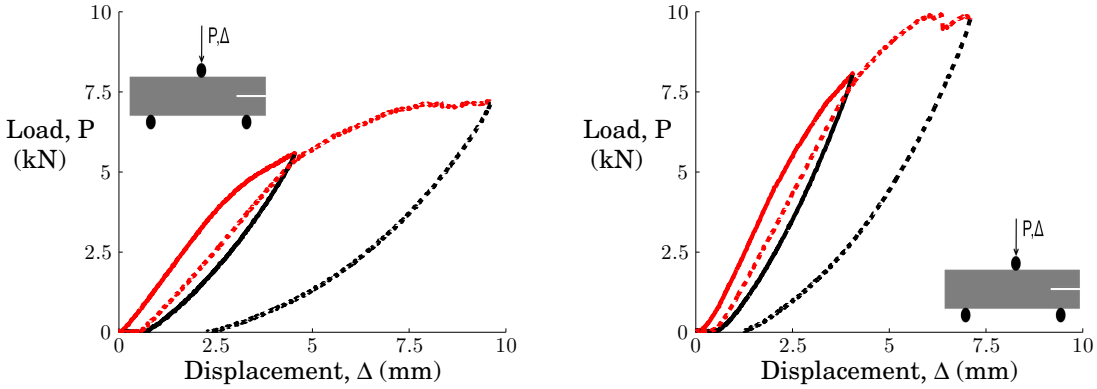

(a) Warp (b) Weft

Figure 4.11 Load vs. Center point displacement with cyclic loading for Albany 7 architecture.

4.4 Elevated Rate Loading (Low Velocity Impact, LVI)

The ENF test was performed using a low velocity drop tower to further investigate the rate effect on G_{IIc} and the maximum load obtained. The ENF test was moved to a drop tower, this is a facility in which a weight is dropped onto the specimen from a pre-determined height in order to induce a certain velocity at the impact point. The impact head contains a force transducer that is used to measure the force applied to the specimen. In these tests the focus was on the Albany 7 panels because they showed the highest strength and largest resistance to crack propagation.

Two separate heights were chosen which provided two separate impact velocities, which

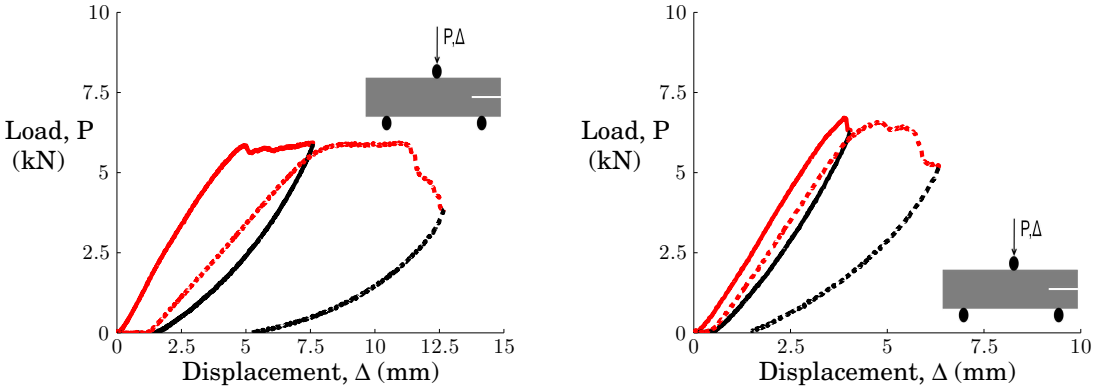

(a) Warp (b) Weft

Figure 4.12 Load vs. Center point displacement with cyclic loading for Albany 2 architecture.

can be seen in table 4.6. The warp and weft orientations were examined to determine the effect of loading rate upon the effectiveness of Z-fibers in resisting crack growth and failure.

Table 4.6 Drop Tower Experimental Setup (mm)

Height		Velocity		Mass	
(in)	(cm)	$(\frac{in}{s})$	$(\frac{m}{s})$	lb	kg
15.75	40	110	2.8	85.1	38.6
31.5	80	156	3.96	85.1	38.6

Figure 4.13 shows a representative load-deflection response for the material in the warp direction for the two different heights. Although the rates are very different there is very little difference between the responses. This is also noticed in the weft direction, see figure 4.14. The two results have been overlayed to show the same discreprency of the weft direction taking higher loads than the warp direction, see figure 4.15. To get an understanding of the full spectrum of responses, the results from all of the tests are compared in figures 4.16 and 4.17. It should be noted that in the Warp direction a unidirectional $[0]_{16}$ layup has been plotted. These were specimens studied by Huang [1], and have been included to show the increase in failure strength through the insertion of Z-fibers.

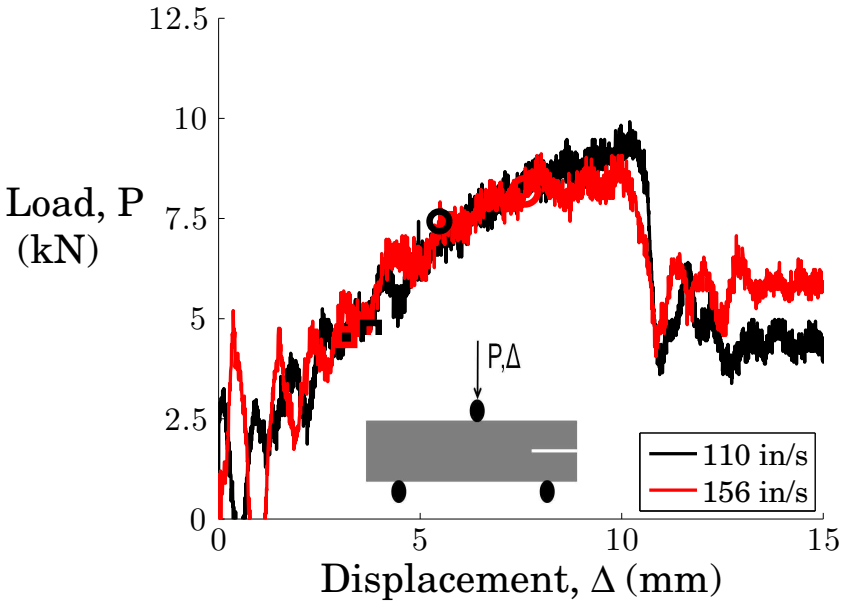

Figure 4.13 Load-Displacement curves from drop tower tests on Albany 7 material in the warp direction.

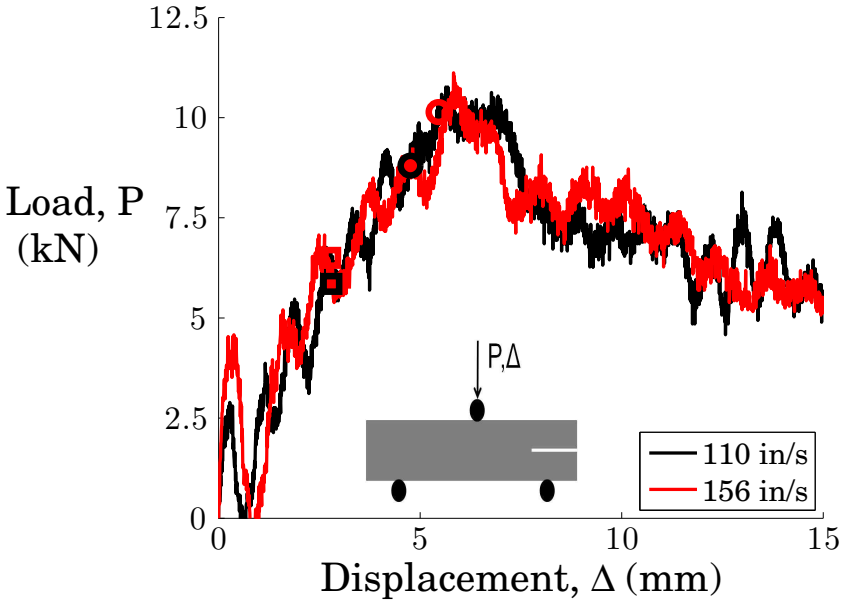

Figure 4.14 Load-Displacement curves from drop tower tests on Albany 7 material in the weft direction

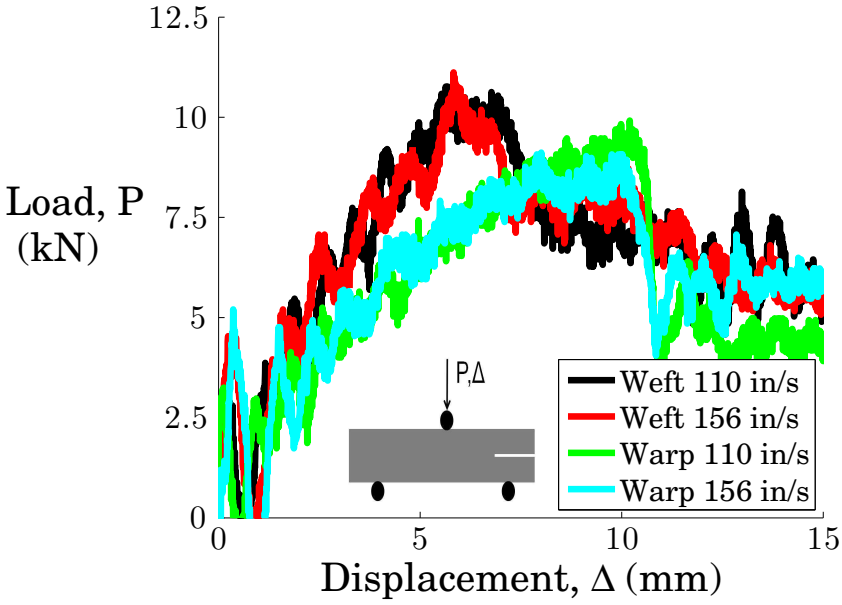

Figure 4.15 Load-Displacement curves from drop tower tests on Albany 7 material in both warp and weft directions.

Figures 4.16 and 4.17 show some were very interesting results, as higher loading rates are studied. It seems that there are two competing effects. The fracture toughness increases as a function of loading rate, but as specimen inertia increases, the relative sliding of the crack faces increases, therefore lowering the effective measured value. These two effects are working against each other, therefore, as the loading rate increases there will be a point where our load is maximum, and then begins to decrease as the inertia of the specimen becomes more dominant. This is evident in the data where it is observed that the final load has dropped at the same deflection and the peak load occurs at a loading rate of 2 in/sec. Additionally, it is seen that the specimens are forced into a separate mode of failure, instead of the material failing by kink band formation under the loading head, the Z-fibers that are bridging the crack, fail causing the load to drop. This is evident in the high speed videos, because the load drop corresponds to a time when the crack begins to open up rapidly as the two surfaces simply slide past each other due to the loss of shearing resistance from the Z-fibers.

The Photron SA.5 camera was used to be able to track the path of the crack. The camera was set at 100,000 fps and captured images that are 320 X 192 pixels in size. These images were then used to back out the crack path as before. Figures 4.18 and 4.19 show the general trends seen in the crack propagation for both the warp and weft specimens respectively. From these plots it appears that with increasing loading rate, the resistance to fracture

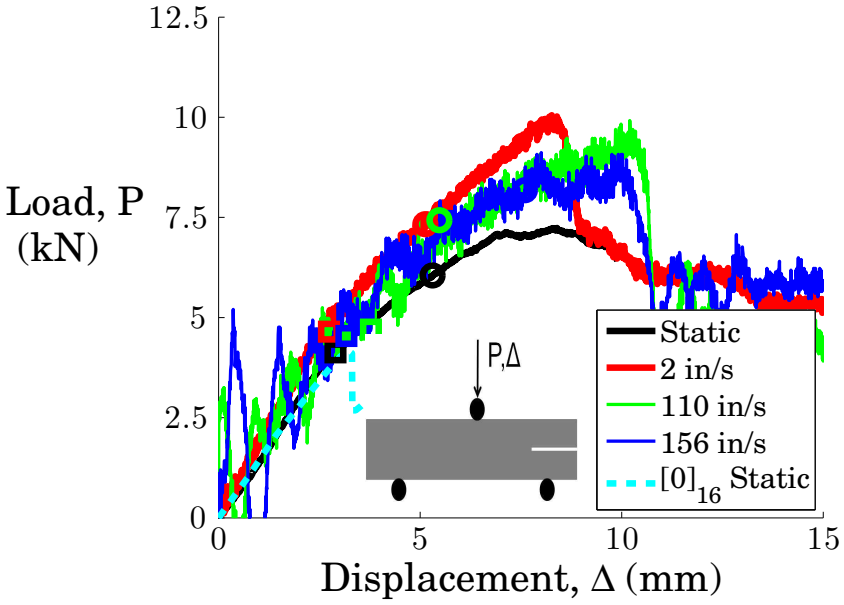

Figure 4.16 Load-Displacement curves for Albany 7 material in the warp direction at the four different rates.

increases. This is seen more in the warp than the weft specimens, but is evident in both. As the rate increases, it takes more deflection for the same amount of crack face opening. This supports the statement made previously that both inertia and fracture toughness are competing against each other because the fracture toughness is clearly increasing with strain rate. However the specimen failing at a lower level indicates that the inertia of the specimen is beginning to take over causing Z-fiber shear failure.

To provide further insight into the material response the energy dissipated to cause failure was also investigated. The warp direction consistently had a higher failure energy compared to the weft. Additionally the energy increase with increasing rate, until the final rate where it began to slowly decrease. Overall there was an increase in energy due to the rate of the material and a higher energy associated with the warp direction. Although the warp direction has a lower failure load the larger deflection associated with each load caused and increase in overall energy dissipation.

4.5 Finite Element Models

To better characterize the tests, a finite element model was created to simulate the mechanical response along with the propagation of the crack as a function of load. A 2D model

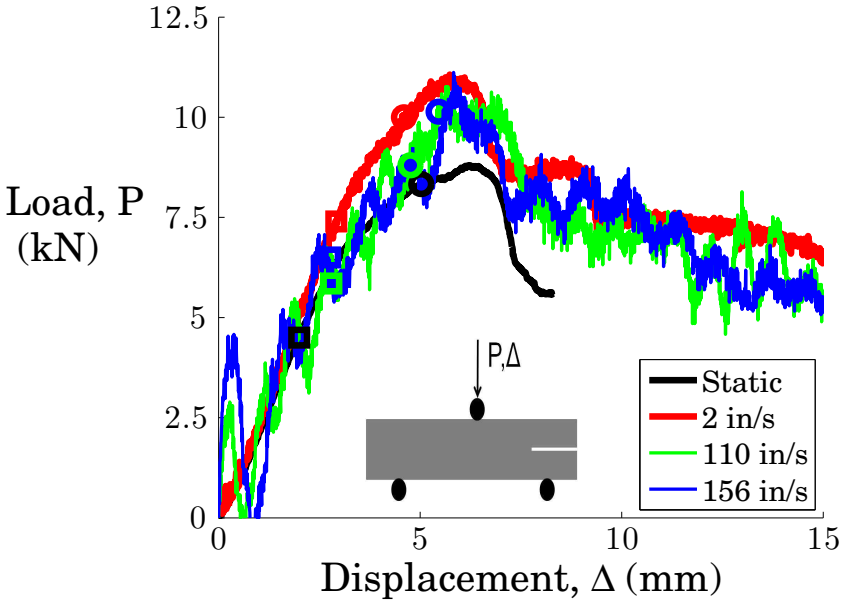

Figure 4.17 Load-Displacement curves for Albany 7 material in the weft direction at the four different rates.

Table 4.7 Comparison of energy dissipation at different rates for Albany 7 architecture.

	Static (kNmm)	2 in/sec (kNmm)	110 in/sec (kNmm)	156 in/sec (kNmm)
Warp	50.2	51.2	62.2	60.4
Weft	41.0	44.3	45.8	44.8
Failure	Kink Band	Kink Band	Z-fiber Shear	Z-fiber Shear

was set up for computational ease since the width of the specimen was relatively small. The bulk of the material was modeled using CPE4R elements, which are 4-node bilinear, reduced integration elements with hourglass control. Additionally the support rollers were modeled to simulate the test as precisely as possible. Contact was added between the rollers and the specimen. Displacement control loading was imposed on the top load roller at a constant rate, described in the tests earlier. In order to properly model the crack path the specimen was modeled as two halves and then joined together using DCZM elements, see figure 4.20(b). The details of the elements will be described in the next section. The DCZM elements are modeled as a bulk material however due to the Z-fiber reinforcement, a large G_{IIc} value is expected. Figure 4.20 shows the finite element model that was used to simulate the ENF test. Only the Albany 7 results were simulated, since the bulk of the experimental

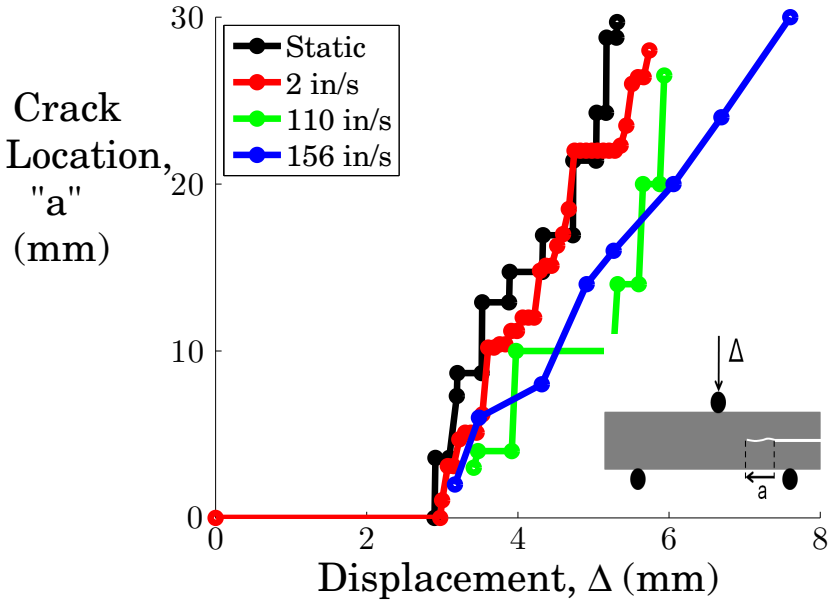

Figure 4.18 Crack Propagation diagram in the warp direction at the four different rates.

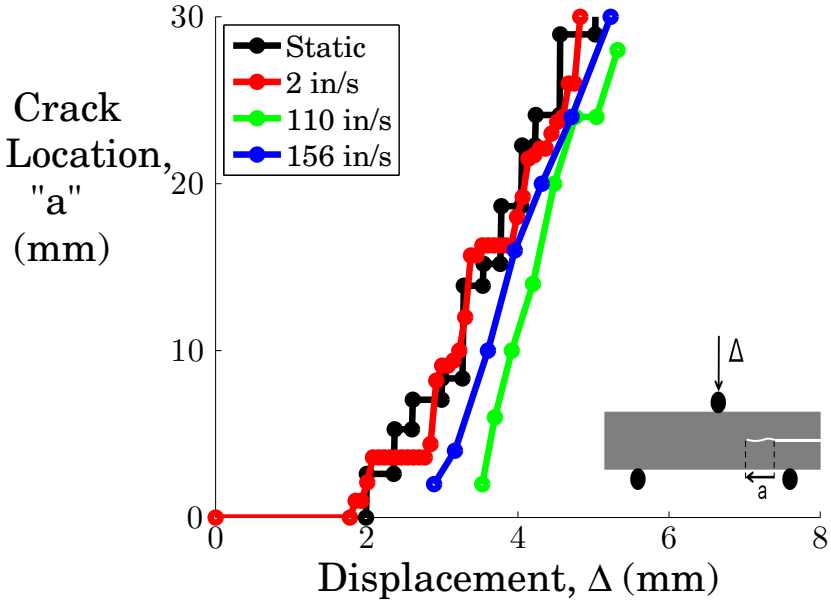

Figure 4.19 Crack Propagation diagram in the weft direction at the four different rates.

results were obtained for this configuration.

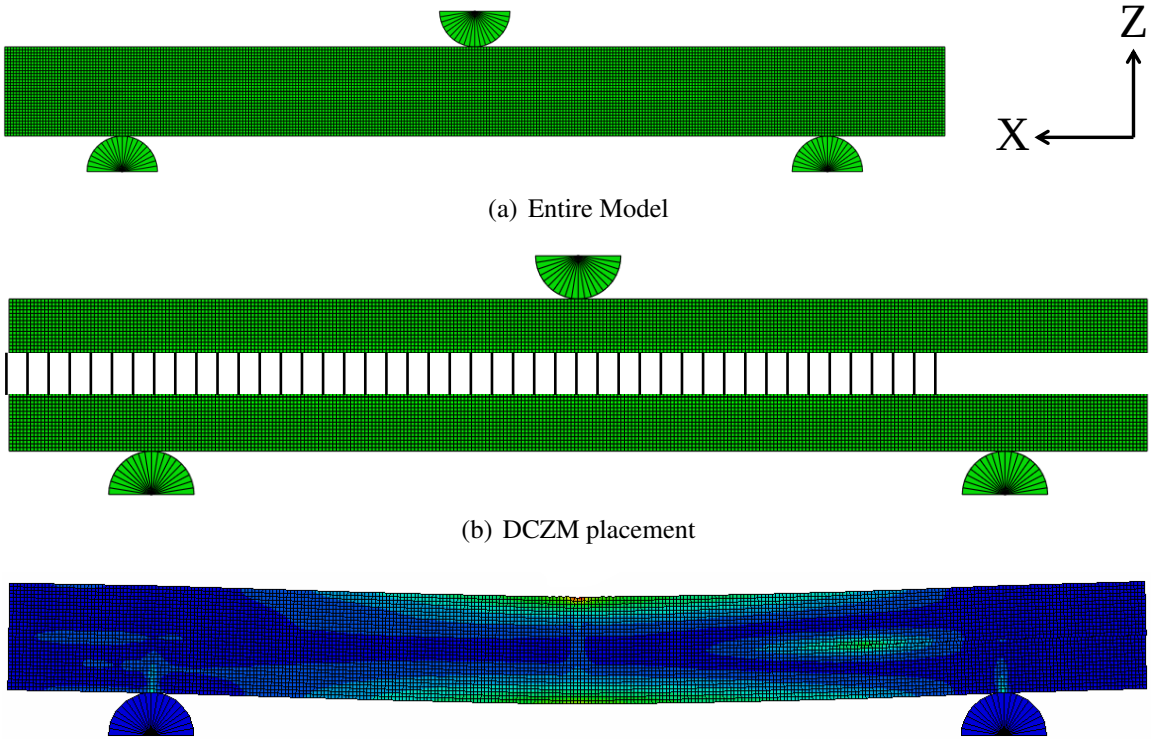

(a) Entire Model

(b) DCZM placement

(c) Deformed

Figure 4.20 Finite Element model used in the ENF simulation.

4.5.1 DCZM Element

The 2D DCZM element is shown schematically in figure 4.21. The element is implemented in ABAQUS® as a explicit user defined element (VUEL). This subroutine consists of zero thickness non-linear 1D spring-like elements between node pairs [65]. Four sub-elements (springs) are used in this 2D element; two are for shear and two are for peel. The relative displacement of the node pairs, transformed into a peel-shear coordinate frame, are used to compute the element force and stiffness from the traction law $(\sigma(\delta))$. For computing stress, the contact area is evenly divided among the node pairs of the element.

The DCZM element, see figure 4.21, used a trapezoidal traction law as shown in figure 4.22. Each fracture mode (I,II) require four separate parameters to properly implement the trapezoidal traction law. Since we are modeling the ENF configuration as a two dimensional plane-strain problem we only need to be concerned with G_{Ic} and G_{IIc} which are the critical energy release rates for mode I and mode II fracture respectively. Along with these parameters we also need the critical strengths, σ_{Ic} and τ_{IIc} the shape factors, α_{pl}^{I} and α_{pl}^{II}, and the initial stiffnesses k_I and k_{II}. The shape factor is bound by zero (representing a triangular

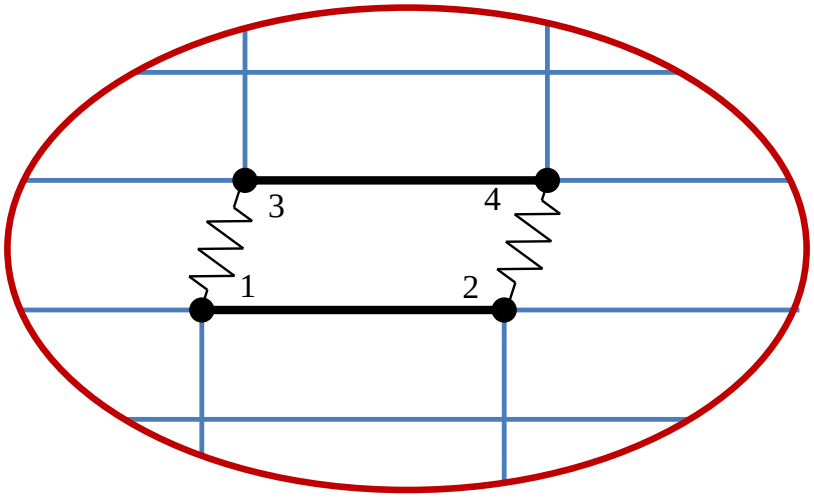

Figure 4.21 Four-node DCZM element with surrounding elements. Adhesion is enforced with non-linear springs between node pairs.

law) and one. The traction separation law is:

$$\sigma(\delta) = \begin{cases} k\delta & \delta > \delta_1 \\ \sigma_c & \delta_1 \leq \delta \leq \delta_1 \\ \sigma_c \left(1 - \frac{\delta - \delta_2}{\delta_c - \delta_2}\right) & \delta_2 \leq \delta \leq \delta_c \\ 0 & \delta > \delta_c \end{cases} \tag{4.2}$$

where

$$\begin{aligned} \delta_1 &= \frac{\sigma_c}{k} \\ \delta_2 &= \frac{\sigma_c}{k} + \alpha_{pl}\frac{G_c}{\sigma_c} \\ \delta_c &= (2 - \alpha_{pl})\frac{G_c}{\sigma_c} \end{aligned} \tag{4.3}$$

It has been shown that the initial stiffness k is a relatively large value [65]. Additionally there is no rate dependent characteristics associated with the DCZM element, thus the rate is seen from the different parameters obtained at the different testing rates. The matrix was modeled with a trapezoidal traction law, see figure 4.22 with alpha set to 0.9, to allow for some load to be carried after fracture. Since we are going to model the entire crack zone as one homogenized material, the DCZM element must simulate the bridging and then fail when the Z-fiber fails, hence the large alpha value to allow very little load after Z-fiber failure. The larger G_{IIc} value will contribute to how long Z-Fiber bridging can occur in the

material.

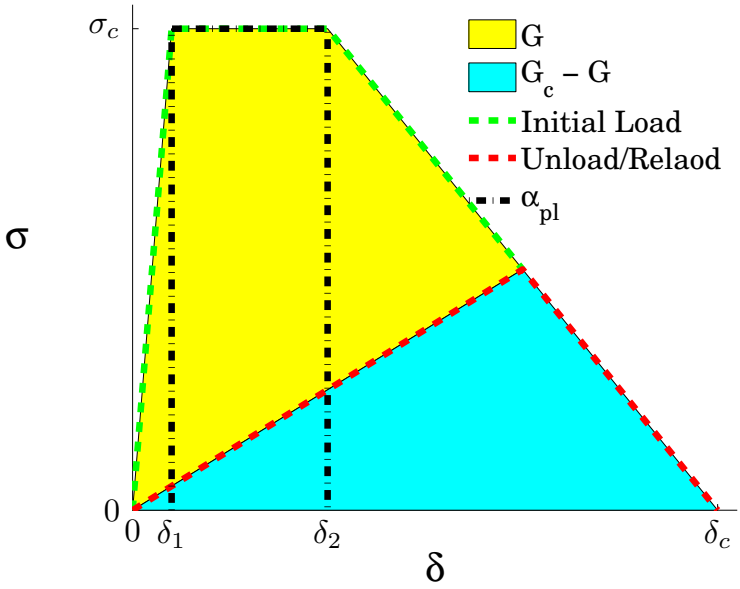

Figure 4.22 The trapezoidal traction law.

4.5.2 Material Properties

Simple tension tests were performed on the same material panels to determine the effective in-plane mechanical properties in both the warp and weft directions. The results were then used to back out the effective through the thickness shear terms by matching the initial load deflection curve where no crack had occurred. The results can be seen in table 4.8.

Table 4.8 A7 laminate properties

	GPa	Msi
E_{11}	31.55	4.575
E_{22}	18.64	2.70
G_{13}	3.00	0.435
G_{23}	2.60	0.377

Table 4.8 shows that there was some difference between the two shear moduli values. This is attributed to two facts, the first is that there are simply more fibers in one direction than the other. Second, the in-plane modulus in the weft direction is nearly double the value of the warp direction. This discrepancy would cause the shear to be much higher. Addition-

ally the orientation in which the Z-fiber is being stitched will have additional reinforcement, due to the fact that the fiber is being pulled tight as it is put in shear. With the 1 direction being that of the weft fibers and the 2 direction, the warp, we can understand the results of the extracted shear values. G_{13} is the shear modulus in the direction of the weft fibers. Although it is larger it is not twice as large because the Z-fiber is woven in the direction of the warp fibers (the G_{23} value). The extra reinforcement of the Z-fiber helps increase it's resistance to shear causing the shear moduli to have closer values.

Figure 4.23(a) shows the correlation between the model and experiment for the slowest rate. The static tests reveal a lot of information about the matrix values. Table 4.9 shows the determined DCZM parameters that were backed out from matching the curves of the material. The results showed that although the warp direction had a smaller critical strength, it had a larger critical energy release rate. This implies that although a smaller stress was needed to cause fracture, more energy was required to propagate the fracture through the rest of the specimen. This was a similar result to that observed in the experiments where we cyclicly loaded the specimen. The weft direction consistently exhibited a lower critical energy release rate for all specimens. This is due to the orientation of the Z-fiber as it is woven in the direction of the warp fibers. The fact that it is woven in this direction means that as it is bridging this gap, the fiber gets stronger, because it is pulling itself in shear. This is an interesting phenomenon and something that should also be noted in correlation to the model fit. As the fiber is pulled more it will have a higher stress, however, with the current model traction laws this is not permitted. It would be advantageous to develop a modified trapezoidal law in which from δ_1 to δ_2 the stress is increasing. Therefore, with the current model, the G_{IIc} value will be over predicted due to its need to carry the load.

Table 4.9 Computational Parameters for DCZM Elements

		DCZM Properties		Failure Mode
		σ_c	G_{IIc}	
Static	Warp	19	40	Kink Band
	Weft	28.5	22.7	
Dynamic	Warp	25	33	Kink Band
	Weft	32.5	28.32	
Drop Tower	Warp	16	27.5	Z-fiber Shear
	Weft	23	21	

When the loading rate is increased from static to 2 in/sec (3m/min) (on the MTS machine) we see a change in the resistance of the matrix material. In both directions the critical strength has increased, in the warp from 19 to 25 MPa, while in the weft it has increased

from 28.5 to 32.5 MPa. This is a fairly large increase in the critical strength, however, the critical energy release rate had a different behavior. In the warp direction a decrease from 40 to 33 $\frac{J}{m^2}$, while in the weft direction an increase from 22.7 to 28.3 $\frac{J}{m^2}$ was seen. The difference in directions is due to two factors. The static values are not necessarily accurate, since the material fails in a mode other than the Z-fiber finally failing. We cannot conclusively state that this was the maximum critical energy release rate, rather it has to be at least this value for the static test. However for the 2 in/sec (3m/min) tests, this value will be more accurate because the fibers began to fail in this loading regime. As was mentioned in chapter 2, the material will have an increasing critical stress as a function of the rate, however it does not detail how the critical energy release rate behaves as a function of the rate. It appears that there is some link however this is not as yet, clear.

When the experiment was switched to the drop tower, the rate of loading was increased dramatically. The critical strength begins to decrease along with the critical energy release rate. The material exhibited a lower yield stress. The critical energy release rate seems to have decreased for both the warp and weft specimens. The results show that the material now takes less energy to prevent fracture, which is directly linked to specimen inertia caused by the impact. As we move to faster loading rates, there is going to be less resistance to the crack propagation causing a lower critical energy release rate. One can relate this phenomenon to the idea of pulling tape off of a an object. If we try and remove it very slowly it provides more resistance to peeling off than if we rip it off quickly. This result provides greater insight into the material behavior. It should also be noted that the critical energy release rate for pure SC-15 is 2 $\frac{J}{m^2}$ [1]. This shows that the Z-fibers offer a dramatic increase in the fracture resistance of this material, under, both static and elevated rate loading.

If we look at the material microstructure and make some observations about the spacing of the Z-fiber in the warp and weft orientations, the influence of microstructure on fracture properties can be understood further. Figure 4.24 shows the spacing and associated dimensions of the Z-fiber, clearly there is a difference between the two types of specimens. The weft direction has a spacing that is 1.57 times larger than the warp direction. This spacing difference will cause a different critical energy release rate since there are simply more fibers per unit crack advance resisting the propagation of the crack in the warp direction. This information can again be related back to the critical stress value that it takes for the crack to form. If we look 90 degrees from the crack plane we see the opposite orientation, i.e. the weft direction now has the warp face. This face is the one that the crack must propagate through. Since there are more Z-fibers in this orientation it causes the critical stress to crack the matrix to increase because it must overcome the strength of the Z-fibers. Table 4.10 shows the predicted values for the weft direction based on the warp values. These

predictions are based on the difference in fiber spacing of 1.57. Overall there is a very good correlation. The predicted values are able to fairly accurately determine the load vs. deflection response for the materials. Figure 4.25 shows the predicted load deflection curves based on the relationship between the spacing. They typically predict that failure will occur sooner that it actually happened, however it is within the error bounds of the experimental data.

Table 4.10 Computational Parameters for DCZM Elements predicted based on spacing

		Matrix		Matrix Predicted	
		σ_c	G_{IIc}	σ_c	G_{IIc}
Static	Warp	19	40	19	40
	Weft	28.5	22.7	29.83	25.4
Dynamic	Warp	25	33	25	33
	Weft	32.5	28.3	39.25	21.0
Drop Tower	Warp	16	27.5	16	27.5
	Weft	23	21	25.12	17.5

All of the predicted values for σ_c seemed to correlate well with suggested scaling of 1.57 (the ratio of spacing). However, the two elevated rate simulations predicted failure earlier in the material than was actually seen. Therefore an estimation of a rate dependent behavior was investigated. To do this the G_{IIc} value was increased in order to increase the failure point in the material. The increase in G_{IIc} allowed for more bridging before failure. The simulations were re-run and the extracted properties can be seen in table 4.11 along with the corresponding load deflection curves of figure 4.26. The ratio at the higher rates drops to about 1.25 from 1.57. This decrease is a rate dependent effect that is related to the material caused by the rate dependence of the matrix.

Table 4.11 Computational Parameters for DCZM Elements predicted based on spacing, with modified G_{IIc} values.

		Matrix		Matrix Predicted	
		σ_c	G_{IIc}	σ_c	G_{IIc}
Static	Warp	19	40	19	40
	Weft	28.5	22.7	29.83	25.4
Dynamic	Warp	25	33	25	33
	Weft	32.5	28.3	39.25	27.0
Drop Tower	Warp	16	27.5	16	27.5
	Weft	23	21	25.12	22

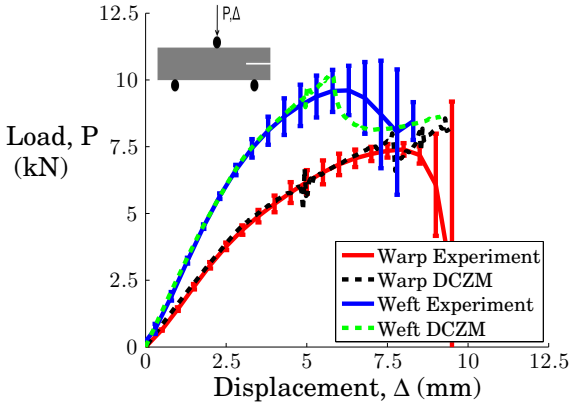

(a) Static

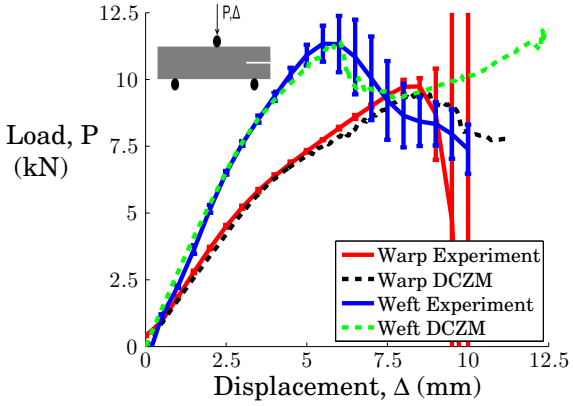

(b) MTS 2 in/sec

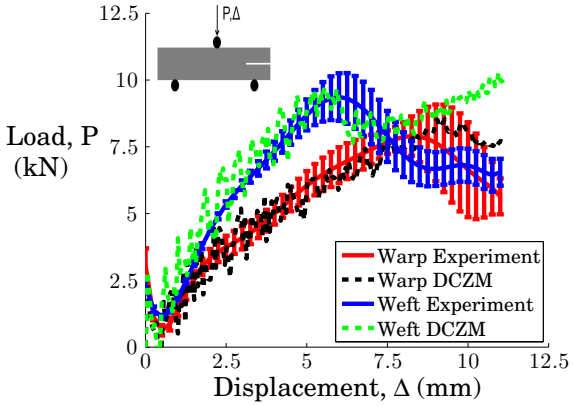

(c) Drop Tower 110 in/sec.

Figure 4.23 Load-Deflection correlations for each of the various different rates.

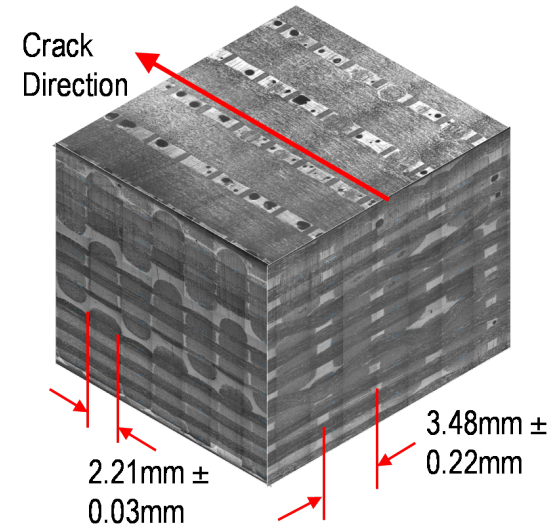

(a) Bending in Warp

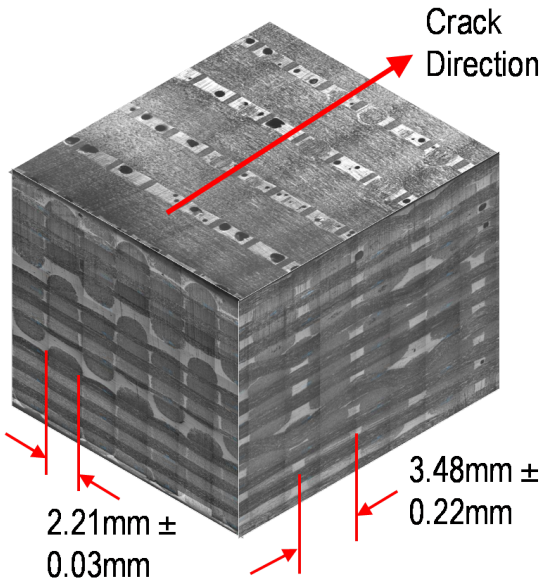

(b) Bending in Weft

Figure 4.24 Z-fiber spacing in both warp and weft directions showing the disparity.

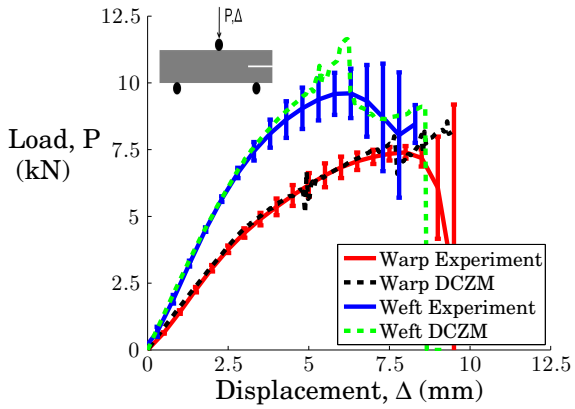

(a) Static

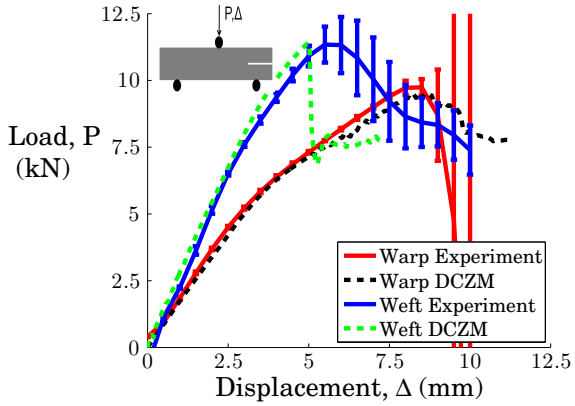

(b) MTS 2 in/sec

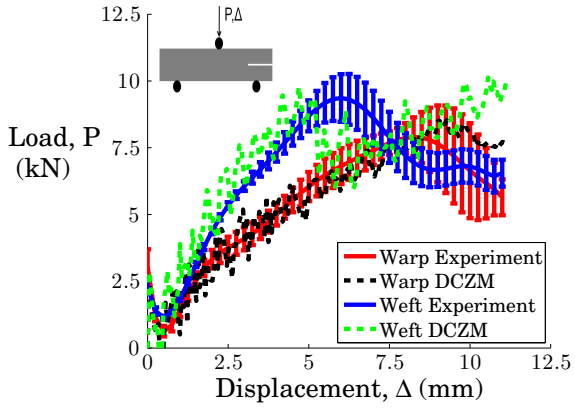

(c) Drop Tower 110 in/sec.

Figure 4.25 Load-Deflection predictions based on Z-fiber spacing for each of the various different rates.

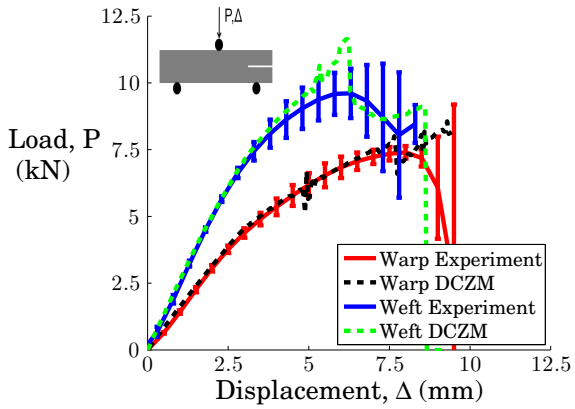

(a) Static

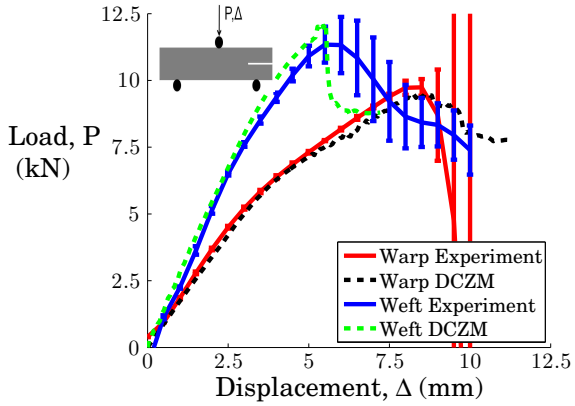

(b) MTS 2 in/sec

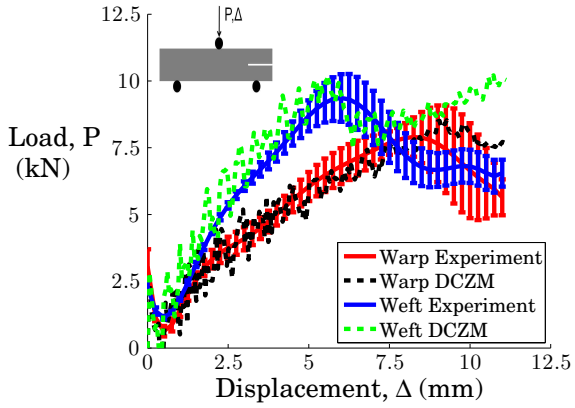

(c) Drop Tower 110 in/sec.

Figure 4.26 Load-Deflection predictions based on Z-fiber spacing with adjusted G_{IIc} for each of the various different rates.

4.5.3 New DCZM Law

In reality, the crack actually travels through a discretely reinforced matrix material, not a "smeared" layer as was previously assumed, as shown in the sketch of figure 4.27(a). There are Z-fibers which can still carry load after a crack has passed, and the matrix which cannot carry load after it cracks. Figure 4.27 shows how the Z-fiber material is not sheared when the crack passes in the matrix. Rather it will bridge the crack and fail in a different failure mode later in the test, this causes the Z-fibers to show distinctly in post failure specimen analysis. This bridging allows for transfer of load between the top and bottom layers, even after the matrix has "cracked".

In order to properly implement a discrete microstructure into a finite element model, a new DCZM law was developed, which implements an increasing stress with displacement to effectively model the Z-fiber bridging that occurs. Figure 4.28 shows what the modified traction-displacement law looks like to simulate the bridging zone that occurs. The new traction-separation law is:

$$\sigma(\delta) = \begin{cases} k\delta & \delta > \delta_1 \\ \sigma_{c1} + (\sigma_{c2} - \sigma_{c1}) \left(\frac{\delta - \delta_1}{\delta_2 - \delta_1} \right) & \delta_1 \leq \delta \leq \delta_1 \\ \sigma_{c2} \left(\frac{\delta_c - \delta}{\delta_c - \delta_2} \right) & \delta_2 \leq \delta \leq \delta_c \\ 0 & \delta > \delta_c \end{cases} \tag{4.4}$$

where

$$\begin{aligned} \delta_1 &= \tfrac{\sigma_{c1}}{k} \\ \delta_2 &= \tfrac{\sigma_c}{k} + \alpha_{pl} \tfrac{2G_c}{\sigma_{c1} + \sigma_{c2}} \\ \delta_c &= \alpha_{pl} \tfrac{2G_c}{\sigma_{c1} + \sigma_{c2}} + \tfrac{2G_c(1 - \alpha_{pl})}{\sigma_{c2}} \end{aligned} \tag{4.5}$$

In order to get proper behavior, both materials are modeled with the same ultimate stress value because we want both to "fracture" at the same level. Previous tests have revealed that G_{IIc} for SC-15 material in an ENF tests is about 2 N/mm [1]. This was used as a baseline for the SC-15 and the effective Z-fiber parameters were determined by matching the experimental load-deflection measurement to the simulation for the "warp" specimens. The rest of the model remains unchanged and the previously used model mechanical properties are used again. Figure 4.29 shows how the Z-fibers are alternated in the DCZM model based on the actual Z-fiber spacing.

In order to show the effectiveness of this new law, a comparison of the parameters has been done to show the effect of the increase in load transfer. The first model is to model all of the elements as triangular DCZM elements with the same matrix properties. The G_{IIC}

value is from the reference described earlier, while σ_c is used from the static simulation run earlier. Next, the Z-fiber reinforcement elements are modeled through a trapezoidal element to allow for bridging. This was accomplished by setting α_{pl} to 0.9 allowing for bridging and $\sigma_{c2} = \sigma_{c1}$, and setting a relatively large G_{IIc}. The final variation will be the application of the new law, with the σ_{c2} and G_{IIc} being backed out from the modeling. The various different input parameters can be seen in table 4.12 and 4.13.

Table 4.12 Computational Parameters for the modified Trapezoidal DCZM Elements in the Warp Direction

	Matrix		Matrix Predicted			
	σ_c	G_{IIc}	$\sigma_c 1$	$\sigma_c 2$	G_{IIc}	α_{pl}
Triangular	19	2	19	19	2	0
Trapezoidal	19	2	19	19	60	0.9
Modified Trap	19	2	19	115	20	0.9

Table 4.13 Computational Parameters for the modified Trapezoidal DCZM Elements in the Weft Direction

	Matrix		Matrix Predicted			
	σ_c	G_{IIc}	$\sigma_c 1$	$\sigma_c 2$	G_{IIc}	α_{pl}
Triangular	28.5	2	28.5	28.5	2	0
Trapezoidal	28.5	2	28.5	28.5	60	0.9
Modified Trap	28.5	2	28.5	160	18	0.9

The results of the analysis can be seen in figure 4.30, where the load deflection curves for each of the different models has been compared. The pure matrix version fails immediately and catastrophically, as soon as the critical stress is reached, since all of the elements fail, dropping the load dramatically. By modeling the Z-fiber elements with a trapezoidal law, a slightly larger load is reached before failure. The failure has some progression in this case, due to the ability to transfer some of the load across the crack surfaces, causing a smooth transition. The one result that should be noticed is that the overall slope after failure is the same, but the load that the specimen carries is much higher due to the load transfer that is still occurring after the matrix has failed. By switching to the new modified trapezoidal law where bridging can truly be simulated, the overall increase in load is evident. The load deflection curves have identical paths (experiment and simulation), the computational one predicts a higher ultimate load but this is really the only difference. The model clearly shows that Z-fiber bridging is indeed a viable mechanism for this stable crack propagation to occur in the material.

The results for the weft direction are very similar to those obtained in the warp direction. Figure 4.31 shows the representative load deflection curves for each of the directions. Since the matrix fails at a lower load in this instance, there is more bridging before failure. Therefore we get a small hump at the onset of the bi-linearity. The results show that the material fails at a higher load and around 9*mm* of displacement. After this point, the load starts to increase because the crack path has reached the center of the specimen, corresponding to a point below the load application point.

If one compares the effective strength of the DCZM elements for the two models, an interesting trend is observed. For the new model, since the Z-fiber is spaced over 6 elements, if we average the stiffness for those elements we can compare it to the results from the lumped model. Figure 4.32 shows the effective stress carried in the element vs. the element displacement. The results show that the new model carries nearly similar loads as compared to those computed earlier for the smeared model. The two results show a strong correlation between the two types of models.

It should be noted that the new model has more parameters that can be changed and studied. The four different input parameters could possibly have numerous combinations of values that would produce similar load deflection curves depending on how the parameters are changed. Two methods could be used to help determine model parameters: Kriging [66] or additional tests to determine some of the parameters to the model.

Kriging is a powerful interpolation scheme that attempts to obtain data for unknown points in a multi-dimensional design space, based upon a limited amount of training points where data is known (other examples of interpolation schemes would be polynomial fits, radial basis functions and neural networks). The Kriging predictor consists of two parts: a global approximation of the n-dimensional field and an error term that takes care of local deviations. Usually a Gaussian distribution is used for the local error terms. The methodology is based upon the idea that points close to each other (or the error in measuring them/computing them) should influence each other more than ones further away. As a by-product of Kriging, one also obtains information of the importance of different input parameters on the output, as for example, shown by Gustafson and Waas [67]

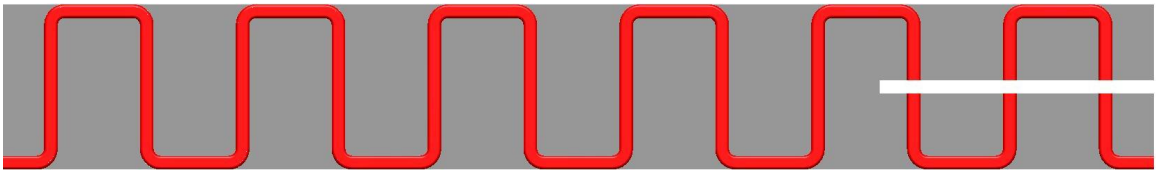

(a) Possible Z-fiber placement in ENF specimen. Notice the distinct points of Z-fiber (red color) and matrix (gray color) crossing the crack path.

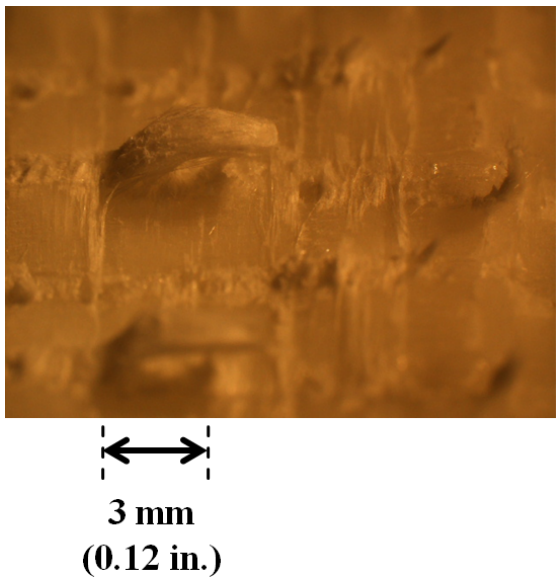

(b)

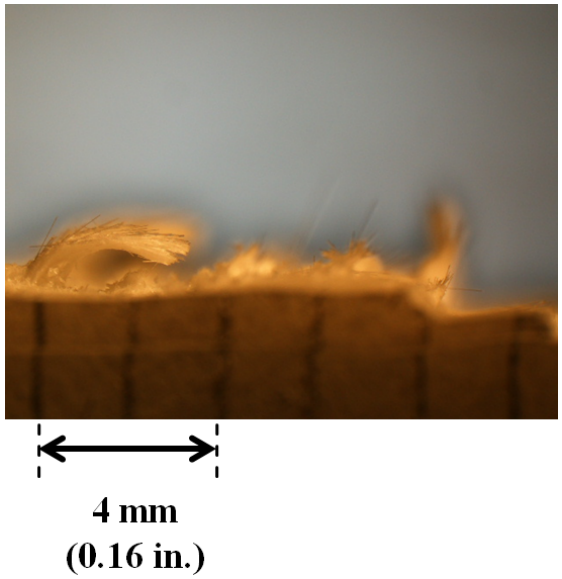

(c)

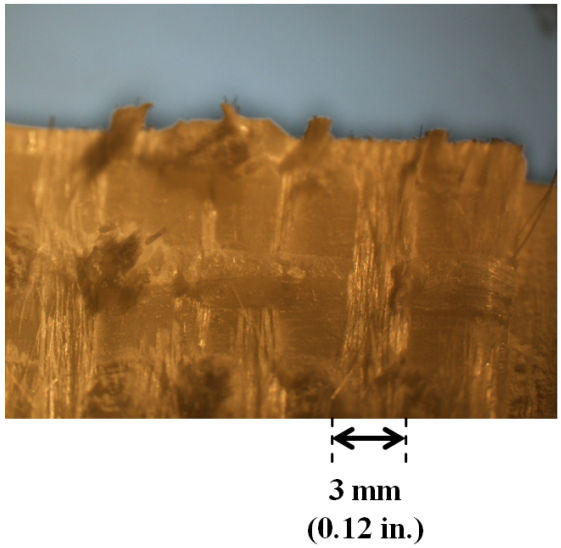

(d)

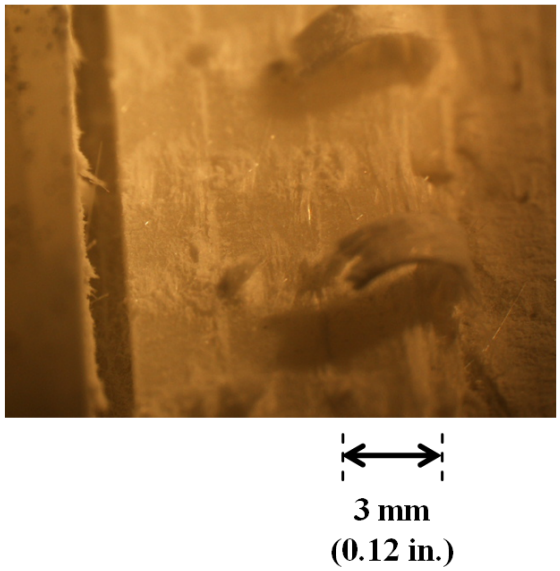

(e)

Figure 4.27 Z-fiber bridging areas as seen from the deformed specimens.

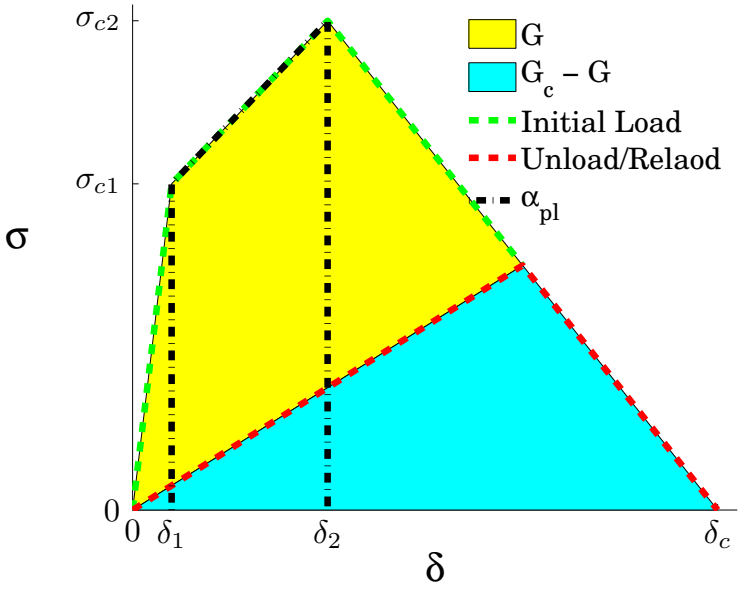

Figure 4.28 The modified trapezoidal traction law.

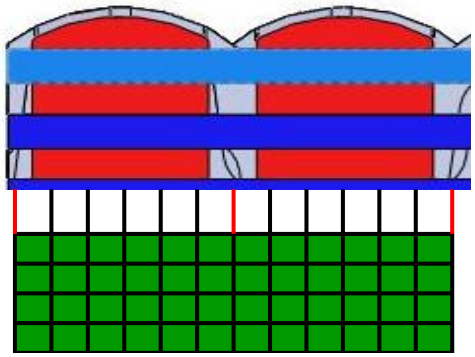

Figure 4.29 Detail of Z-fiber Placement. The red bars represents a Z-fiber DCZM element while black is a matrix DCZM element.

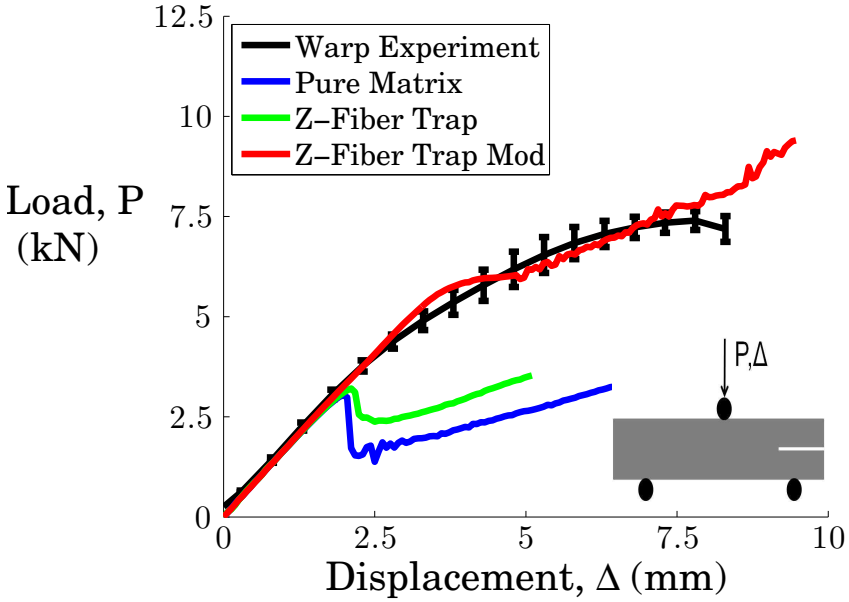

Figure 4.30 Modeling results showing the effectiveness of the Z-fiber bridging zone against typical models in the warp direction.

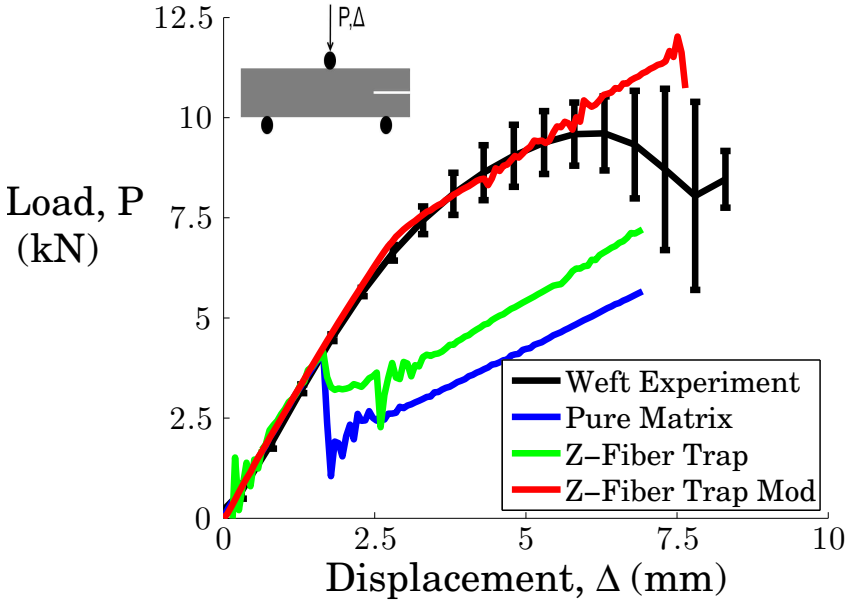

Figure 4.31 Modeling results showing the effectiveness of the Z-fiber bridging zone against typical models in the weft direction.

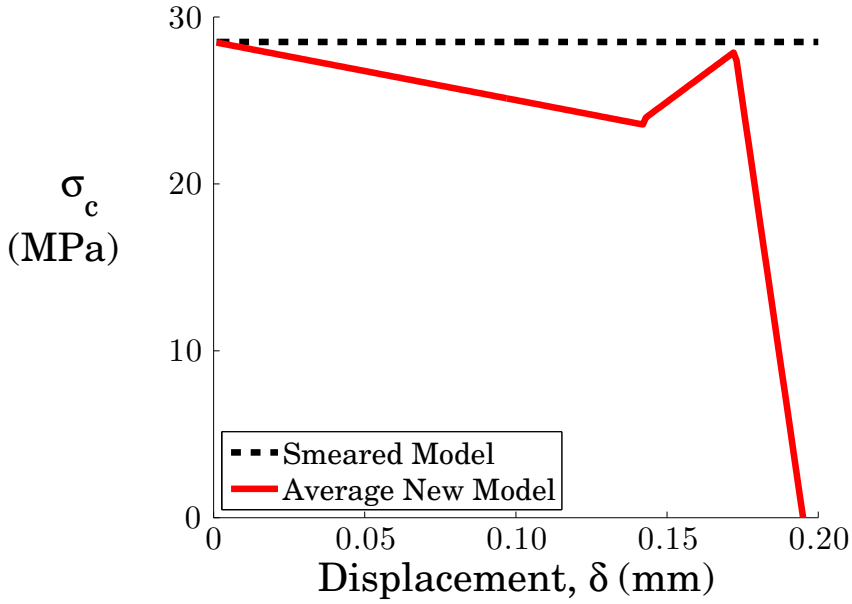

Figure 4.32 Average element stiffness based on spacing for the new model vs. the smeared model.

4.6 Conclusions

End Notch Flexure (ENF) tests for three types of Albany woven composite panels were performed to examine mode II fracture response. The tests showed that the Albany 2 architecture did not allow for crack propagation, but rather failed by localized delamination. This localized delamination is induced by the architecture design of the specimen because the fiber tows are staggered through the thickness, preventing a clear path for a pre-existing crack to follow.

The Albany 1 and Albany 7 panels produced similar load-deflection responses. Albany 7 provided the maximum fracture strength in static testing , although Albany 1 was comparable. It was determined from the digital images to track the cracks that the Albany 2 architecture would have localized delamination under the indenter tip instead of having a crack propagate. The results also showed that for both Albany 1 and Albany 7 a bi-linear relationship in the load-deflection response was observed. This relationship is induced by the Z-fiber reinforcement, that continues to transfer load from the top section to the bottom section after matrix cracking has initiated. It was also found that the elastic recovery was very large from both specimens. After fracture, the samples would return to a nearly flat shape. This was uncovered through results from cyclic testing that showed elastic recovery and subsequent loading with a new but reduced stiffness, suggesting that unloading occurs in the "secant" sense.

Numerical simulations were done to back out many of the parameters from the test. The use of DCZM elements allowed for numerical simulations that would produce a crack in the material. It was shown that both the critical strength and the critical energy release rate have rate dependent properties.The results showed that there was a critical transition in the panel response when inertia began to play a dominant role, lowering the maximum load that can be achieved in the material. Overall, the material showed a dramatic increase in the fracture resistance compared to an un-reinforced material. Additionally a new type of DCZM element has been presented with experimental and computational validation.

Chapter 5

Use of a Shock tube as a Blast Loading Device.

The first shock tube was designed and built in 1861, [68]. It was first used to study explosion problems in combustion. Later it was used more carefully to study the characterization of shock waves. In modern research they are typically used as supersonic wind tunnels in aerodynamic investigations. However, recently they have been turned into blast testing facilities. These devices are relatively useful and versatile because they have multiple functions, from shock impact, to projectile impact by acceleration caused by a shock wave, to nozzle testing with focused shock waves. The devices are useful experimentally due to the constant pressure that is produced that lasts for several milliseconds, allowing for very controlled dynamic loading.

Shock loading of panels is a relatively new technique, with its first publication coming in 2000. This article focused on isotropic material panels and had only strain gauges and pressure transducers for measurement techniques [69]. Most of the analysis was based on post test inspection for areas of damage [70], while others used post shock compression tests to determine the residual properties [71, 72]. Displacement measurements were introduced through the use of capacitive probes that were calibrated to the system, [73]

A new experimental method to obtain displacement data relies on a single high speed camera that can take images of the specimen perpendicular to their loading direction, from which the curvature of the simply supported beam is backed out. The accuracy of this method is based on the resolution of the images, [74]. Although composite material panels perform well at mitigating a blast, others have investigated the insertion of a soft material to absorb the shock, [75].

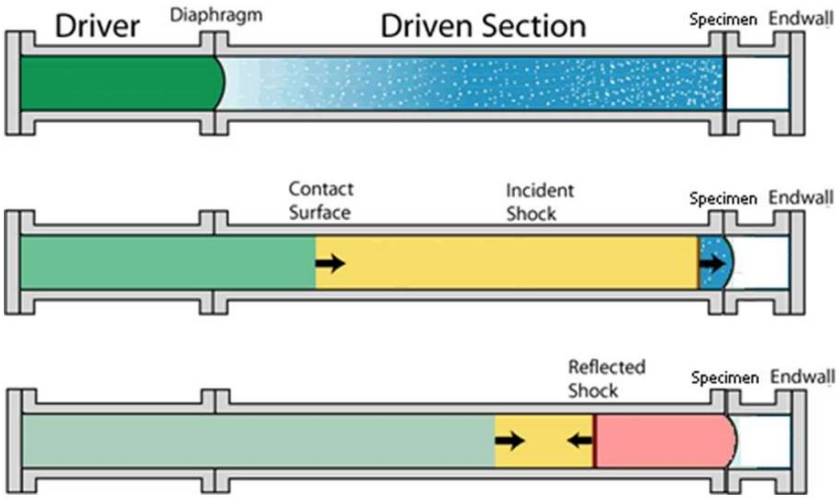

Figure 5.1 Schematic of the shock tube setup.

5.1 Experimental Method

Figure 5.1, shows a schematic of the experimental shock tube facility. The driver section is loaded with high pressure, which is separated from the driven section by a diaphragm designed to burst at a desired pressure. When the diaphragm ruptures, a shock wave is formed which travels down the tube at a much faster rate than the pressure can equilibrate. When the shock wave hits the specimen at the end, it is rapidly loaded with pressure causing it to dynamically deform, with effects of both pressure and inertia. The equations to determine the shock pressure and speed can be seen in appendix C. The shock tube in the University of Michigan Composites Structures Lab (UMCSL) is equipped with pressure transducers, as shown in figure 5.2 along with a complex viewing port system so that high speed cameras can be used to take images to perform Digital Image Correlation (DIC) measurements. The cameras are mounted to the viewing port housing so that there is no relative motion between a transparent lexan protective plate and the imaging camera which can cause a parallax error. The accuracy of the measurements will be related to the facet size in the DIC software. The resolution of the measurement will be $4mm(0.16in.)$. Although the step size is $0.238mm(0.0094in.)$ the size of the computation box will determine the resolution to which we can resolve the individual constituents in the material.

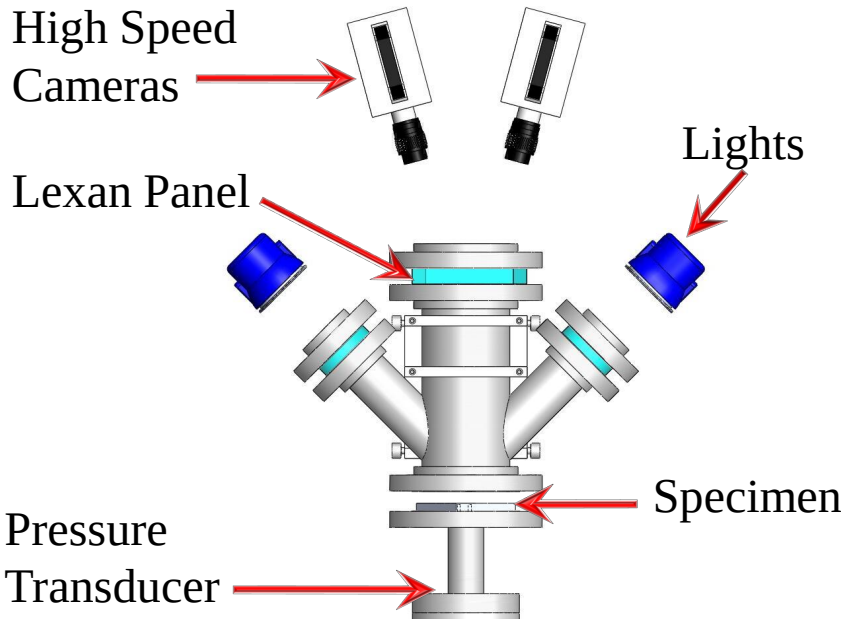

Figure 5.2 DIC setup and pressure transducer location.

5.2 Experimental Results

Tests were performed on $\frac{1}{4}in.(6.35mm)$ thick flat composite panels designated as the 6% Z-fiber reinforced T.E.A.M. panels as described in chapter 2. The 3% and 10% Z-fiber reinforced and baseline panels (Chapter 2) were also examined. Additionally "Baseline" panels were examined which contained a 0-90 in-plane woven architecture that would represent current manufacturing with no reinforcement. These were cut out in $5in.(127mm)$ by $5in.(127mm)$ squares to allow for adequate clamping room by the $6in.(152mm)$ clamping ring with a $3in.(76mm)$ through hole that matches the diameter of the shock tube. The tests were conducted using identical diaphragms so that the burst pressure, and hence the pressure pulse on the specimen would be nearly identical. Two different burst pressures were evaluated against the various architectures. A lower pressure test of 1600psi (15 layers of mylar as the diaphragm) and a higher pressure test of 2250psi (19 layers of mylar as the diaphragm). The resulting shock waves produced a maximum pressure of 1000psi and 1450psi respectively. These pressures were induced by steeply rising pulses, that changed magnitude from 14psi to 1000 psi in 0.5 microseconds, in the "low" pressure case, and from 14 psi to 1450 psi in 0.5 microseconds in the "high" pressure case, respectively. The maximum out of plane deflection can be seen in table 5.1. A comparison of the maximum out of plane deformation vs. time can be seen in figure 5.3.

The strain in the weft and warp directions were examined. Since the weft direction

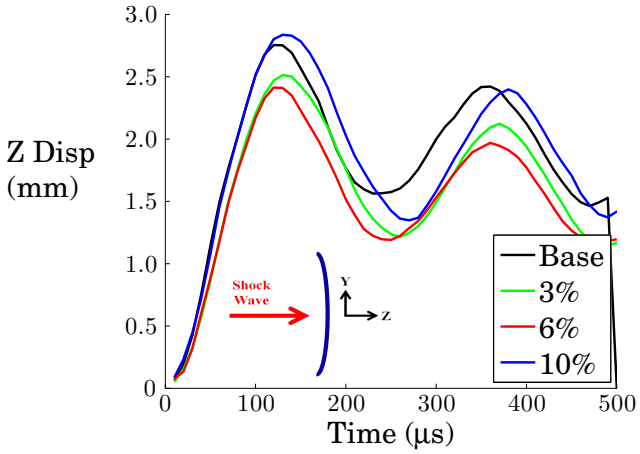

(a) 1000 psi shock pressure

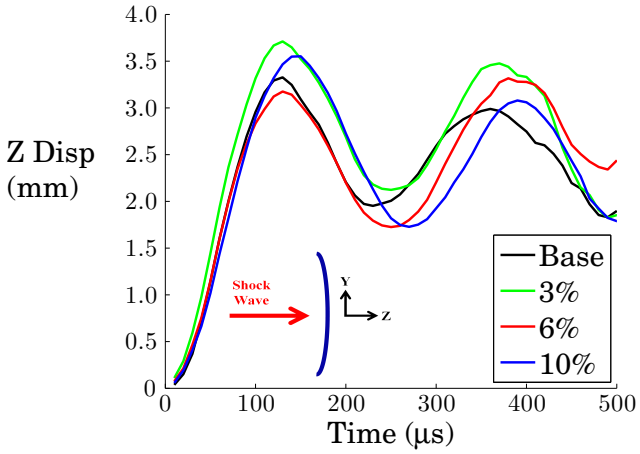

(b) 1450 psi shock pressure

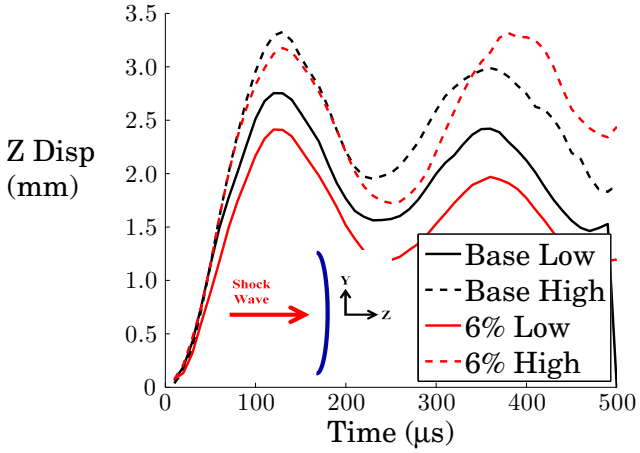

(c) Comparison of 6% Z-fiber and Baseline

Figure 5.3 Comparison of out-of-plane (Z) displacements.

Table 5.1 Out of plane deformation (mm)

Burst Pressure	1600psi	2250psi
Shock Pressure	1000psi	1450psi
Base	2.754	3.326
3%	2.514	3.711
6%	2.413	3.175
10%	2.836	3.552

corresponds to the outer most layer of the panel, DIC results will determine the strains in the fiber tows of the outer layer, while the warp direction strains correspond to the strain in the matrix. Figure 5.4 shows a comparison of ε_{weft} and ε_{matrix} versus time for the center of the panel. The results show that the 6% Z-fiber panel has the lowest strain in the weft fibers while the 3% Z-fiber panel has the lowest strain in the matrix. However this result does not tell the entire story. Figure 5.5 shows a comparison of the different panels strain fields at the point of maximum deflection. These results show in more detail the extent of matrix strain and fiber strain. As can be seen with all of the architectures, the strain in the fiber tows is relatively similar and localized at the center. The matrix strain indicates how localized the damage is, and also the magnitude of the maximum strain. So, although the 3% panel shows a relatively small strain, there is a very wide spread area that has a strain close to the maximum causing a relatively large area for possible matrix cracking. In the 6% panel, the strain is very localized at the center and drops off dramatically with distance from the center of the specimen. This would indicate that micro-cracking occurs on the outer surface, however it is very localized. If we compare it to that of the 10% panel, the results (distribution) are similar, however, the magnitudes are much larger, by almost 0.5% strain.

The results show that the 6% Z-fiber architecture panels outperformed all of the other panels for these out of plane deflection tests with respect to panel stiffness. Since the deflection indicates the stiffness of the panels, a measure of stiffness was used as a first indicator to decide which panel to study further. The strains were a secondary parameter in the panels because we wanted to determine the values at which the matrix would first crack.

Due to the variability that is introduced in the weaving and from the VARTM process, the scatter in the data was relatively large for the six percent panels in comparison to the baseline panels. Multiple tests were done on each panel at each pressure and the standard deviation was was found to be larger on the six percent panels, as shown in figure 5.6. The Baseline has a much smaller standard deviation in terms of deflection. The error was due to the manufacturing defects from the VARTM process. Since the 6% Z-fiber panels did not

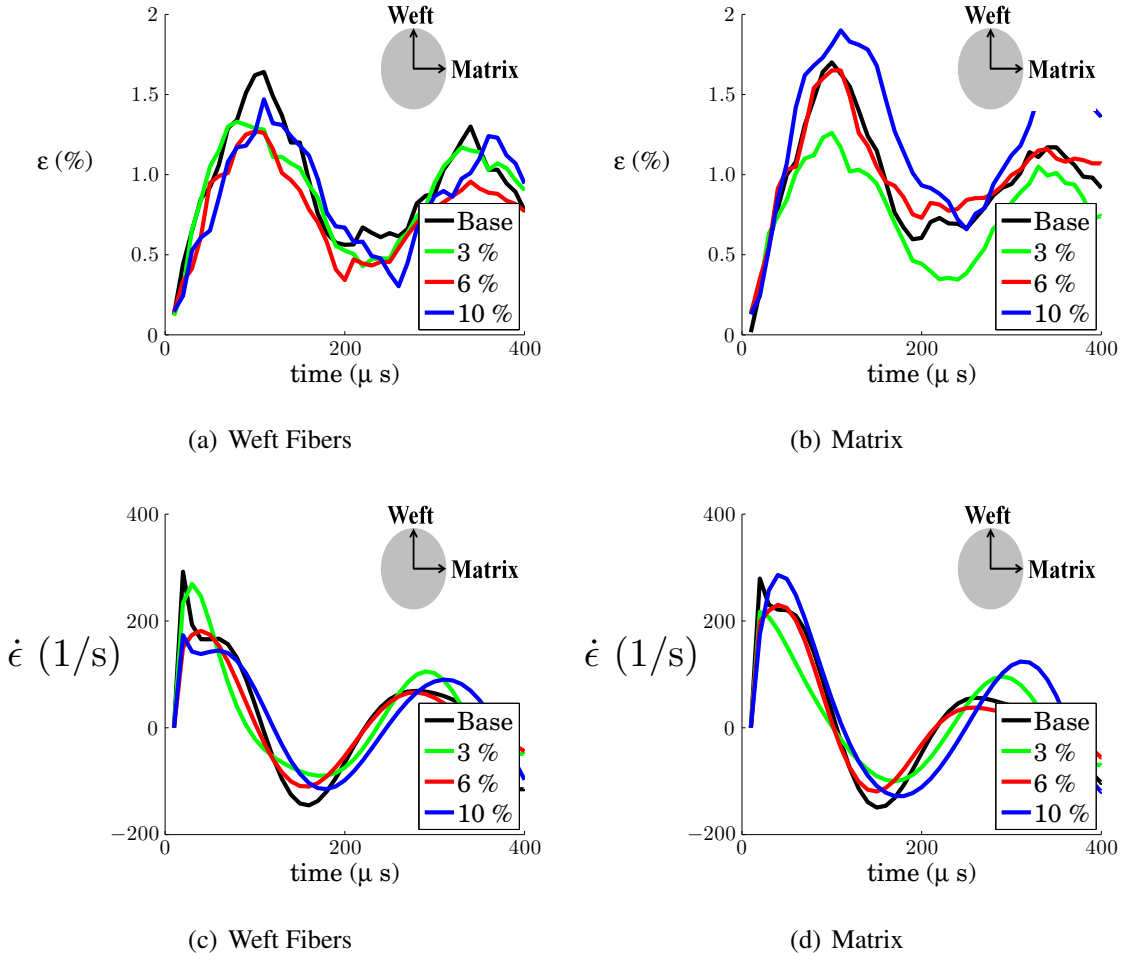

(a) Weft Fibers

(b) Matrix

(c) Weft Fibers

(d) Matrix

Figure 5.4 Strain vs. time at the center of the panel for the four different architectures at 1000 psi shock pressure.

wet out as well as the baseline, voids in the material will create a larger spread in the data.

5.3 Multi-hit Test

In order to better understand the mechanical response of the 6% Z-fiber reinforced architecture, a panel was subjected to multiple loadings, to observe the progressive damage that occurs from the matrix cracking in tension. The panel was subjected to four shock waves in succession that had the same shock pressure of 1000 psi. This test was done to understand the progression of failure in the specimen. The panel was placed at the end of the shock tube and clamped in place. The diaphragm was chosen to be fifteen sheets of mylar. After the first shock loading, the specimen remained intact and clamped, only the diaphragm was

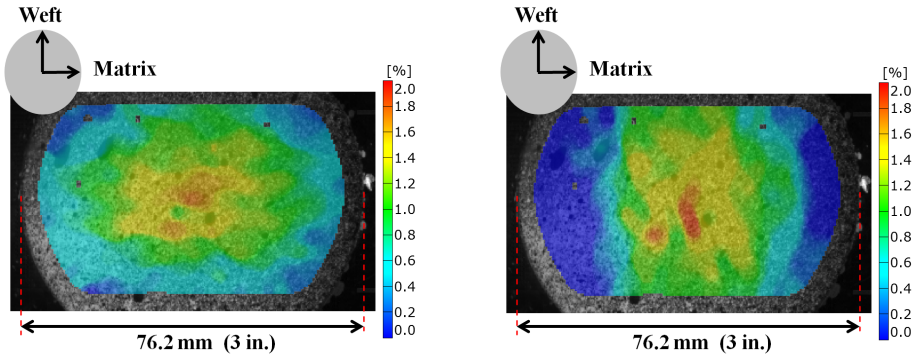

(a) Weft Base

(b) Matrix Base

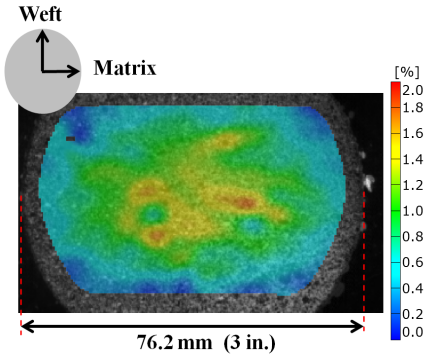

(c) Weft 3 percent

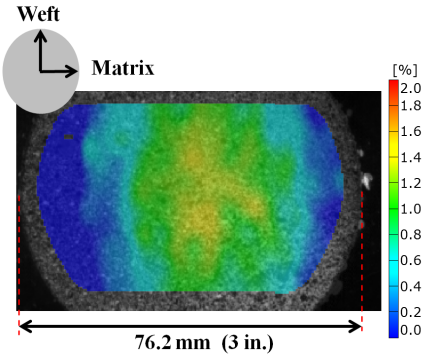

(d) Matrix 3 percent

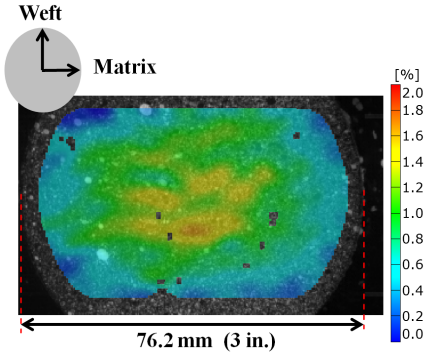

(e) Weft 6 percent

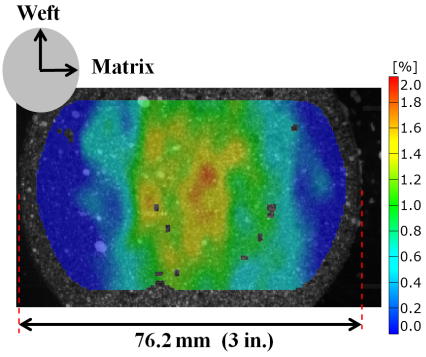

(f) Matrix 6 percent

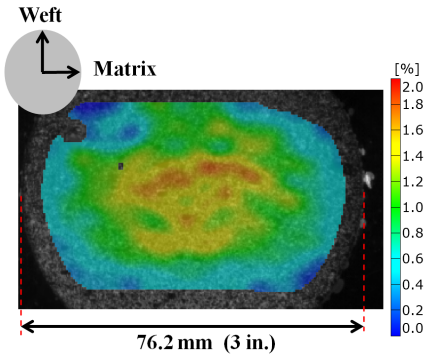

(g) Weft 10 percent

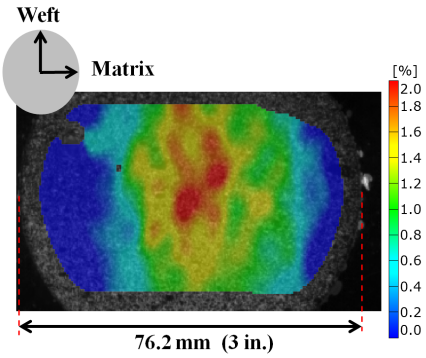

(h) Matrix 10 percent

Figure 5.5 Comparison of ε_{weft} and ε_{matrix} at the point of maximum deflection.

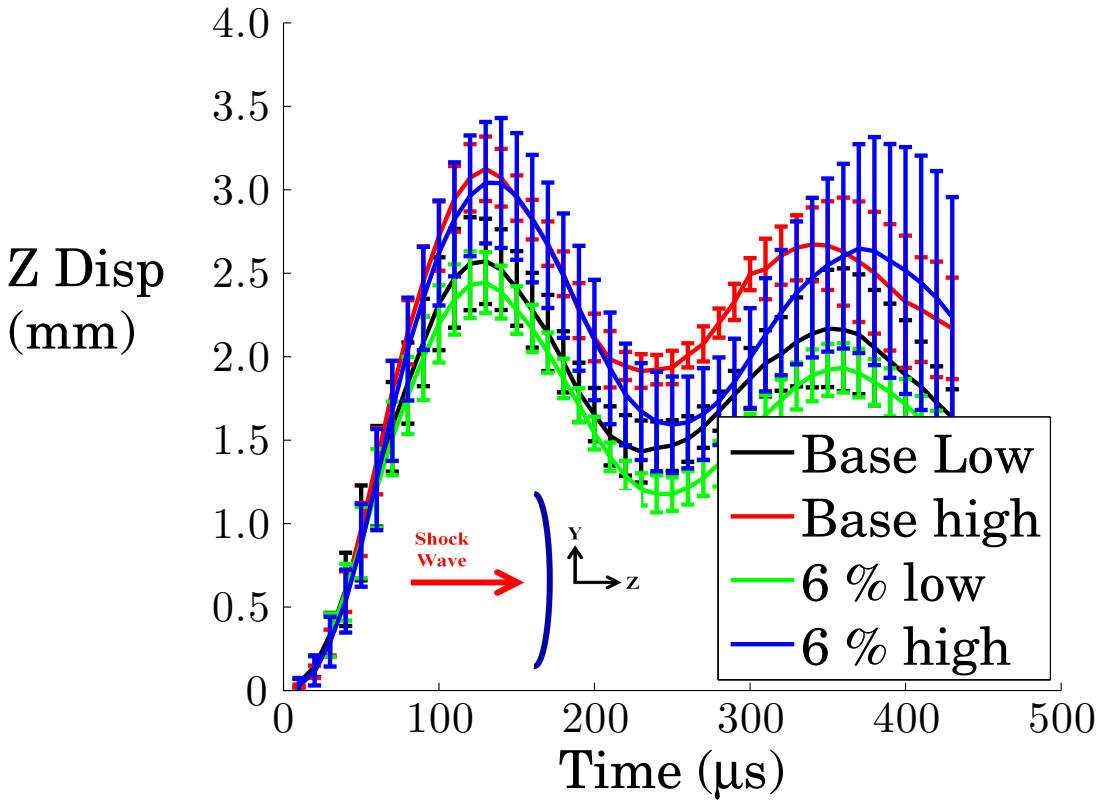

Figure 5.6 Center Deflection vs. Time showing the error bars for each of the specimens.

removed and then fifteen sheets of mylar were reinstalled to create a new diaphragm (the specimen was not handled in any way, this was so that no new error was introduced into the system). This same procedure was performed two more times to get a total of three repeat hits on the same specimen, four impacts in total. Figure 5.7 shows the center point deflection time history for each of the four tests. Each measurement was made on the deformed shaped prior to the incoming shock wave. Therefore the first hit was done on virgin material, while subsequent hit were performed on a deformed state. This deformed state is accounted for with the residual center deflection. Therefore figure 5.7(c) shows the total deflection for the panel. The strains in each subsequent tests are measured from a deformed configuration. This causes the maximum strain to decrease although we see a spreading of the data over a further area with each hit, since each specimen had some permanent or pre-strain from the previous test.

As can be seen with each successive hit the maximum deflection decreases, but seems to be converging on a single time history. With each successive hit on the specimen there was more and more permanent deformation as can be seen in figure 5.7, when we look at the

residual displacement at the center of the specimen. It should be noted that although the residual on test four seems large there is some inherent error induced, since the calibration had deteriorated, and a subsequent calibration was rerun to determine the time history for the fourth test. The error increases inversely to the quality of the calibration. Since only matrix micro-cracking was occurring it appeared that a threshold was reached where the panel was saturated and no further deformation could occur in the specimen, this is why the center point deflection curves seem to converge on a single history. As the matrix cracking propagates further and further a permanent set occurs but the matrix only cracks in tension in this case. Therefore when the all the matrix in tension has cracked and the fiber tows are now carrying the load, we can not progress this damage any further. Since the tows are now carrying the load there is no way to put further matrix into tension to cause failure, except if we were to fail some of the fibers. Figure 5.8 shows the strain field at the maximum displacement for each of the four hits. Although the maximum value of strain goes down, this is expected since the maximum displacement goes down, the strain field becomes more widespread on the specimen. With each successive hit the damage propagates even further smearing the strain over more of the specimen.

5.4 Zoom on Micro-Cracking

To further show the localization and architecture dependence on the formations of the micro-cracks another test was run in which only the center of the specimen was looked at and zoomed in upon to provide higher resolution on the individual fiber tows and matrix. The test was done using 19 sheets of mylar at a pressure of about 2200 psi. This was chosen to ensure that matrix micro-cracking would occur on the 6% Z-fiber architecture. The center point time history was identical to those performed in the un-zoomed configuration. Figure 5.9 shows the time history of the various tests and the close up version clearly follows the same trend. However, more noise is picked up in the sample due to the micro-cracking that occurs, therefore the data after the initial peak is not as smooth as the other samples at lower magnification.

Examining the matrix strain it is clear that there are areas where the micro-cracking occurs. Figure 5.10 shows what the strain in the outer layer of the matrix looks like. The representative frame corresponds to the time at maximum deflection. At this point we can see that there are many small bands that are formed, indicated by both the yellow and red colors at strains above 3%. These bands are the locations where the matrix has cracked, they are often large values because it creates a point wise discontinuity in the DIC algorithm,

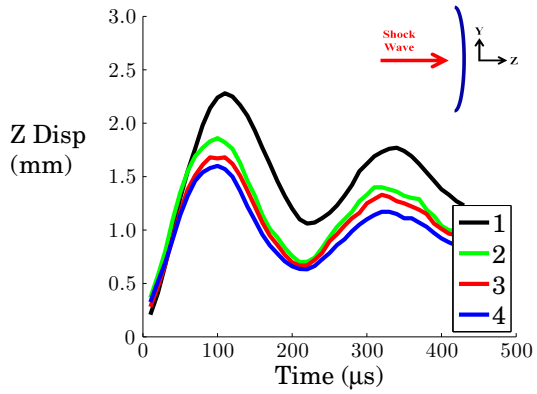

(a) Center Deflection vs. Time

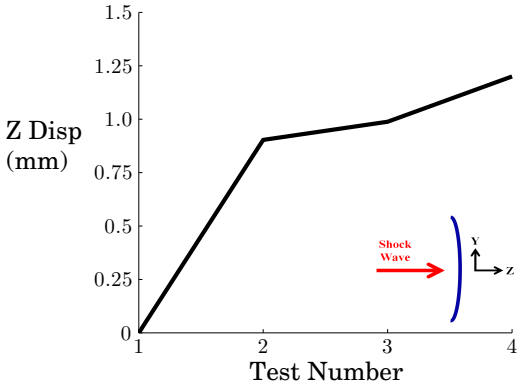

(b) Residual center deflection after each test

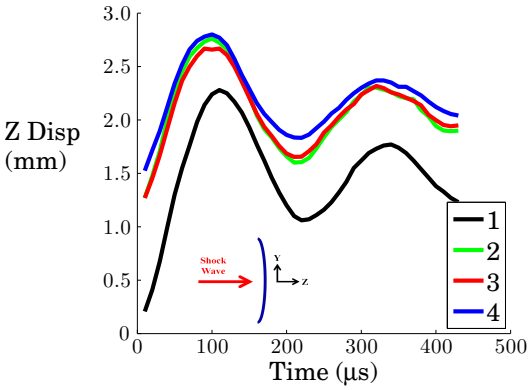

(c) Corrected Center Deflection Accounting for Residual

Figure 5.7 Center point deflection time history for 6% Z-fiber panel hit four times including the residual displacement.

where a new speckle is introduced. If one overlays the architecture of the specimen onto the DIC field (see figure 5.11), we can clearly see that the cracking (the localized bands of red) occurs at a point in the architecture where the Z-fiber is inserted through the thickness. This occurs because this is an area with little reinforcement and a pure matrix pocket. The cracks are arrested because of the offset weaving pattern which causes them to appear in a pattern and be stopped locally. Figure 5.12 shows the location where two Z-fibers are drawn from the top layer to the bottom. The insertion caused the piece of matrix to fail locally, additionally, the matrix had no fibers to hold it in place after failure or to prevent failure. Figure 5.13 shows the location and depth of the matrix microcrack that occur on a specimen.

The fiber strain was also examined. Figure 5.14 shows the fiber tow strain field. Two observations can be made here, the first is that the values are much lower than those observed

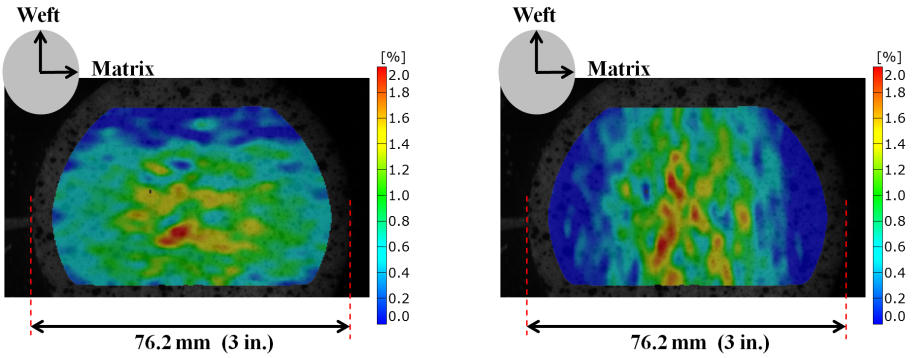

(a) Weft 1^{st} (b) Matrix 1^{st}

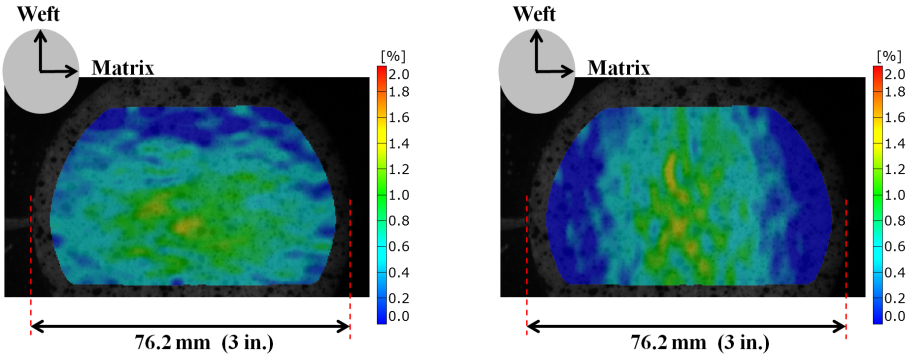

(c) Weft 2^{nd} (d) Matrix 2^{nd}

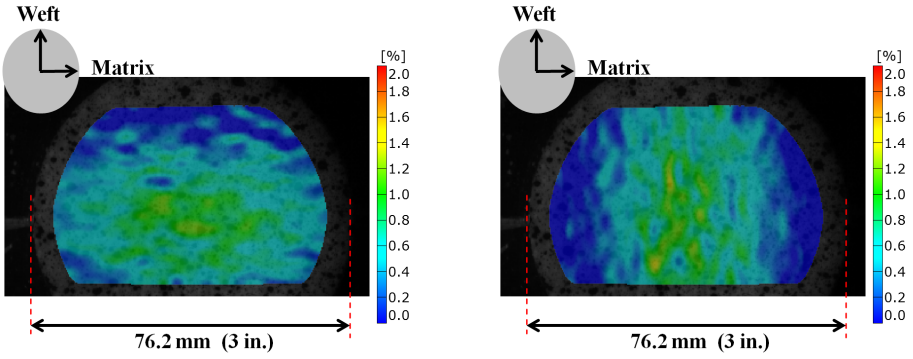

(e) Weft 3^{rd} (f) Matrix 3^{rd}

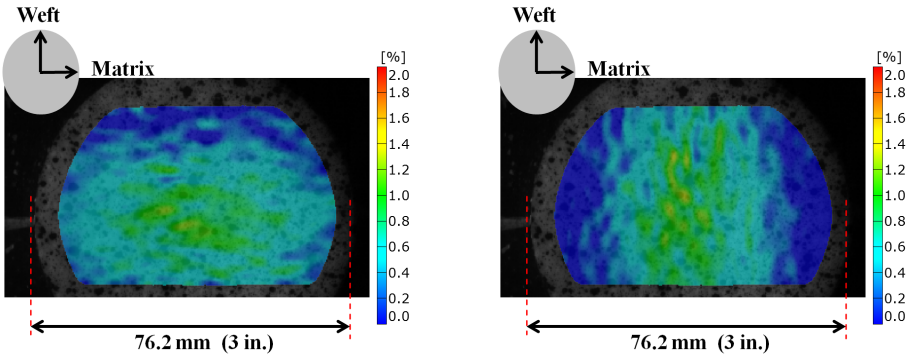

(g) Weft 4^{th} (h) Matrix 4^{th}

Figure 5.8 Comparison of ε_{weft} and ε_{matrix} at the point of maximum deflection for the multiple hit tests.

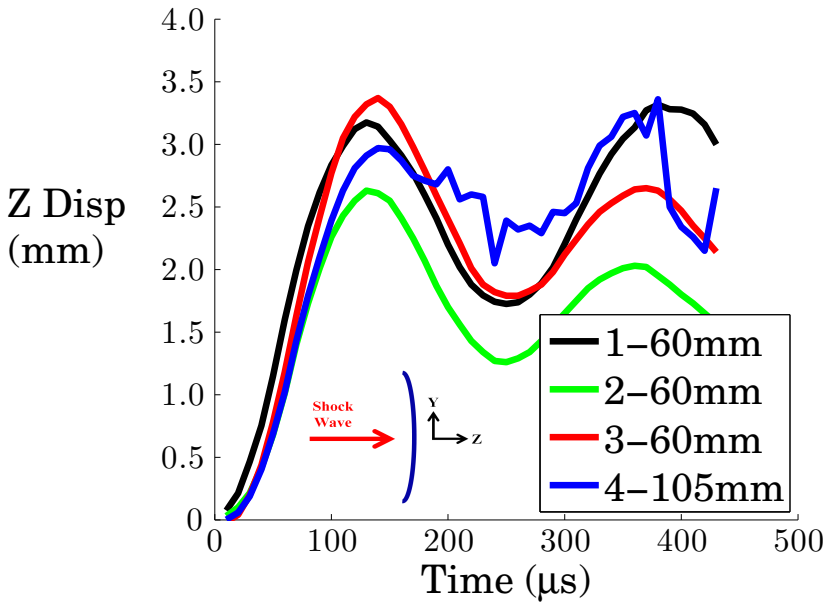

Figure 5.9 Center point deflection time history for four different 6% Z-fiber reinforced composite panels.

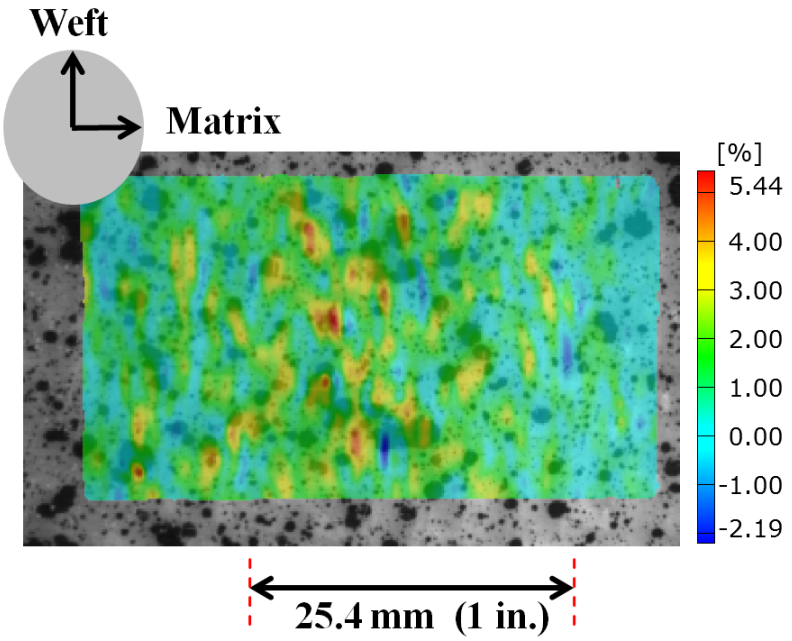

Figure 5.10 DIC strain map showing the matrix strain. The bright red spots indicate locations of matrix cracking.

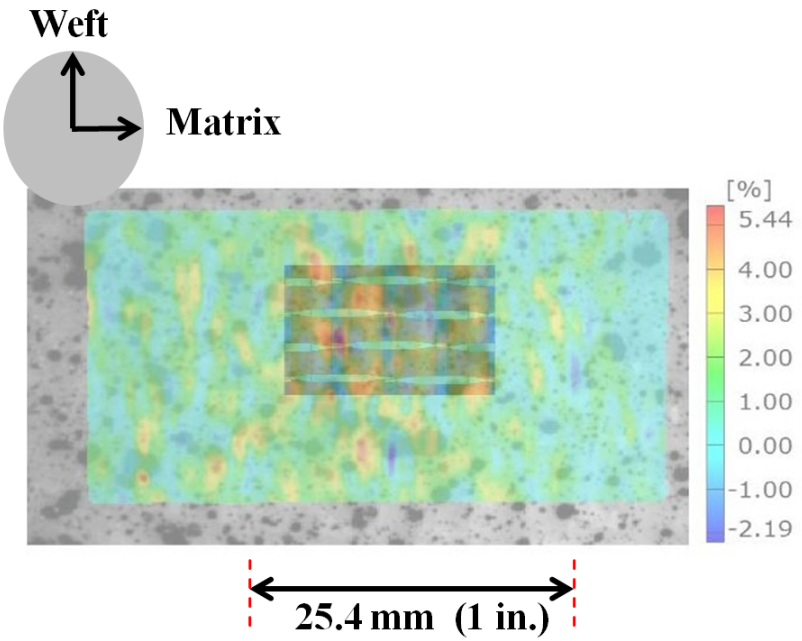

Figure 5.11 Overlay of the 6% Z-fiber architecture onto the DIC measurements to show the locations of matrix cracking.

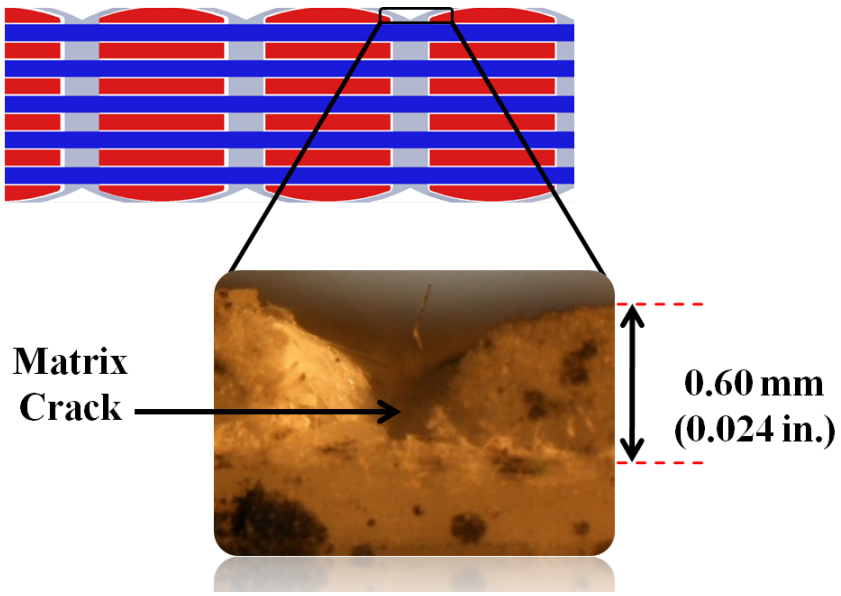

Figure 5.12 Microscope photo of matrix crack that occurred at the insertion of the Z-fibers. In this photograph the matrix has completely cracked removed from the material, this is evident since the top surface would normally be flat.

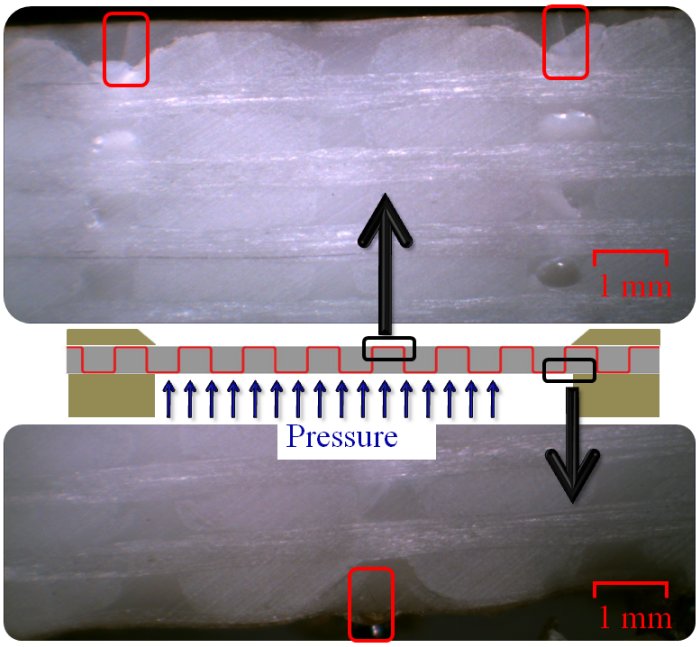

Figure 5.13 Microscope photos of matrix crack that occurred at the insertion of the Z-fibers. Each photo is shown at the centerline of the specimen, Showing the location where the cracks have formed. Notice they are only present in the first layer.

in the matrix with fewer hot spots. The second is that the strain map doesn't have any point wise discontinuities as before. The map shows a much smoother strain profile. Many of the strain concentrations coincide with points where the matrix cracking occurred, which will overlap due to the insertion of a new point in the DIC algorithm. Overall the results show that the majority of straining is sustained by the matrix, which causes the matrix to undergo micro-cracking first.

5.5 Discussion

The 6% Z-fiber panels outperformed the other architectures for many reasons. First we will examine the other architectures for a detailed comparison.

The baseline is the current production standard for most companies. It is a simple nine layer 2D in-plane woven fabric. There is no through the thickness reinforcement, thus providing no resistance to delamination. Thus the properties are good for bending response until interlaminar shear values become too large, leading to delamination and a reduction in bending stiffness.

The 3% Z-fiber panels do not have much reinforcement from the Z-fiber. Figure 5.15(a) shows how the Z-fiber has very little tension on the rest of the tows and thus provides little

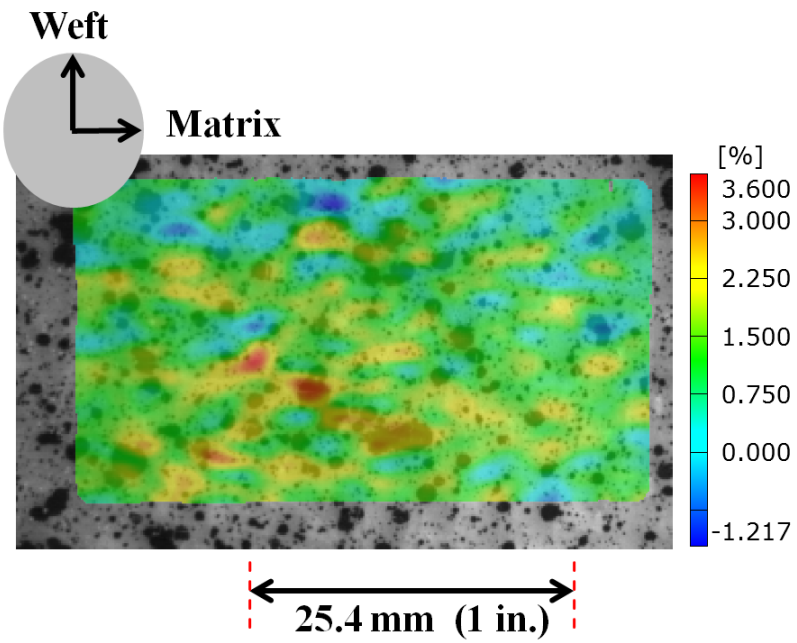

Figure 5.14 DIC strain map showing the Fiber strain.

reinforcement and delamination resistance. Additionally if we look at figure 2.3(a), we can see that some of the Z-fibers do not completely bind all the layers together, rather only the top few layers. With only the top few layers resisting delamination there is no resistance to delamination, offered by the lack of Z-fibers across the other layer interfaces.

The 10% Z-fiber panels provide copious amounts of reinforcement. Between every tow, the Z-fiber is woven from top to bottom or vise versa. Initial inspection would seem to indicate that this would possibly be the best solution, however with all the Z-fiber weaving, many imperfections are introduced as shown in figure 5.15(c). This Z-fiber binding creates a weak pocket between the tows at the top row as indicated in figure 5.15(c). In bending this is the location of maximum strain, causing the matrix to be the weak point. The high speed videos reveal that there are bands of cracking in the matrix that occur periodically, where the Z-fiber has been inserted.

The 6% Z-fiber architecture provides a compromise between the 3% Z-fiber and 10% Z-fiber, in that we have good binding between the layers, but there are not too many insertions to create a weak plane. In fact due to the architecture, the Z-fibers actually bridge the weak gaps that occur in the matrix as seen in figure 5.15(b). This bridging adds a small amount of stiffness to prevent matrix cracking early on while the Z-fiber prevents delamination between the layers. Overall this architecture provides considerable benefits over the Baseline 2D woven panels in terms of stiffness and delamination. Thus this architecture was chosen for further study.

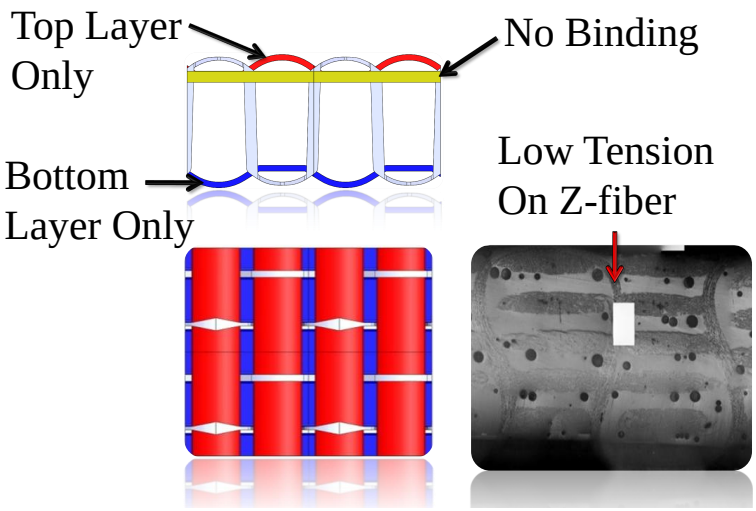

(a) 3% Z-fiber architecture

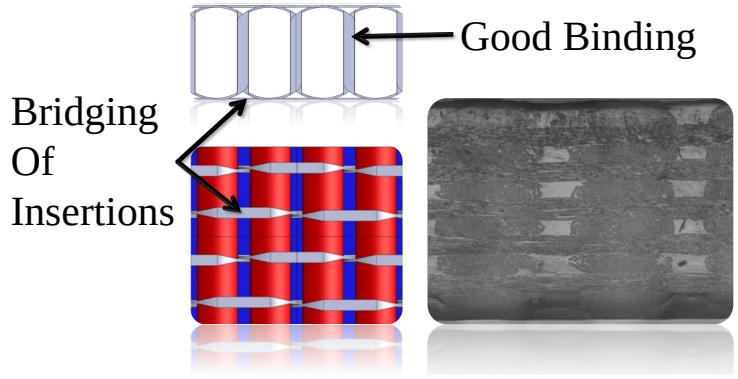

(b) 6% Z-fiber architecture

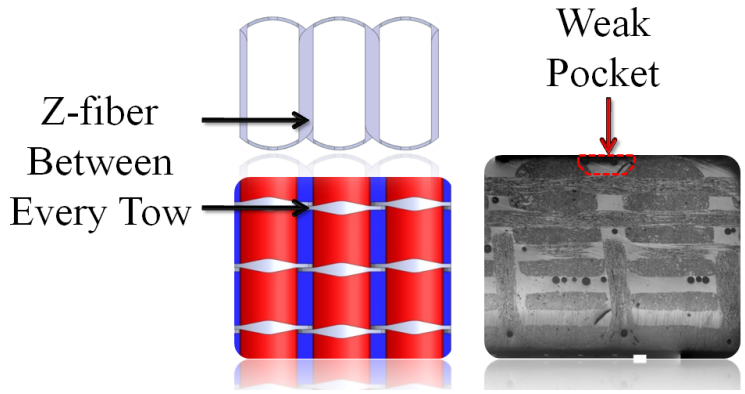

(c) 10% Z-fiber architecture

Figure 5.15 Details of Z-fiber architectures.

5.6 Modeling

Impact modeling of 3D woven composites has been attempted before with some success. Most of the models focus on objects impacting the surface of a material and comparing the strain gauge response with that of the finite element strain-time history. In these simulations the material is assumed to be anisotropic with anisotropic plastic and failure properties, representing a bulk material and not the individual constituents [30]. More complex models using the individual components of the material representing the architecture have been evaluated [31], however typically properties are "made up" and they are used only as proof of concepts, never validated against experimental results. Additionally, analytical models of the fluid shock interaction have been looked at showing that for relatively stiff panels the interaction is small. However, for soft panels this interaction becomes important [50].

To better understand how the matrix micro-cracking occurred in the shock loaded panels studied here, a detailed finite element model was created that would closely resemble the microstructure, but was not so computationally complex that it would take a long time to run. Therefore the panel was modeled using S3R, linear tetrahedral shell elements. The shells were then restricted with a rigid plate with a hole in the center to more accurately simulate the shock tube clamping plate. The plate was meshed using R3D3 and R3D4 rigid elements. In order to better simulate the architecture of the plate, 11 different shells were combined to represent the 6 layers of weft fibers and the 5 layers of warp fibers. Each of the shells were then modeled as anisotropic elastic-plastic materials, the properties have been homogenized for the entire layer. This was done to incorporate the fact that the modulus in the fiber tow directions was much stronger than in the transverse direction, the later being matrix dominated. This method is very similar to the unidirectional layups that would be available as a user defined material in the ABAQUS commercial FE software, however these only alow for linear elastic material properties, which does not permit for matrix plasticity. The linear elastic constants were derived from the mechanical properties from the tension tests in chapter three. For the 6% Z-fiber reinforced composite, the material properties used are shown in table 5.2.

Table 5.2 6% Z-fiber composite modeling parameters

E_{warp}	3.113 ± 0.16	Msi
E_{weft}	3.56 ± 0.21	Msi
E_{SC15}	0.361	Msi

From these properties, the effective ply properties were backed out after making some assumptions about the material. The 2 direction of any ply is modeled as a pure matrix,

therefore, the transverse modulus is E_{SC15}. E_3 was assumed to be E_{SC15} and has very little effect on the result of the model. The poisson's ratio was unknown and was set at a value of 0.3 for the simulation, but due to the bi-axiallity of loading has less than 1% error on the results. The shear moduli were set to a value similar to that of the matrix with some reinforcement from the Z-fiber. These values were calculated from a rule of mixtures, with the volume fraction based on the volume fractions of fiber and matrix observed in chapter 2. The properties used in the model are presented in table 5.3.

Table 5.3 6% Z-fiber composite modeling parameters

E_{11}	Warp	7.398	Msi
	Weft	6.226	Msi
E_{22}		361	ksi
E_{33}		361	ksi
ν_{12}		0.3	
ν_{13}		0.3	
ν_{23}		0.3	
G_{12}		1.08	ksi
G_{13}		261	ksi
G_{23}		261	ksi
Matrix Micro-Cracking Strain		0.9%	

The shear moduli can be compared to two experimental results; the first comparison is based on the Albany 7 composites shown in the previous chapter. For these thicker specimens the shear modulus was comparable to that of the 6% Z-fiber but a little on the high side. Short beam shear tests performed at the University of Florida produced a shear modulus of 152 ksi. The students conducting the test reported that their specimens were filled with matrix voids and produced very low material properties compared to ARMY testing which has been described earlier.

In order to implement the plasticity of the matrix the potential suboption of the plasticity material model was implemented. This allowed setting the yield stress for the fibers to be very large to account for the yield of the matrix independently of the fibers. Additionally the rate dependent sub option was also used to implement the Cowper-Symonds model developed in chapter 2 of this thesis. The plastic values were derived from the tables in chapter 2 of this dissertation. The yield stress ratios needed in the plastic potential were assumed to be the ratio of the moduli in the respective directions. In classical anisotropic yield, the plasticity is modeled through yield stress ratios, since only one yield curve can be

implemented. These ratios are seen as,

$$\sigma_{ij}^{y} = R_{ij}\sigma_o \tag{5.1}$$

where σ_{ij}^{y} is the yield stress if the material is only pulled in that one direction, and σ_o is the reference yield value. After rearranging yield stress ratios can be rewritten as

$$R_{ij} = \frac{\sigma_{ij}^{y}}{\sigma_o} \tag{5.2}$$

Where each yield ratio will look like the following.

$$R_{11} = \frac{\sigma_{11}^{y}}{\sigma_o}$$
$$R_{22} = \frac{\sigma_{22}^{y}}{\sigma_o}$$
$$R_{33} = \frac{\sigma_{33}^{y}}{\sigma_o}$$
$$R_{12} = \frac{\sigma_{12}^{y}}{\tau_o}$$
$$R_{13} = \frac{\sigma_{13}^{y}}{\tau_o}$$
$$R_{23} = \frac{\sigma_{23}^{y}}{\tau_o}$$

Where $\tau_o = \frac{\sigma_o}{\sqrt{3}}$. However, since we do not know the actual yield in all directions the Modulus ratio was substituted yielding the following ratios.

$$R_{11} = \frac{E_{11}}{E_o}$$
$$R_{22} = \frac{E_{22}}{E_o}$$
$$R_{33} = \frac{E_{33}}{E_o}$$
$$R_{12} = \frac{G_{12}}{G_o}$$
$$R_{13} = \frac{G_{13}}{G_o}$$
$$R_{23} = \frac{G_{23}}{G_o}$$

A schematic of what the model looks like can be seen in figure 5.16. This figure shows the different layers that have been modeled and shows the individual material properties orientations for each type of layer.

In order to incorporate the matrix micro-cracking, a user defined field to degrade the matrix stiffness of the anisotropic material properties, after it has reached a critical value was implemented. The VUSDFLD user subroutine works by using a tabular array for the mechanical properties of the material. The subroutine calculates the strain in the material and then compares it against a user defined failure limit. If this returns a value greater than one, the modulus in that direction is set to a new value. Within the table are various different combinations of moduli based on the field variables. In this case if the matrix surpasses a critical stress the modulus is set to zero in the 2 direction of the model, and the poisson's ratios are also zeroed to eliminate numerical difficulties. The source code for the VUSDFLD along with the values used for the different panels analyzed in this thesis are given in appendix E.

In order to know the pressure that should be applied to the model, a separate test was performed with a "rigid" plate mounted with pressure transducers to record the pressure that was reached on the plate impacted surface, see figure 5.17. The plate is a $19mm(0.75in.)$ thick steel plate. The pressure time history measured with this steel plate is assumed to correspond to those experienced by the panel specimen. This assumption is valid if the composite panel response time is significantly larger than the rise time of the shockwave pressure pulse. The two tests ("rigid" panel and a comparatively soft pure epoxy panel compared to the steel panel and the 3DWC panels) were done to experimentally determine the effect of panel deflection on the pressure felt by the panel (i.e. the fluid-structure interaction

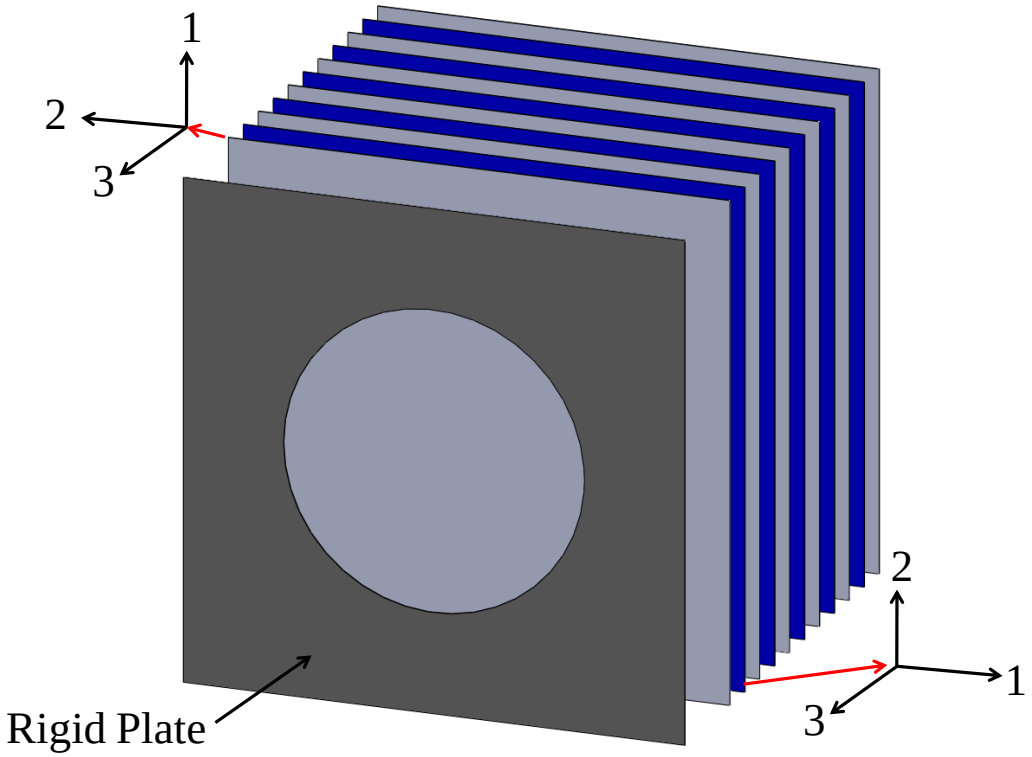

Figure 5.16 6% Z-fiber model with anisotropic layers stacked with alternating directions to represent warp and weft fibers.

effect). This information is very important in the subsequent finite element modeling, since one needs to know the input pressure time-history. Figure 5.18(a) shows the two reflected shock pressure time histories (that have been shifted in time) corresponding to the rigid plate and the epoxy panel as measured through pressure transducers situated very close to the panel, see figure 5.17. The pressure time history of the reflected shock wave on the tube transducer is shown in figure 5.18(b) along with the pressure measured on the rigid plate surface. The results show that the pressure-time histories are very similar, even on the deformable epoxy panel. One clear reason for this is the time scales involved in the problem. The pressure pulse increase occurs over a time duration of 0.5 μs, while the panel deflection, in response to this pressure pulse, occurs over a time duration of 250 μs. Clearly, these time scales are very different. In summary, the pressure that is measured by the pressure transducer can be used as the pressure pulse experienced by the panel specimen. It should be noted that this does not account for interaction with the shock wave and other effects.

By knowing the pressure-time history on the panel, it is possible to compare its temporal scale to the time history of the center deflection, which is shown in figure 5.18(c). Since the

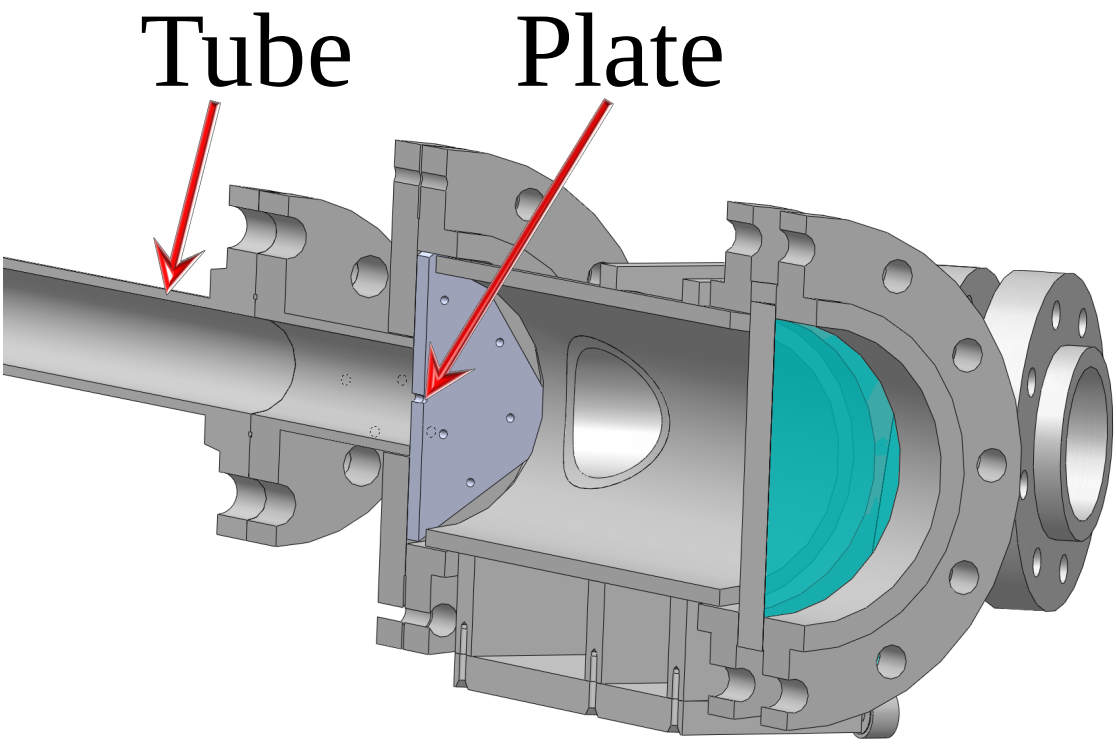

Figure 5.17 Pressure transducer locations on tube and the plate.

center deflection-time history shows a clear separation in scale, the center plate pressure now appears very similar to a square wave. This result is important in simulations because the shock pulse can be modeled as a square wave to determine what pressure level is needed to cause certain strains and stresses in a given plate specimen. This calculated pressure can then be related back to a needed burst pressure to produce the required pressure pulse.

5.6.1 Model Results

The model was run for the 6% Z-fiber reinforcement low pressure case in which a shock pressure 1000 psi (Mach # 3.2) was impacted on the plate. The deflection-time comparison can be seen in figure 5.19. This model was used to calibrate the model and determine if the selection of material properties was correct. The model shows a very good correlation. Although the model predicts more elastic behavior, it correctly identifies each of the peaks of the displacement responses and the characteristic oscillatory time is the same. The small disagreement in plastic strains could be accounted for in the predicted yield stress ratios in

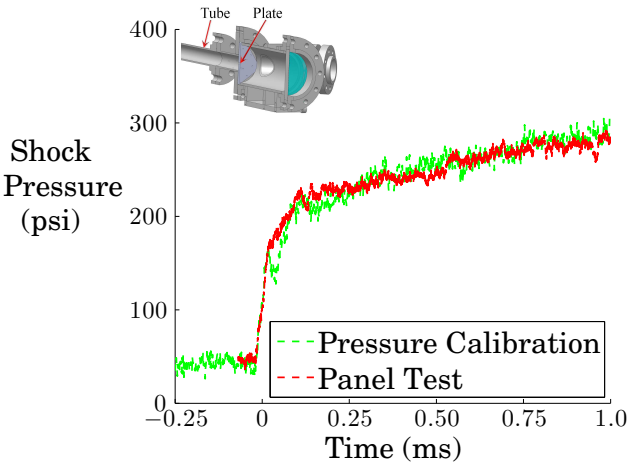

(a) Tube pressure sensor time history

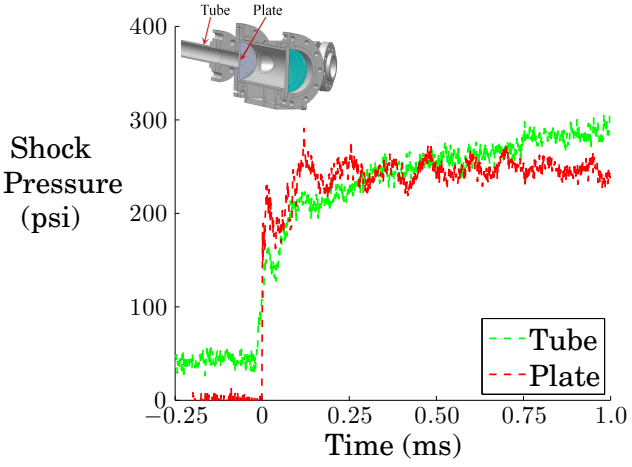

(b) Tube vs plate pressure response

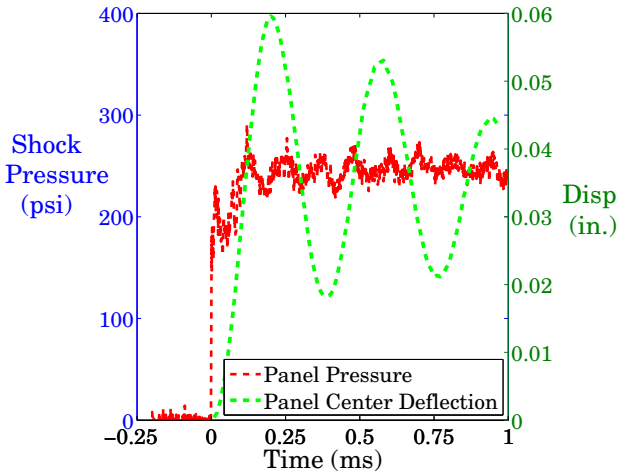

(c) Plate pressure and center deflection

Figure 5.18 Pressure time histories and center deflection of shock tube test. Time has been shifted to show relative data comparison.

each of the constituents.

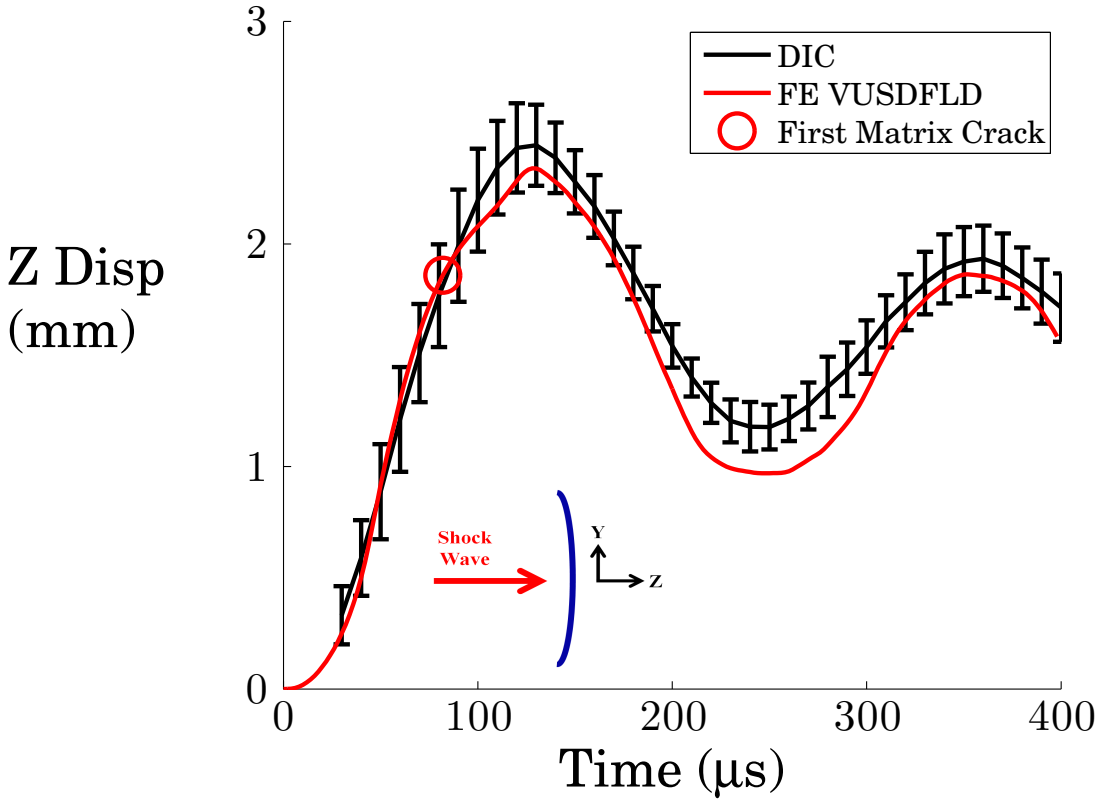

Figure 5.19 Layered anisotropic finite element simulation of 6% Z-fiber reinforced architecture subjected to 1000 psi shock wave. The circle indicates the point of first failure in the model.

A detailed comparison of the strain field can be seen in figure 5.20. The model does a very good job of predicting the strain values. The peaks in both the warp and weft direction are clearly not as high, however, when the micro-cracking occurs it creates a false value of strain as was seen in figures 5.10 and 5.14. This false value is due to the new surface that was introduced by the DIC algorithm, therefore the peaks are not actual values as would be seen in the finite element solution. If we look at the failed region in the FE model, we can see that it correlates very well to the areas in the experimental plots where the highest values were reported, the area where micro-cracking occurred.

Matrix micro-cracking was predicted on both outer surfaces as can be seen in figure 5.21. The plots of damage show that first and last surface had some damage occurring in them. The results show that there is very little damage internal to the material. Additionally there is very little damage on the surface impacted by the shock wave as seen in subfigure d. There is only very localized cracking that occurs close to where the ring has clamped the material.

Additionally the energy contained in the system can be examined computationally. The Total work done corresponds to the amount of energy put into the system. This work is converted into different types of energy: Strain energy, energy stored in the material due to linear elastic strains. Plastic Strain, energy dissipated to cause permanent deformation. Kinetic energy, related to inertia of the plate. Viscus energy is related to the damping of the system oscillating in two different pressure environments. Finally frictional energy, associated with the plate trying to pull itself through the hole of the material. The strain energy is the largest portion of energy that is converted in the system. Inertial energy plays a large role early, however it is converted to strain energy and then dissipated in viscus damping also. The viscus and frictional energies contribute to about 10% each of the energy use. The plastic energy dissipation is very small 1% as can be seen in figure 5.22. One of the energy dissipation mechanisms can not be captured properly, which is the energy that is dissipated through the matrix micro-cracking. Since the model simply degrades the modulus, and does not properly fail the element the energy associated with the damage is not accounted for.

After the model had been calibrated it was then validated by predicting the response of the same plate subjected to a higher pressure. The model was able to capture the main details of the displacement-time history. The responses were very similar as seen in figure 5.23. The FE model initially over predicted the deflection, however the overall response had a very good correlation. The model was within the experimental error described by the error bars of the plot, however the numerically predicted response shows some secondary oscillations that were not seen in the experimental results.

A comparison of the strain field at maximum time, as seen in figure 5.24, reveals trends that were noticed in the initial comparison. The strains are under estimated, however the damage area comprises the entire area where the strains are under estimated. The damaged area covers the same region seen in the large band in the experimental matrix plot. The strain contours additionally are very similar in shape. They seem to form as bands of horizontal and vertical lines across the specimen, which is very similar to trends observed in the computational results. The shapes are not circular but rather like bands that are similar to those predicted in the experiment, but at a lower value. Thus, the layered anisotropic model with anisotropic damage is seen to be able to predict the response of the panels adequately, while capturing the most significant experimental results of matrix cracking.

The Damage in the material was again only predicted in the first and last layer of the material as can be seen in figure 5.25. These results show a wider area of damage on the top surface seen by the cameras. While the surface impacted by the shock wave shows localized damage near the clamp ring where bending is dominant. The damaged area shown here

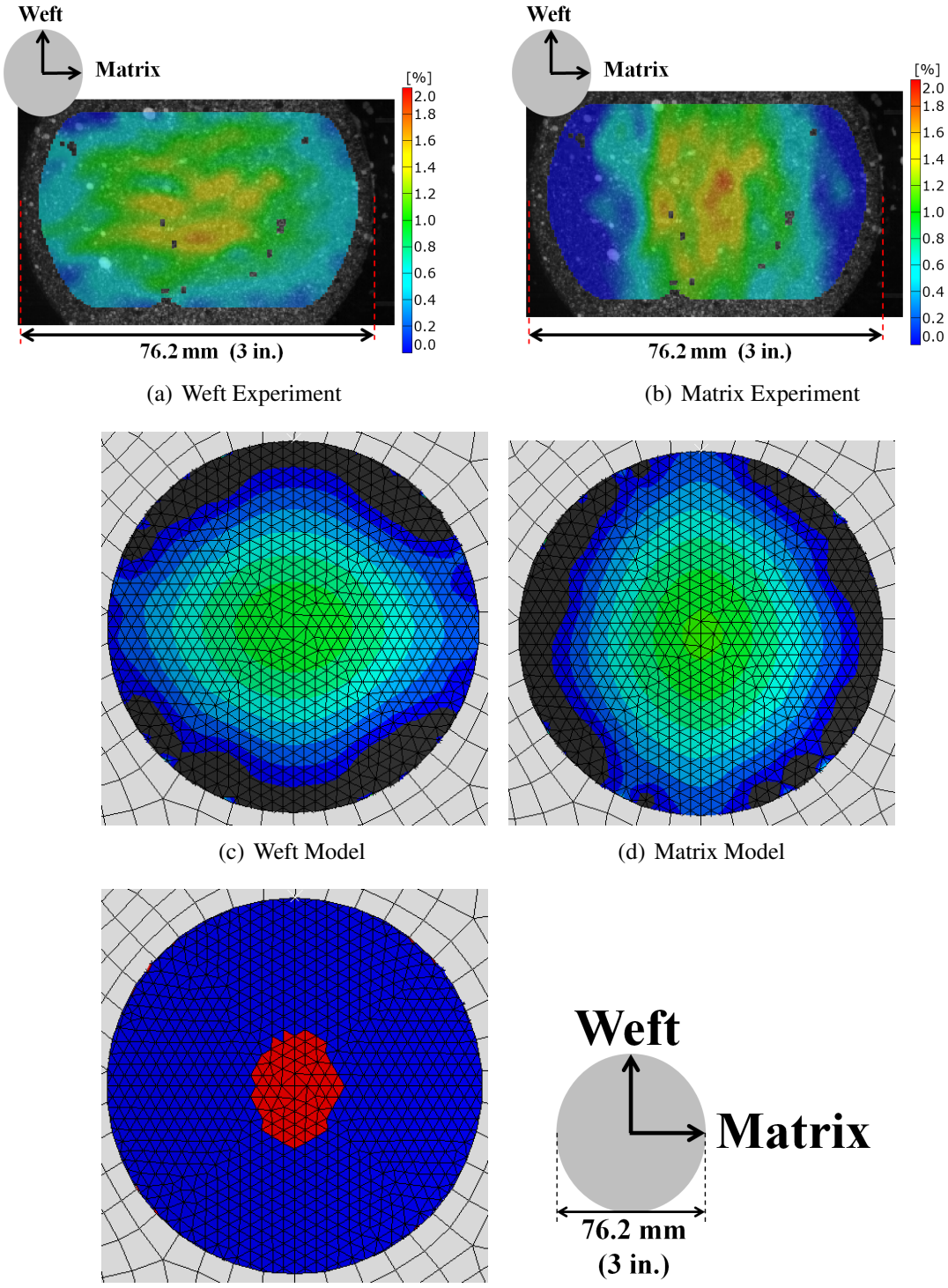

(a) Weft Experiment

(b) Matrix Experiment

(c) Weft Model

(d) Matrix Model

(e) Matrix Failure Model

(f) Size and Orientation

Figure 5.20 Comparison of ε_{weft} and ε_{matrix} for a shock pressure of 1000 psi at the point of maximum deflection from experimental and computational results from the layered anisotropic model.

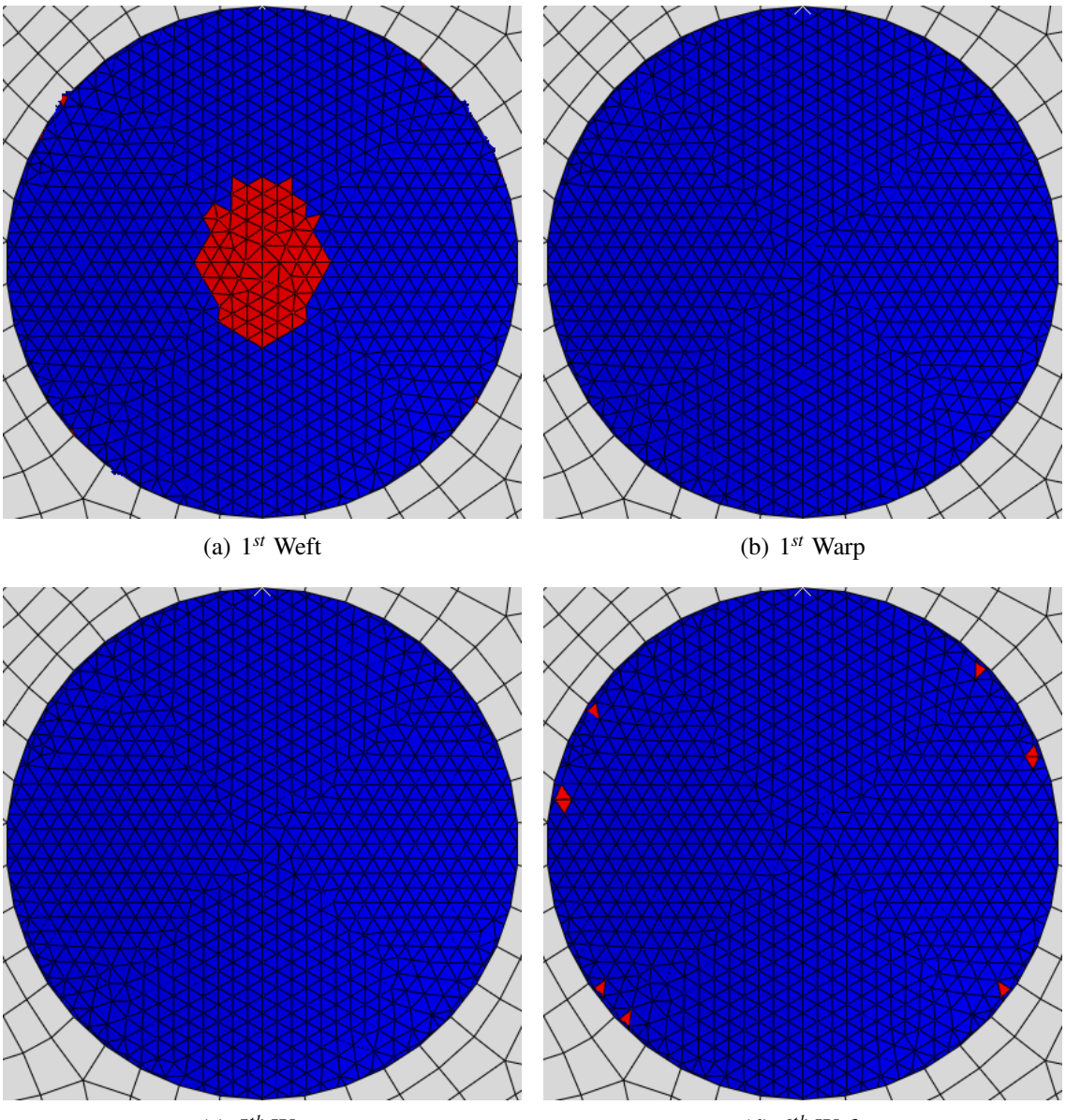

(a) 1^{st} Weft (b) 1^{st} Warp

(c) 5^{th} Warp (d) 6^{th} Weft

Figure 5.21 Damage predicted in each layer for a shock pressure of 1000 psi at the point of maximum deflection for the layered model.

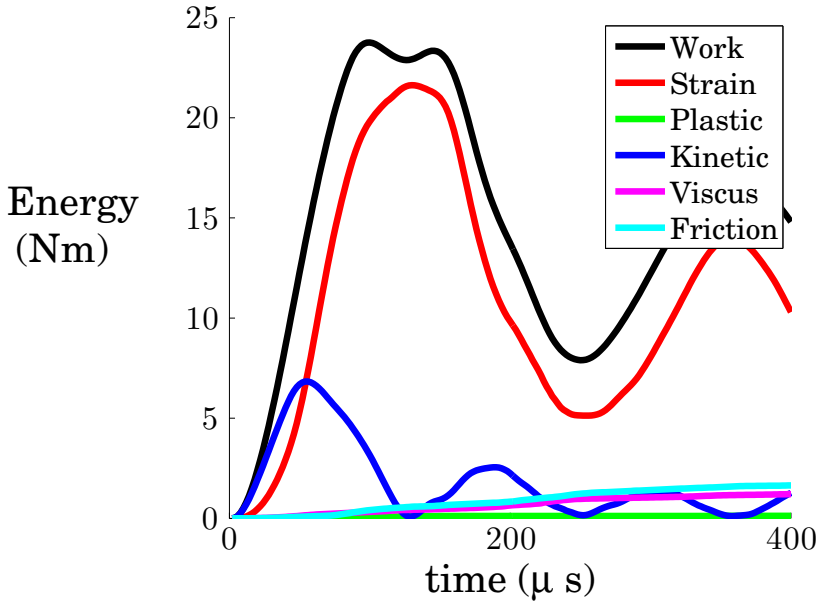

(a)

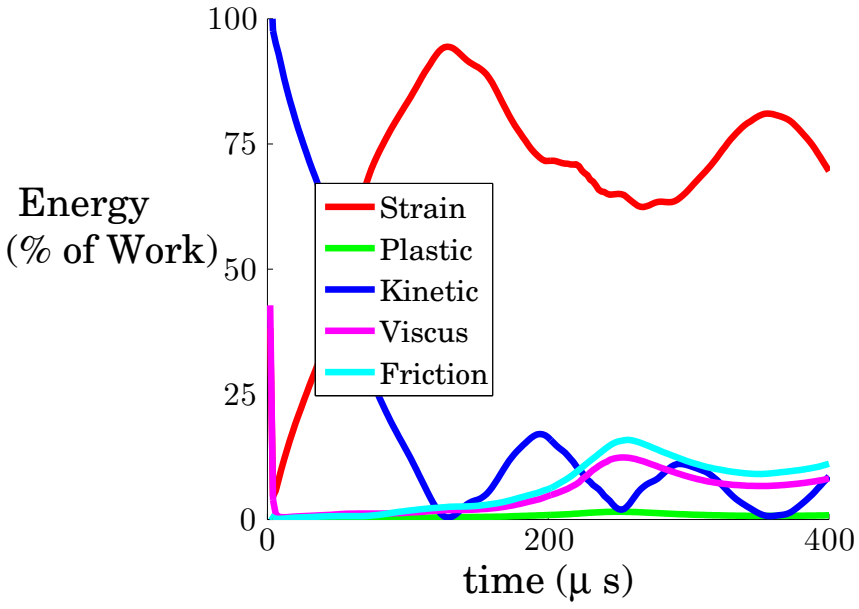

(b) % of Work

Figure 5.22 Energy associated with shock wave loading.

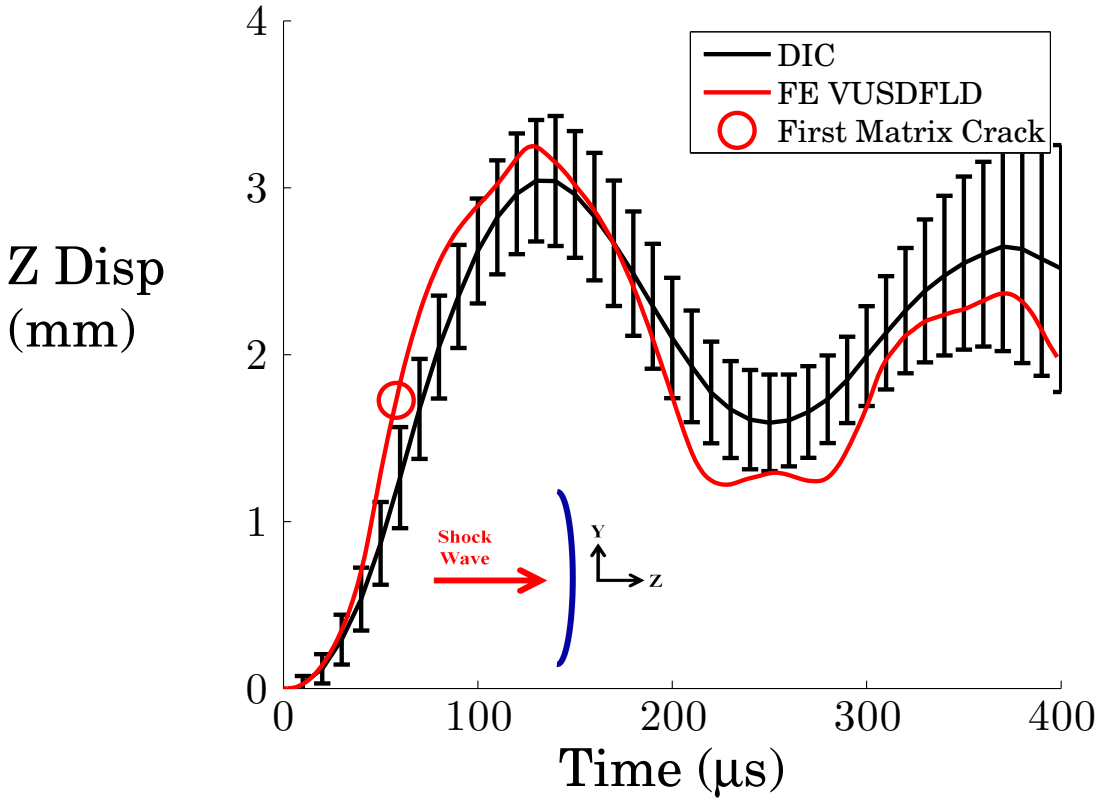

Figure 5.23 Layered anisotropic finite element simulation of 6% Z-fiber reinforced architecture subjected to 1450 psi shock wave.

corresponds very well to those seen in figure 5.13, where only the top and bottom layers are predicting failure.

Figure 5.26 shows the energies associated with each of the different storage and dissipation mechanisms. Again the strain energy is the dominant mechanism, while the Viscus and frictional play large roles. The Plastic energy has increased to 2.5%. This is due to the large deformation and more permanent deformation that occurs.

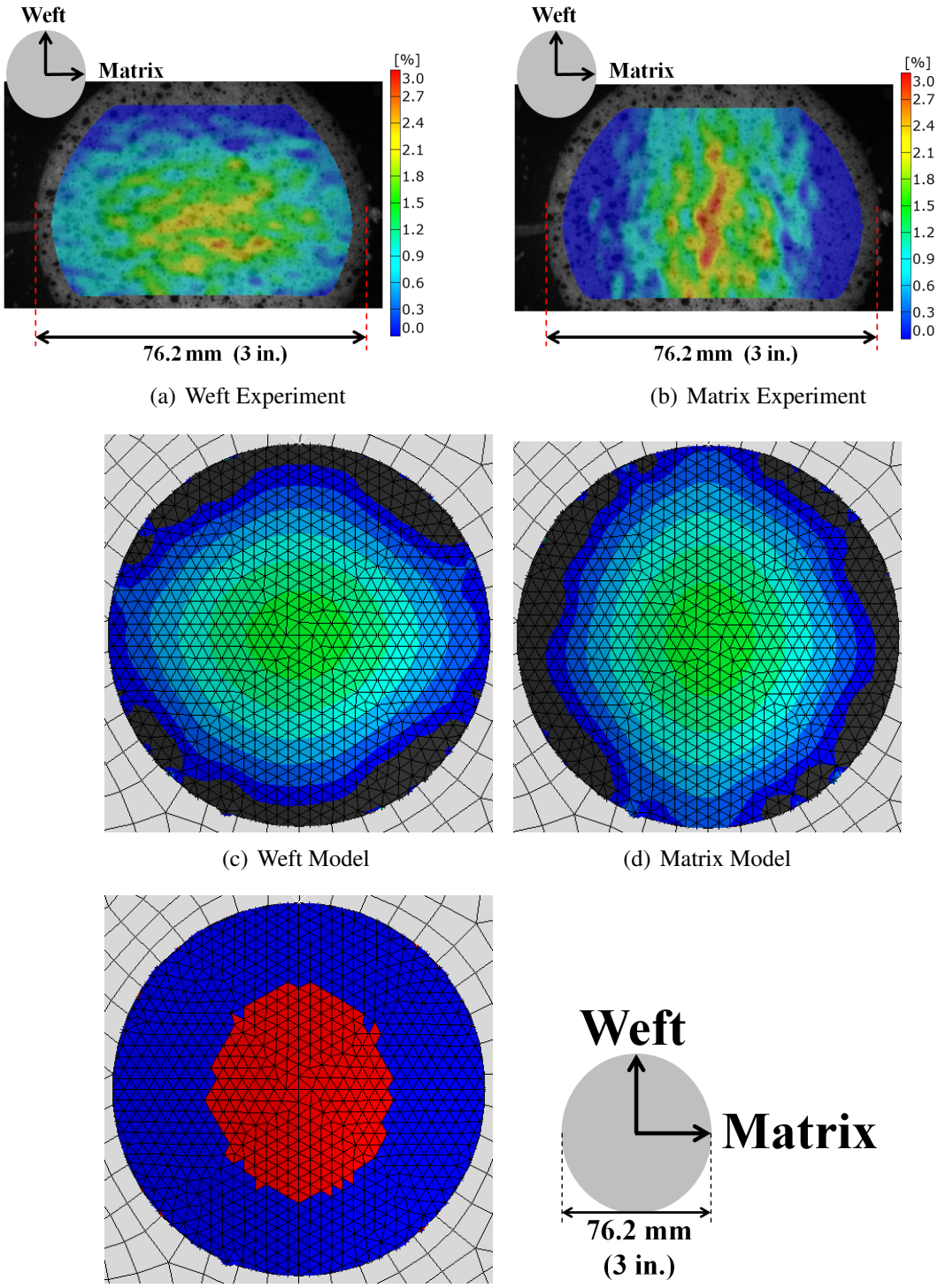

(a) Weft Experiment

(b) Matrix Experiment

(c) Weft Model

(d) Matrix Model

(e) Matrix Failure Model

(f) Size and Orientation

Figure 5.24 Comparison of ε_{weft} and ε_{matrix} for a shock pressure of 1450 psi at the point of maximum deflection from experimental and computational results from the layered anisotropic model.

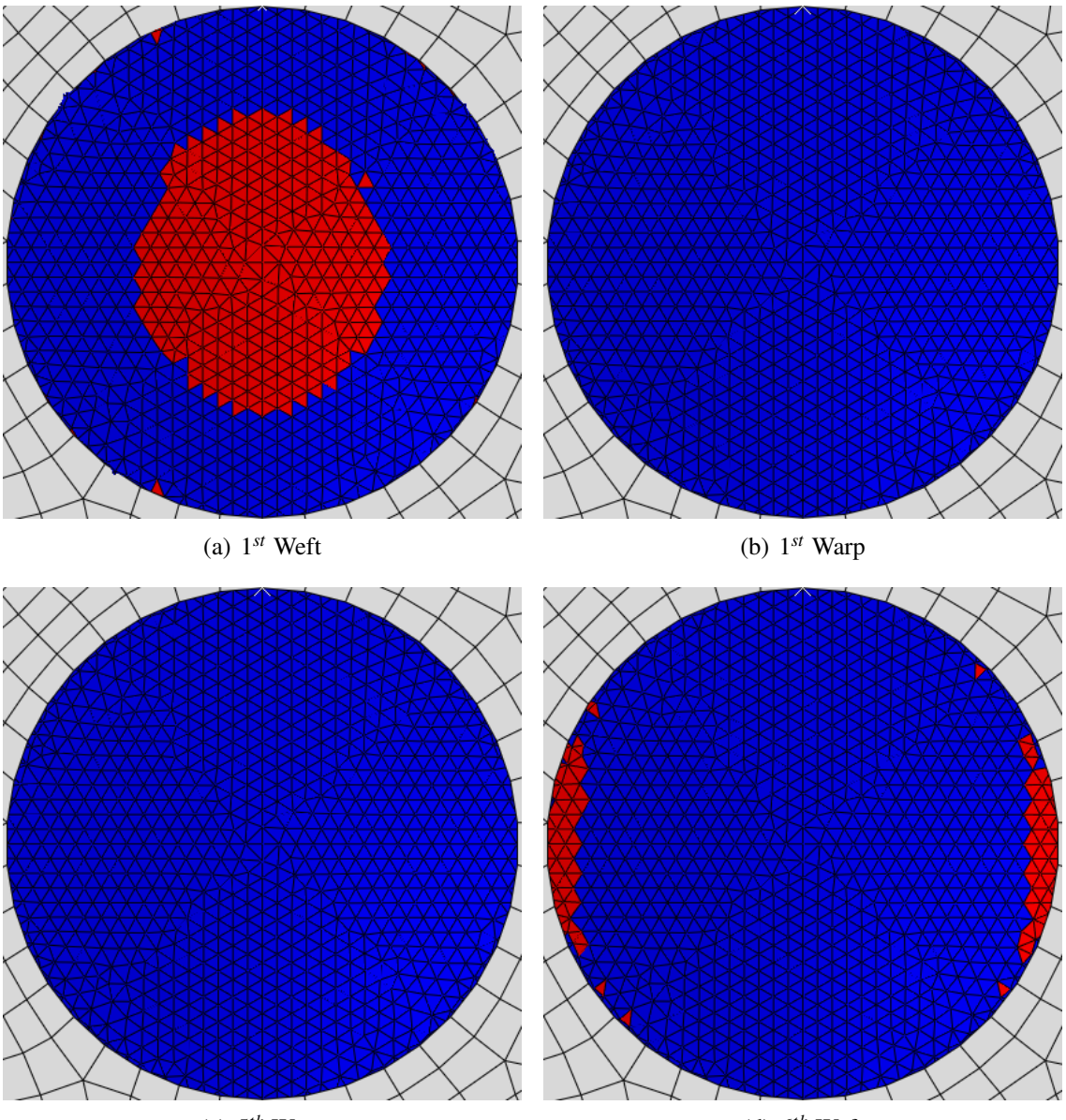

(a) 1^{st} Weft

(b) 1^{st} Warp

(c) 5^{th} Warp

(d) 6^{th} Weft

Figure 5.25 Damage predicted in each layer for a shock pressure of 1450 psi at the point of maximum deflection for the layered model.

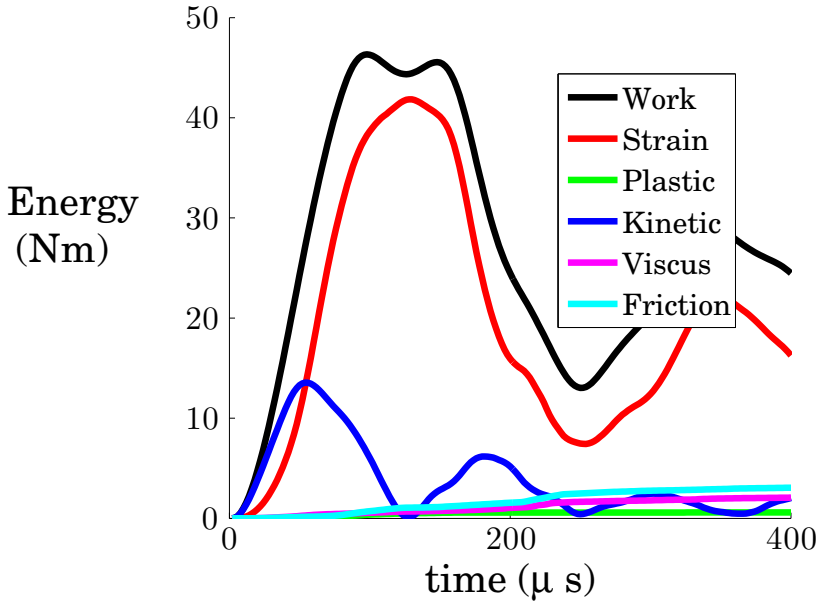

(a)

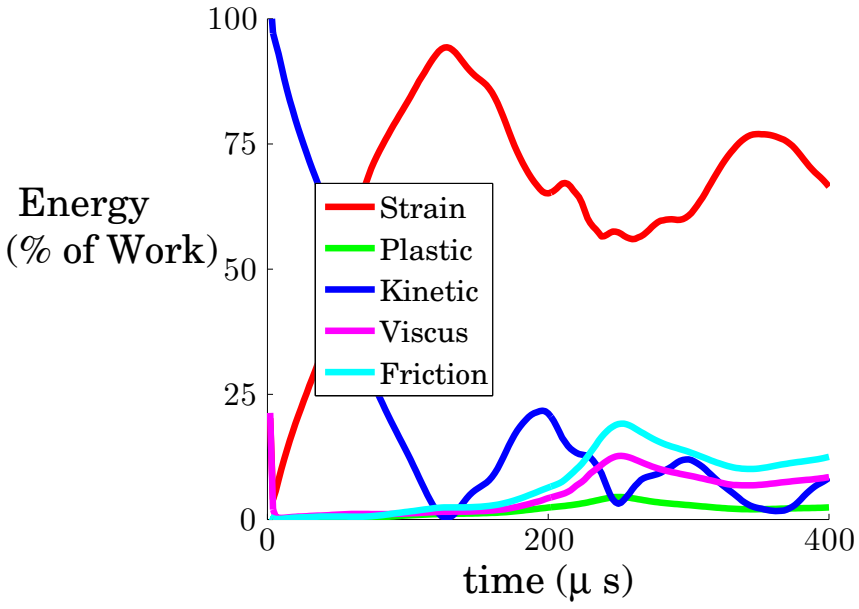

(b) % of Work

Figure 5.26 Energy associated with shock wave loading.

5.6.2 Fiber Matrix Model

A second model was created to attempt to capture the discrete nature of the matrix and fiber tows seen experimentally. The second model used a similar method to model the 6% Z-fiber 3DWC panels, however, each of the different layers was segmented up into separate regions, consisting of tow regions with properties derived from the Concentric Cylinder Model (CCM) model using a fiber tow volume fraction of 54%. The expression for the CCM model are given in appendix B, and are also described in Pankow and Waas, 2009 [19]. The tow volume fraction was based on macroscopic Scanning Electron Microscope (SEM) photographs and the derived properties are shown in table 5.4. The tows were modeled as anisotropic, plastic, rate dependent solids. Other areas were modeled as matrix material with properties determined from chapter 2 of this thesis (i.e. modeled as an isotropic, plastic material with rate dependent material properties). Figure 5.27 shows a schematic of what the model with its many different layers of fiber tows and matrix with orientations. The model was meshed using S4R linear four node quadrilateral shell elements. Element failure was accomplished using the same user subroutine discussed earlier. The same critical matrix cracking strain value was used as in the previous model.

Table 5.4 6% Z-fiber modeling parameters

Fiber	E_{11}	9077	ksi
	E_{22}	882	ksi
	E_{33}	882	ksi
	ν_{12}	0.2718	
	ν_{13}	0.1899	
	ν_{23}	0.1899	
	G_{12}	421	ksi
	G_{13}	370	ksi
	G_{23}	370	ksi
Matrix	E	361	ksi
	ν_{12}	0.35	

The center deflection time history can be seen in figure 5.28, which shows a good correlation between the predicted and experimental data. The results show an overall agreement on maximum load and the oscillatory behavior of the panel. However the model predicts less permanent deformation than the experimental results. The smaller permanent strain is again related to the assumption of the yield ratios that were calculated based on the moduli ratios, as described earlier in section 5.6 of this thesis.

Figure 5.29 shows the calculated and experimental strain fields at the time of maximum deflection, although it under predicts the maximum value obtained by the DIC, the overall

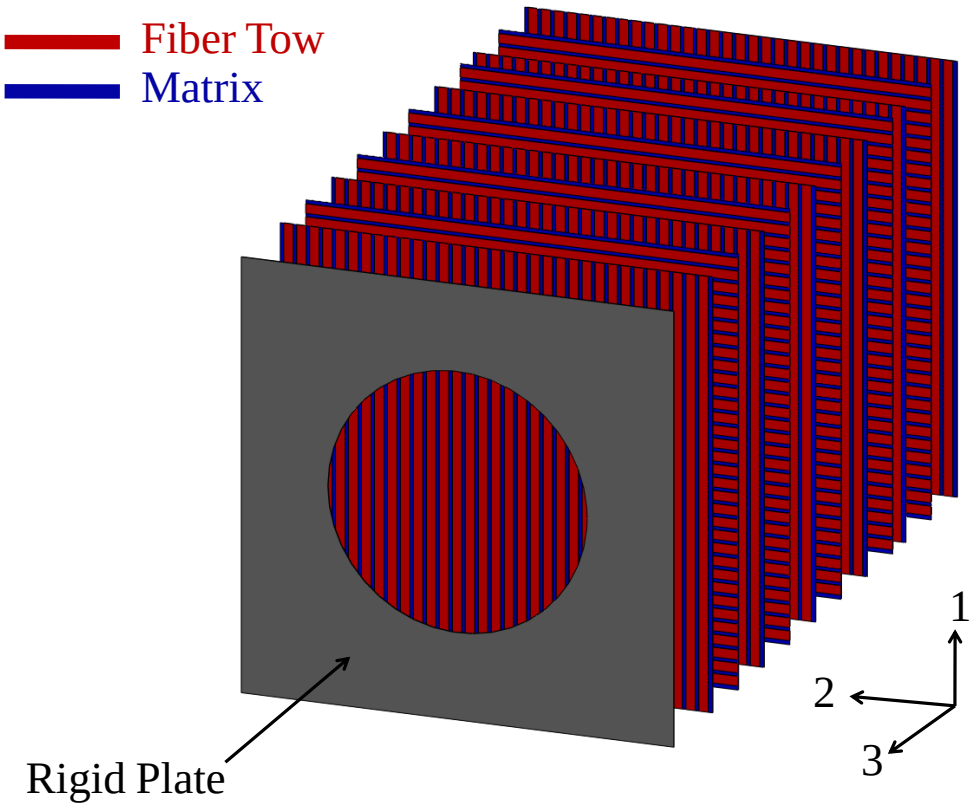

Figure 5.27 6% Z-fiber shock tube model with fiber tow bundles and matrix areas to represent the material microstructure.

field has the same trend. What should be noticed in this plot however is that there are distinct bands formed in the computational matrix strain fields. The yellow bands are formed in the matrix areas of the model highlighting the fact that these areas are undergoing different amounts of strain. The model shows a prediction of some small bands of matrix cracking that occurs in the material. It lies in a similar area to those predicted by the DIC measurements. This implies that a strong correlation exists between the two, except for the false strains presented in the DIC data. The vertical and horizontal bands of constant strain in the DIC are also present in the computational results.

The predicted damage areas are smaller and localized due to the distinct bands of material that exist. These bands can be seen in figure 5.30, where damage is only predicted on the top and bottom surfaces, with no internal damage predicted. The Small amount of damage on the impacted surface seen in subfigure d, shows a concentration around the clamping ring again. Comparing to figure 5.13, the model may over predict the matrix microcracking. The results suggest that the first two layers may have cracking and the last layer has cracking.

The fiber matrix model will more accurately capture the localized plasticity of the matrix

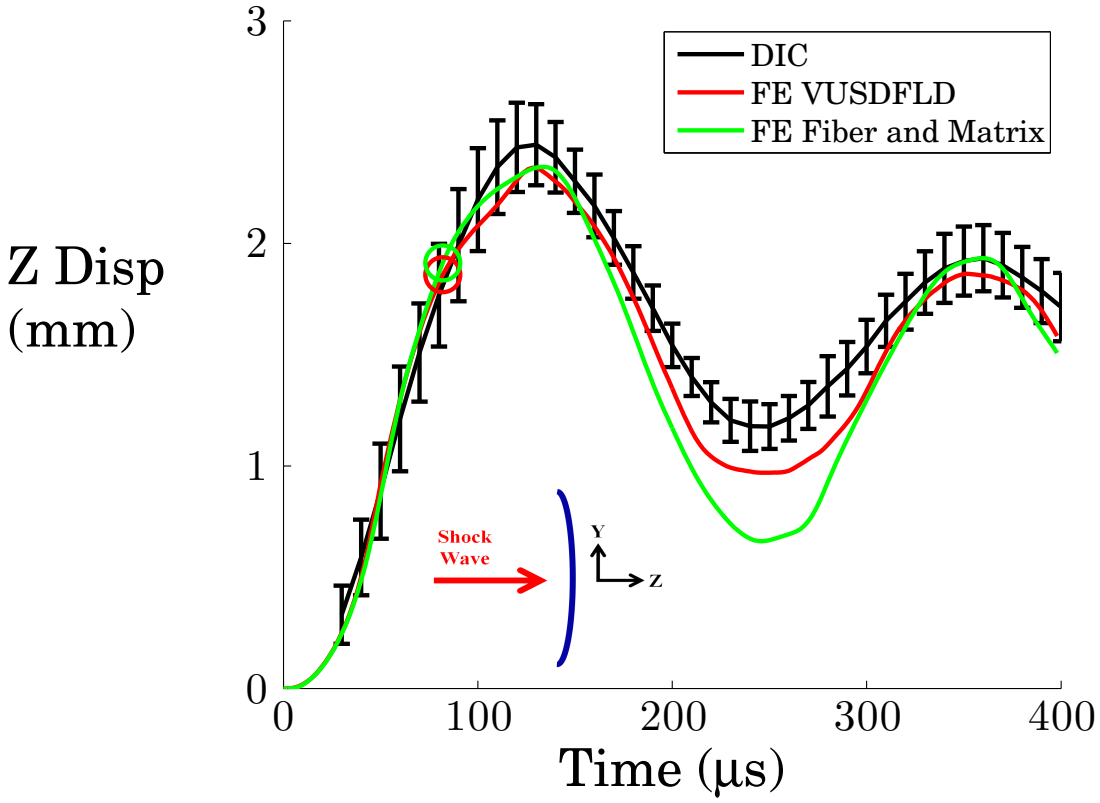

Figure 5.28 Finite element simulation of 6% Z-fiber reinforce architecture subjected to 1000 psi shock wave. The circle indicates the point of first failure in the model.

material producing a larger dissipation of energy. The different energies can be seen in figure 5.31. The plasticity energy dissipation accounts for 5% of the energy in the system. This is much larger than the anisotropic layer level model predicted. Again the energy dissipated due to the matrix micro-cracking can not be captured accurately.

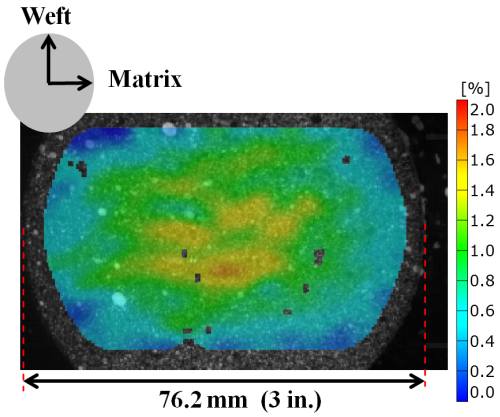

(a) Weft Experiment

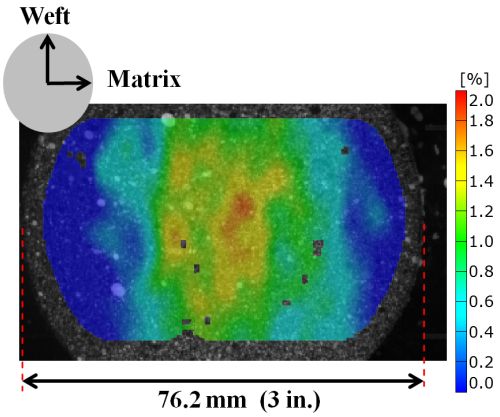

(b) Matrix Experiment

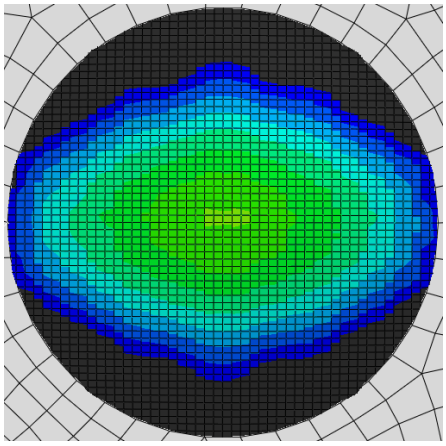

(c) Weft Model

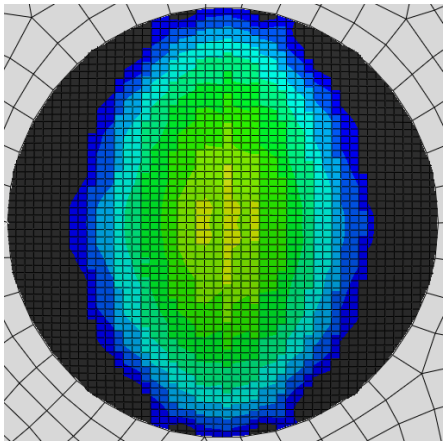

(d) Matrix Model

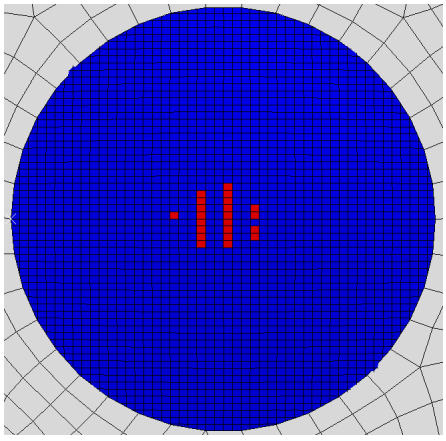

(e) Matrix Failure

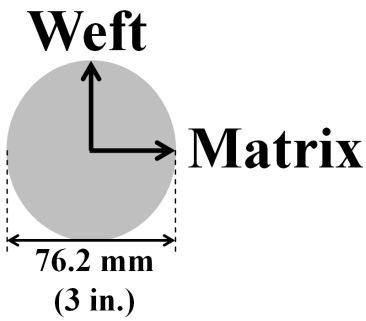

(f) Size and Orientation

Figure 5.29 Comparison of ε_{weft} and ε_{matrix} for a shock pressure of 1000 psi at the point of maximum deflection from experimental and computational results from the fiber and matrix shell model.

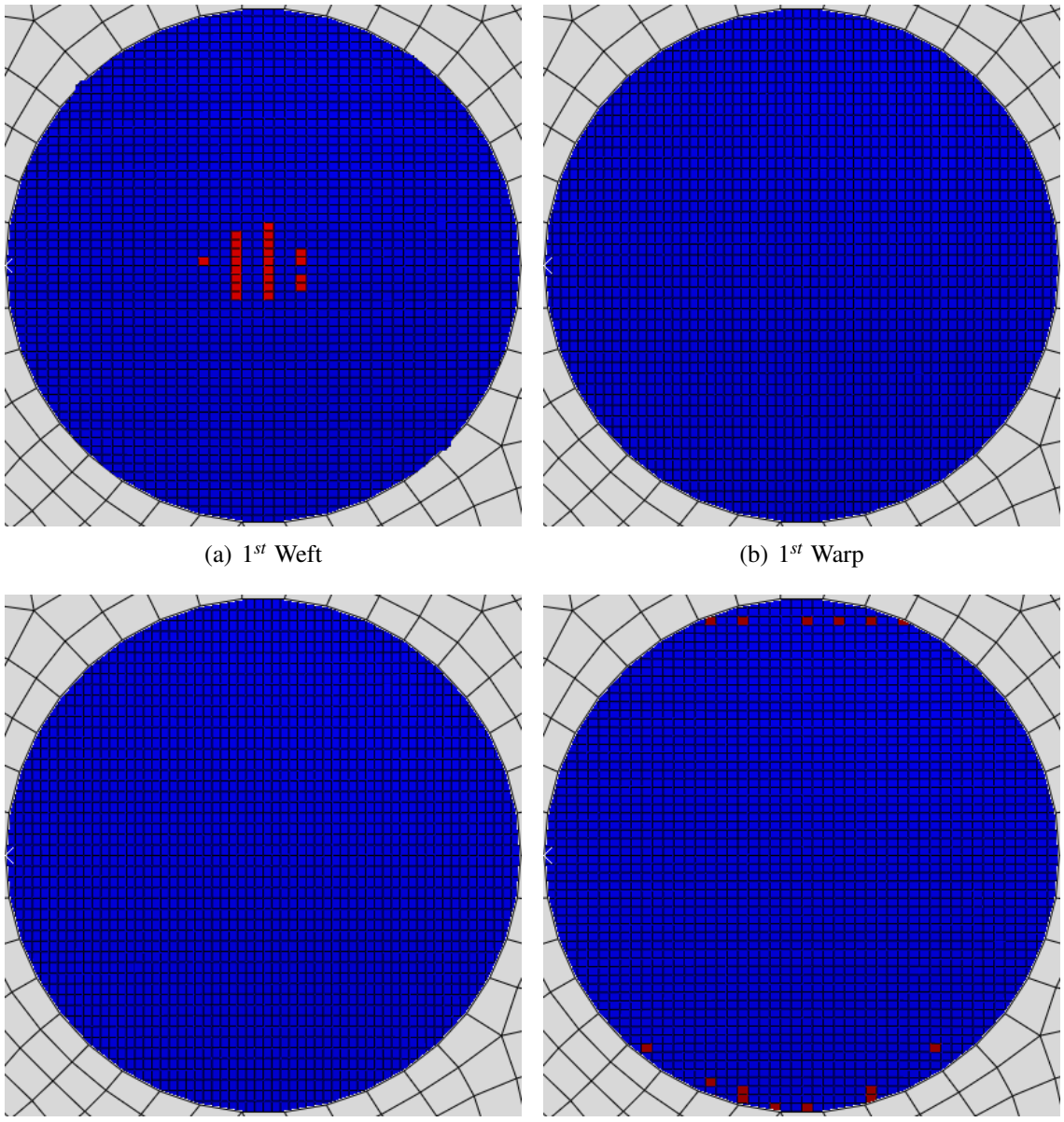

(a) 1^{st} Weft

(b) 1^{st} Warp

(c) 5^{th} Warp

(d) 6^{th} Weft

Figure 5.30 Damage predicted in each layer for a shock pressure of 1000 psi at the point of maximum deflection for the fiber and matrix shell model.

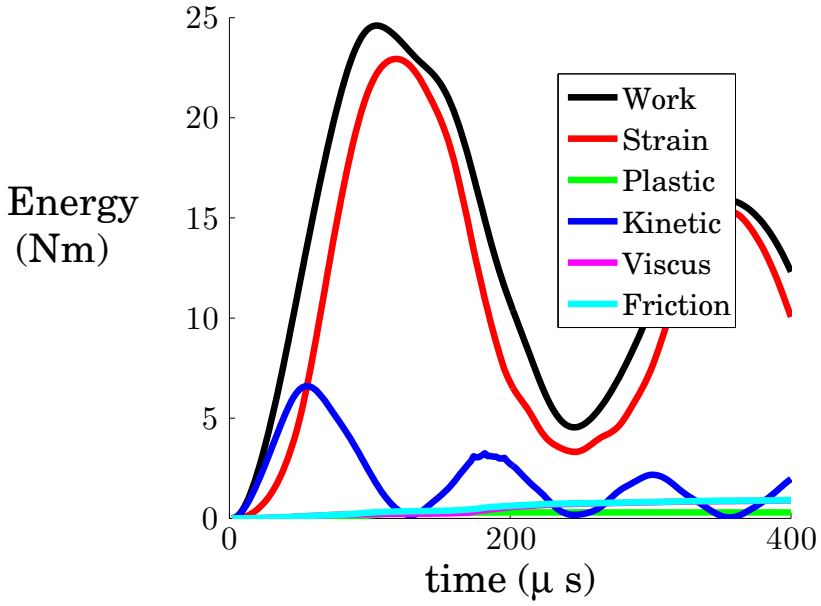

(a)

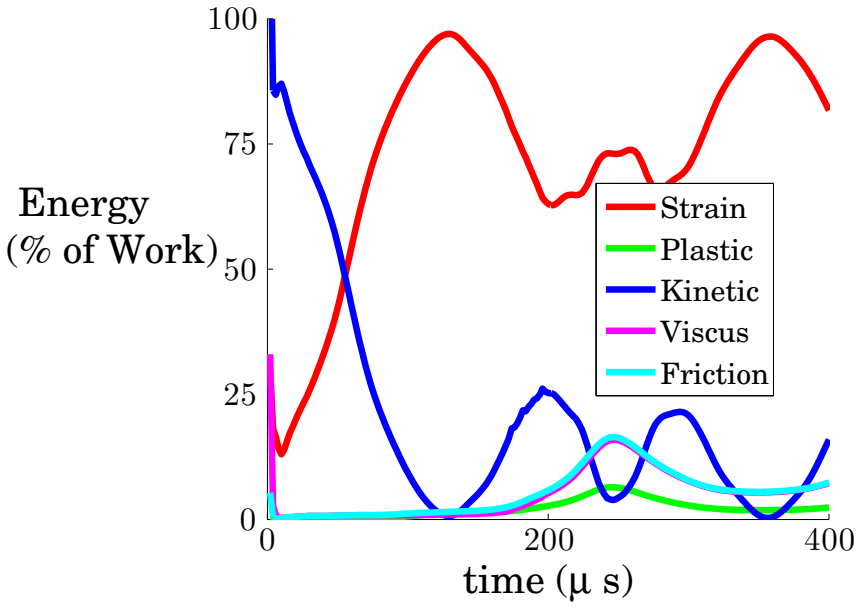

(b) % of Work

Figure 5.31 Energy associated with shock wave loading.

With a good understanding of the mechanical properties a second, simulation was run to predict the response of the panel to a higher shock load of 1450psi. The maximum out of plane displacement vs time history is shown in figure 5.32. The results show that a much larger elastic response is suggested, however the maximum displacement and oscillatory behavior shows a strong correlation. This model however does not show the secondary oscillation that occurred in the first model. Rather it predicts more of an elastic response of the material.

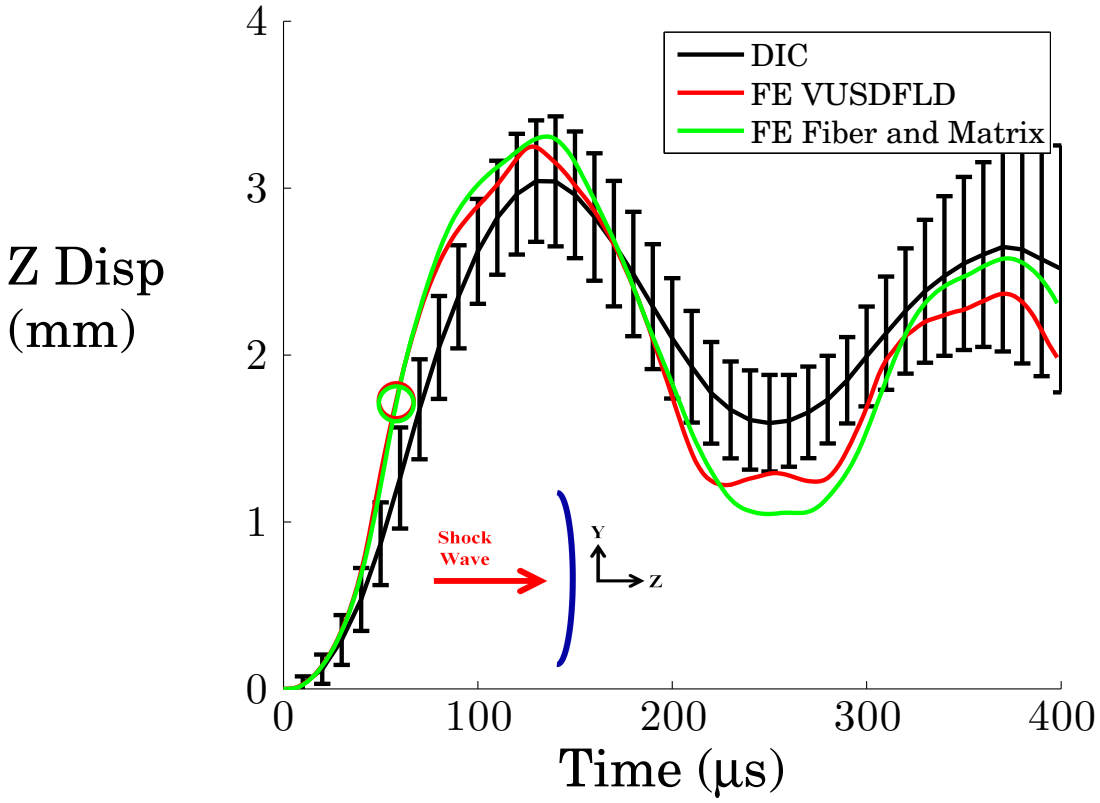

Figure 5.32 Finite element simulation of 6% Z-fiber reinforce architecture subjected to 1450 psi shock wave.

When the strain field at maximum deflection is examined, there is a very good correlation between the experimental data and the predicted values, as seen in figure 5.33. However, the maximum values are not achieved again. The results show again that there are distinct bands that form where the matrix has a higher strain value than the fibers and will cause failure in the matrix at these locations. These bands appear in similar locations on the experimental plots indicating the fact that we have a matrix failure and a localized strain due to that matrix failure. The length of the strain band failure predicted by the model is similar to the experimental results. The steep gradient in material properties (due to the discrete nature of

the model) also suggests that the strain field of the DIC is being mis-represented. Overall, the second model shows a strong correlation to the observed panel response, including matrix micro-cracking. Additionally, the model is based on actual characteristics, since the tows are modeled as discrete entities rather than the homogenized singe layer representation of the previous model.

The damage predicted propagates through the first two layers as seen in figure 5.34. Here the damage has progressed from the top layer down to the first layer of warp tows. The impacted surface have some damage predicted on around the clamped ring that may propagated through to the last warp layer. Overall there is very little internal damage in the material, mostly external to the surface.

Figure 5.35 shows different energies associated with the model. Again most of the energy is converted to linear elastic strain energy, however about 10% of the energy is converted to plastic strain energy. This would correspond to a larger area being closer to matrix micro-cracking. The plastic energy and the damping energy are comparable in terms of magnitudes.

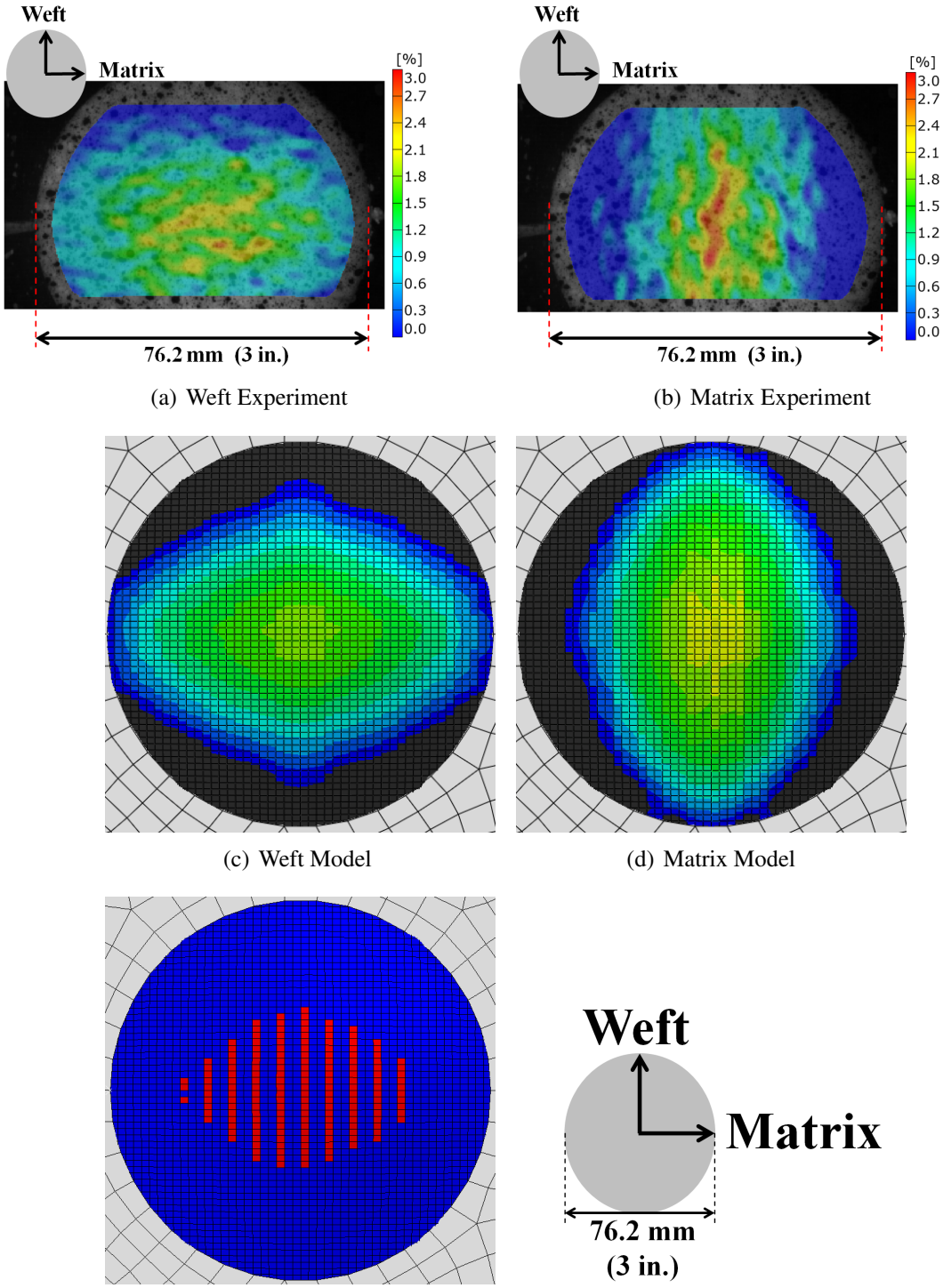

(a) Weft Experiment

(b) Matrix Experiment

(c) Weft Model

(d) Matrix Model

(e) Matrix Failure

(f) Size and Orientation

Figure 5.33 Comparison of ε_{weft} and ε_{matrix} for a shock pressure of 1450 psi at the point of maximum deflection from experimental and computational results from the fiber and matrix shell model.

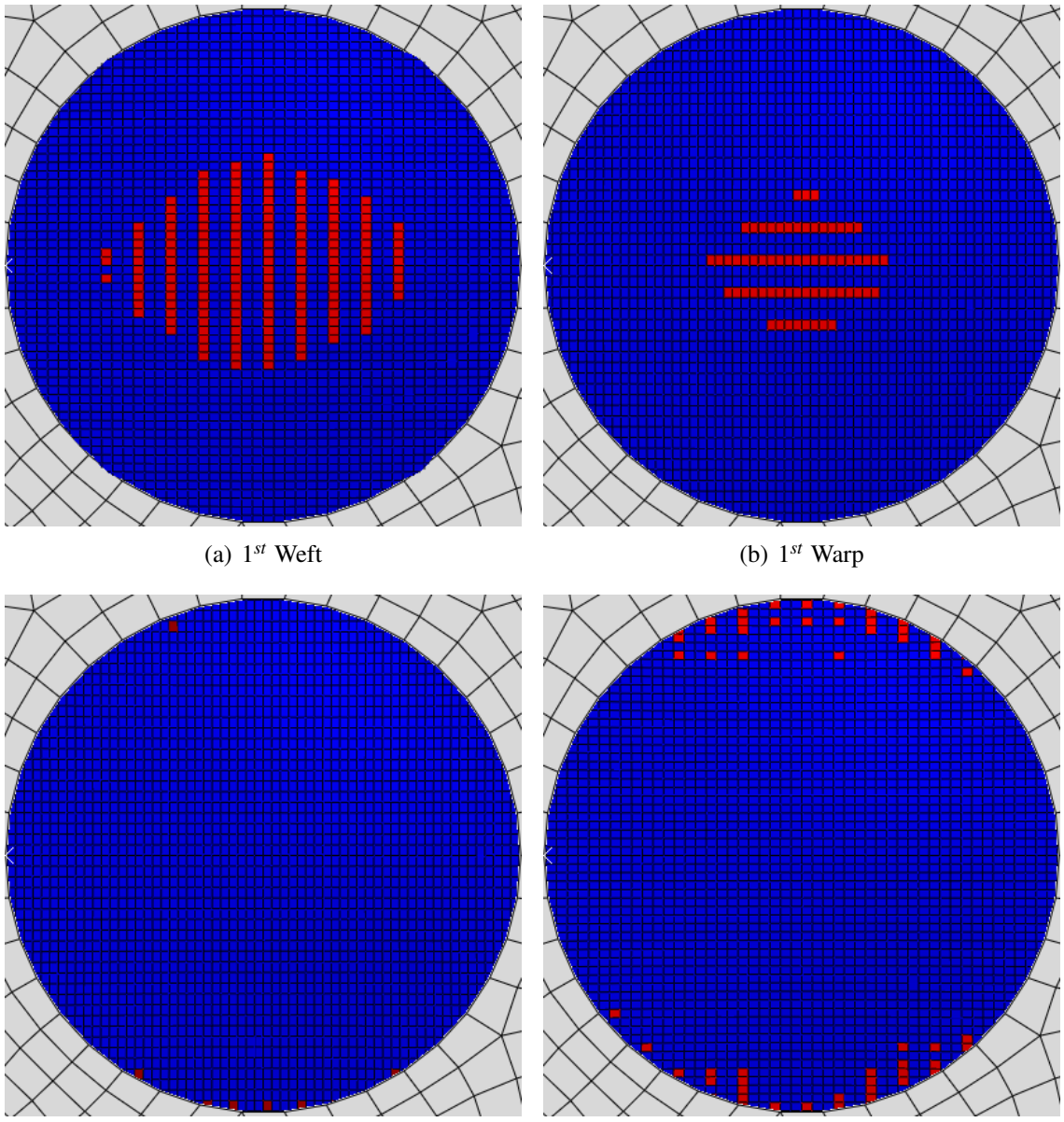

(a) 1^{st} Weft

(b) 1^{st} Warp

(c) 5^{th} Warp

(d) 6^{th} Weft

Figure 5.34 Damage predicted in each layer for a shock pressure of 1450 psi at the point of maximum deflection for the fiber and matrix shell model.

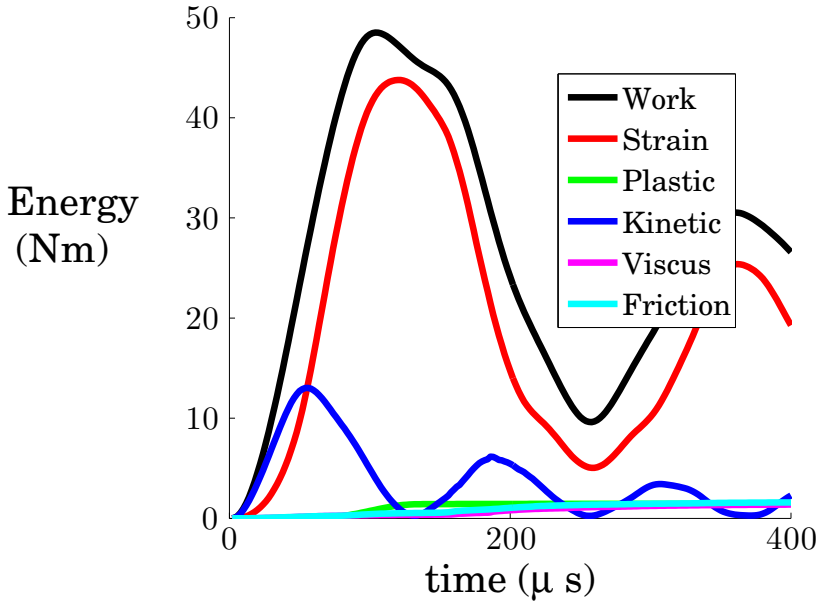

(a)

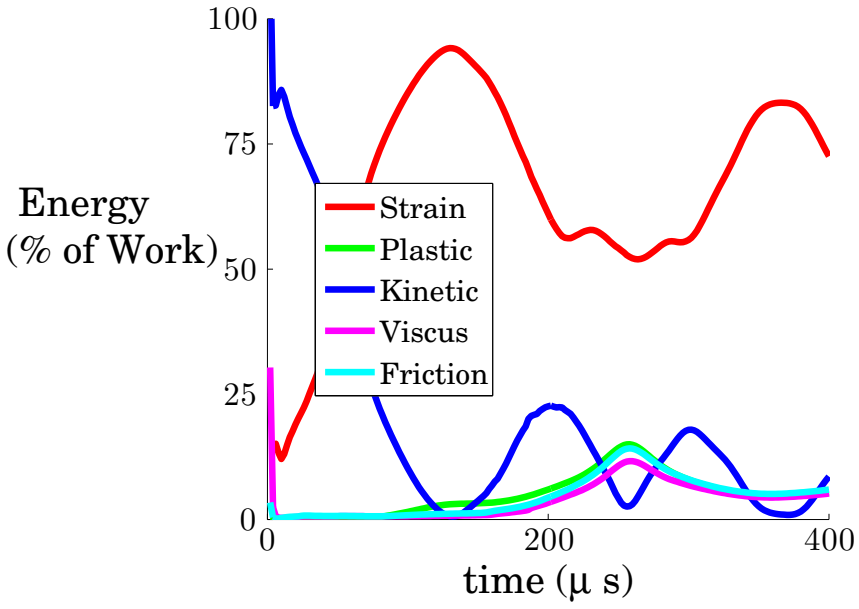

(b) % of Work

Figure 5.35 Energy associated with shock wave loading.

5.7 Conclusions

An experimental investigation into the shock loading response of 3DWC panels has been carried out. A modified shock tube was used to determine the response of various different architectures to shock loading. The 6% Z-fiber reinforced 3DWC offered the best performance in both strength and resistance to micro-cracking. Further studies were done to show the accumulation of damage and the formation of the micro-cracks. The presented results clearly showed that this was the only type of damage that was occurring in the specimens.

Two finite element representations of the test configuration were developed to simulate the response of the 6% Z-fiber 3DWC. In the first model, each layer of the 3DWC was represented as a homogenized equivalent anisotropic plastic solid with an anisotropic failure criterion to capture the failure of the matrix. Additionally , the anisotropy in the plastic response was assumed to scale as the respective elastic moduli ratios in the different loading planes. The second model segmented each layer up to have discrete fiber tow bundles and areas of pure matrix, within each layer. Both models produced a very strong correlation to experimental data. Both models were "calibrated" using results from a low pressure differential shock (Mach # 3.2) After this, both models were seen to predict the response of the 3DWC panels to a shock test that subjected the panels to a shock at Mach # 3.6. In particular, both models were able to predict the onset of matrix cracking damage that was clearly evident in the DIC strain field maps.

Chapter 6
Split Hopkinson Pressure Bar

A large diameter split Hopkinson pressure bar (SHPB) was created for the sole purpose of testing composite specimens due to the relatively large unit cell size of the 3DWC material. Tests were performed in the three orthogonal principal material directions to determine the effective through the thickness and in-plane compression response. Attention was confined to the the 6% Z-fiber reinforced composites. Initial tests showed scatter in the data, due to issues of specimen flatness from the the VARTM manufacturing process, which will be discussed. After "flattening" specimens further tests were run to determine the in-plane and out-of-plane mechanical response of this material. It was found that smaller specimen size was needed to produce failure in the specimen. SHPB testing of 2D in-plane woven S-2 glass fiber with SC-15 matrix composites has been shown to have a rate dependency [76]. Additionally studies into off-axis layered composites have been reported in [77].

SHPB testing of 3DWC has also been done previously [39, 48], although in these studies the authors simply assume equilibrium, but a constant strain rate is never achieved. Other researchers have examined the tensile rate dependent properties of woven composites showing and explaining the rate dependent behavior due to the reinforcement [49]. A modified Hopkinson bar has been used to perform high strain rate punch shear tests [45], showing the rate dependency of the 3DWC. In this chapter, results from SHPB testing of the 6% Z-fiber reinforced 3DWC are presented. A novelty in these test are the real time in-situ deformation fields that are captured at high rates with the DIC method.

6.1 SHPB Test Protocol

The SHPB test procedure has been developed and refined over several decades, starting with the pioneering work by Kolsky [78]. Most routine SHPB tests are based on a 1D wave propagation analysis in a solid as described in Appendix C. The results obtained from such an analysis of the experimental data are used in this chapter to obtain the effective

stress-strain curve of the material as obtained from strain gauge data. The results will also be validated using DIC techniques to better understand the full field strain field and interpret the inferred results since, traditionally, SHPB testing is reserved for homogeneous monolithic materials. DIC measurements were taken on all of the samples during deformation to determine the effective strain field of the samples. This aspect is very important since it shows the "synthesis" of the strain signal that is recorded due to a highly complex stress and strain field that is present in a non-homogeneous 3DWC sample. Figure 6.1 shows the specimen as it would be situated between the two bars. It is necessary that the specimen is perfectly flat between the two bars otherwise there will be a very poor transmission of the stress waves, at the interface between the incident bar, the 3DWC specimen and the transmission bar.

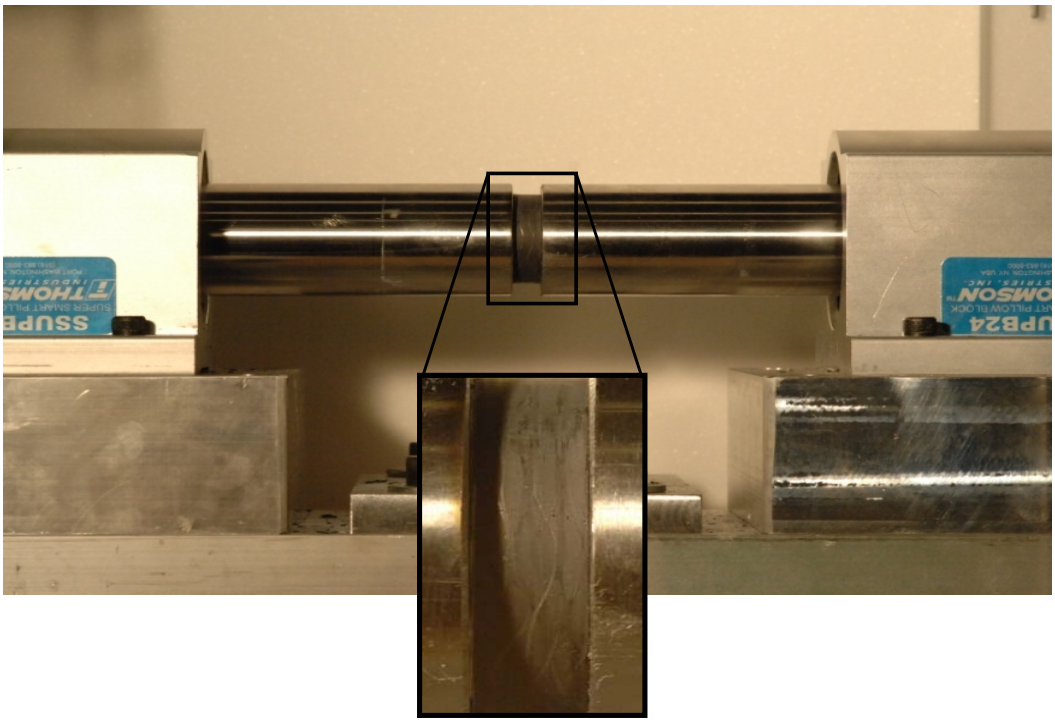

Figure 6.1 SHPB setup showing the placement of the specimen in the apparatus.

6.2 DIC Data interpretation

The DIC data will be used to not only validate the measurements, but also for further information on failure and strain non-uniformity. Preliminary tests showed that the average strain in the sample strongly agreed with the strain measured from strain gauges in the bars. When the two measurements are plotted as a function of time, the two results have a strong agreement, however the results diverge at a certain point, see figure 6.2. The DIC results show that the strain reaches a critical value, however the strain gauges continue to predict strain. From the images we can determine that the inferred measurement often produces more strain than measured in the specimen, therefore the DIC will be used to determine where to truncate the measurement of the stress strain curve, derived from the strain gauges. The reason for "more" strain production in the bars is due to the fact that this is an inferred measurement. The calculation for strain is based on the integral of the reflected signal. Therefore it does not know if failure has occurred or the maximum strain for the test has occurred. Additionally, when the strain field in the specimen becomes highly localized due to failure, the specimen will soften and continue to compress, however, strain relaxation in other areas of the specimen leads to a net decrease in the DIC data. Additionally strain relaxation cannot occur in the 1D wave analysis since a negative reflected signal would need to occur. This means our compressive wave would have to turn into a tensile wave during it's propagation.

Due to the complex nature of the specimen architecture, the DIC was also used to determine if the strain field was in equilibrium. It was observed from these tests that the results were heavily dependent upon the surface flatness. In VARTM manufacturing, only one surface is kept flat (see section 2.1.3) and the other is heavily dependent upon the architecture and the vacuum conditions while curing the specimens. This non-flat undulated surface produces very localized concentrations of strain. The surface waviness inhibits the strain from transferring properly from the bars into the specimen causing localized failure in the specimen.

Larger specimens exhibited a phenomenon where the transmitted strain gauge would have a steeper slope than the incident strain gauge. Since 3DWC has a complex architecture that is highly non-homogeneous, it is not surprising that the strains are not as uniform as would be seen in a corresponding isotropic homogeneous specimen. The material is not in equilibrium during the early phase of loading due to interactions of propagating stress waves internal to the microstructure. Two stress waves in different constituents will interact with one another and cause false strains in the material. The DIC data helps to make the details of these observations clear, since the evaluation of the non-uniformity in the strain

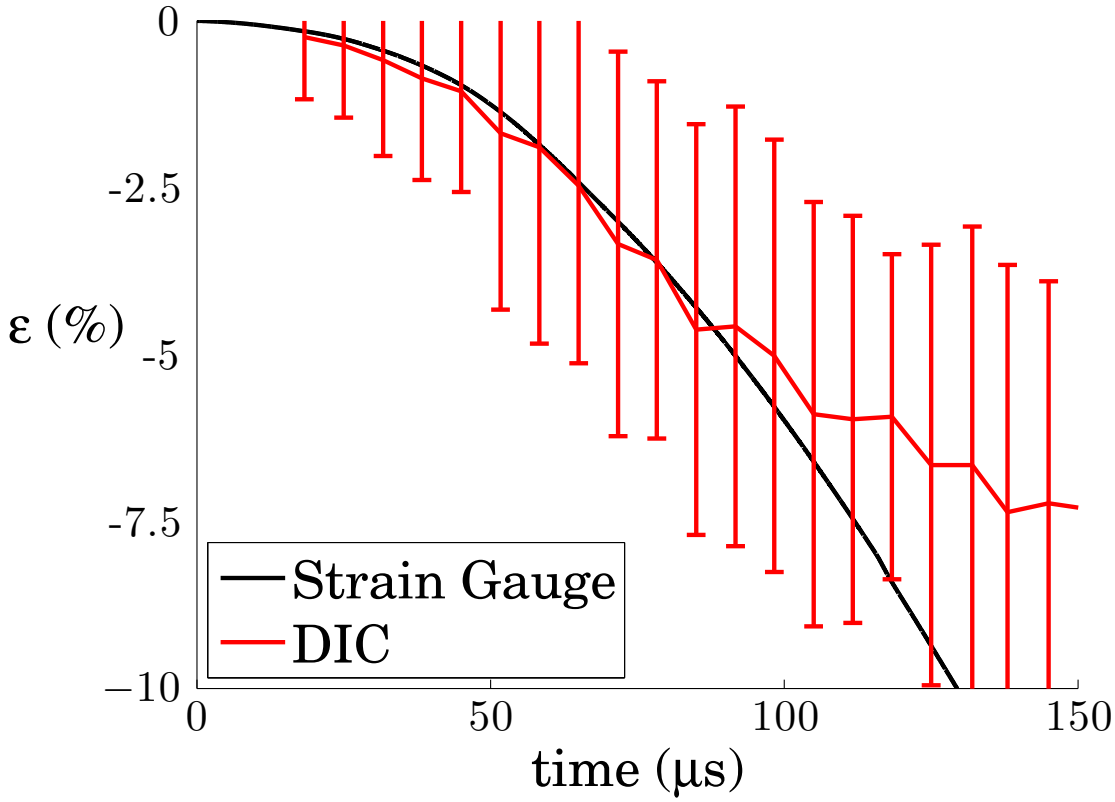

Figure 6.2 Strain gauge vs. DIC data comparison for a typical SHPB test.

field is captured. The DIC strain evolution maps will be presented later in section 6.3.

6.3 Experimental Results

Hopkinson bar testing was carried out in both in-plane orientations, warp and weft, with a third direction being tested through-the-thickness. Each of the orientations were subjected to four separate strain rates. Failure was observed in all of the orientations producing stress-strain response until failure. The through-the-thickness test results will be examined first.

6.3.1 SHPB Testing Through-the-Thickness

One of the more critical aspects of this study was the through-the-thickness response of the 3DWC material, since this is related to how the material will respond to distributed pressure

pulse loading over a small surface area. Additionally the information about how the material would fail either from shear banding or delamination was also of interest.

A comparison test was run on the hydraulically activated MTS machine to characterize the through the thickness compressive response of the material. This test was performed to determine a baseline response for the material to understand how it would behave under different loading rates. The effective stress-strain curve will be used later on in many of the comparisons. The test was run at a rate of 0.0004 in/sec on an identical specimen used in the testing of $15.8mm(0.622in.)$ by $15.5mm(0.611in.)$ and $5.95mm(0.234in.)$ thick 3DWC material (6% Z-fiber architecture produced by T.E.A.M.). The material failed through individual fiber tow delamination and matrix failure in compression as can be seen in figure 6.3. It can be seen that the matrix and fiber tows have separated apart in all of the layers, which can be characterized as delamination of the fiber tows. This is evident in figure 6.3 where the left hand side of the image shows how the fiber tow has separated from the block of matrix.

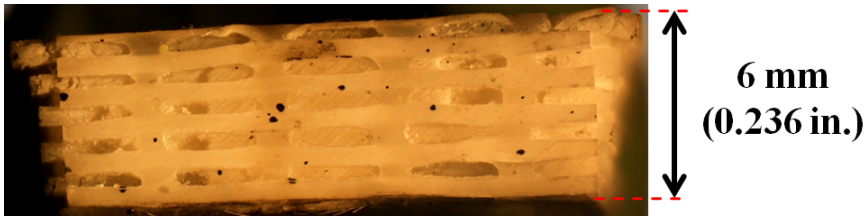

Figure 6.3 Through the thickness compression specimen, post failure image of the side view.

Initial SHPB tests used a one inch square specimen (25.4mm square) which would contain somewhere between 8-16 unit cells (repeat units) depending on where the specimen was cut. It was found that these specimens would sustain a maximum stress of about 200-250 MPa, as seen in figure 6.4 and result in no failure, observed in both experimental data and from visual observation of the specimens. The specimen would reach about 7% strain at the maximum stress and then go through an unloading phase where the strain would relax to near zero strain.

The overall response obtained by the Hopkinson bar shows similar trends. The initial modulus is similar in both the static and dynamic rates, however the maximum load is much less, which is dictated by the specimen size if one does not change anything in the experimental setup.

By switching to a smaller specimen size one can achieve a much larger load for the same stress pulse. The reduction in initial cross sectional area to $15.2mm(0.6in)$ square will increase the stress by a factor of four. This will increase the stress from approximately 200 MPa to 250 MPa, to about 560 MPa to 700 MPa, which should produce failure in the samples, based on the static response.

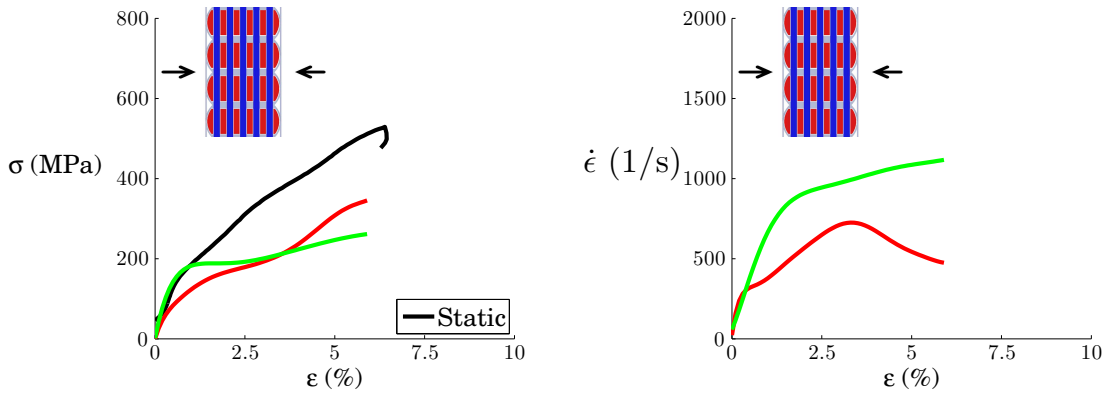

(a) $\sigma vs.\varepsilon$ (b) $\dot{\varepsilon} vs \varepsilon$

Figure 6.4 Stress-Strain-Strain Rate plots for 1 inch specimens through the thickness.

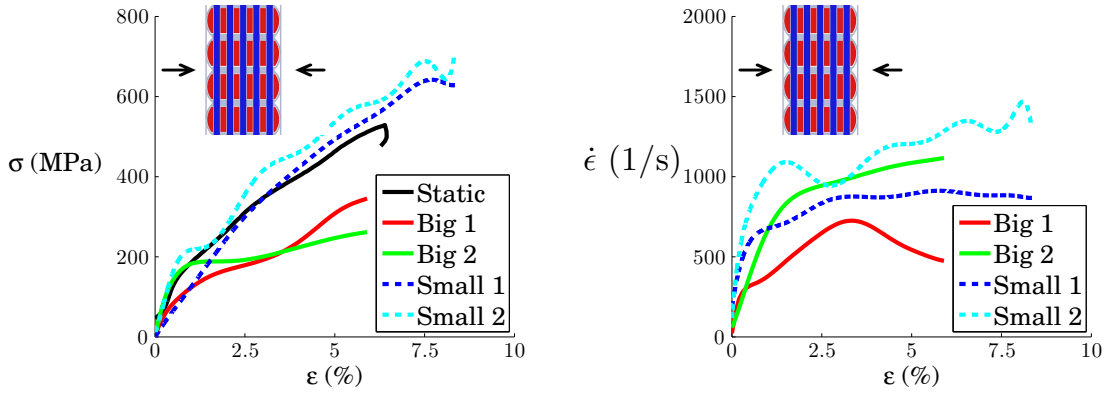

(a) $\sigma vs.\varepsilon$ (b) $\dot{\varepsilon} vs \varepsilon$

Figure 6.5 Stress-Strain-Strain Rate plot comparison for the two different specimen sizes. The solid lines represent the large specimens, while the dashed lines represent the small specimens.

Figure 6.5 shows a comparison of difference in specimen size affecting the results of the Hopkinson bar testing. The solid lines refer to the large specimens and the dashed line refers to the smaller specimens. Not only do the smaller specimens produce much larger stress, but specimen failure is easily achieved. The smaller specimens also had a better force equilibrium balance as compared to the larger specimens. This is attributed to less wave interaction in the smaller samples.

The smaller specimens contain about 4-8 unit cells, however the increase in stress in the material produces failure. The effective through the thickness stress-strain curve can be seen in figure 6.6. The plot shows the material response subjected to four different constant strain rates of 750, 1000, 1500, 1750 strain per second, which were all achieved through

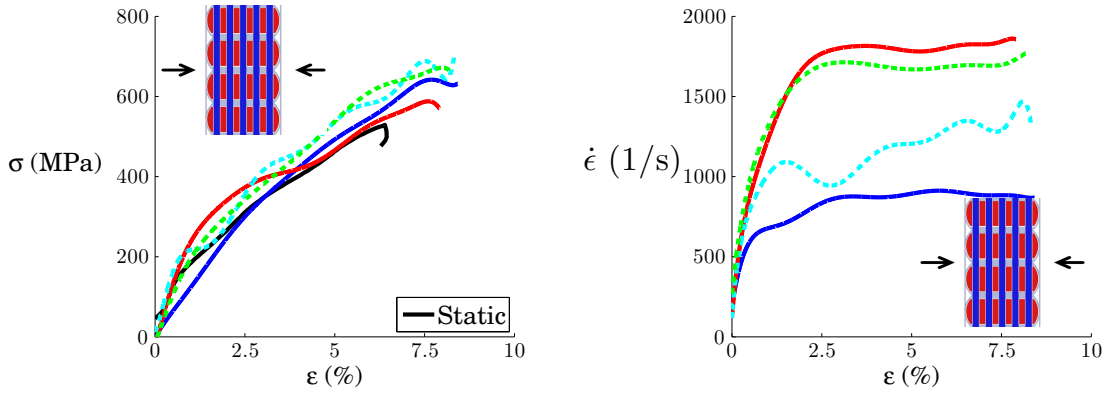

(a) $\sigma vs. \varepsilon$ (b) $\dot{\varepsilon} vs \varepsilon$

Figure 6.6 Stress-Strain-Strain Rate plots for small specimens tested through the thickness.

different methods of pulse shaping. The stress-strain response had nearly identical results. The data does not suggest any form of rate dependent behavior in the material at these rates. All of the specimens had a maximum stress of about 600 MPa and a maximum strain of about 7.5%. The small amount of variation seen is within the experimental error of the system. However, it is noted that there is an increase in load from the static compression test values. This increase is from 500 MPa and 6.5% strain to 600MPa and 7.5% strain. This increase is attribute to the rate dependent properties of the material. The results show that the rate dependent behavior at lower rates is not captured in the SHPB tests. The observed rate dependent behavior is attributed to the rate dependency of the matrix material.

Figure 6.7 shows the rate dependent behavior of the pure SC-15 matrix material. The plot shows the increase in yield stress as a function of rate. Note that σ_o is a reference (static) yield stress, while σ is the current yield stress corresponding to the strain rate being considered. Beyond about 3000 per sec. it is see that R approaches a fairly constant value suggesting that for strain rates larger than this the matrix would be insensitive to strain rate. Thus, when 3DWC are examined using the SHPB, rate dependency can be expected as strain rates corresponding to matrix strain rates of 0-3000 per sec.

The failure of 3DWC material was seen through a shear band forming in the specimen. Figure 6.8 shows the full field strain data as a function of time. In the later DIC images the formation of a dark blue band of highest strain forms, which can clearly seen in subfigure o, indicating the failure path, in this case a shear band failure. The band corresponds to the shear plane that is formed in the specimen. In the subsequent images one can see the shear band consolidate.

The surface oriented at ninety degrees to the shear band shows a different phenomenon.

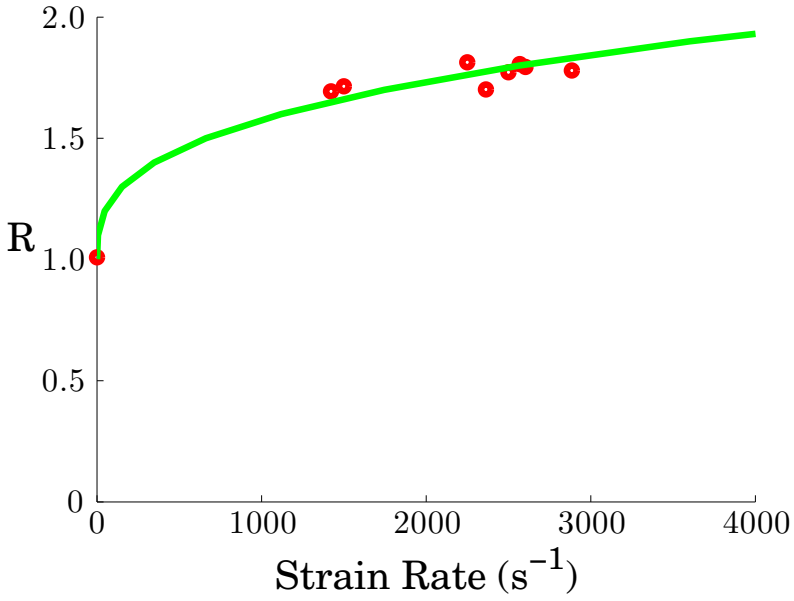

Figure 6.7 $\dot{\varepsilon}$ vs. R : Strain Rate Dependency of SC-15 Where R=$\frac{\sigma}{\sigma_0}$

Figure 6.9 shows this opposite face as the specimen deforms. This surface again does not show a constant strain, but rather we can see distinct bands where the matrix and fibers exist in the different layers. Since the shear band occurs in the plane ninety degrees to this face, failure on this specimen will look like a separation of layers which can clearly be seen in sub-image k. The right most layer has separated, this is where the shear band is exiting the sample.

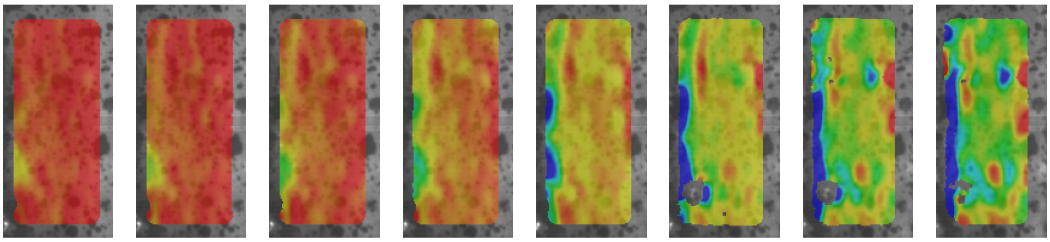

(a) $0\mu s$ (b) $7.6\mu s$ (c) $15.2\mu s$ (d) $22.8\mu s$ (e) $30.4\mu s$ (f) $38\mu s$ (g) $45.6\mu s$ (h) $53.2\mu s$

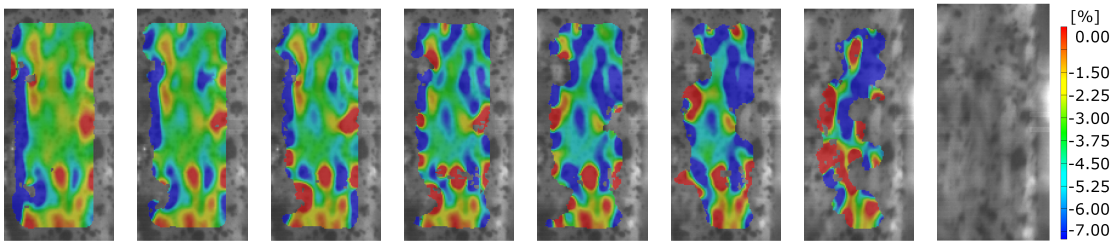

(i) $60.8\mu s$ (j) $68.4\mu s$ (k) $76\mu s$ (l) $83.6\mu s$ (m) $91.2\mu s$ (n) $98.8\mu s$ (o) $106\mu s$ (p) $114\mu s$

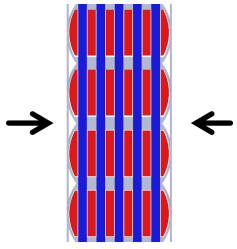

(q) Loading Diagram

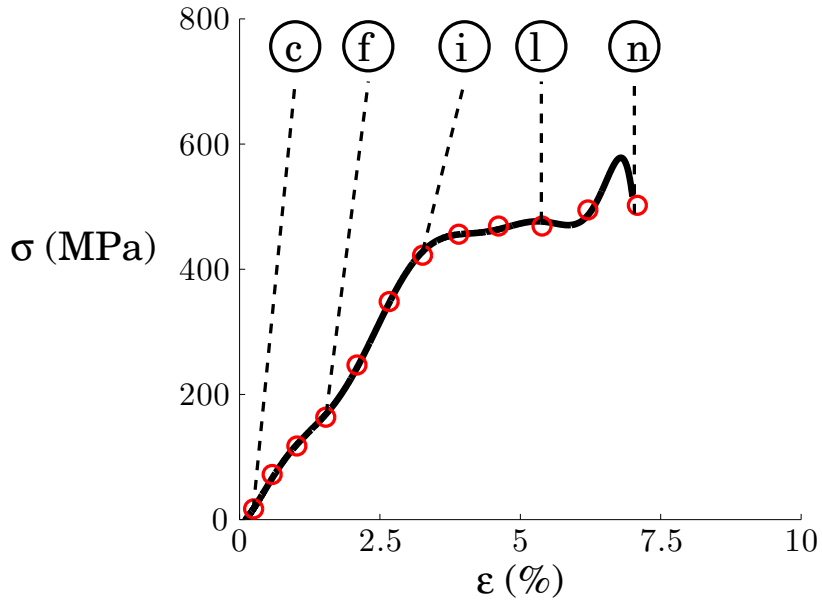

(r) Stress Strain plot with photo events

Figure 6.8 ε_x DIC time history for through the thickness hopkinson bar testing.

This shear failure follows closely the architecture of the material, as can be seen in figures 6.10 and 6.11. This photograph of a specimen after SHPB testing clearly shows some of the different constituents in the architecture. The shear band that formed followed many of the different warp and weft fibers in the material. Often the individual tows will remain intact except where they have sheared across and the matrix will be turned into "powder" from the impact due to coalescence of matrix microcracks. Fiber tow bundles near the edges of the material will often fail earlier by shearing out before ultimate failure of the specimen. This type of shear banding failure leads to a loss of load carrying capacity.

The compression response of the 6% Z-fiber reinforced material offers insight into the rate dependent behavior of the 3DWC material and shows a transition in failure mode with and increase in loading rate. As the material is stressed at higher rates it does not fail by delamination as noticed in the static test, but rather through a shear band formation. This transition in failure mode is important to note. The transition is likely due to the transition of the matrix material from a low yield stress solid to a fairly brittle elevated yield stress solid. Therefore, it is clear that this change in the behavior of the matrix material is responsible for inducing a transition in the failure mode from delamination at low loading rates to shear banding at elevated rates. This transition is important in understanding how to design structures made of 3DWC materials.

6.3.2 In-plane loading

The in-plane compression response of the material was investigated to determine the effect of strain rate on the in-plane compression strength. Preliminary tests were performed statically to determine a baseline for the material. The test was run at a rate of 0.0004 in/sec using an identical specimen to that used in the SHPB tests, that will follow. The specimens measured $12.7mm(0.500in.)$ by $12.7mm(0.500in.)$ and $6.60mm(0.260in.)$ thick. The results show that the weft has a higher initial modulus while the warp is able to sustain a higher failure load. These results are consistent with tensile tests discussed in chapter 3. The material failed by delamination between the layers in the center with kink band formation on the outside of the material, occurring in both the warp and weft directions, as seen in figure 6.13. The stress-strain curves for each of these orientations can be seen in figure 6.12. The strain to failure is about 1%.

Initial tests were performed using the same two specimen sizes in the through the thickness response. The experimental setup is not ideal for these specimens due to their thin thickness. There is very little area to transmit stress so the concentration is very high. If the strain gauge data from a representative test, as seen in figure 6.14 is examined, the

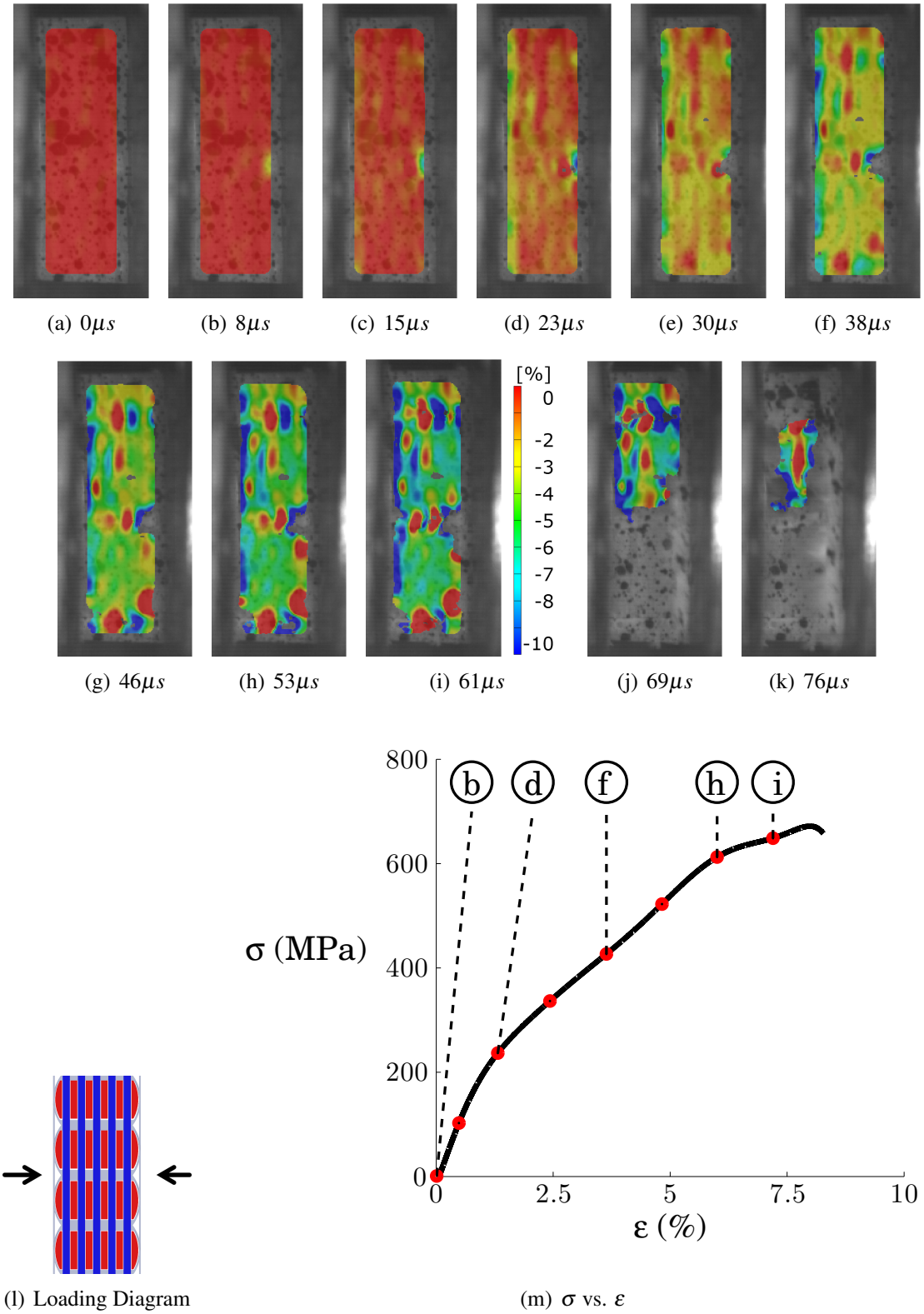

(a) $0\mu s$ (b) $8\mu s$ (c) $15\mu s$ (d) $23\mu s$ (e) $30\mu s$ (f) $38\mu s$

(g) $46\mu s$ (h) $53\mu s$ (i) $61\mu s$ (j) $69\mu s$ (k) $76\mu s$

(l) Loading Diagram

(m) σ vs. ε

Figure 6.9 ε_x DIC time history through-the-thickness of the specimen.

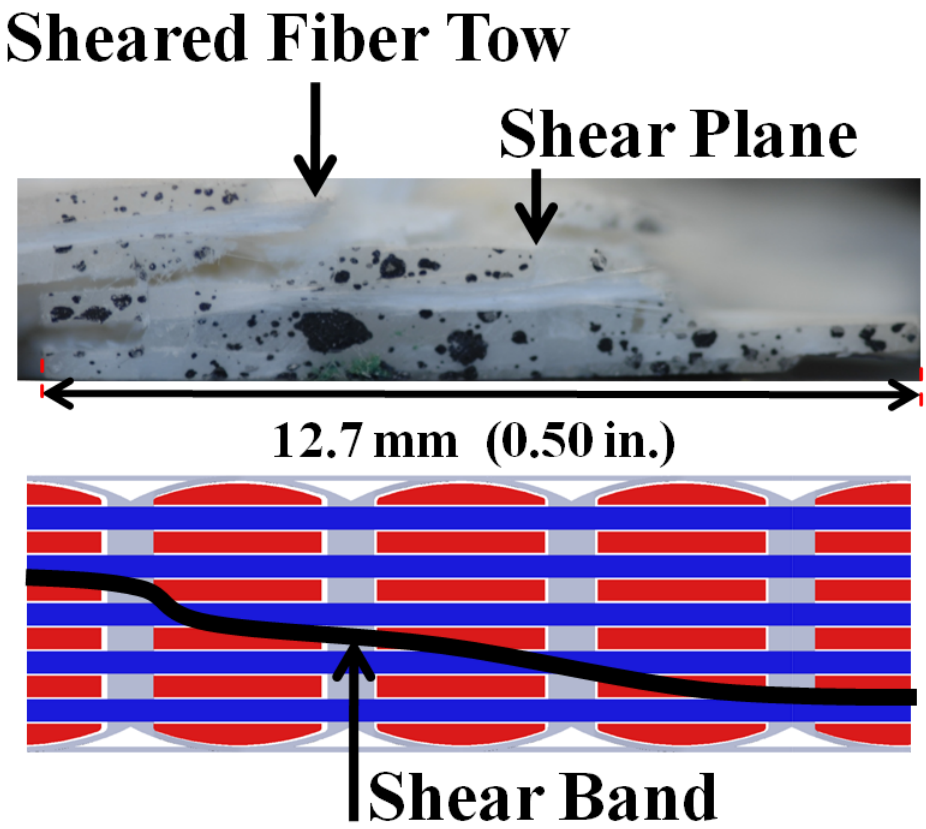

Figure 6.10 Failed 6% Z-fiber specimen after in-plane compression test.

transmitted bar sees nearly no strain and since there is a very small signal amplitude it will be difficult to get reliable data from the gauges. Thus, a smaller diameter bar, or thicker specimen must be used.

The initial experimental tests on the larger bar showed clear failure in the specimens. The impacted end begins to delaminate and form two distinct fronds where the material will separate out. Figure 6.15 shows how the material separates out to release the energy due to failure. The material separates around the midplane and this separation (crack) persists until the crack runs into a Z-fiber where it will take more energy, from a secondary hit (in the SHPB, multiple impacts can occur), to cause further delamination.

The DIC data obtained from these experiments shows that there is a maximum of about 2% strain. These preliminary tests of longer specimens showed that the specimen would undergo a small relatively uniform strain until the impacted end of the material began to fail. Once the material fails locally at one end, the strain in the specimen relaxes to nearly zero while the end of the specimen fails catastrophically, this can be seen in figure 6.16. These results led us to investigate the response of these specimens using a smaller diameter SHPB.

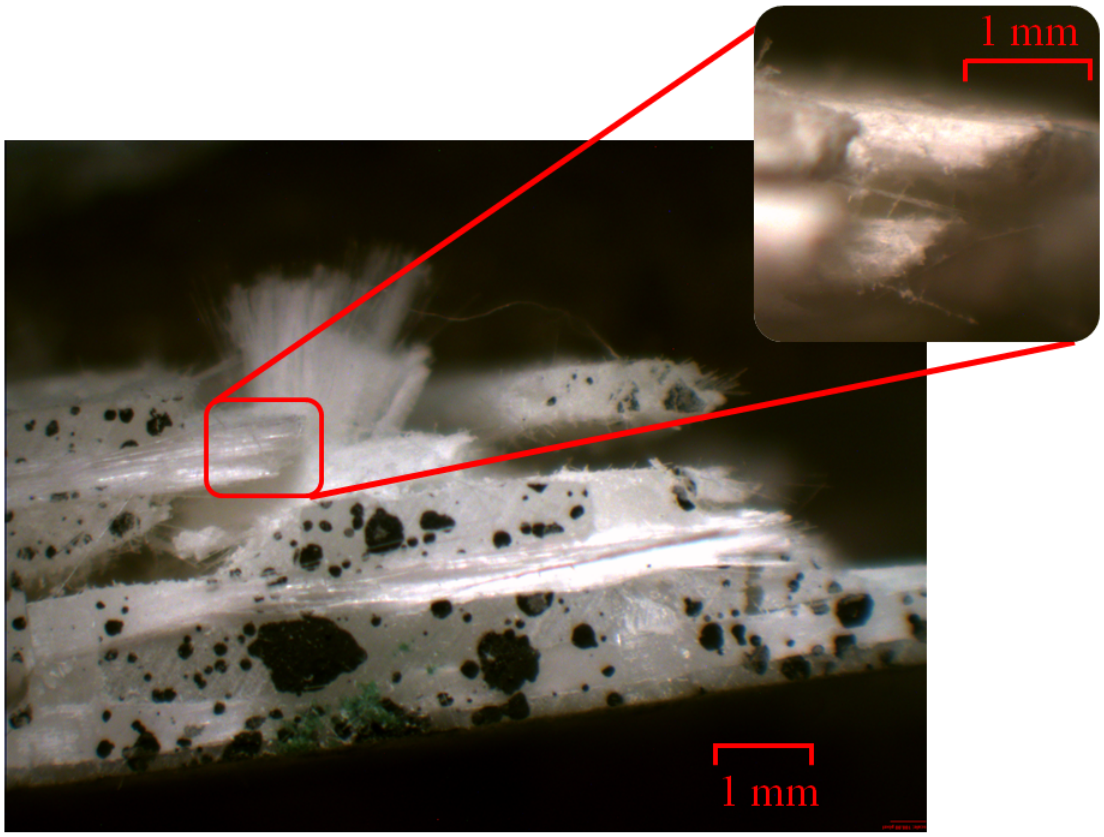

Figure 6.11 Failed 6% Z-fiber specimen after in-plane compression test emphasizing the fiber shear failure.

Smaller bars produce less concentration in the specimen, and the transmitted signal will be much larger due to the cross-section area of the specimen relative to the cross-section area of the bars.

For the smaller diameter, $12.7mm(0.5in.)$, bar SHPB testing, specimens were cut into squares of dimensions $12.7mm(0.50in.)$ by $12.7mm(0.50in.)$ and $6.60mm(0.260in.)$. The specimens were kept as large as possible to ensure that there were roughly 4 RUC's present in each of the specimens. The dimensions of the specimen were matched to the $12.7mm(0.50in.)$ incident and transmitted bars. The test procedure was identical to the tests performed on the larger diameter SHPB.

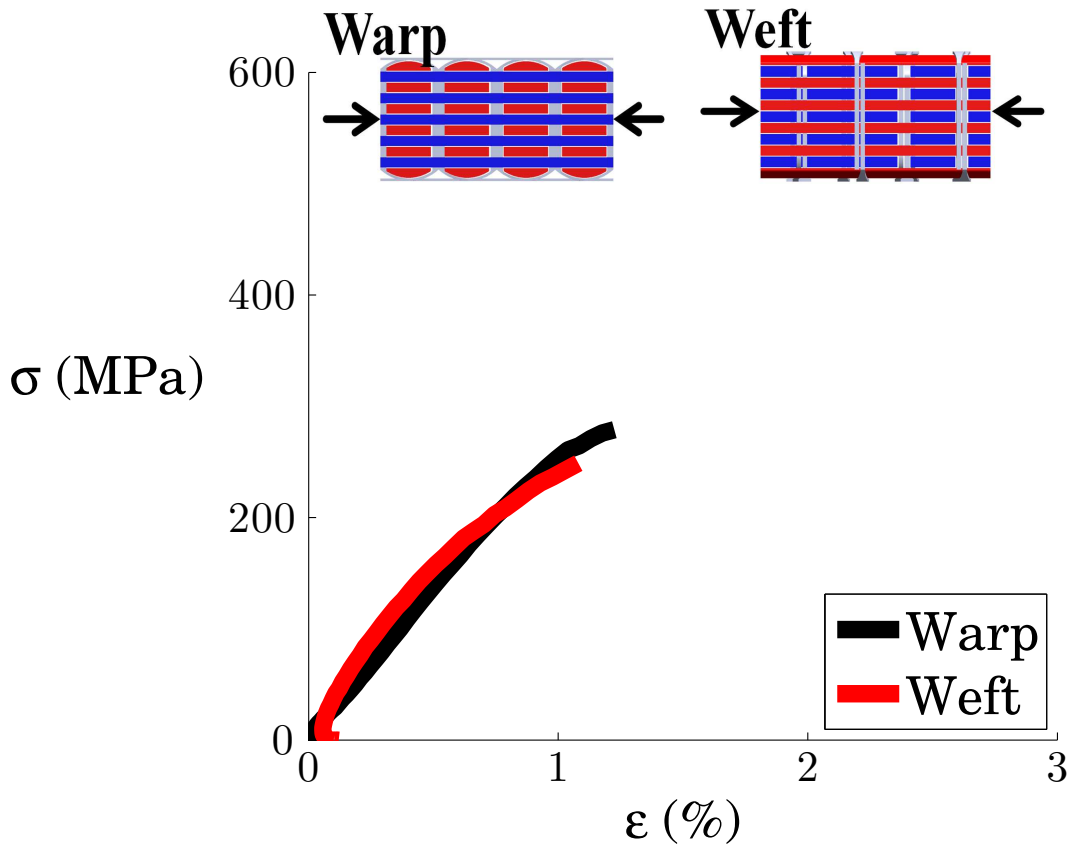

Figure 6.12 Static compression test results for 6% Z-fiber reinforced composite material.

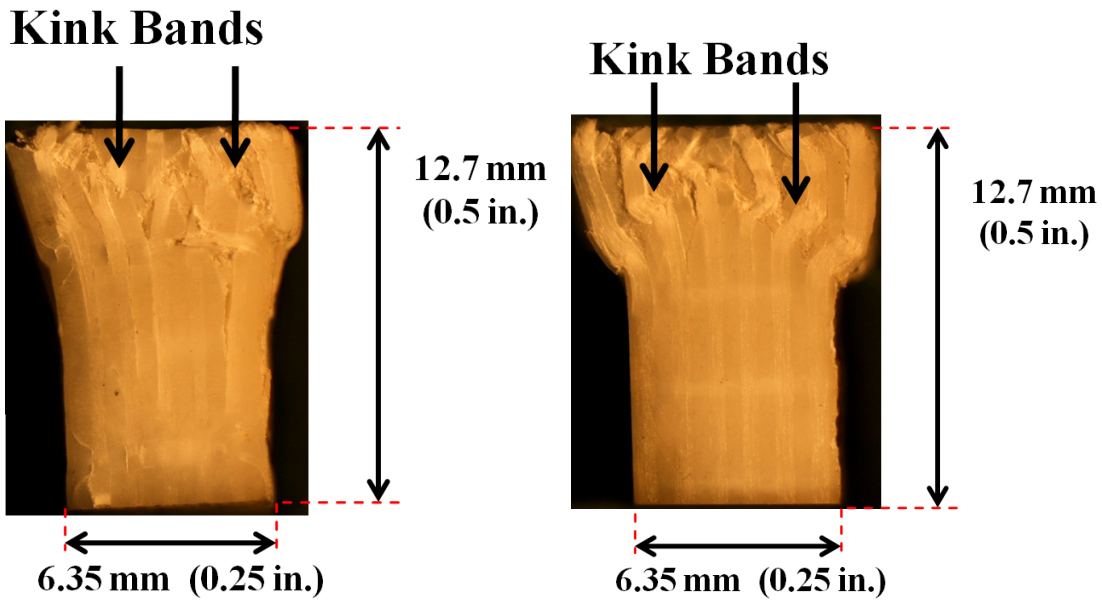

(a) Warp (b) Weft

Figure 6.13 Failed in-plane specimens for the warp and weft directions. The "brooming" failure is clearly observed with kink band formation in the tows.

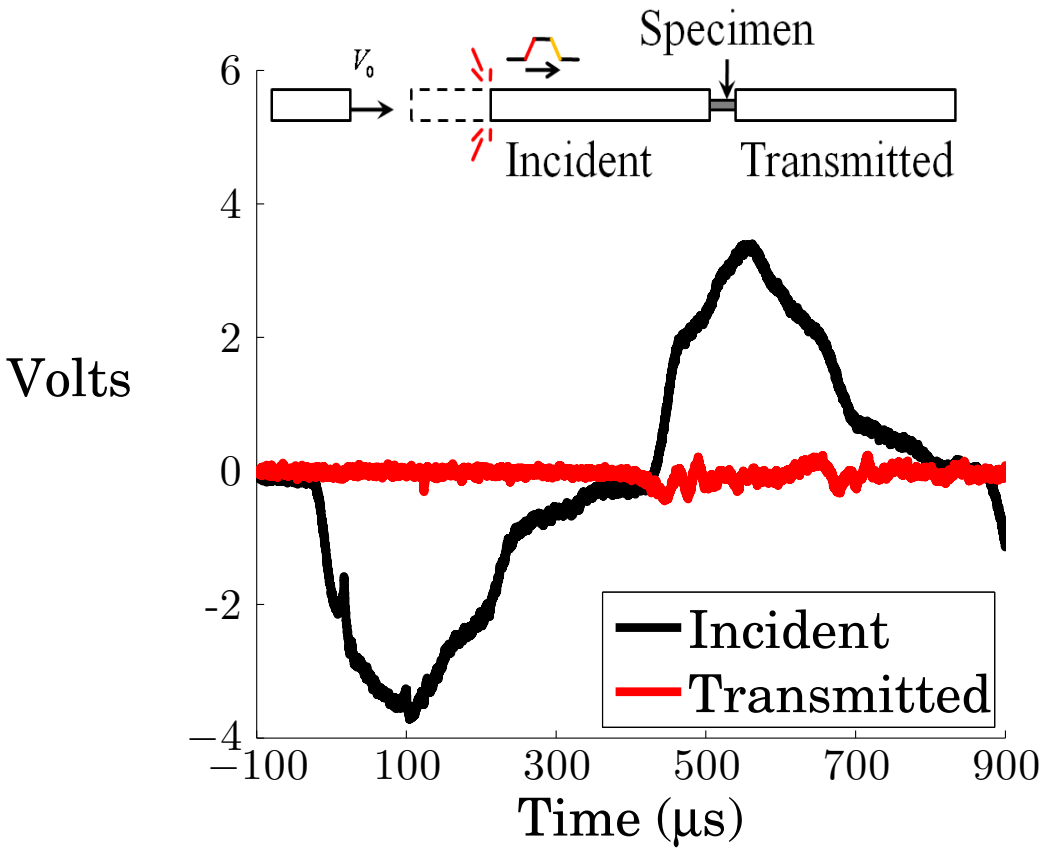

Figure 6.14 Strain gauge vs. time data for a typical in-plane SHPB compression test.

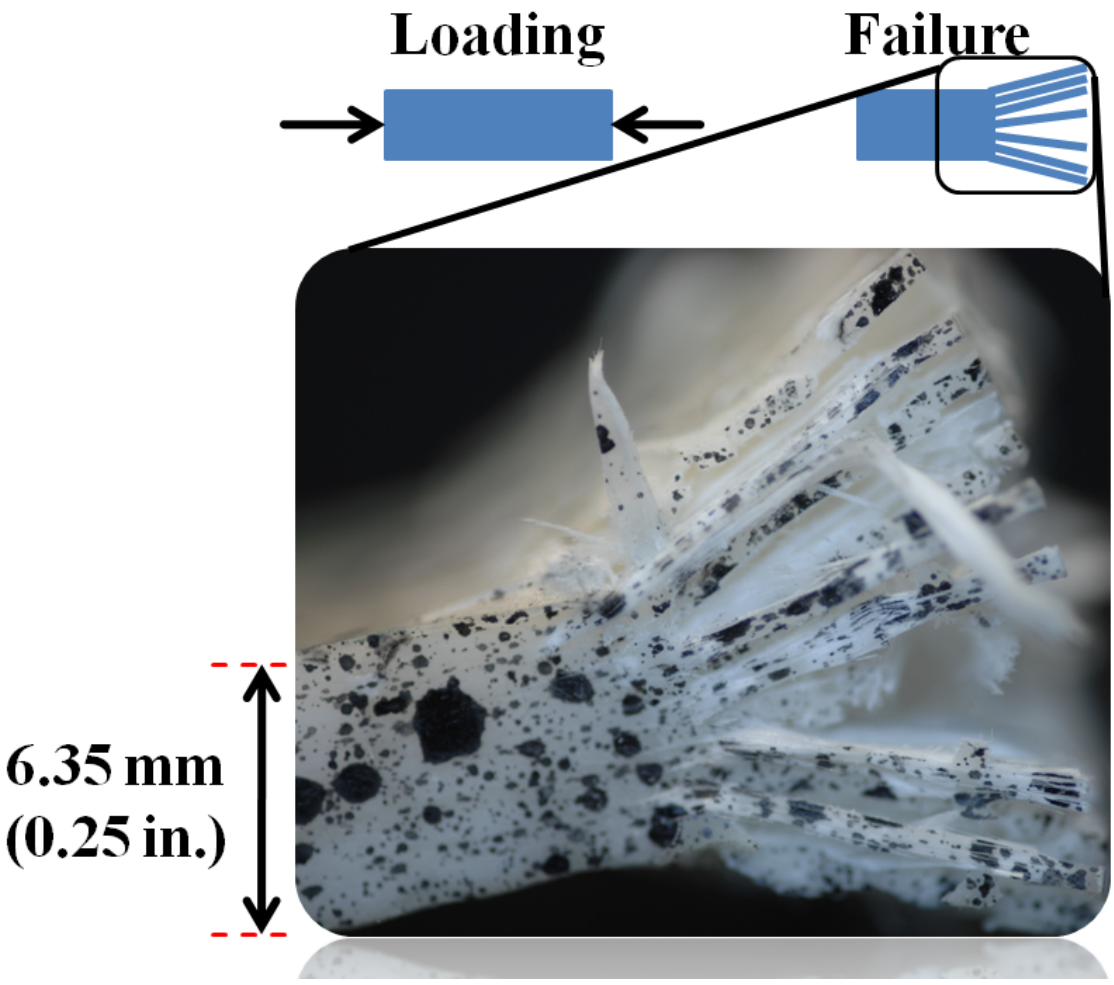

Figure 6.15 Failed 6% Z-fiber specimen after in-plane compression test.

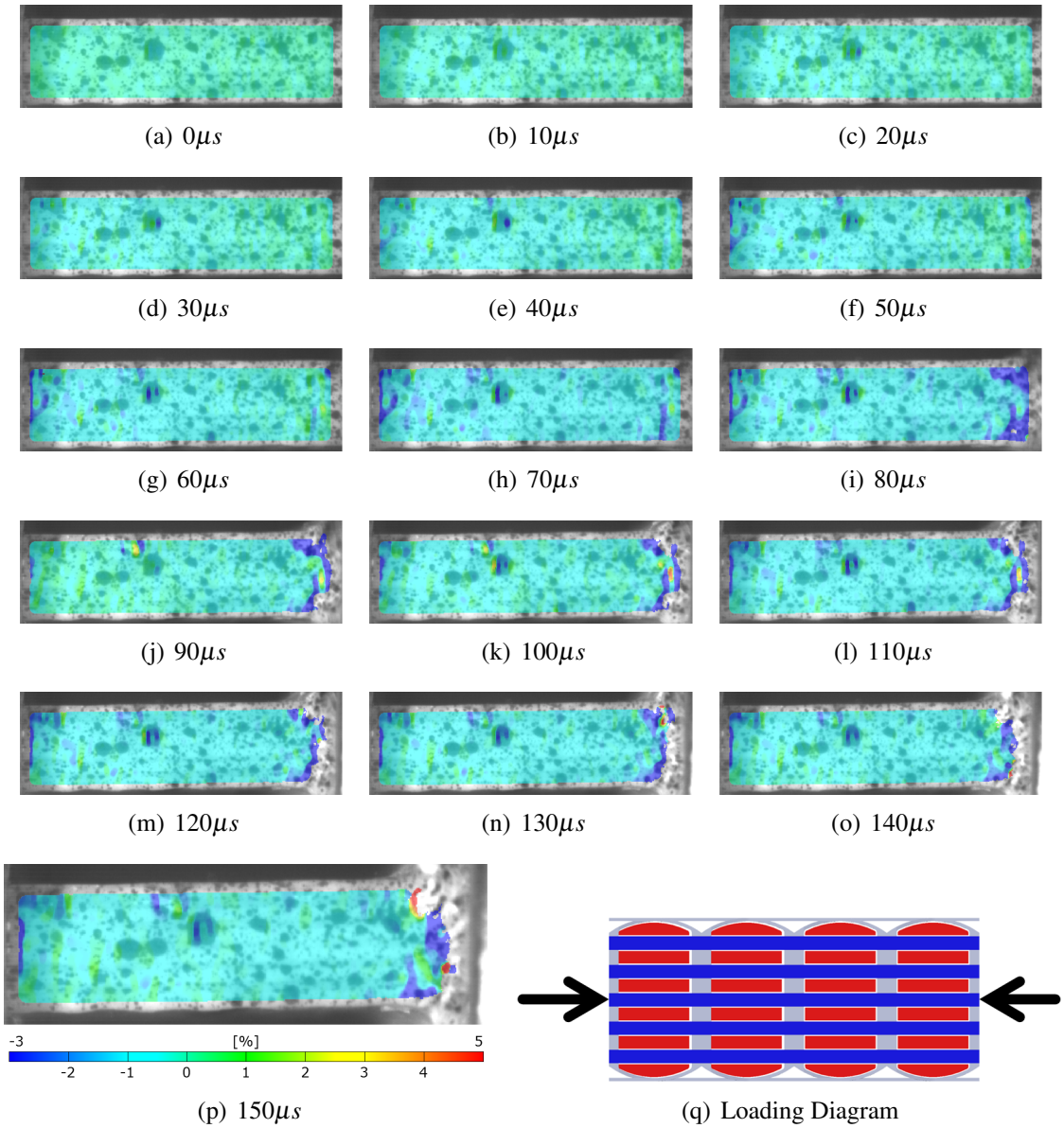

(a) $0\mu s$ (b) $10\mu s$ (c) $20\mu s$

(d) $30\mu s$ (e) $40\mu s$ (f) $50\mu s$

(g) $60\mu s$ (h) $70\mu s$ (i) $80\mu s$

(j) $90\mu s$ (k) $100\mu s$ (l) $110\mu s$

(m) $120\mu s$ (n) $130\mu s$ (o) $140\mu s$

(p) $150\mu s$ (q) Loading Diagram

Figure 6.16 ε_x DIC time history for in-plane Hopkinson bar testing.

The warp direction was tested first, and four separate strain rates were attempted. However an interesting phenomenon occurred. In all of the in-plane tests, the strain rate would reach a peak at about 0.5% strain and then begin decreasing. Looking at the strain gauge signals from the bars, the reason for this result is present. The incident wave is essentially a square wave while the transmitted wave is similar to a linearly increasing wave. Initially, the separation between the two gauges is large causing a high strain rate, but as the transmitted value approaches the square wave value it causes the strain rate to decrease. Experimentally, this is due to the fact that we don't have a "clean" propagation of the strain waves through the highly non-homogeneous specimen. The waves enter the specimen cleanly, but due to the complex microstructure of the 3DWC, the waves inherently interact with one another and the different constituents present. This result is consistent with every test run in the in-plane geometry. Normally, this would indicate that the testing method does not work properly, however since the result is consistent and correlates strongly with the DIC data, it suggests that the results are accurate. The difficult part is determining what strain rate the response actually occurs at. Perhaps the strain rate can be taken as the average over the duration of the test, since we are taking the effective properties of the specimen, and the strain rate never reaches a constant value.

The warp direction results can be seen in figure 6.17, which clearly shows the decrease in strain rate as the specimen deforms further. The figure also contains a static compression test for comparison. The SHPB experimental responses clearly follow the same material modulus as the static test case. Additionally, the strength of the material increases with rate. The static test showed failure in the material at 275 MPa, while the SHPB testing revealed a maximum stress of 375-450MPa. There is clearly a strain rate dependence of the material with increase in strength as a function of strain rate. Additionally, as the strain rate increases, the samples were able to undergo larger strains before failure. Since the material had the same modulus this result is expected.

The DIC time history is shown in figure 6.18. The plots show that the material does not experience a uniform strain. The strain has some consistency, in that the general trend indicates that the specimen seems to be deforming consistently, although there are localized concentrations. The onset of failure shows that one end of the specimen will fail, releasing the energy due to the built up strain. The data in figure 6.18 shows that the right end has failed, while the left end returns to near zero strain.

The failure seen in the DIC data was delamination of the individual tows. There were no kink bands formed. This result is consistent with the longer specimens initially tested. In the static test, the specimen failed through delamination and kink band formation. There is a clear transition in failure mode from kink banding at slow rates to delamination at higher

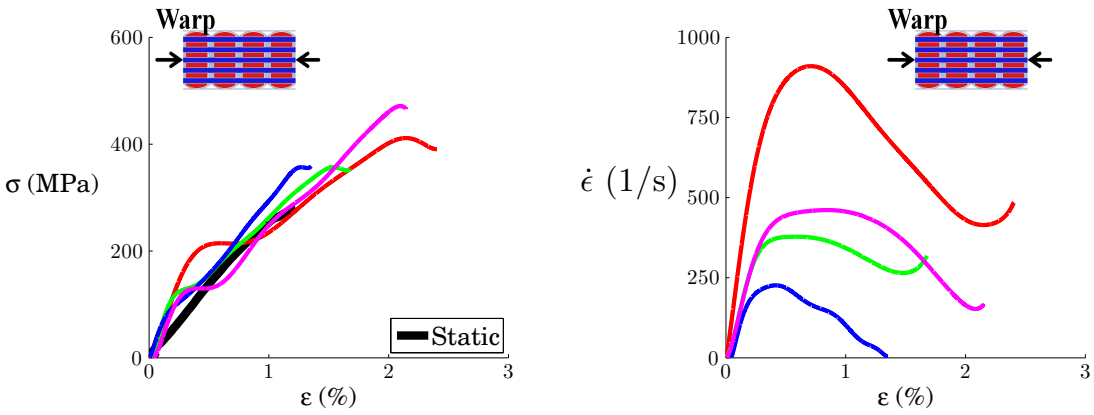

(a) $\sigma vs. \varepsilon$ (b) $\dot{\varepsilon} vs \varepsilon$

Figure 6.17 Stress-Strain-Strain Rate plots for small specimens subjected to compression in the Warp direction.

rates. Figure 6.19 shows a comparison of the two failed specimens, it is evident that there are different failure mechanisms corresponding to the different loading rates. This transition could lead to the higher load, since the kink band may be a lower energy failure mode. It is also interesting to note that the result for in-plane response is reversed from that observed in the through-the-thickness case. In that case, delamination occurred at low rates and shear banding at elevated rates. Since the matrix is common to both types of testing, this suggests that the 3DWC architecture with respect to load direction also plays a role in influencing the failure modes.

The warp direction shows some clear strain rate dependency, in both the maximum stress, but also in the failure mode. The kink bands associated with the static test disappear and we only see delamination occurring in the specimens.

The weft direction had very similar results and trends. Figure 6.20 shows the correlations obtained experimentally. These results show that there seems to be a rate dependency in the material once again. There is not as much dependency in the maximum strain, but rather in the load achieved. The result also shows a static compression test for comparison, which again shows a strong correlation to the experimental to the modulus. The material has similar trends however the failure strength has increased from 250MPa to 500MPa and the strain has increase from 1% to 2%. This result is very similar to the results seen in the warp direction, however, the strength has doubled. This is a dramatic increase due to the rate dependency of the material.

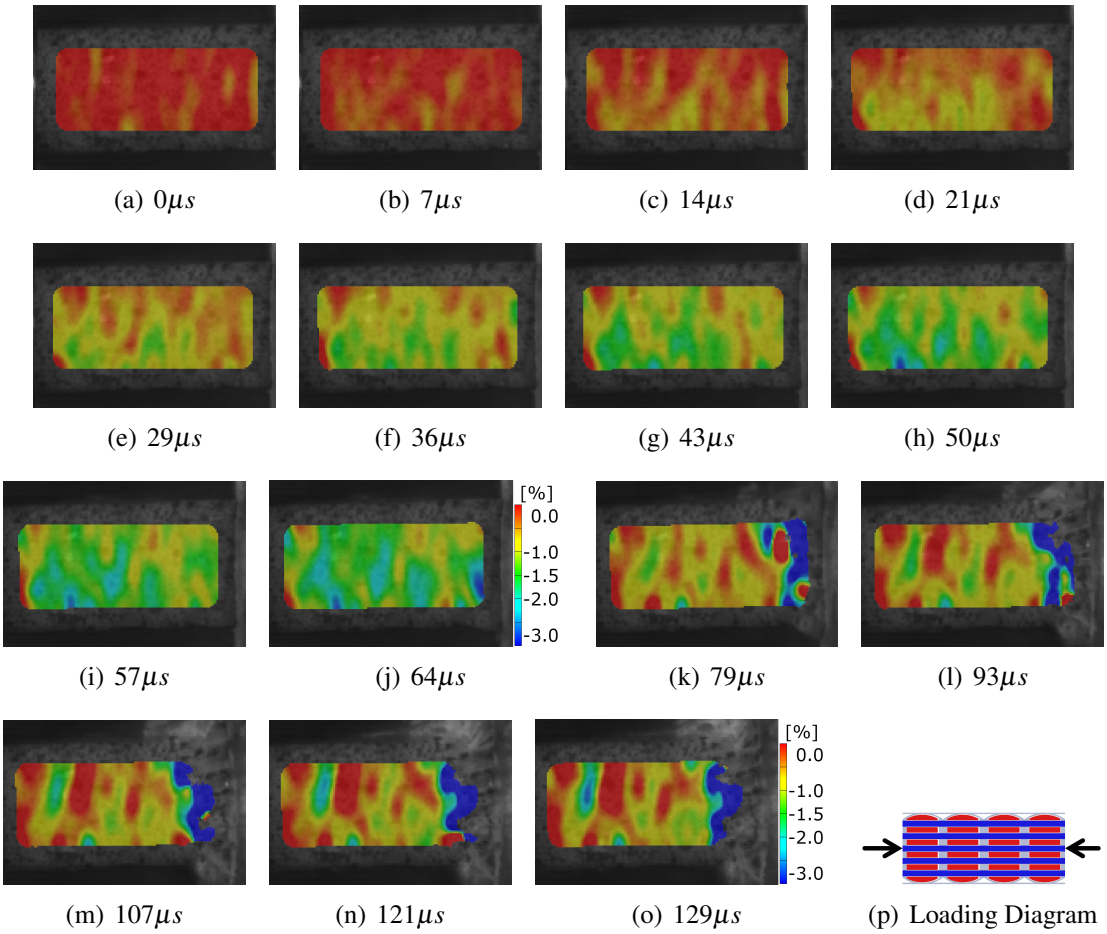

(a) $0\mu s$ (b) $7\mu s$ (c) $14\mu s$ (d) $21\mu s$

(e) $29\mu s$ (f) $36\mu s$ (g) $43\mu s$ (h) $50\mu s$

(i) $57\mu s$ (j) $64\mu s$ (k) $79\mu s$ (l) $93\mu s$

(m) $107\mu s$ (n) $121\mu s$ (o) $129\mu s$ (p) Loading Diagram

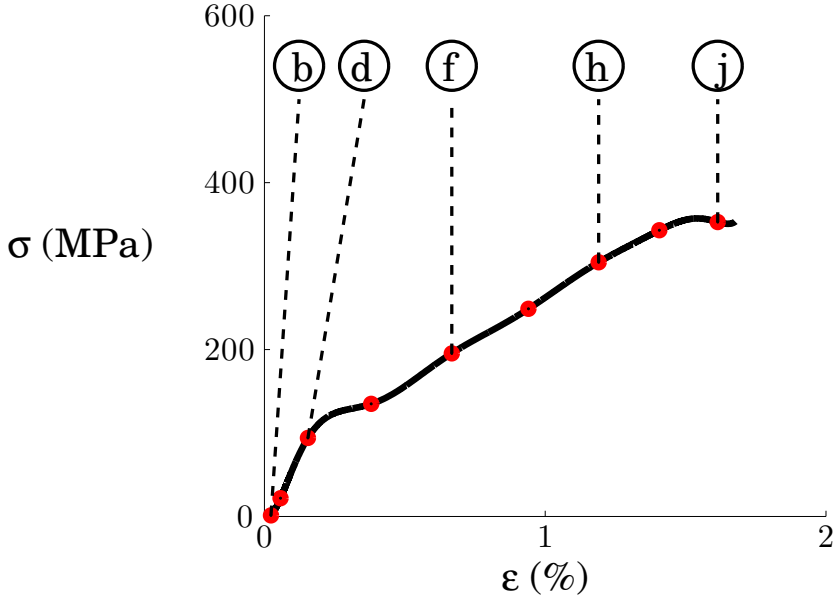

(q) σ vs. ε

Figure 6.18 ε_x DIC time history in the warp direction.

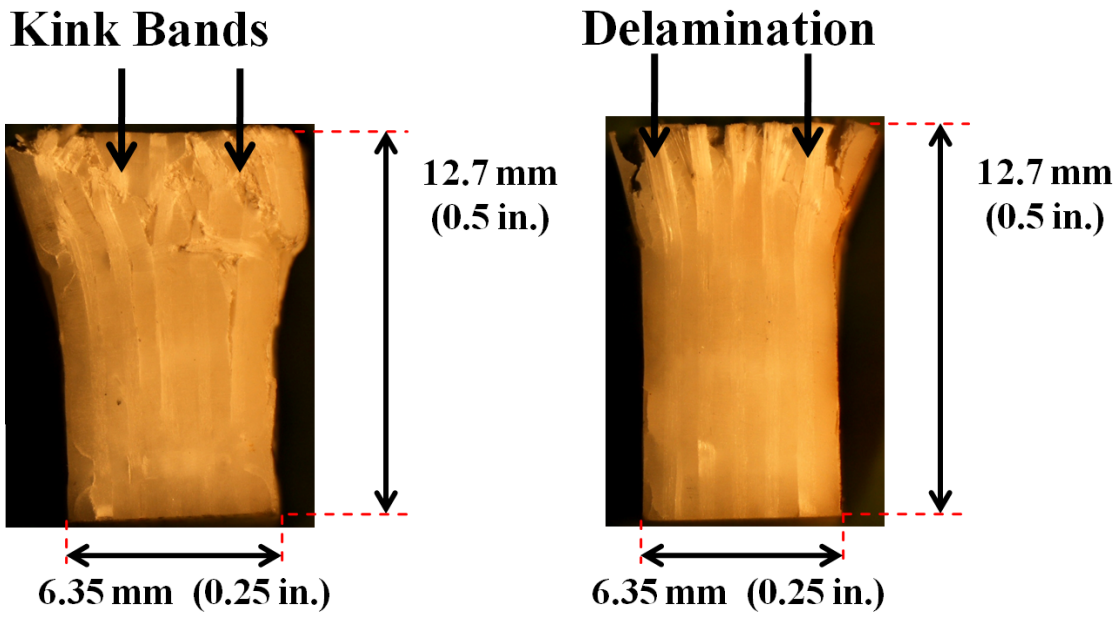

(a) Static (b) Dynamic

Figure 6.19 Failed in-plane specimens for the warp direction. The failure from kink band formation and delamination to delamination only at higher rates of loading.

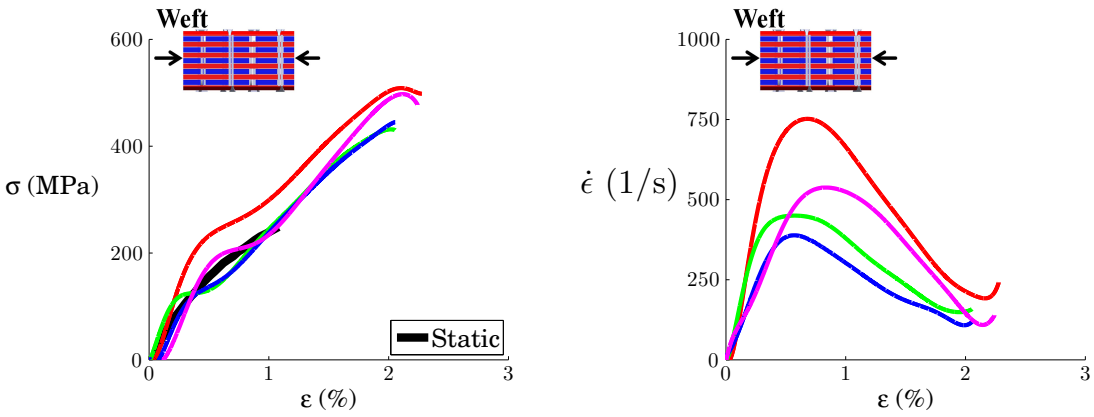

(a) $\sigma vs.\varepsilon$ (b) $\dot{\varepsilon} vs \varepsilon$

Figure 6.20 Stress-Strain-Strain Rate plots for small specimens subjected to compression in the Weft direction.

The DIC time history is shown in figure 6.21. The specimen is observed to not be in equilibrium, however there is less deviation in the warp and weft directions compared to the through the thickness direction. It appears to be closer to strain equilibrium in these two orientations than the through the thickness orientation. There are some strain concentrations near the end, and this is the location of failure in the specimen. Failure relieves the strain energy of the specimen, relaxing much of the strain in the un-failed region except near the actual failure site, where permanent deformation has occurred.

The observed failure modes and mechanisms were identical to the warp direction in the weft specimens. Delaminations occurred in the material causing the different tows to separate from the matrix. Figure 6.22 shows a comparison of the static and higher rate failure modes. The transition from kink band to delamination observed in the warp direction is also noticed in the weft direction. All of the SHPB testing revealed a transition in failure as the specimen moved from static failure as a function of loading rate.

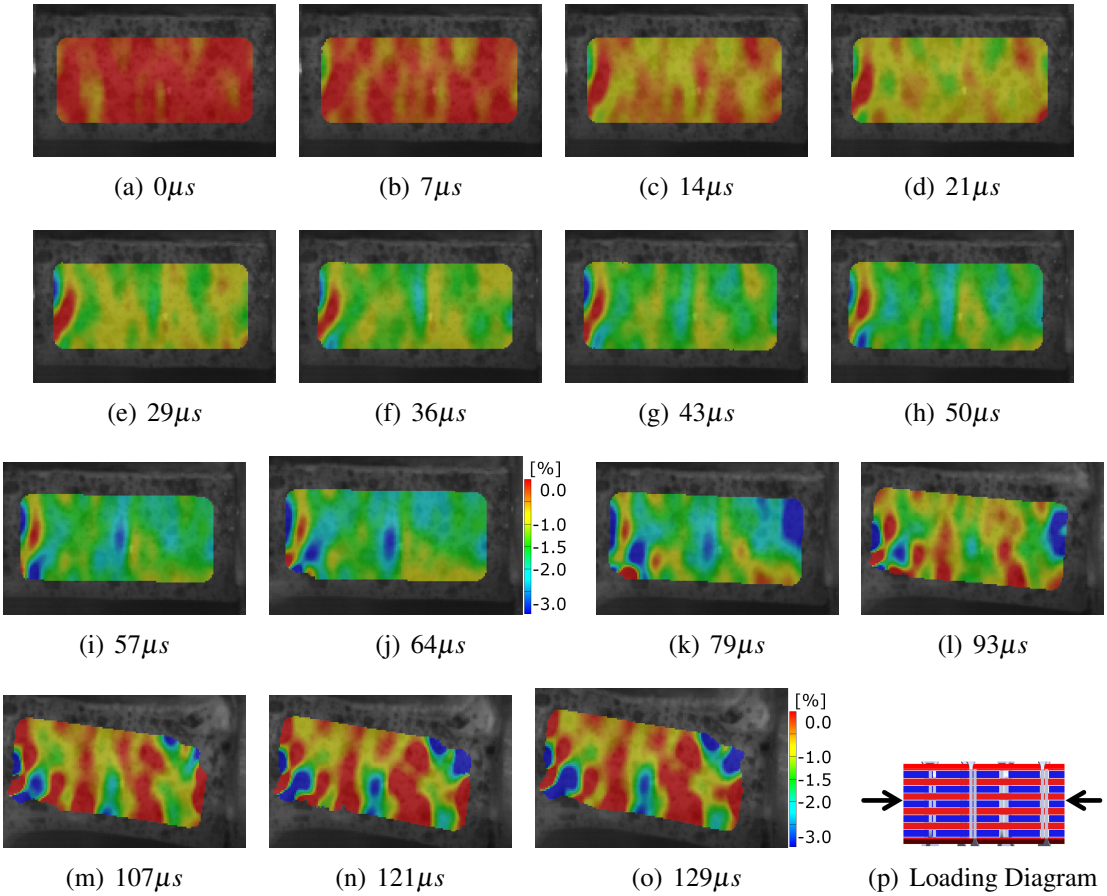

(a) $0\mu s$ (b) $7\mu s$ (c) $14\mu s$ (d) $21\mu s$

(e) $29\mu s$ (f) $36\mu s$ (g) $43\mu s$ (h) $50\mu s$

(i) $57\mu s$ (j) $64\mu s$ (k) $79\mu s$ (l) $93\mu s$

(m) $107\mu s$ (n) $121\mu s$ (o) $129\mu s$ (p) Loading Diagram

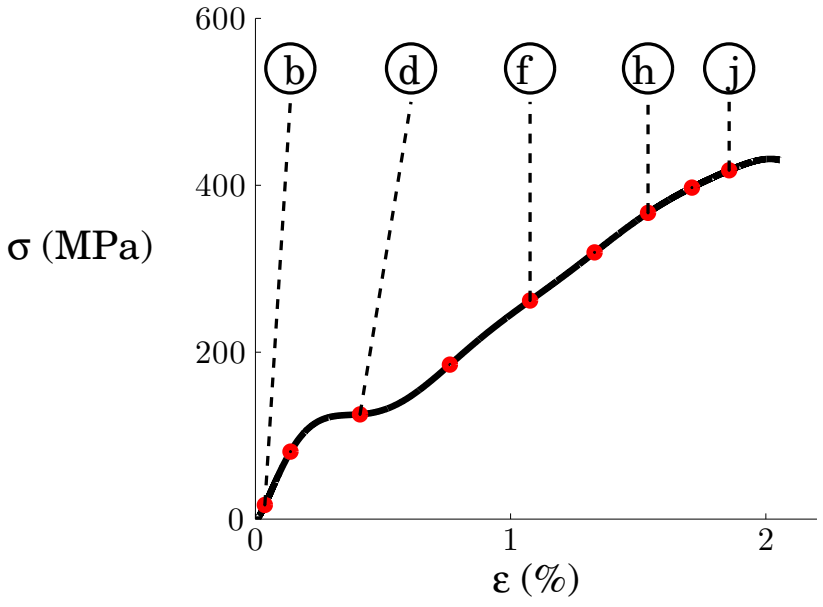

(q) σ vs. ε

Figure 6.21 ε_x DIC time history in the weft direction.

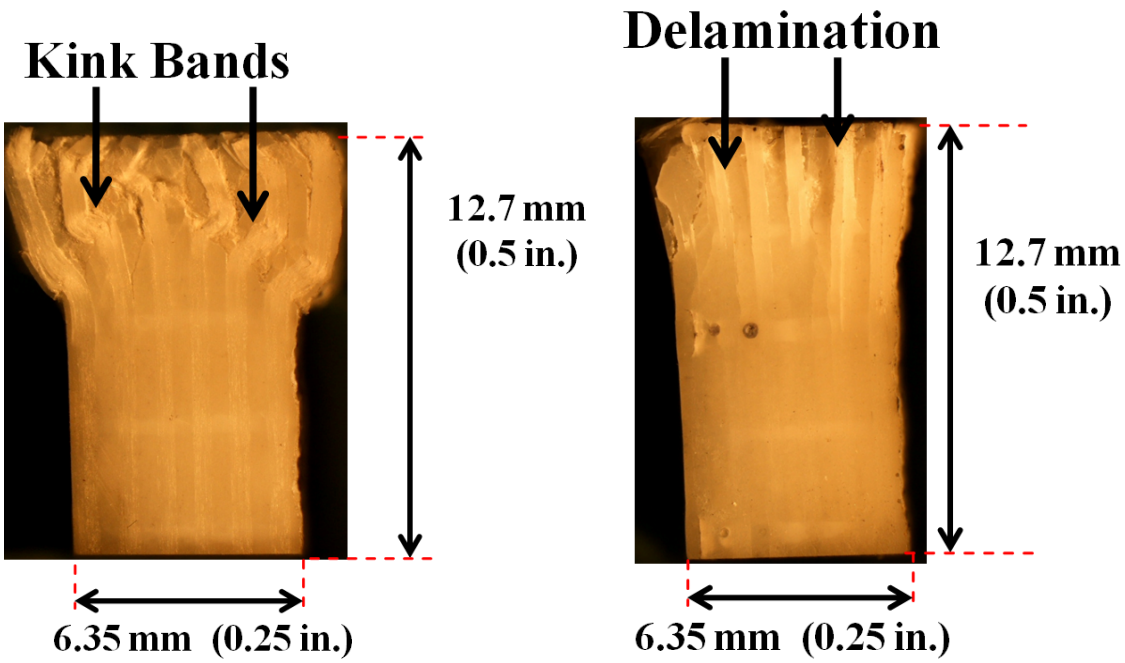

(a) Static (b) Elevated rate

Figure 6.22 Failed in-plane specimens in the weft direction. The failure from kink band formation to delamination at higher rates of loading.

6.4 Conclusion

The SHPB provided a means for evaluating the rate dependence of the through the thickness and in-plane compression response of the 6% Z-fiber woven composite. Through the thickness testing revealed information about the rate dependent parameters and a transition in failure mode at higher rates. Architecture dependent strains were noticed in the DIC results, showing distinct bands where tows and matrix existed in different strain states.

The in-plane testing revealed similar trends to the through the thickness, however a large difference in measured values was observed. The strength of the material nearly doubled in the in-plane compression testing when compared to static results. The material had a clear transition in failure mode from kink band formation at low rates to delamination at much higher rates. The in-plane compression response showed the largest rate dependent properties in all of the testing. The non-constant decreasing strain rate is unique to the 3DWC as well, due to the complex architecture and interaction of waves between constituents. Further, the failure mode transition from delamination to shear banding observed in the through-the-thickness testing was reverse for the war and weft in-plane responses.

The experimental results presented in this chapter are modeled using the finite element method in the next chapter.

Chapter 7

Finite Element Based Representative Unit Cell (RUC) Modeling.

3DWC's have a nearly periodic architecture as was described in chapter 2. Simplified analytical models can be used to predict bulk properties of a 3DWC representative unit cell (RUC). These models, however, because of their homogenized nature, are not suitable for modeling failure mechanisms (such as kink band formation in compression [34, 79, 36] , or localized stress concentrations that occur from fiber tow undulations). Analytical models for braided composites including manufacturing induced imperfections were developed by Pankow and Waas [19], however this development did not include failure mechanisms. Therefore, finite element based models are needed to correctly model the more complicated features of failure and to properly capture material nonlinear response.

This chapter will focus on the establishment of detailed finite element models to represent the complex architecture of 3DWC and then use different tests to validate the models that are developed. Complete failure of the specimens will be modeled for the SHPB test configurations that were reported in chapter 6.

7.1 Previous Related Work

Much of the past work on textile composites has been limited to studying in-plane mechanical properties of layered textile laminates. An extension of classical laminated plate theory has been accomplished in [80] with a derivation to 3DWC being reported in [19]. Since the Z-fiber is the hardest constituent to model, some have tried a simplified approach to model the sinusoidal Z-fiber tow, however the method relies on a newly derived special element [81] and a solution strategy similar to that of the finite element method has been used. Many of the weaving companies use their own in-house codes to predict the initial in-plane mechanical properties, with some able to predict failure of the material [3]. However all

of these models cannot capture architecture dependent failure such fiber tow crimping or matrix pockets, and are only capable of predicting in-plane properties.

In order to capture true material behavior, finite element codes have been developed to more accurately represent the architecture and model non-linear material response with a view to capturing some of the failure mechanisms. A detailed model incorporating consolidation of the various layers has been incorporated into RUC modeling of textile composites producing good experimental correlations [36, 37]. Many different models have been proposed based on the geometry of a representative unit cell [8, 22, 25, 26, 27, 28, 29, 30, 31, 33]. However each of these models tends to simplify the geometry or neglect certain aspects of the material. Often the Z-fiber is turned into a rectangular element, often seen as the block approach, to fit into a grid of warp and weft fibers [82, 25], neglecting the crimp and actual path followed by the Z-fiber. Other types of models break the individual elements into representative sub-cells showing the type of fibers that occurs in each [27], however each subcell must be calibrated and are approximate for the geometry and also mesh dependent. Periodic RUC's have been investigated for stitched material [83], however this model does not account for damage due to stitching, and has many problems producing a correct shear response of the material.

In many of these models, the simulations use simple block geometry, where the architecture is modeled to have smooth continuous curves that can be represented by splines. Such models cannot capture fiber tow undulations and other byproducts of the actual weaving process, even though an approximation to the geometry can yield reasonable accuracy for stiffness prediction. Therefore, new, more accurate models must be implemented to better predict the actual mechanical properties, specifically with a focus on strength prediction. The proposed models are extensions of references [79, 36], where the true measured geometry is used. These references have shown good correlations with 2D in-plane woven systems for determining stiffness and *strength* properties, and also in describing progressive damage. Extensions of these studies are the logical starting point.

7.2 Proposed models.

A finite element (FE) model was developed to understand how the fiber tows carry the load for different woven architectures. Specimens were polished and then observed under an optical microscope to extract microstructural geometric details. The images were analyzed to determine the average dimensions of each of the fiber tows, the separation between tows, and any other dimension required to accurately recreate the RUC for the architecture.

These dimensions were then turned into three dimensional models in SolidWorks 2009. The dimensions can be seen in table 7.1, where the Z-fiber consisted of a spline fit that would wind around the architecture, holding a constant cross section of $0.104mm^2$ $(1.61x10^{-4}in.^2)$. The SolidWorks model was then imported into ABAQUS version 6.8. Appendix E contains the details of how to convert a model from SolidWorks to ABAQUS. The ABAQUS finite element (FE) model is comprised of quadratic tetrahedral elements. The mesh size chosen is dependent on geometry and computation size. There is ultimately a trade off that needs to be effected. The finer the mesh size is, the more computation time is needed. A "relatively" coarse but "converged" mesh is used in the present study because of the end goal of dynamic simulations in order to reduce computational time. The RUC model used consists of 70,000 elements.

Table 7.1 Sample Geometry of RUC and constituents

	Width		Length		Thickness		Distance between Fibers	
	(mm)	(in.)	(mm)	(in.)	(mm)	(in.)	(mm)	(in.)
RUC	6.80	.2676	8.03	0.3162	7.29	.2872		
Warp	2.71	0.1065	8.03	0.3162	0.63	0.0248	0.69	0.0273
Weft	3.11	0.1225	6.80	0.2676	0.60	0.0235	0.90	0.0356

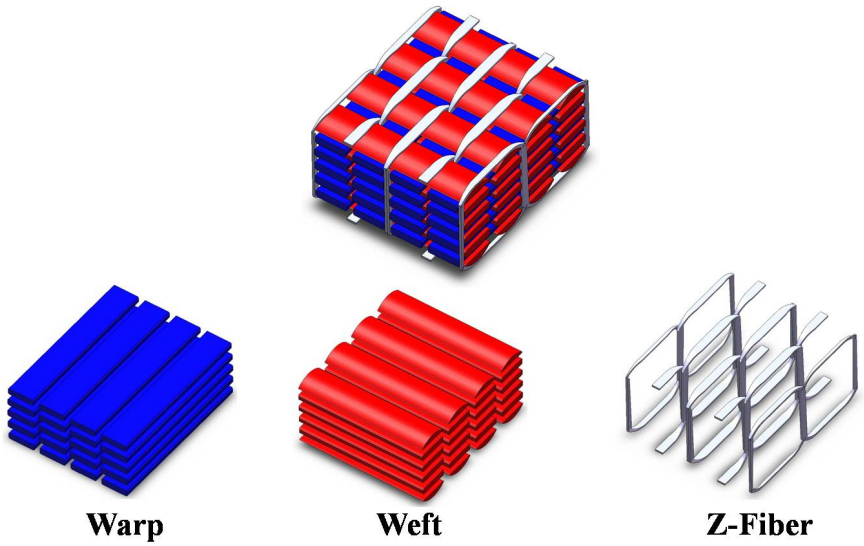

Figure 7.1 Representative Geometry of 3D woven RUC geometry.

7.2.1 Tow Interactions

Two methods for characterizing the tow interaction have been investigated to determine how to properly model the complex woven architecture. Idealizing the architecture requires some assumptions to be made since in reality the fiber tows can touch each other and interact with each other through "point" or "area" contact. This is often a fact that is overlooked in much of the modeling. Historically most methods simply have adjacent tows joined together and the mismatch in material properties prevents transfer of much of the load, however the shared nodes produce localized stress concentrations. In order to avoid this, we first attempted to model this architecture and actually model the contact between the two tows. This method works very well for simple geometries, in-plane weaves or RUC's that have very few tows. However, for the 3D woven samples there exists in excess of 50 such contact pairs. Due to the internal convergence criterion of contact pairs in ABAQUS, this produced many issues in the solution process that would allow for reasonable computational times. The solver must take smaller and smaller initial step sizes with each added contact pair. Additionally the matrix will not be properly bonded to the fiber, since the contact pair will not allow for tension between the two.

Due to these limitations another method was chosen, which inserts a small amount of matrix material between the tows. This softer material does not provide the direct load sharing as seen with shared nodes, but also simulates the effects of contact due to the very thin layer of elements inserted. It was decided that a thin matrix layer of about 5% of the height of a tow cross-section would be added between the tows to allow for separate tow interaction. It was found that this small amount of material had little impact on the results. On a microscopic scale, after the impregnation of the fibers with the matrix, there is in reality a small layer of matrix that is found between each of the fiber tows. The existence of this small layer of matrix has been shown in optical micrographs [84].

7.2.2 Material Orientations

In order to properly model the material, the correct orientation of all of the elements needed to be provided in the input file. In ABAQUS this is accomplished through the use of the *DISTRIBUTION command. The command allow users to input their own material orientations for individual elements. A Matlab code was written to take elements that belong to an individual fiber tow and find their orientation in a 3D space, then output this orientation to the correct format needed for the ABAQUS input file. The results of this method can be seen in figure 7.2

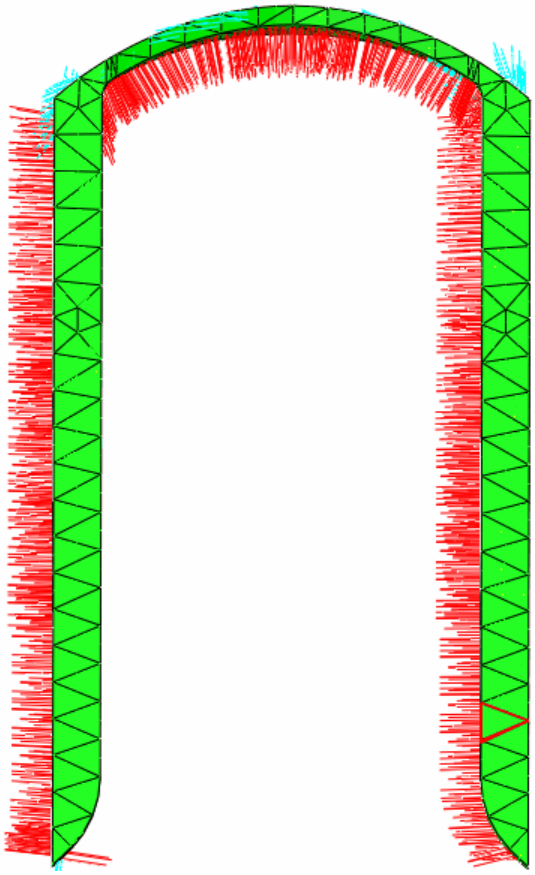

Figure 7.2 Plot of the material orientation for each of the elements of a single Z-fiber tow in the RUC model.

7.2.3 Material Models

The epoxy material was modeled using J2 flow theory of plasticity [85]; the strains were assumed to be small, a von Mises yield criterion was used and isotropic hardening plastic behavior was also assumed. The material properties were determined through SHPB tests to determine the rate dependent properties. For materials which have a rate independent modulus (this means that the modulus is constant, while only the yield ratio changes with rate), the Cowper-Symonds overstress power law is used. It has the form:

$$\dot{\varepsilon}^{pl} = D(R-1)^n, \tag{7.1}$$

where D and n are material constants and R is the yield stress ratio, $\frac{\sigma}{\sigma_0}$. Since the rate dependence of the epoxy is an unknown, an initial attempt was made using the rate dependent properties of a similar polymer material. Split Hopkinson pressure bar test results for the rate dependence of the SC-15 matrix was used as a guide for an "initial guess". The

assumed rate dependence for SC-15 is plotted in figure 7.3, where the circles represent the experimental data.

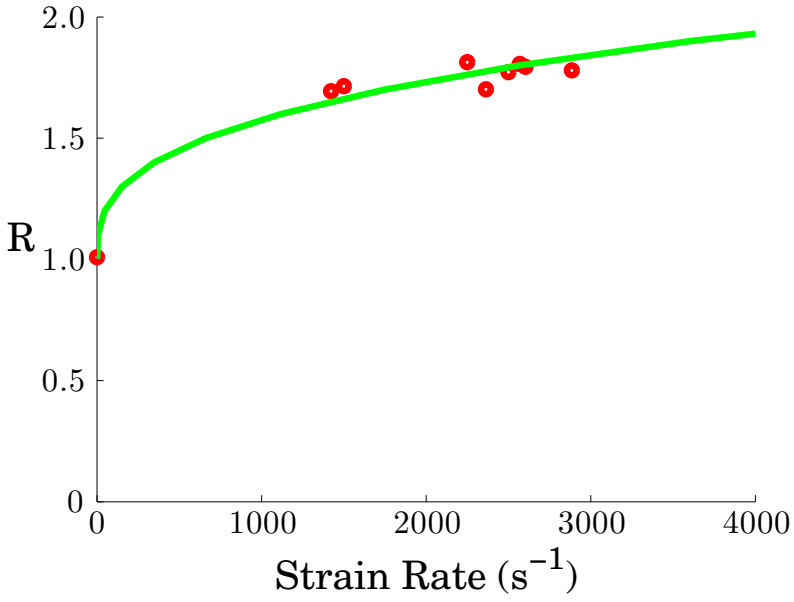

Figure 7.3 $\dot{\varepsilon}$ vs. $\frac{\sigma}{\sigma_0}$ for SC-15 Matrix

Table 7.2 Sample Matrix Material Properties

Modulus	360,000	$\frac{lbs}{in^2}$
Poisson's Ratio	0.36	
σ_y	7,000	$\frac{lbs}{in^2}$
D	4880	
n	2.883	

Each fiber tow is modeled as a transversely isotropic tow using the concentric cylinder model (CCM). The details of the CCM are given in appendix B. The respective tow fiber volume fraction is used to calculate the material properties of each tow in the warp and weft directions. The fiber volume fraction is measured through the use of Scanning Electron Microscope (SEM) photos. This method was performed as can be seen in figure 7.5 revealing a volume fraction of $57.6\% \pm 8\%$ for the weft and $54\% \pm 4\%$ for the warp. There is a large standard deviation compared to other materials studied [36]. Figure 7.4 shows a macroscopic view of the entire fiber tow, where we can clearly see that there is no uniformity in the packing within the fiber tow. There are areas which have no fiber in them at all while other areas seem to be uniformly spaced. These results provide a wide range for

mechanical properties that can be predicted, producing one source of error in modeling.

Table 7.3 6% Z-fiber modeling parameters

	Warp	Weft	
E_{11}	9077	9658	ksi
E_{22}	882	953	ksi
E_{33}	882	953	ksi
ν_{12}	0.2718	0.2673	
ν_{13}	0.1899	0.1725	
ν_{23}	0.1899	0.1725	
G_{12}	421	463	ksi
G_{13}	370	406	ksi
G_{23}	370	406	ksi

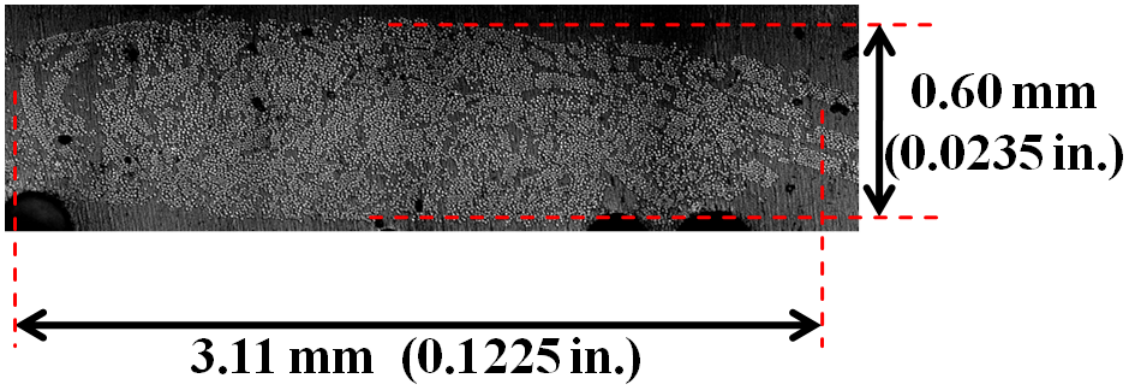

Figure 7.4 Fibers that make up a tow as seen from multiple microscope photos that are stitched together.

The periodic boundary conditions that are required for RUC modeling have been discussed in detail [86], however it was found that it would only change the mechanical properties by about 1%, if instead, "free" boundary conditions or "symmetry" boundary conditions are used, as has been discussed before for braided composites by Song [36].

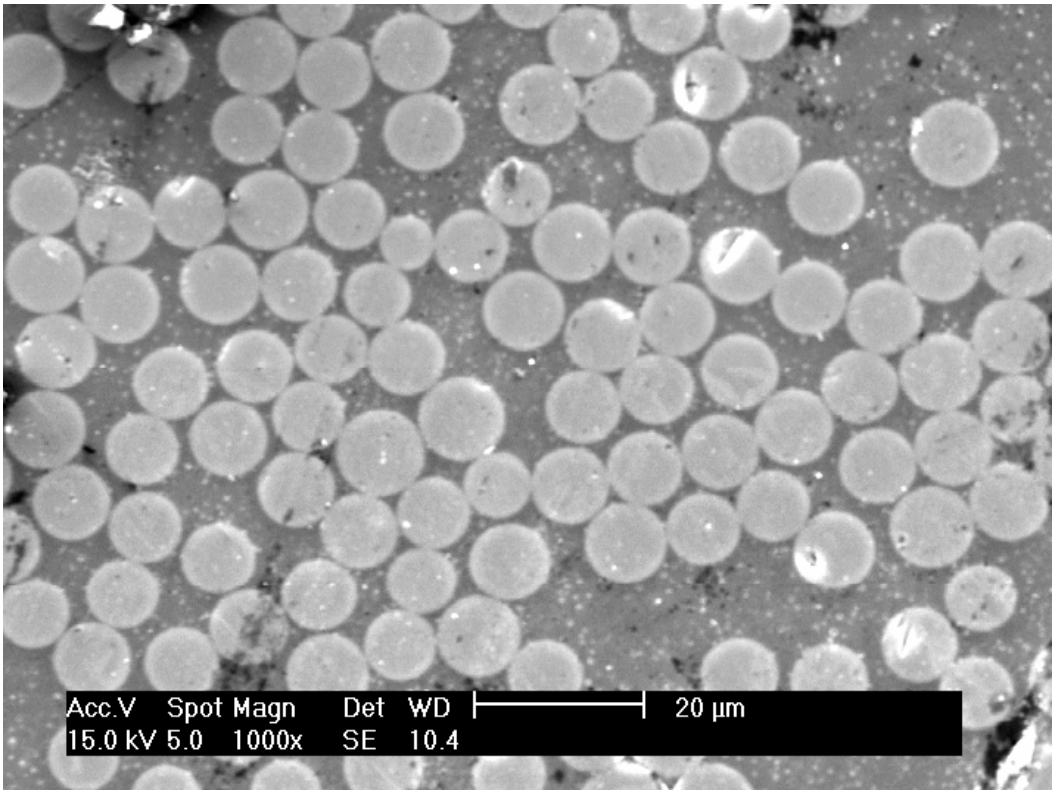

Figure 7.5 Individual fibers in a tow taken from the SEM.

7.3 Computational Results

7.3.1 Static Loading

In order to determine the accuracy of the computational model, simple static tests were performed as baselines to determine if they could accurately represent the mechanical properties obtained from tension and compression tests. In order to compare the mechanical properties, a way to measure the modulus of the RUC had to be determined. In order to calculate the linear elastic properties, a very small displacement was imposed. The resulting nodal forces on the surfaces were then computed. With these results we can calculate the modulus. The macroscopic nominal stress σ on a loading face, in the direction of loading is calculated from the sum of the nodal forces, divided by the cross sectional area of that face. The macroscopic stress is:

$$\sigma = \frac{\sum_{i=1}^{n} F_i}{A} \tag{7.2}$$

where n is the number of nodes on the face and A is the cross sectional area of the face. The macroscopic strain, ε is:

$$\varepsilon = \frac{\delta}{L} \tag{7.3}$$

where δ is the imposed displacement and L is the length of the side parallel to the loading direction. Combining these, we can use Hooke's law to obtain the average modulus.

$$E = \frac{\sigma}{\varepsilon} \tag{7.4}$$

or

$$E = \frac{\sum_{i=1}^{n} F_i}{A} * \frac{L}{\delta} \tag{7.5}$$

The simple tension test was used to validate the mechanical properties of the model by loading the RUC in both the warp and weft directions. Figure 7.6 shows the stress contour plot from a tension test in the warp fiber direction, while table 7.4 compares the experimentally obtained results. The model has a relatively good agreement, it predicts good overall trends. Since we are using it to compare against the SHPB data we are more concerned about the general trends that occur and seeing if we can capture the trends observed in the test.

Table 7.4 Tension Test

	Msi	Msi	%
Weft	3.560 ± 0.206	3.48	-2.25
Warp	3.113 ± 0.16	3.29	5.92

7.3.2 SHPB Simulations

Additional parts were added to the RUC model to recreate the SHPB test. The incident and striker bars were modeled as elastic bars. The properties of the bars are given in table 7.5. The bars were modeled using identical elements as the ones used in the RUC. The bars were set at some arbitrary length to allow for proper strain wave propagation. A sketch of the model with inputs are shown in figure 7.7. The incident strain gauge signal from the experimental test was used as an input to the model as shown in figure 7.7. The incident and transmitted bars were constrained from moving in the lateral directions to simulate the bearings that exist in the actual experimental setup.

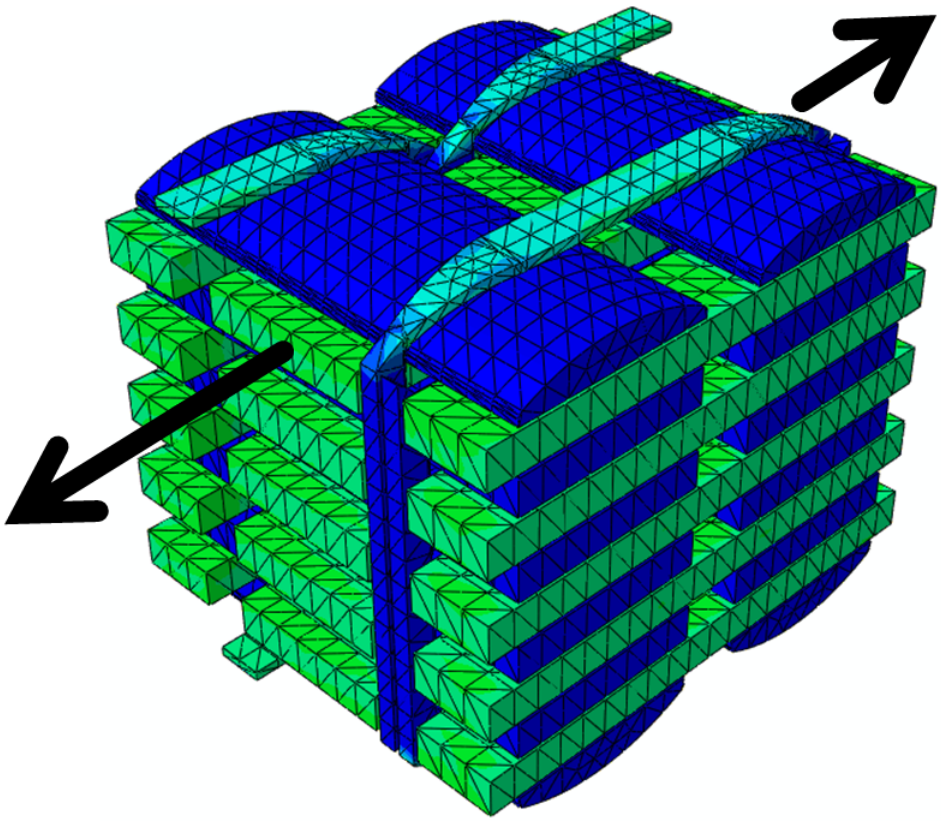

Figure 7.6 6% Z-fiber RUC warp tension test.

Table 7.5 Physical Properties of Incident and Transmitted Bars

Material	440C Stainless Steel
Density	7620 $\frac{Kg}{m^3}$
Young's Modulus	220 GPa
Ultimate Tensile Strength	1965 MPa
Brinell Hardness	580

A convergence study was run on the incident and transmitted bars, since the mesh of the RUC is relatively fixed. Both linear and quadratic elements were investigated, with the maximum strain in the transmitted bar being used as the comparison value. The results can be seen in figure 7.8, which shows that both the linear and quadratic element provide similar values for the strains. The quadratic elements were able to predict accurate results with very few elements, therefore they were chosen as the bar elements for the remaining simulations.

The strains in elements for the incident and transmitted bars were tracked and compared to the strain gauge signals from the tests. Figure 7.9 shows both the experimental and computational strain gauge results. The computational results show two issues. 1) the length

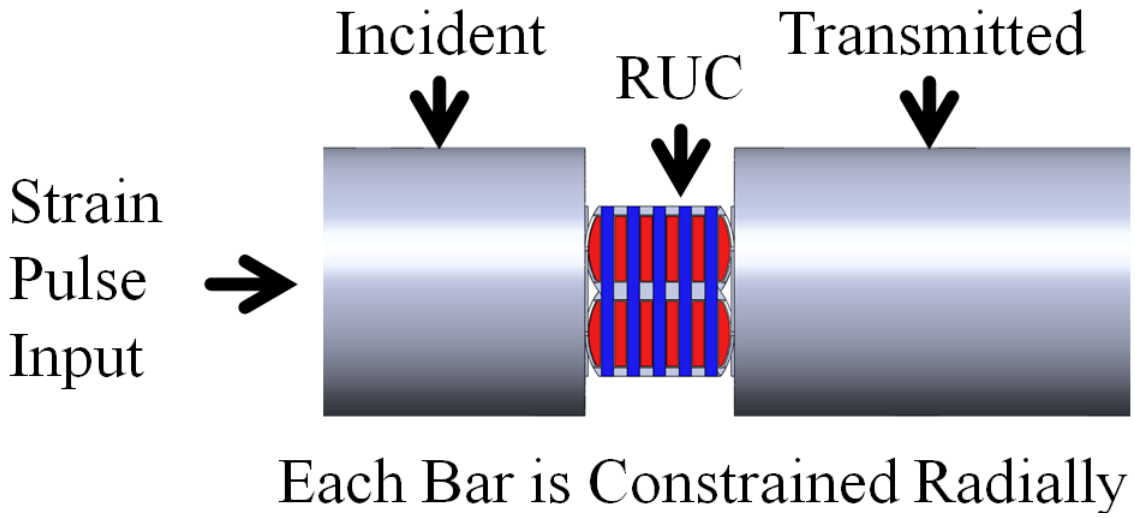

Figure 7.7 Model of the SHPB FE simulation

of the simulated incident bar is not sufficient due to wave interaction at around $80\mu s$, 2) due to the large deformation of quadratic elements in the matrix material of the RUC, the simulation terminates before the transmitted bar can experience a full signal. This problem will be discussed further later. Overall the agrement is very good for the experimental and computational model.

Using the simulated strain gauge signals and the 1-D Hopkinson bar wave theory assumptions and the simplification that the reflected wave is:

$$\varepsilon_R(t) = \varepsilon_T(t) - \varepsilon_I(t) \tag{7.6}$$

we can simplify the SHPB equations shown in Appendix C to:

$$\sigma_s(t) = E_{bar}\frac{D_{bar}^2}{D_s^2}\varepsilon_T(t) \tag{7.7}$$

$$\frac{d\varepsilon_s(t)}{dt} = -2\frac{C_o}{L_s}\varepsilon_R(t) \tag{7.8}$$

$$\varepsilon_s(t) = -2\frac{C_o}{L_s}\int_o^t \varepsilon_R(t)dt \tag{7.9}$$

Thus, the strain gauge signals are fed into the analysis and the results determine the effective properties in a similar manner to the experimental results.

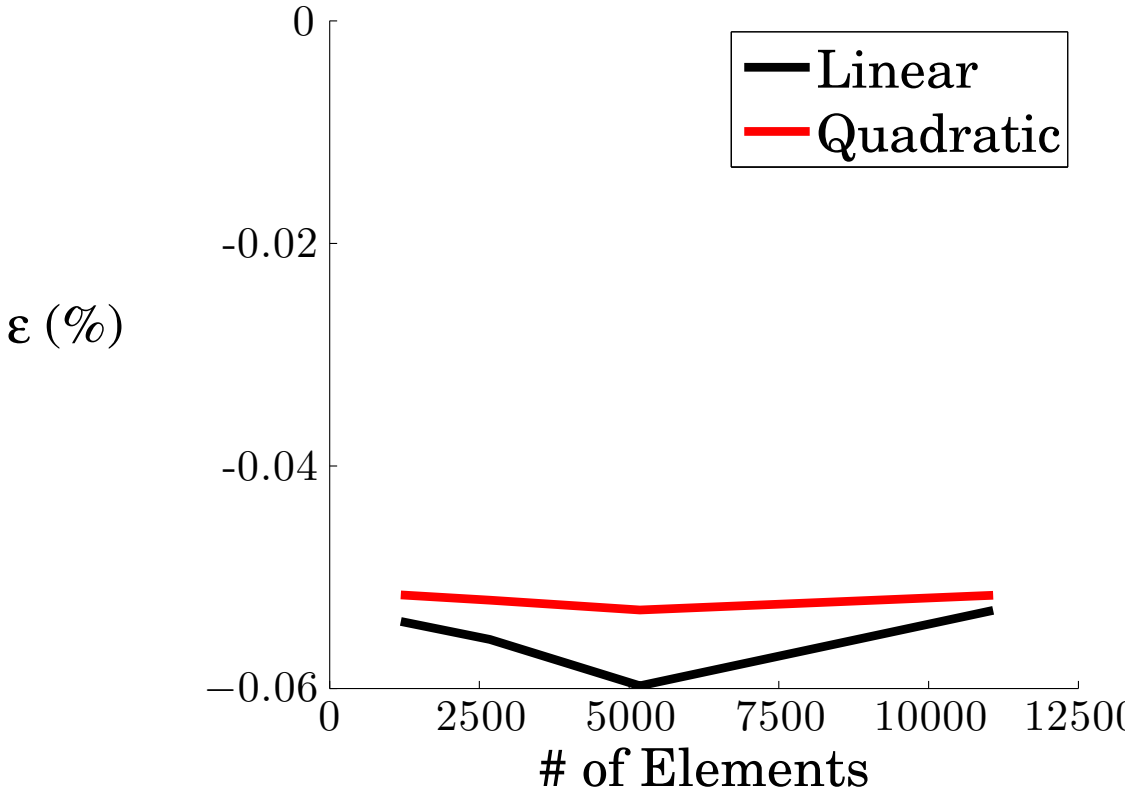

Figure 7.8 Convergence of elements with respect to meshing of the incident and transmitted bars.

Matrix Failure and Element Deletion

In addition to modeling the matrix as an elastic-plastic J2 flow theory solid, element deletion was added. In order to properly implement this option, the material is assumed to have a failure model with element degradation built into it. The failure model was accomplished through the *DAMAGE INITIATION option in ABAQUS, where a ductile criterion was used. Additionally the *DAMAGE EVOLUTION was enabled to model element degradation through a reduction in stiffness. The element degradation occurs by reducing the stress based on a solution dependent damage parameter D. Thus,

$$\sigma_{ij} = (1 - D)\,\bar{\sigma}_{ij} \tag{7.10}$$

The above relation shows how the stress σ_{ij} in the element is degraded based on the parameter D which is dependent upon the strain in the element. Further details of this degradation approach are given in the ABAQUS theory manual, see ref [87]. As D approaches 1 the stress approaches zero showing the element has completely failed. For the current model

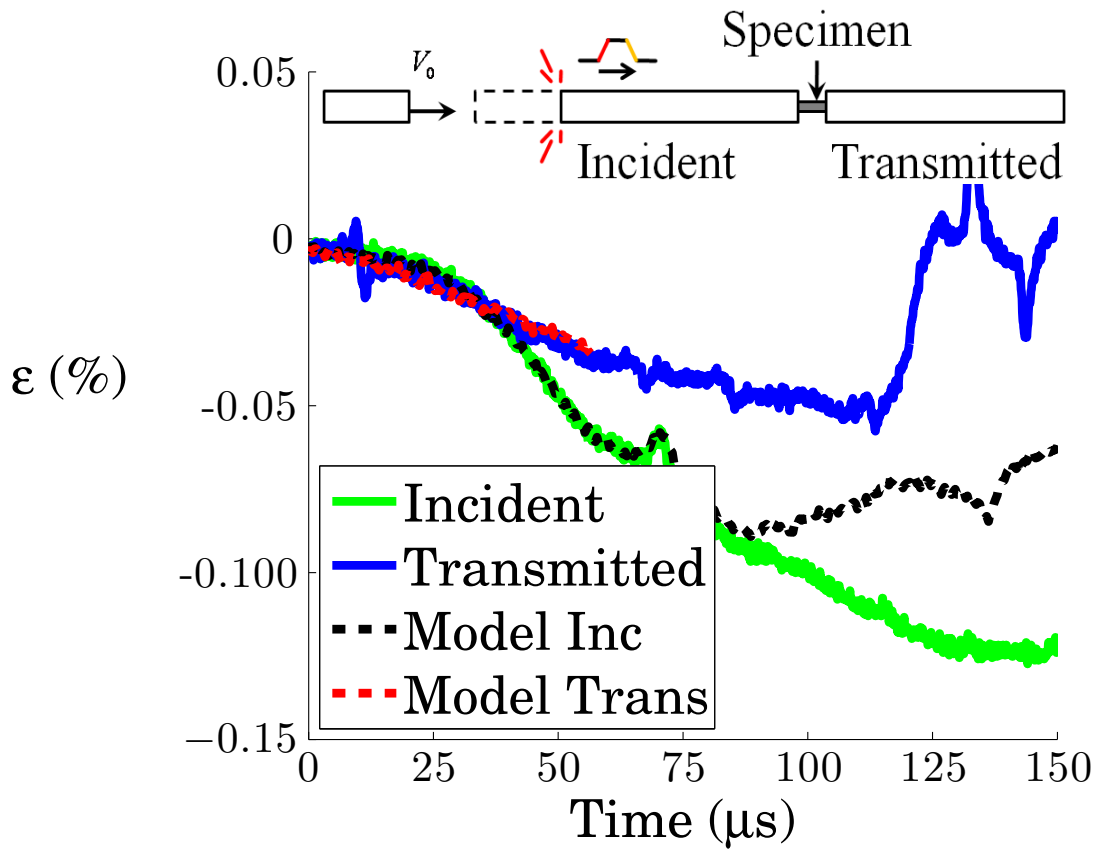

Figure 7.9 6% Z-fiber RUC strain gauge data comparison from experimental and computational model for quadratic RUC elements.

an energy approach was used with the energy of failure set to 2 since this is defined as the fracture energy per unit area, which should be identical to the values associated with the DCZM model and G_{IIc} for pure SC-15 was found to be this value [1]. When this element fails it should be removed from the model, therefore, the element deletion was added in the computational model through the addition of the *SECTION CONTROLS option by enabling element deletion. The maximum degradation was 0.01 for these tests, because only a small amount of failure was wanted due to the brittle nature of the matrix. Additionally in ABAQUS, the STATUS output option must be enabled to determine which elements have failed.

Linear vs. Quadratic Elements

The one caveat of this problem is a computational issue in ABAQUS due to the relatively high loading rates that occur in this simulation. With the use of quadratic elements, as

the elements approach failure some are often very contorted due to the thinness of the elements. As this occurs a limit is reached where the deformation rate will exceed the wave speed of the material causing a numerical instability forcing the ABAQUS solver to exit. This is due to one element failing locally and then a surrounding node will show unduly large displacements while the rest of the element remains stable, therefore the one node will exceed the displacement corresponding to the maximum strain allowed becoming excessively distorted. Thus, the simulation was also run with linear elements to compare the results. The linear elements have fewer degrees of freedom, preventing the elements from ever having these excessively distorted shapes.

Identical simulations were run, only changing the RUC elements to linear vs. quadratic. The predictions of the computational models are compared against the strain gauge data in figure 7.10 where the difference between the two computational models is very minimal, and does not show up in these simulations. The RUC model contains a large number of elements in order to properly mesh the complex architecture. The small elements will accurately capture the strain in the elements. Since there is no appreciable difference between the strain gauge signals and the model prediction as shown earlier, it was decided to use linear elements in subsequent calculations. There are two benefits to the linear elements, the first being that the model runs quicker, the second is the fact that the solution will never exit due to numerical issues, from the overly constrained elements.

All three loading directions were examined to determine the effective through the thickness results and in-plane compression response. Figures 7.11-7.26 show a comparison between the experimental and computational results. Both the warp and weft direction results agree well with experimental results, while the through-the-thickness direction has some disparity. The strain rates in the both the warp and weft direction are high because they are based on the theoretical reflected wave as compared to the actual reflected wave obtained from the experiment.

Through-the-Thickness Computational Results

The through-the-thickness result suffers from a computational problem. In-order to properly create the model there are areas of pure matrix on the top and bottom surfaces. This is not the case experimentally. Therefore the FE model was remeshed with these excess elements removed to determine more accurately the response of the material. This extra area of matrix causes localized deformations preventing the rest of the material from undergoing strain. The modified model was run for both the linear and quadratic cases. The results showed a strong correlation with the experimental data until the Z-fiber becomes the load carrying

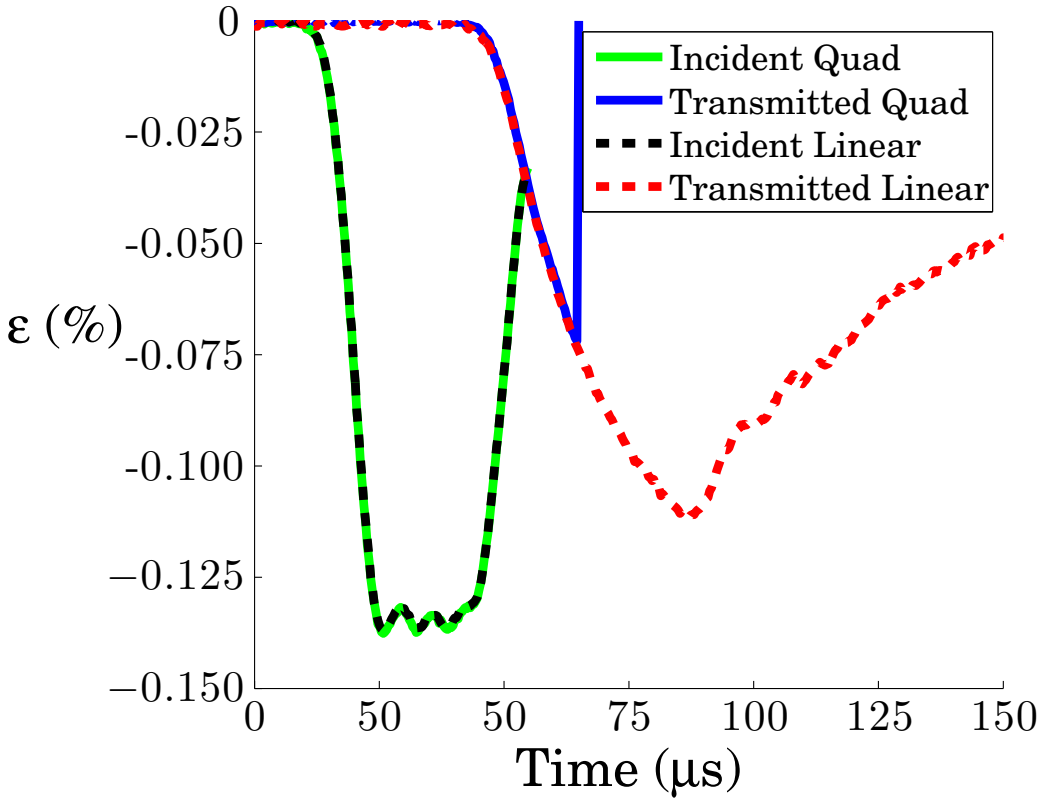

(a)

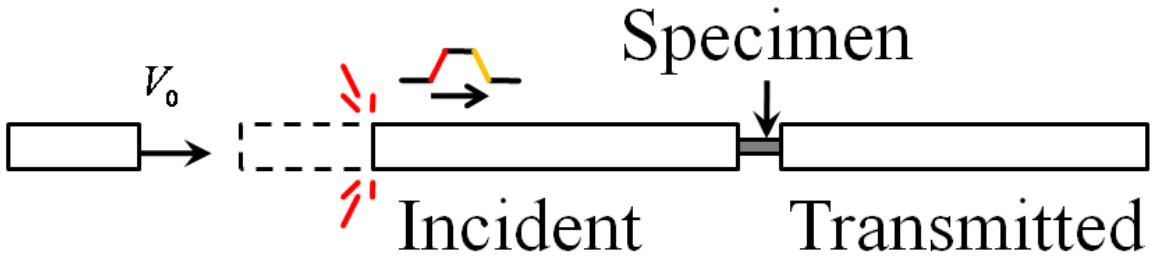

(b)

Figure 7.10 Strain Gauge measurement comparison for Quadratic vs. Linear Elements.

member. Figure 7.11 shows the correlation of the stress-strain curves to the experimental data. The strong Z-fiber limits the strain in the material because it becomes the primary load bearing member of the architecture.

A second model was run where the Z-fibers were completely removed. This model was done to test the effectiveness of the Z-fiber in the material and to also simulate better the response of the actual experimental setup due to the grinding of the specimens that was required for flat contact surfaces. The results showed a strong correlation to the experimental

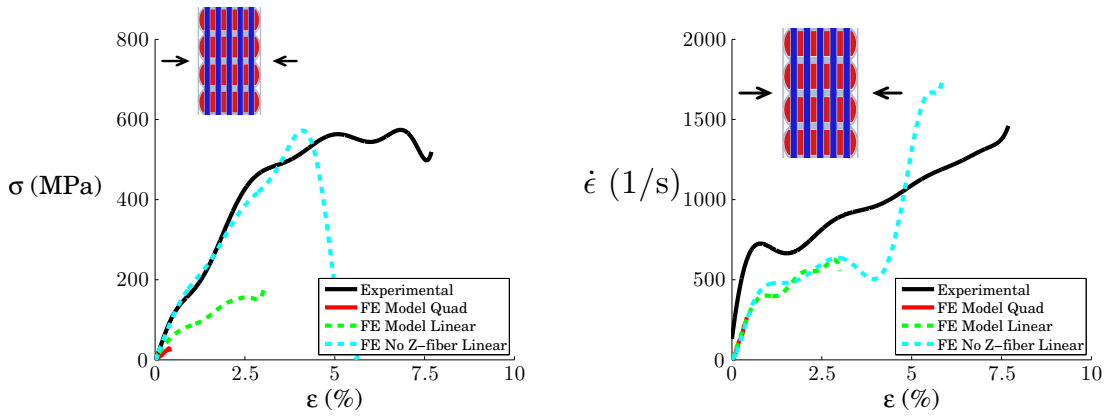

(a) $\sigma vs. \varepsilon$ (b) $\dot{\varepsilon} vs \varepsilon$

Figure 7.11 Stress-Strain-Strain Rate plots for through the thickness specimens.

measurements. Two observations can be made, the first is that there is very little increase in stiffness from the Z-fiber, the second is that the areas of pure matrix cause artificial softening. This result can be backed up through experimental tests where a thin layer of matrix was inserted on top of the specimen. During testing this was the only area to undergo strain.

Figure 7.12 shows the effective stress-strain curve for simulation where the Z-fibers have been removed. Additionally the strain field on the surface of the material has been plotted. It can be see that there are clearly different strains that exist in the material at any one given time. The strain field is heavily architecture dependent. The different strain concentration areas correspond to the fiber tows and matrix areas. Onset of failure is observed in subfigure k. Here, we notice that the strain field begins approaching non-equilibrium. This occurs due to matrix element failure that would be separating the fiber tows. The earlier onset of failure comes from the fact that failure is predicted by the element deletion of thin matrix layer separating the tows, it does not capture matrix cracking and shear band failure that occurs in the actual experiment. Therefore as soon as the matrix elements are deleted the load drops instead of the shear band formation, which is a much more complex failure mode to capture computationally.

The simulation can additionally be compared to the DIC results obtained experimentally. Figure 7.13 shows a comparison of the DIC results obtained at different time steps to those observed computationally. Although the RUC model is roughly a fourth in size compared to the experimental specimens, clear conclusions and comparisons can be drawn between the two. The model shows the reason why we saw clear “bands” of strain experimentally. The strain bands are formed by the difference in material properties between tows and matrix. The fiber tows are oriented in opposite directions with pockets of pure matrix. The

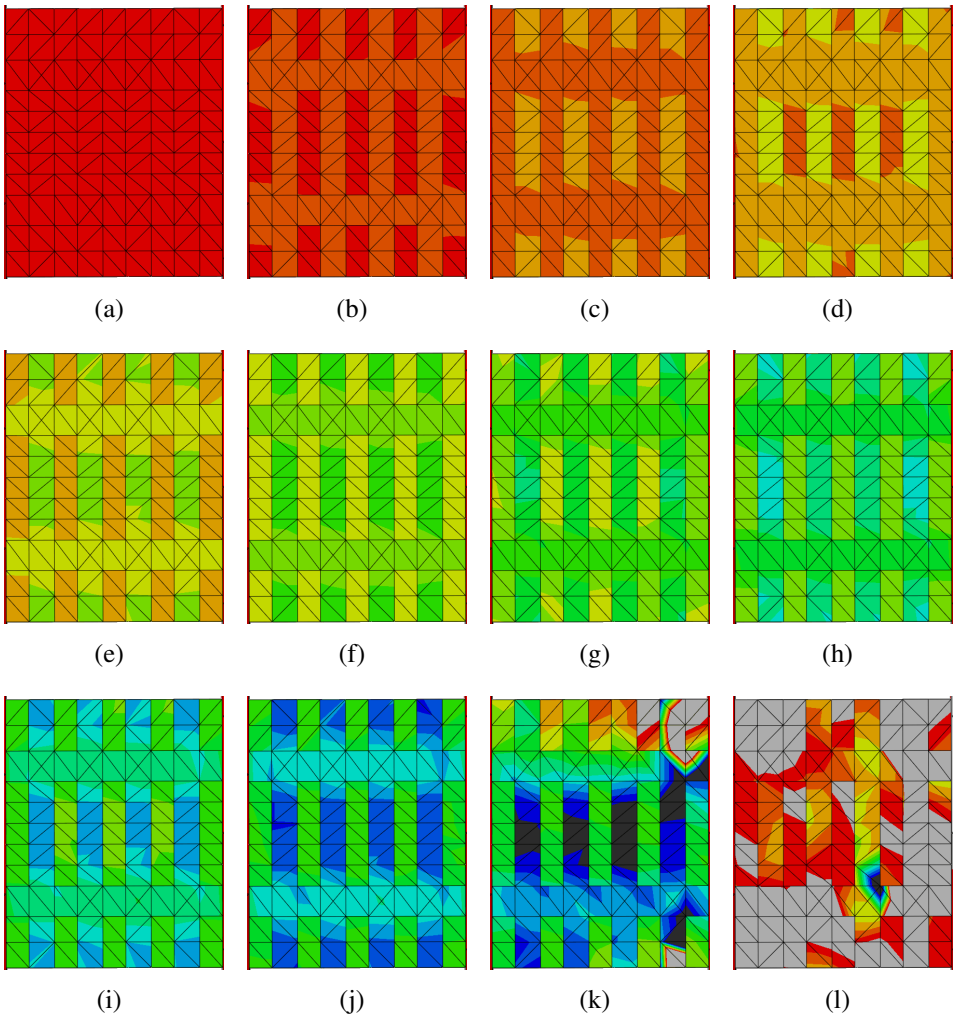

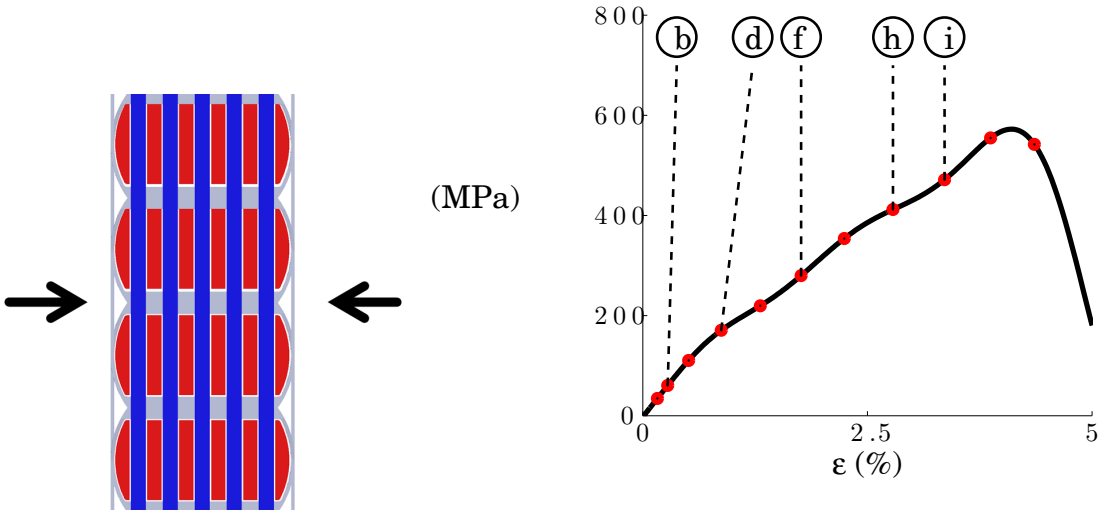

(m) Loading Diagram

(n) Stress Strain plot with photo events

Figure 7.12 ε_x DIC time history for through the thickness computational model.

pure matrix has a different modulus and different stress wave propagation characterization than the tows. Both factors combine to provide a non uniform strain field in the material. The material clearly fails at the desired point however it does not form a shear band. The numerical model is currently being refined to include other possible influences, such as imperfections in the architecture (geometry).

Additionally the energy associated with failure was plotted, see figure 7.14. All of the energy in the specimen is termed as internal energy. Initially all of the energy is turned into linear elastic strain energy. After the onset of plasticity over a quarter of the energy is used in plastic deformation. The onset of failure is indicated when the kinetic energy starts to spike up around 180 μs. Overall about 25 % of the energy is converted to non-recoverable plastic energy before failure occurs in the material.

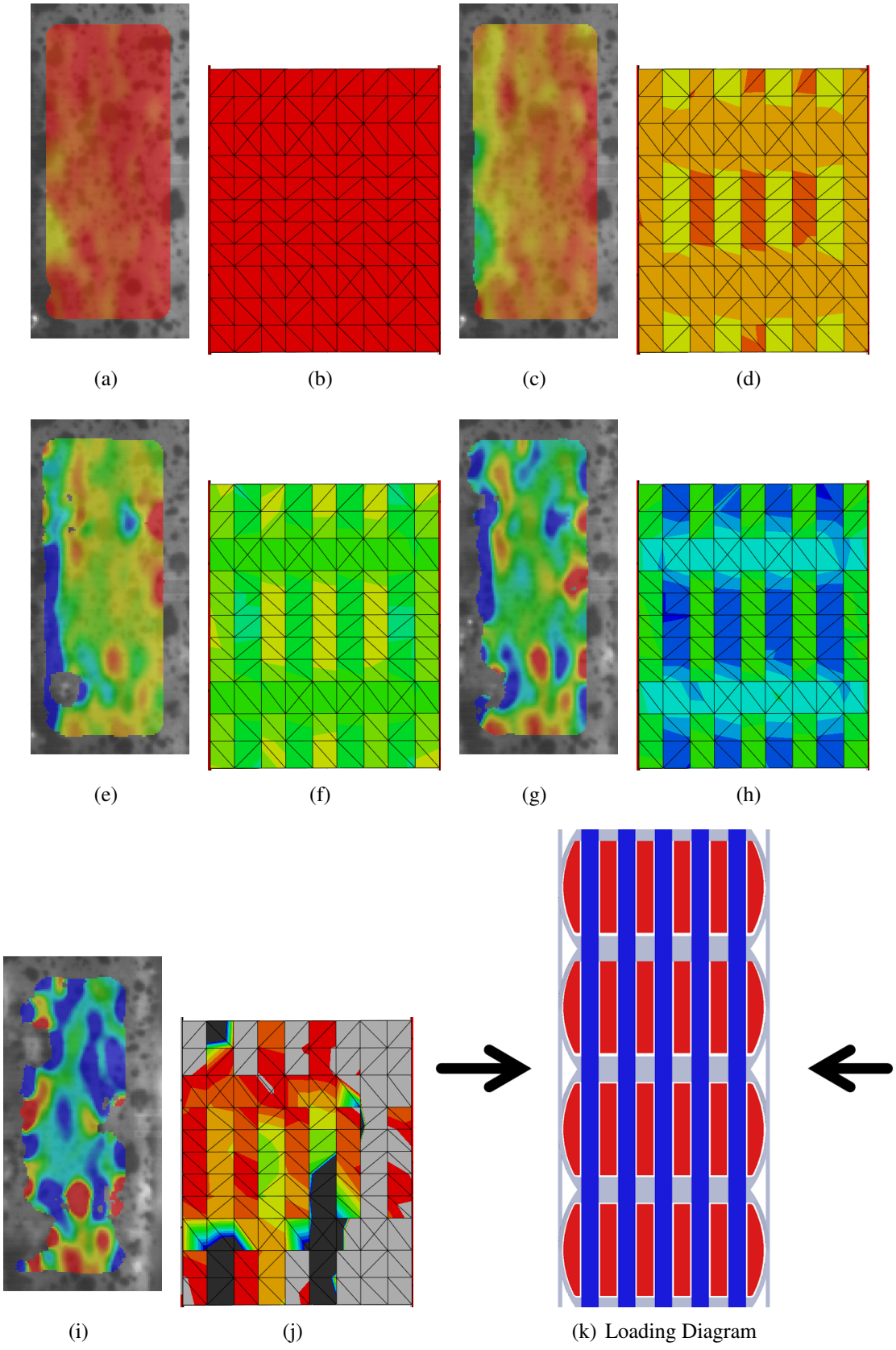

Figure 7.13 ε_x FE and DIC comparison for through the thickness Hopkinson bar testing.

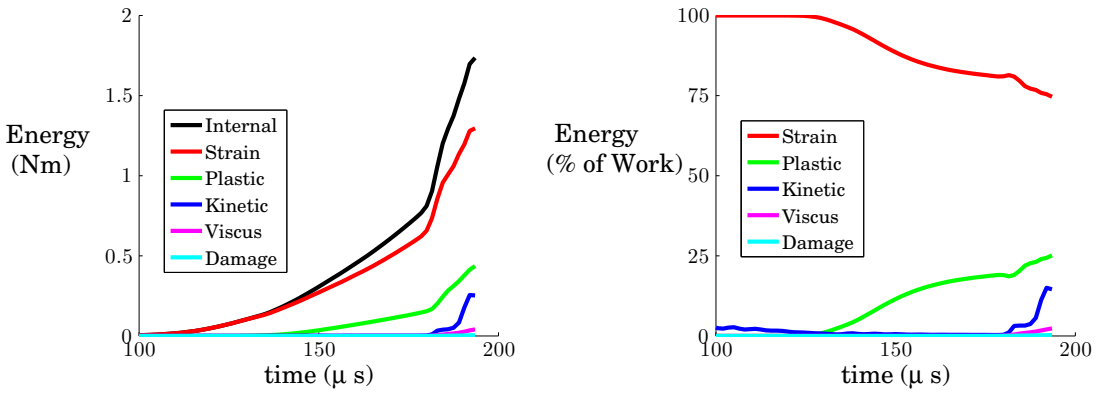

Figure 7.14 Energy associated with different modes of deformation.

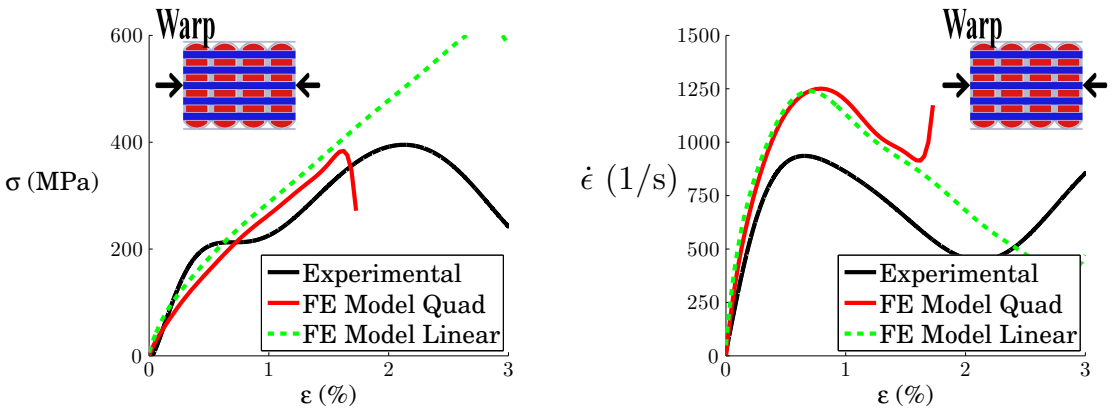

(a) $\sigma vs. \varepsilon$ (b) $\dot{\varepsilon} vs \varepsilon$

Figure 7.15 Stress-Strain-Strain Rate plots for the warp direction.

In-Plane Computational Results

Both in-plane directions were tested, with the RUC being hit in both the warp and weft direction as was reported in chapter 6. The same RUC used for initial studies with the Z-fiber in place was used to test the mechanical response of the material. The warp direction showed a strong correlation to the material properties obtained in SHPB testing. The effective stress-strain response is very similar, however the strain rate is a bit over predicted as seen in figure 7.15. This over-prediction was explained earlier due to the manner by which the transmitted bar signal is used. Both the linear elements and the quadratic elements showed a strong correlation to determining elastic modulus of the material. The quadratic elements will typically exit due to non-convergence when localized micro-cracking is approached. The linear elements predict the same material response however they can not accurately predict failure. Due to the idealized architecture assumed in the modeling, the tows would need a perturbation to cause the buckling and subsequent delamination to occur as was observed in the experiments. This concept will be examined further.

The weft direction showed very similar computational characteristics to those of the warp direction. The model showed a strong correlation to experimental moduli, as seen in figure 7.16. The quadratic elements again exited due to numerical errors, however was able to predict the same moduli as observed with the linear elements. The linear elements accurately predict the response of the material, however the idealized architecture will not accurately predict failure in the specimen.

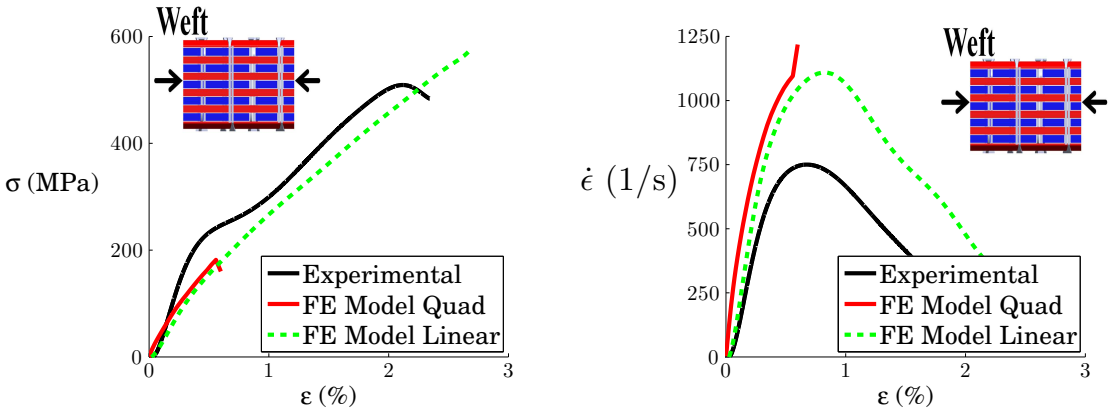

(a) $\sigma vs. \varepsilon$ (b) $\dot{\varepsilon} vs \varepsilon$

Figure 7.16 Stress-Strain-Strain Rate plots for the weft direction.

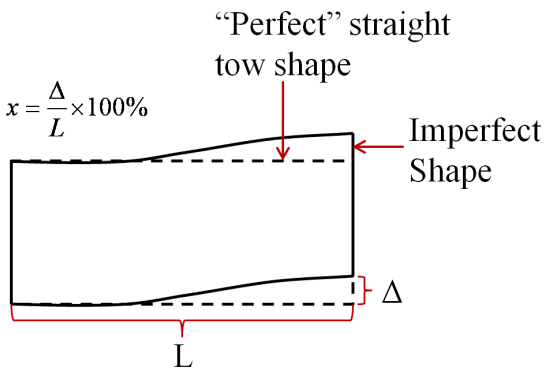

Figure 7.17 Amplitude perturbation to seed initial imperfection.

Buckling Analysis to Induce Failure in Specimen, due to initial geometrical Imperfection.

Due to the idealized architecture, perfect tows were assumed as part of the model. This leads to a problem computationally since the tows will undergo "perfect" compression and will not buckle due to lack of initial geometrical imperfections. A linear buckling analysis was done to determine the first mode that corresponds to buckling. This mode shape was then seeded into the RUC model to simulate the initial geometric imperfection in the material architecture. This method has been successfully used before by Song [36]. The *IMPERFECTION command was used which references buckling modes to seed the initial imperfection. This deformation will be seeded as some percentage of the calculated buckling mode. We only need a small imperfection to induce a response other than the "perfect" response. In this study, the maximum amplitude of the imperfection is chosen to be x=2.5% for the warp and x=3.3% for the weft, as shown in figure 7.17.

The weft direction was examined to determine the specimen failure due to compression. The distortion control feature had to be enabled in the *SECTION CONTROLS suboption to ensure that the elements would not excessively distort. The model was seeded with a 1% imperfection corresponding to 1% amplitude of the buckling mode shape. A 1% amplitude of the buckling mode shape leads to x=2.5% for the warp and x=3.3% for the weft. This small amplitude was chosen to simply provide some non uniformity to RUC architecture. The effective stress-strain curve of the imperfect model can be seen in figure 7.24 which shows a good correlation to the experimental results. The material moduli agree strongly, with failure predicted at the same peak stress value as in the test. The strain rate is over predicted as usual, however the results show a strong correlation between the model and the experiment including observed failure modes. It is important to note that the computational results due to the inclusion of geometric and material non-linearity, is able to predict the

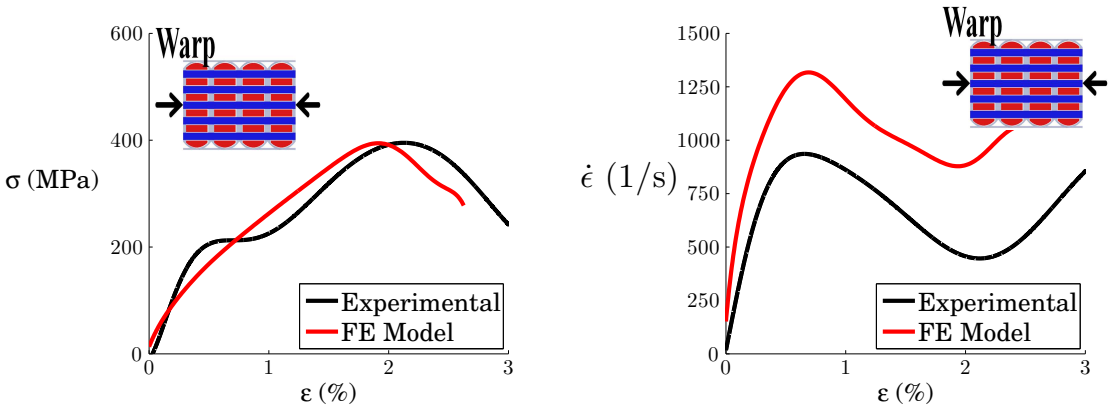

(a) $\sigma vs. \varepsilon$ (b) $\dot{\varepsilon} vs \varepsilon$

Figure 7.18 Stress-Strain-Strain Rate plots for the warp direction.

maximum strength of the specimen. Such a prediction cannot be performed without the inclusion of the material and geometric non-linearities.

Figure 7.19 shows the strain contour plots for various different points in the Hopkinson bar tests. The material initially has very little strain and appears to be very uniform. However as the strain increases there seems to be a different strain field in the different constituents. The results show that strain wave propagation will cause interactions between the different tows in the material. There is clearly not a uniform strain state in the material, however, there is less variation in the strain field in the in-plane measurements than in the out-of-plane measurements. As the strain progresses there are vertical strain bands that seem to develop. These occur in areas where the material contains Z-fiber and matrix pockets. Failure begins occurring in subfigure j. Here, we can see a clear progression towards buckling and delamination occurring

To further compare the computational model with the experimental results the FE were correlated with the DIC results. Figure 7.20 shows the DIC images for different times compared with the FE strain field for the corresponding time. The results agree well. The strain fields look similar and have similar characteristics. There are distinct strain bands that occur which were discussed earlier. Additionally the materials begins failing from one edge as can be seen in the last figure. The FE model over-predicts the strain at failure in the entire specimen, however the computational specimen was half the length of the experimental specimen. The FE model predicts the same type of failure as observed in experiments and since the failure is localized, there should be no size effects to be concerned with in the model.

Figure 7.21 shows the energy in the model and the percent of energy associated with the

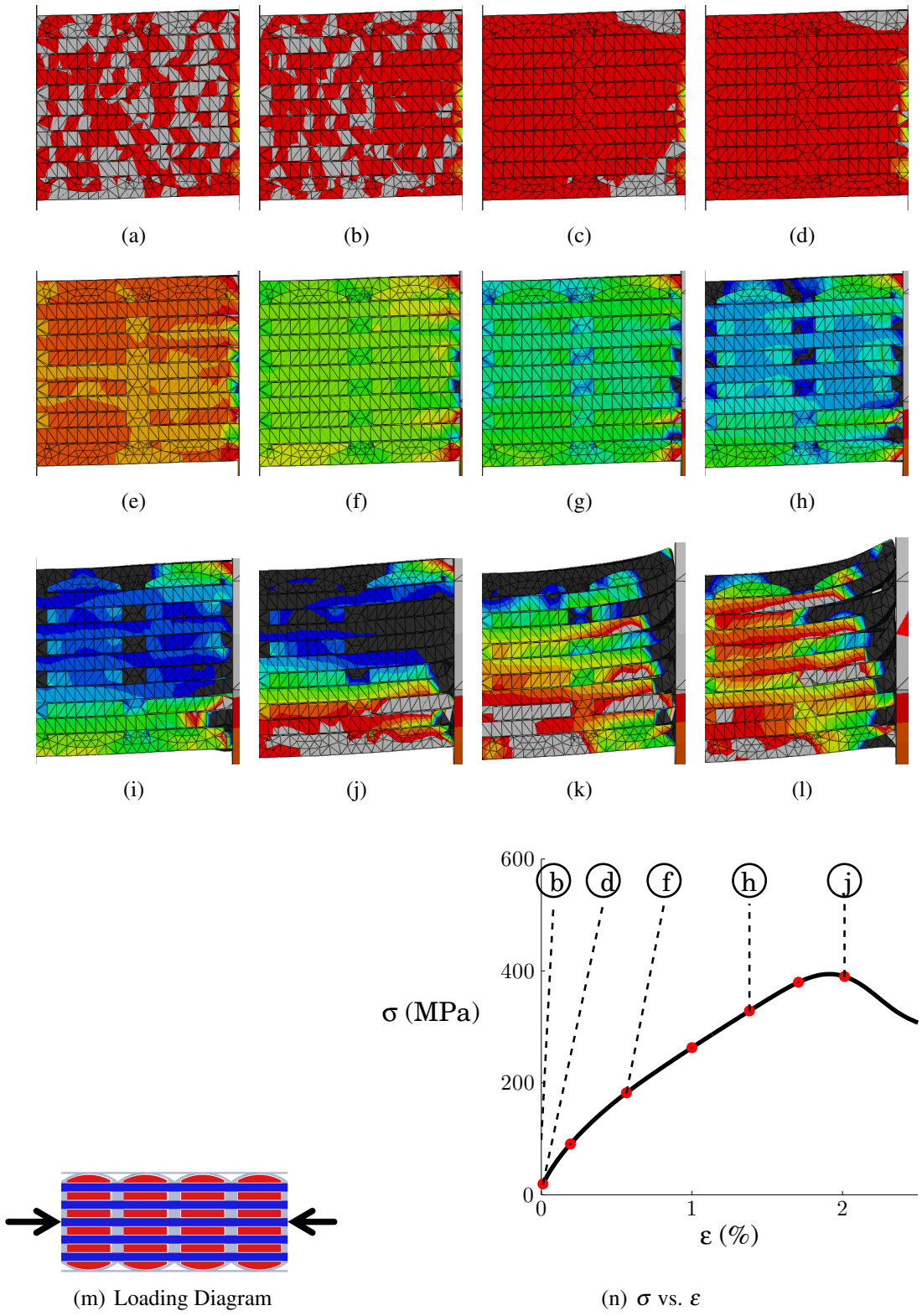

(m) Loading Diagram

(n) σ vs. ε

Figure 7.19 ε_x strain field from computational model for the warp direction.

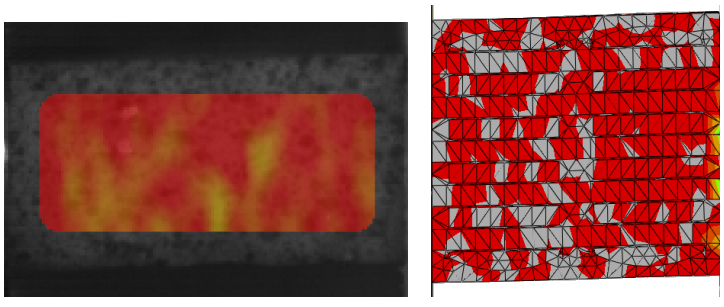

(a) (b)

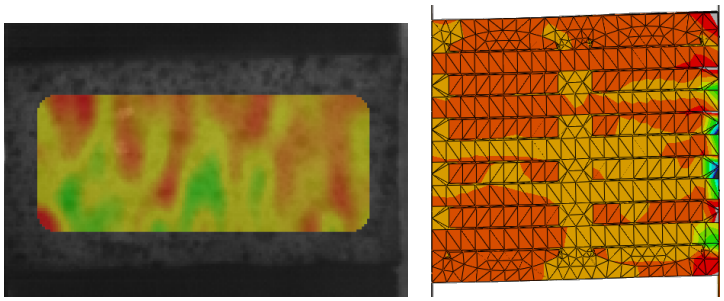

(c) (d)

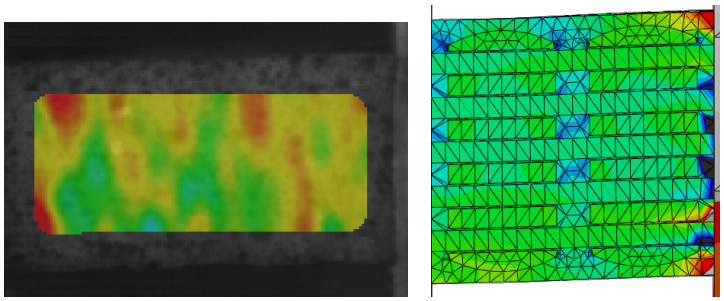

(e) (f)

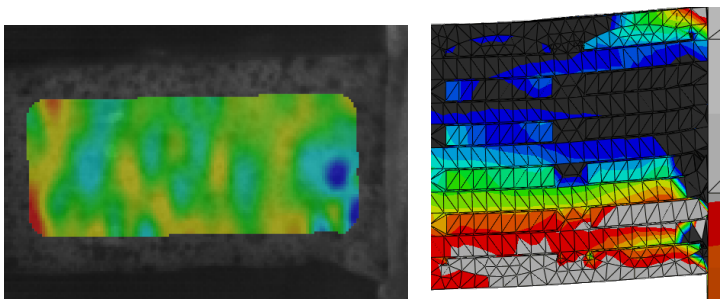

(g) (h)

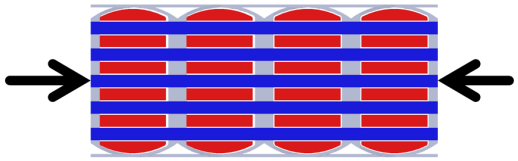

(i) Loading Diagram

Figure 7.20 ε_x comparison of Computational Model and DIC data for the warp direction.

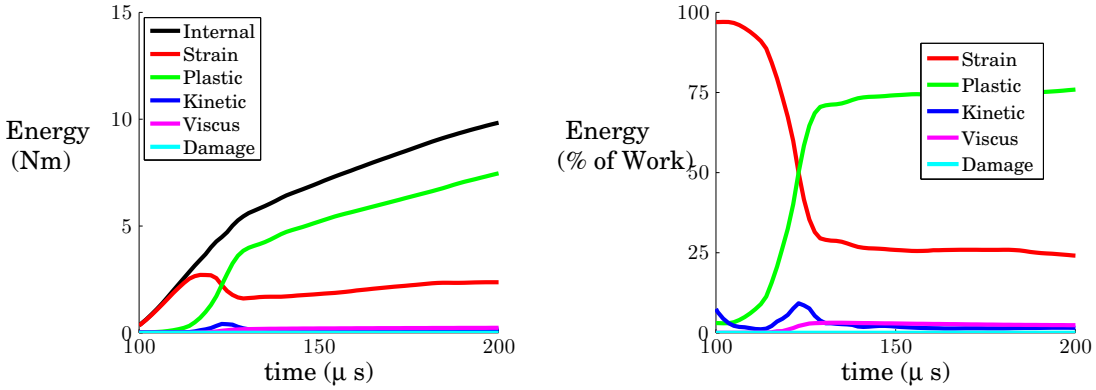

Figure 7.21 Energy associated with different modes of deformation.

different failure modes. The plots show initially all of the energy is associated with linear elastic strain energy. Near the onset of failure the strain energy begins to decrease and the plastic energy increase to nearly 75% at brooming failure of the specimen. The failure is seen as the spike in the kinetic energy. The linear elastic strain energy is mainly released as, only 25 % of the energy is associated with this failure mode.

To further test the computational model the simulation was rerun at a quasi-static rate to determine the failure mode of the material with out rate effects. Figure 7.23 shows a comparison of the two different predicted failure modes in the material. The corresponding macroscopic stress vs. macroscopic strain plot for the quasi-static case can be seen in figure 7.22. It should be noted here that the yield stress of the individual tows is significantly lower. R_{11} was set to 7 in the anisotropic elastic-plastic tow material model to achieve the proper stress-strain curve. The effect of the matrix material on the initial elastic properties is seen in figure 7.28, which shows predictions for both measured material properties and also for matrix at half of the yield strength ("Low Matrix"). There is very little difference in the stress-strain response. The only noticeable result is for the post kinking loads. The lower yield stress is due to the poor compression response of a fiber tow compared to a fiber tow in tension.

The results show that at the different loading rates different failure modes are predicted for the same model. At the quasi-static rate, kink band formation is seen in the fiber tows. While at the Hopkinson bar rates, a brooming failure was predicted in the material. This transition is caused by the rate dependent parameters of the SC-15 matrix material. The material transition from ductile to brittle causes a transition in material response and failure.

The weft direction was also examined. The same procedure and buckling amplitude was

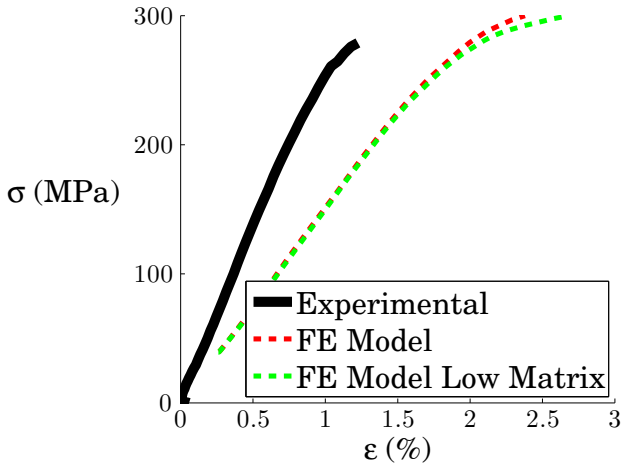

Figure 7.22 Macroscopic stress vs. macroscopic strain response comparison of static results. Low matrix refers to the matrix yield strength being cut in half.

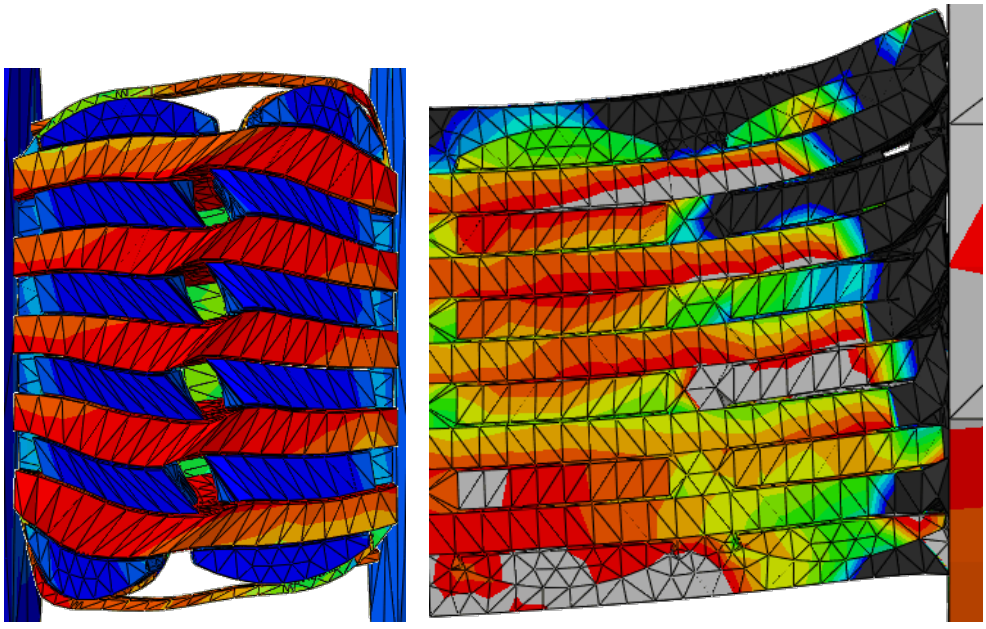

(a) Static (b) Dynamic

Figure 7.23 Comparison of the different computational failure modes predicted.

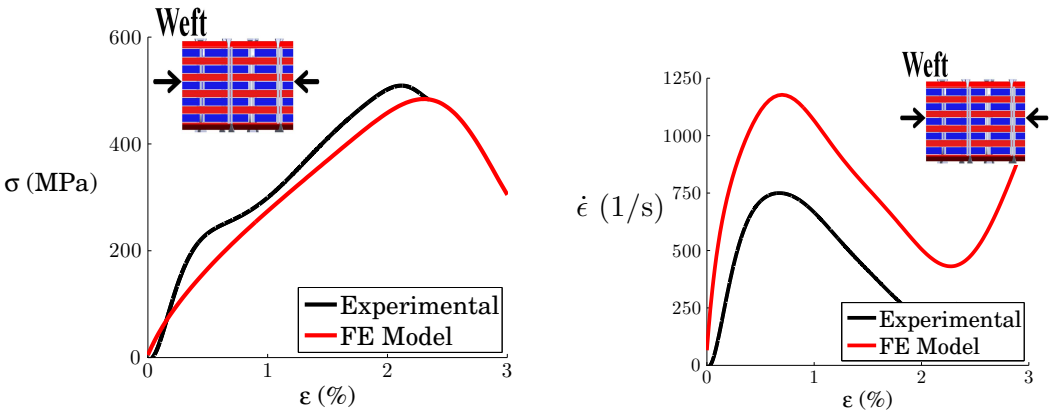

(a) $\sigma vs. \varepsilon$ (b) $\dot{\varepsilon} vs \varepsilon$

Figure 7.24 Stress-Strain-Strain Rate plots for the weft direction.

used to generate a small initial geometric imperfection. Figure 7.24 shows the experimental and computational effective stress-strain response for the material. The results show a strong correlation to the material modulus and failure, obtained experimentally.

The strain at different points in the material can again be looked at in figure 7.25. This shows similar characteristics to those seen in the warp direction. Early in the test there is a better strain uniformity in the material. At higher values of effective strain, the material begins to develop strain bands near the location of the Z-fibers. Failure begins to occur around subfigure j. Here, the material begins to buckle and delaminate. The model predicts larger values of strain near the onset of failure.

The computational results were again compared with the DIC data in figure 7.26. Initially the two have a strong agreement. At higher strains, the bands of strain around the Z-fiber are formed and coincide with areas similar to those seen in the DIC processed images. The strain values have a good correlation and the onset of failure is predicted in a similar manner. The bottom left corner of the final DIC picture predicts the failure of the material, while in the computational model, the bottom right hand corner has this same trend. The area becomes locally compressed having a higher strain concentration than the rest of the material, causing buckling and delamination to occur. Again it should be noted that the computational result examines only one half the length of the specimen.

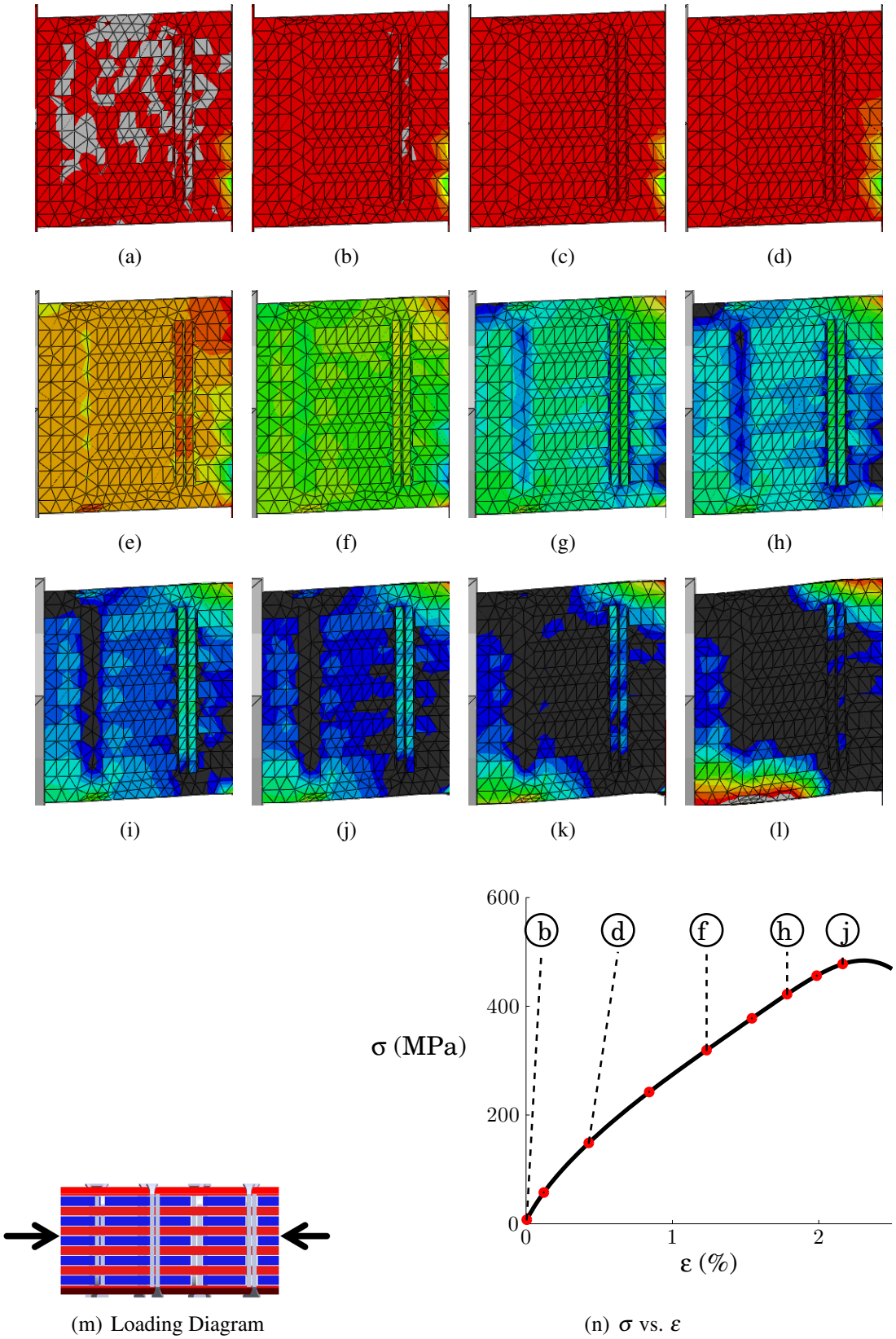

(m) Loading Diagram

(n) σ vs. ε

Figure 7.25 ε_x strain field from computational model for the weft direction.

Figure 7.27 shows the breakdown of the energy associated with the different energy storage mechanisms. The weft results are nearly identical to those predicted in the warp direction. The plastic energy is about 75% again.

Failure was again shown to have a transition in failure mode. The corresponding macroscopic stress vs. macroscopic strain plot can be seen in figure 7.28. Figure 7.29 shows the transition from kink banding at static rates to brooming at the higher loads. The Z-fiber was seen to provide some binding at the lower rates as can be seen in the failure figure of the static rate.

Overall the computational methods are able to accurately predict the material behavior of these woven composites subjected to SHPB type loading. Even material failure modes as observed in the SHPB tests are accurately captured by the FE models. Initial geometrical imperfections were included as a perturbation to create an "imperfect" composite architecture which is closer to the "real" specimens tested in the laboratory.

7.4 Conclusions

Detailed representative unit cell (RUC) models have been created to determine the effective mechanical properties of 3DWC when subjected to SHPB type loading. Based on geometric inputs and parameters computed from the CCM calculations, a strong correlation between experimental results and computational predictions was observed for static loading. The models were then subjected to virtual SHPB testing to determine the response of the material to elevated strain rate loading. Again a strong correlation was found in the material. The simulations provided insight into the locations of failure in the material. The simulations showed that the specimen is not under uniform strain rate because of internal stress wave propagation and interaction.

Extended simulations with buckling perturbations were able to accurately predict the failure in the in-plane compression response. Additionally, the models were able to accurately predict the failure load and delamination that occurred experimentally. Further simulations showed that the Z-fiber contributed very little to the through-the-thickness response. Since the Z-fiber is not a perfect entity in the actual material, the initial model was over predicting its response through-the-thickness. The waviness of the Z-fiber prevents it from carrying an appreciable load in that direction.

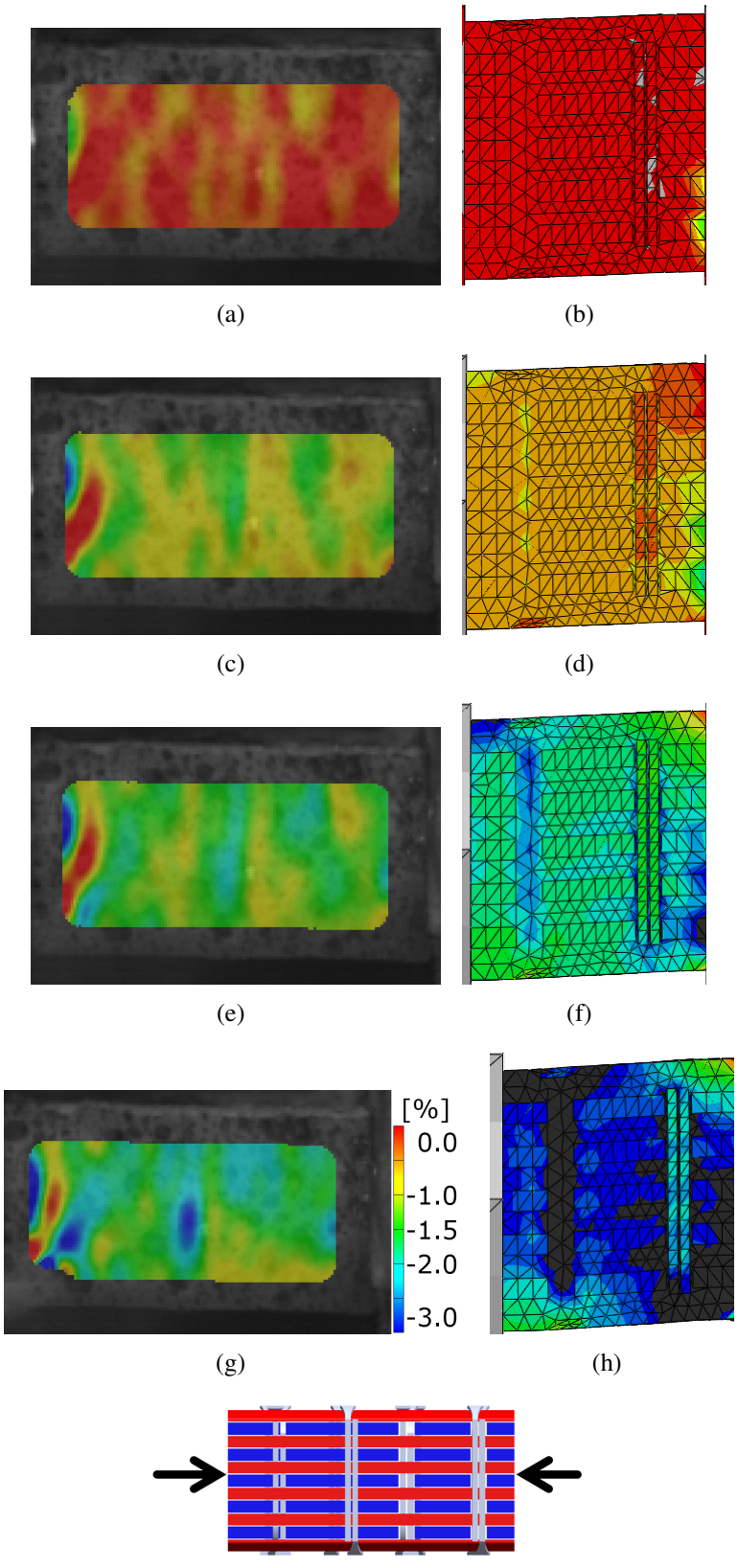

Figure 7.26 ε_x comparison of Computational Model and DIC data for the weft direction.

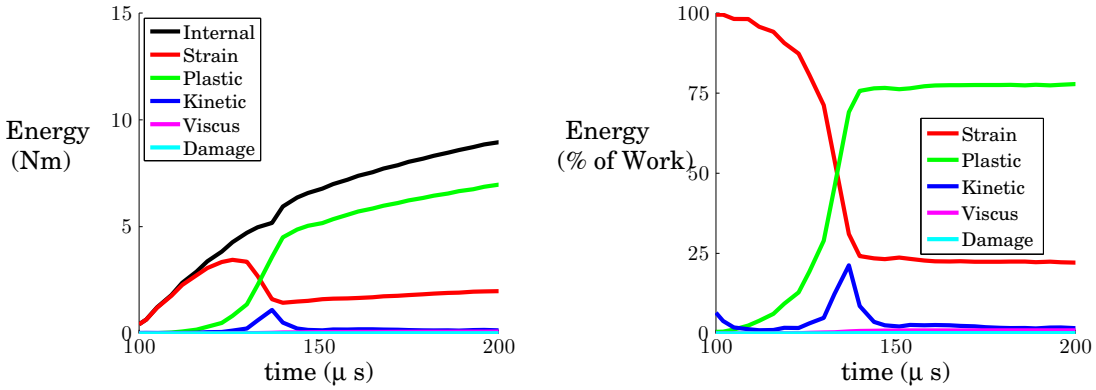

Figure 7.27 Energy associated with different modes of deformation.

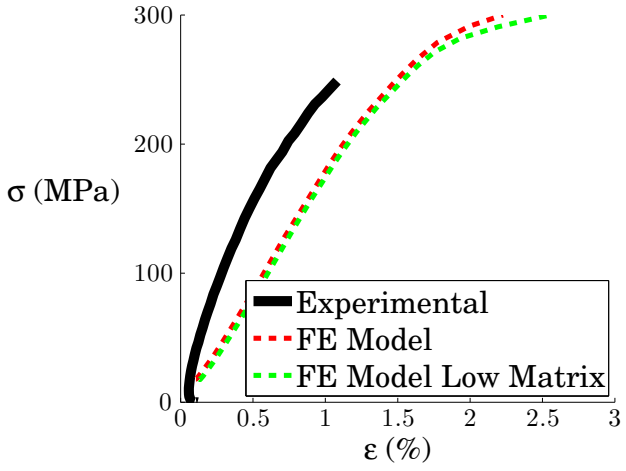

Figure 7.28 Macroscopic stress vs. macroscopic strain response comparison of static results. Low matrix refers to the matrix yield strength being cut in half.

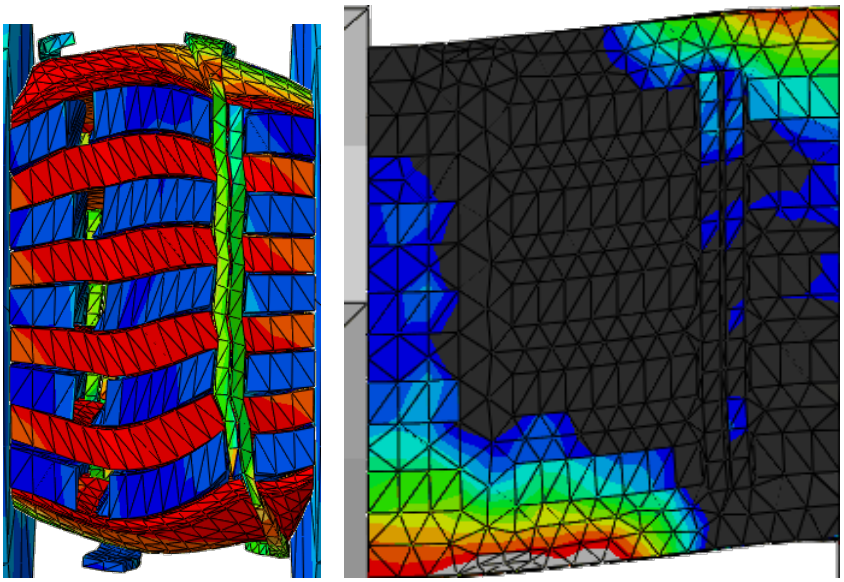

(a) Static (b) Dynamic

Figure 7.29 Comparison of the different computational failure modes predicted.

Chapter 8
Concluding Remarks

3D woven geometry allows development of new complex, integrally bound layers that eliminate the delamination failure modes that plague laminated composite designs. This is accomplished by adding Z-fiber tows (referred to as Z-fibers) woven into the geometry. This fiber addition creates an effective stiffness through the thickness. The fiber addition has minimal influence on the in-plane properties, and also significantly increases shear performance. The overall resistance to failure and damage tolerance is greatly increased, while also localizing damage zones.

The effect of the Z-fiber has been studied experimentally through the use of end notch flexure tests. The insertion of Z-fibers offers large gains in both fracture toughness and also in fracture resistance. The material proved to be effective both statically and dynamically having stable crack growth under different loading conditions. The results showed that at higher loading rates, inertia plays a dominant role in the failure of the specimens, overcoming some of the resistance to fracture toughness. It was additionally found that the architecture of the Z-fiber, and the weaving pattern has a strong correlation to the materials fracture strength and the materials fracture resistance.

The 3DWC was then subjected to blast loading to determine its ability to mitigate shock loading while preventing damage to the entire panel. The shock tests showed the initial failure mode of matrix cracking was directly related to the architecture. Accurate finite element models have been created that are able to predict the response of the panel subjected to shock loading. These models can accurately capture the onset of matrix micro-cracking that occurs in the panels. The models proved to be very useful in predicting the out of plane deformation of the panels. It was also found that the architecture of the Z-fiber played an important role in the shear properties of the material.

The 3DWC material was finally tested using a slit Hopkinson pressure bar (SHPB). The testing showed that the specimens would fail in a shear band that followed the warp and weft fibers, while also shearing some of the fibers in the transverse direction. Tests in the in-plane loading direction showed that the Z-fiber would arrest the crack and damage from further

propagation until more energy was put into the system. A detailed RUC based finite element model was created to capture many of the stress concentrations that occur in the specimen. The model was able to predict the variances in strain due to the fiber tow bundles creating a non-uniform state of strain in the material. The model also showed that due to internal stress wave interactions in the material, wave propagation occurs in a different manner than the incident and transmitted bars show.

Overall, a detailed high strain rate characterization of 3DWC's has been carried out. The results point to many failure mechanisms that are architecture dependent, however there are many architecture dependent mechanisms that enhance the mechanical properties. High strain rate testing facilities have been completely developed and validated, allowing for accurate testing of the materials. Mechanism based models have been developed to simulate the mechanical response, with the incorporation of rate dependent behavior.

8.1 Future Work

The material and techniques described in this dissertation have the potential for new applications and methods of testing.

8.1.1 Shock Loading

The shock tube has been shown to be very beneficial at examining the deflection of 3DWC panels while experiencing a strain rate of about 200 per second. These ranges are historically very difficult to create accurate rate dependent tests. This method may be very beneficial for testing polymers and films to determine their rate dependent behavior. The shock tube also can be tailored to perform shaping of the shock wave or creating a stronger pulse through the use of nozzles. This work would open up a whole new area of shock loading related materials research that would help the field better characterize the response of structural panels to shock loading

A collaboration that I am very interested in pursuing is that with someone interested in biomechanics, to look at how shock waves interact with the human body. By using simulated subjects with ballistics gels, and high speed cameras we can look at how the body will respond to a blast wave.

In most situations, the shock is associated with a blast, and following a blast shrap metal is typically associated as parts fail. These projectiles often cause more harm and damage than the actual blast. The shock tube is an excellent source for studying this problem

because we can create both scenarios at the same time. A projectile could be something as simple as sharp metal (something that would be seen in an explosion) or a cylindrical shaped projectile.

A separate facility with a gas gun could easily be created to fire projectiles and simulate impact and if catastrophic enough, the characteristics of penetration. Such a facility could aid in the simulation of meteorite impact or high velocity impact damage on cellular materials (like metallic and polymer foams).

8.1.2 Woven Composite Finite Element Modeling

Many of the FE models presented only look examined certain aspects of the material. The DCZM elements were aimed at modeling delamination resistance. The shock tube modeling was focused on panel level modeling with the addition of matrix micro-cracking. Each of these models should be extended to include other types of failure. The ENF model should be expanded to include matrix micro cracking on the outside surface of the material and the possibility of a kink band formation. These will reflect more accurately the experimental results of the tests.

The shock tube panel level model should be expanded to include fiber shear failure. This was not done in the present body of work because there is no experimental data to support a finite element formulation. Punch shear tests could be performed to examine the effect of fiber shear. Additionally, laterally constrained compression tests could be performed since fiber shear is the typical failure mode. These could then be expanded into rate dependent behavior though a laterally constrained Hopkinson bar test.

8.1.3 Comparison of Finite Element Models

A detailed comparison of the different finite element models that can be created for RUC testing should be evaluated. Models can be created from both idealized architecture, microCT scans and additionally a woven model produced through a weaving simulation. These models should then have the same parameters used as inputs and while the outputs of the models can be compared against each other and against experimental results. The MicroCT and Woven model should be better at predicting failure. This is a computationally intensive process.

Appendices

Appendix A
Void content determination procedure

A.1 Equipment

The following items are needed for this procedure

Latex gloves, large tweezers, small beaker half full of RT tap water, long stem Q-tip (for wiping bubbles), lab balance with water immersion kit, 1 crucible per specimen, acetone, fine grit sand paper

A.2 Weight Measurements Procedure

1: Lightly sand and de-burr all specimens. Wipe clean with acetone and place in dust-free storage. Allow enough time for air moisture to re-condense on the specimen.

2: Gather 1 crucible for each specimen. Each crucible needs an identification mark that will survive the furnace cycle. Clean with acetone and place in dust-free storage. Allow enough time for air moisture to re-condense on the crucible.

3: Find a lab balance with a water immersion setup kit, including a thermometer to measure the water temp.

4: Fill the balance beaker with enough water so that, when immersed the specimen will be ", but no less than 1/8" from the surface.

5: The water should be equilibrated to RT. Record the density of water at RT (for example at 23C it is 0.9976 g/cc).

6: Tare the balance and measure the dry crucible weight.

7: Mark each specimen to match it's crucible identification. Place the specimen in the crucible and measure the combined weight (or tare the balance and weigh the specimen directly).

8: Remove the crucible, tare the balance, swish the specimen in the side beaker of water to pre-wet it. Place the specimen in the immersion pan, and look carefully for air bubbles. Tap the pan gently to dislodge bubbles. Record the weight. It is important to remove all air bubble on both the specimen and the pan.

9: Repeat 6-8 for each specimen. It is especially important to re-tare the balance if specimens differ in size.

10: Place each crucible and specimen into the muffle furnace and heat to 1050F (565C). Once at 1050F, soak for at least 4 hours.

11: Allow to completely cool to RT.

12: Tare the balance and record the combined weight of the crucible and bare fiber.

A.3 Fiber, Resin, and Void Content Calculations

1: using an EXCEL spreadsheet set up to calculate the fiber, resin, and void contents, enter the data under each heading.

2: The composite density is

$$\rho_{composite} = \frac{M_{dry}}{M_{dry} - M_{wet}} * \rho_{water} \tag{A.1}$$

3: The fiber weight is the weight remaining after burnout

4: The Resin weight is the

$$M_{resin} = M_{dry} - M_{fiber} \tag{A.2}$$

5: The fiber volume fraction is

$$V_{fiber} = \frac{\frac{M_{fiber}}{\rho_{fiber}}}{\frac{M_{composite}}{\rho_{composite}}} * 100 \tag{A.3}$$

6: The matrix volume fraction is

$$V_{matrix} = \frac{\frac{M_{matrix}}{\rho_{matrix}}}{\frac{M_{composite}}{\rho_{composite}}} * 100 \tag{A.4}$$

7: The void volume fraction is

$$V_{void} = 100 - V_{fiber} - V_{matrix} \tag{A.5}$$

Appendix B

CCM model for fiber tow properties.

In order to obtain the homogenized material properties of the axial fiber tow, several assumptions are made. The axial fiber tows were treated as one entitity with the assumption of transverse isotropy. That is, the axial fiber tows are assumed to be 3-D space undulating curved 3D solids. The CCM relation for the elastic constants are as follows;

The axial modulus is defined as

$$E_1 = E_1^f(1+\gamma)V^f + E^m(1+\delta)(1-V^f) \tag{B.1}$$

where

$$\gamma = \frac{2\nu_{21}^f E^m(1-\nu_{23}^f - 2\nu_{12}^f\nu_{21}^f)V^f(\nu_{12}^f - \nu^m)}{E_2^f(1+\nu^m)(1+V^f(1-2\nu^m)) + E_m(1-\nu_{23}^f - 2\nu_{12}^f\nu_{21}^f)(1-V^f)} \tag{B.2}$$

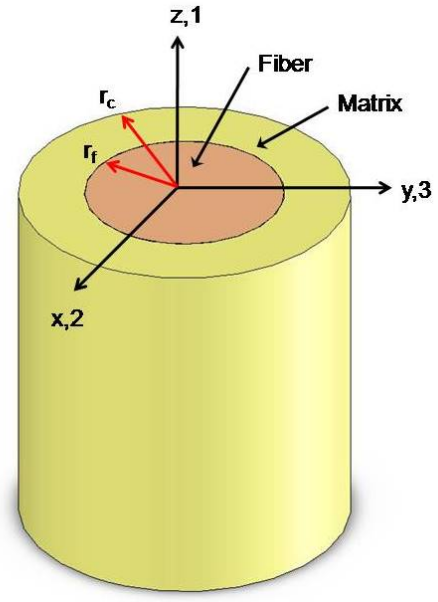

Figure B.1 A sketch of the concentric cylinder model. Fiber volume fraction $V_f = \frac{r_f^2}{r_c^2}$

$$\delta = \frac{2E_2^f \nu^m V^f (\nu^m - \nu_{12}^f)}{E_2^f (1+\nu^m)(1+V^f(1-2\nu^m)) + E_m(1-\nu_{23}^f - 2\nu_{12}^f \nu_{21}^f)(1-V^f)} \tag{B.3}$$

The transverse modulus is defined as

$$E_2 = \frac{1}{\frac{\eta^f V^f}{E_2^f} + \frac{\eta^m (1-V^f)}{E^m}} \tag{B.4}$$

$$E_3 = E_2 \tag{B.5}$$

where,

$$\eta^f = \frac{E_1^f V^f + \left[(1-\nu_{12}^f \nu_{21}^f)E^m + \nu^m \nu_{21}^f E_1^f\right](1-V^f)}{E_1^f V^f + E^m(1-V^f)} \tag{B.6}$$

$$\eta^m = \frac{[(1-\nu^{m^2})E_1^f - (1-\nu^m \nu_{12}^f)E^m]V^f + E^m V^m}{E_1^f V^f + E^m(1-V^f)} \tag{B.7}$$

Poisson's ratio can be obtained from

$$\begin{aligned} \nu_{12} \quad = \quad & \frac{[(1-V^f)(1-\nu_{23}^f - 2\nu_{12}^f \nu_{21}^f)]\nu^m E^m}{((1-V^f)(1-\nu_{23}^f - 2\nu_{12}^f \nu_{21}^f))E^m + (1+V^f + (1-V^f)\nu^m - 2V^f \nu^{m^2})E_2^f} \\ & + \frac{[\nu^m + V^f(2\nu_{12}^f - \nu^m) + (\nu^{m^2}(1-2V^f \nu_{12}^f - V^f))]E_2^f}{((1-V^f)(1-\nu_{23}^f - 2\nu_{12}^f \nu_{21}^f))E^m + (1+V^f + (1-V^f)\nu^m - 2V^f \nu^{m^2})E_2^f} \end{aligned}$$

The shear modulus is

$$G_{12} = G^m \left[\frac{(G^m + G_{12}^f) - V^f(G^m - G_{12}^f)}{(G^m + G_{12}^f) + V^f(G^m - G_{12}^f)}\right] \tag{B.8}$$

Although G_{23} can not be solved for explicitly, the widely accepted expression for this term is

$$G_{23}^* = \frac{1}{\frac{\frac{1}{G_{23}^f} V^f + \eta_4 \frac{1}{G^m}(1-V^f)}{V^f + \eta_4(1-V^f)}} \tag{B.9}$$

where,

$$\eta_4 = \frac{3 - 4\nu^m + \frac{G^m}{G_{23}^f}}{4(1-\nu^m)} \tag{B.10}$$

A more involved iterative technique can be used which is

$$\frac{V^f k_{23}^f}{k_{23}^f + G_{23}^{**}} + \frac{(1-V^f)k^m}{k^m + G_{23}^{**}} = 2\left(\frac{(V^f G^m}{G^m - G_{23}^{**}} + \frac{((1-V^f)G_{23}^f}{G_{23}^f - G_{23}^{**}}\right) \tag{B.11}$$

where k^m is the bulk modulus of the matrix and the fiber constants can be solved for as follows.

$$k_{23}^f = \frac{1}{2}(C_{22}^f + C_{23}^f) \tag{B.12}$$

$$C_{22}^f = \frac{(1-\nu_{12}^f \nu_{21}^f)E_2^f}{1-2\nu_{12}^f \nu_{21}^f - \nu_{23}^{f^2} - 2\nu_{12}^f \nu_{21}^f \nu_{23}^f} \tag{B.13}$$

$$C_{23}^f = \frac{(\nu_{23}^f + \nu_{12}^f \nu_{21}^f)E_2^f}{1-2\nu_{12}^f \nu_{21}^f - \nu_{23}^{f^2} - 2\nu_{12}^f \nu_{21}^f \nu_{23}^f} \tag{B.14}$$

The Poission's ratio in the plane of isotropy can be solved for as follows

$$\nu_{23} = \frac{E_2}{2G_{23}} - 1 \tag{B.15}$$

Here, the subscripts f and m refer to the fiber and matrix phases.E represents the modulus, G the shear modulus, V the volume fraction, ν poisson's ratio. The 1 axis is in the fiber direction and the CCM model and fiber tow are shown in Figure B.1.

Appendix C
Split Hopkinson Pressure Bar

C.1 1-D Wave Analysis

In the SHPB test method, specimens are situated between two strain gauged bars, an incident and a transmitted bar, see figure C.1. A third striker bar is fired into the incident bar to create a strain pulse that will travel through the bar and into the specimen. When the pulse reaches the specimen, a fraction of it gets transmitted through the specimen into the transmitted bar, while the the rest is reflected back into the incident bar due to the material mismatch, see figure C.2. The length of the striker bar can be used to control the pulse characteristics.

A detailed derivation of the one dimensional wave theory used to arrive at the equations for stress, strain and strain rate can be found in ref [88, 89]. The 1-D theory makes several simplifying assumptions, all of which become increasingly accurate as the bar diameter becomes infinitesimally small, and the bars are uniform in diameter with a circular-cylindrical cross-section. For the sake of brevity, only the pertinent equations will be presented here. Based on the data collected from the two strain gauges, the incident strain ε_I, the reflected strain ε_R, and the transmitted strain ε_T, are,

$$\sigma_s(t) = \frac{E_{bar}}{2}\frac{D_{bar}^2}{D_s^2}[\varepsilon_I(t) + \varepsilon_R(t) + \varepsilon_T(t)] \tag{C.1}$$

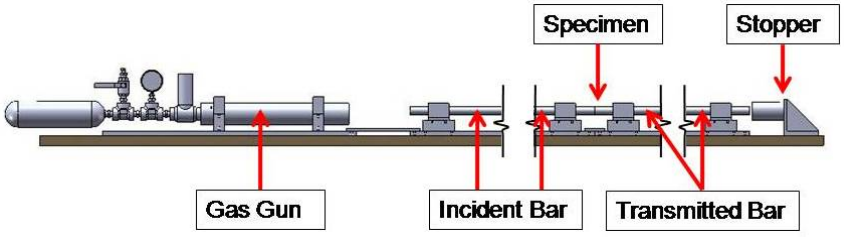

Figure C.1 Experimental Setup of Split Hopkinson Pressure Bar

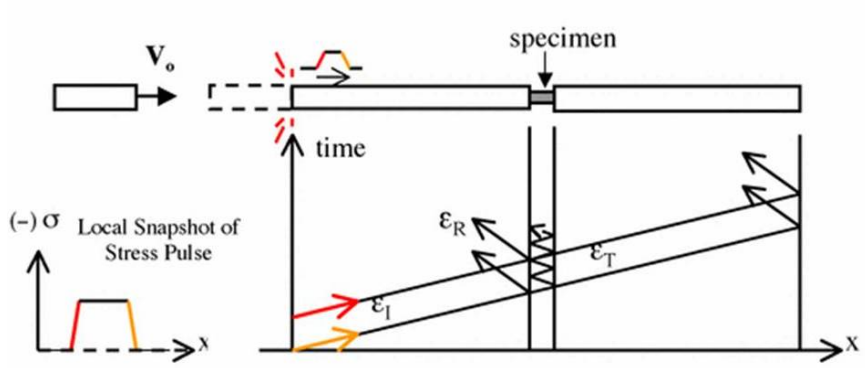

Figure C.2 Schematic X-T Diagram of incident, reflected and transmitted waves in SHPB

$$\frac{d\varepsilon_s(t)}{dt} = -\frac{C_o}{L_s}[\varepsilon_T(t) - \varepsilon_I(t) + \varepsilon_R(t)] \tag{C.2}$$

$$\varepsilon_s(t) = -\frac{C_o}{L_s}\int[\varepsilon_T(t) - \varepsilon_I(t) + \varepsilon_R(t)] \tag{C.3}$$

In equations C.1-C.3, the variables E_{bar}, D_{bar}, D_s, L refer to the Young's Modulus and diameter of the pressure bars and the diameter and length of the specimen, respectively. The variable C_o refers to the wave velocity in the pressure bar calculated from the following equation.

$$C_o = \sqrt{\frac{E_{bar}}{\rho_{bar}}} \tag{C.4}$$

In the case that the specimen deforms uniformly, the strain in the incident and reflected pulses sum up to equal the strain present in the transmitted pulse.

$$\varepsilon_I(t) + \varepsilon_R(t) = \varepsilon_T(t) \tag{C.5}$$

Applying this simplification to equations C.1-C.3 creates simplified relations for the specimen stress, strain rate and strain as can be seen in the following equations

$$\sigma_s(t) = E_{bar}\frac{D_{bar}^2}{D_s^2}\varepsilon_T(t) \tag{C.6}$$

$$\frac{d\varepsilon_s(t)}{dt} = -2\frac{C_o}{L_s}\varepsilon_R(t) \tag{C.7}$$

$$\varepsilon_s(t) = -2\frac{C_o}{L_s}\int\varepsilon_R(t) \tag{C.8}$$

From these equations, the stress-strain history of the specimen can be obtained for high rates of strain.

C.2 Experimental Setup

The incident and transmitted bars are made from case hardened steel. The incident bar measures 2.438 m long, while the transmitted bar is 1.778 m long and the striker bar is 305 millimeters long. The incident and transmitted bars are 38 mm in diameter while the striker bar is 50.8 mm in diameter.Table C.1 provides mechanical properties of the bar material. Pulse shapers in the form of indented brass disks were placed on the front of the Hopkinson bar to create more of a square wave instead of the spike that would normally be seen when using just the impact. A typcial impact test will produce strain time history curves that are similar to those seen in figure C.3.

Table C.1 Physical Properties of Incident and Transmitted Bars

Material	440C Stainless Steel
Density	7620 $\frac{Kg}{m^3}$
Young's Modulus	220 GPa
Ultimate Tensile Strength	1965 MPa
Brinell Hardness	580

C.2.1 Data Analysis

A method for eliminating the effects of dispersion has been implemented into the data processing. This is based on the correction methods presented by Kaiser [89] and Corham [90, 91] and based on tabulated data, courtesy of Bancroft [92].

Additional considerations need to be taken into account to determine the beginning and end points of the strain pulses. A numerical method for the identification of the start and end points of strain pulses is described in [89]. This method is devoid of human interpretation as it depends strictly on the data collected and the prescribed algorithm. The authors chose a method presented in [93] for data processing. It uses a series of steps to determine the starting points of the transmitted and reflected waves. Using a theoretical approximation of the transmitted wave velocity, based on one-dimensional wave theory and an assumption of the expected Young's modulus of the specimen, the starting point of the transmitted wave can be identified, since the early linear portions of the theoretical and experimental waves should be in agreement. By establishing an equilibrium solution for the specimen based

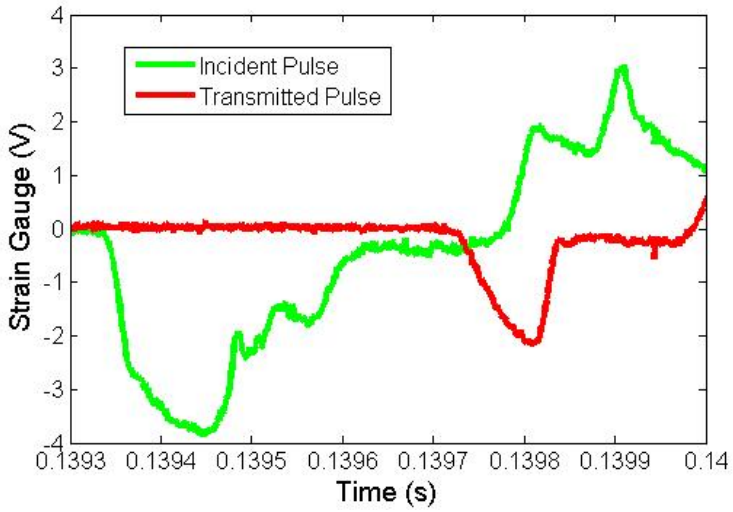

Figure C.3 A strain vs. time diagram of the two strain gauge pulses from the incident and transmitted bars. This test has a clear point of failure in the transmitted pulse

on the incident and transmitted pulses, a theoretical reflected wave can be solved for and compared with experimental data to establish the beginning and end points of the reflected wave. More details of this method are given in [93].

C.2.2 Stress Equilibrium

A critical assumption in the SHPB technique is that of stress equilibrium in the sample. There are many different techniques for determining stress equilibrium. The two main methods are, (1) a theoretical force balance compared to the experimental, and (2) a time derivation from the wave equation. Both methods are employed in the present analysis and will be described here. The dynamic force balance has been derived by others and will not be reproduced here, for further information see references [94, 93].

A secondary check on stress equilibrium can be made by estimating the time required as a function of the number of reflected waves. Historically, the method chosen for this check is based on wave propagation theory [95, 96, 94] and produces the following equation,

$$t_{equilibrium} = \frac{nL_s}{c_s} \tag{C.9}$$

where L_s and c_s are the length and speed of sound in the specimen respectively. The

parameter n is the number of times the wave is reflected in the specimen. Classically it is assumed that $n = 4$, based on experimental results. A better approximation based on the Taylor-Von Karman theory [78] for plastically deforming solids produces the following equation.

$$t_{equilibrium} \geq \sqrt{\frac{\pi^2 \rho_s L_s^2}{\frac{\partial \sigma}{\partial \varepsilon}}} \tag{C.10}$$

where, the material properties are related to the specimen. This equation was plotted for various materials, see figure C.4. It can be seen that softer materials take a much longer time to reach dynamic stress equilibrium than stiffer materials of the same specimen geometry. Additionally shorter specimens reach equilibrium much faster in SHPB testing. Both methods have been evaluated in connection with the present study and the theoretically predicted time to equilibrium will be plotted along with experimental data.

A final means to determine the stress equilibrium is through DIC measurements that will provide the user with a full strain field of the specimen. This will eliminate a lot of the guessing work and also allow us to validate the 1-D theory assumption.

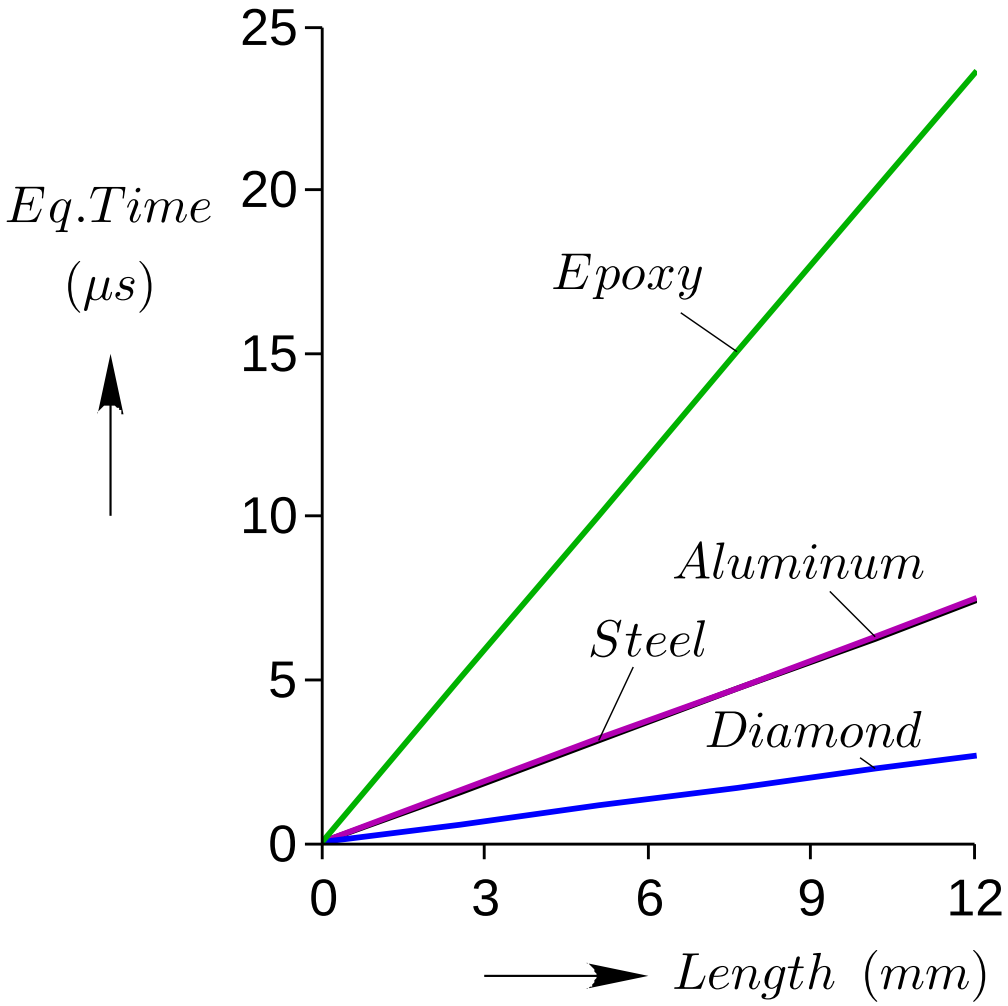

Figure C.4 Equilibrium Time vs. length for various different materials

Appendix D

Shock Tube

The purpose of a shock tube is to propagate large amplitude one-dimensional waves in a controlled fashion. It generally consists of two chambers, the driver section and the driven section, separated by a disposable diaphragm. The low-pressure region is labeled "1" while the high pressure region is labeled "4", as shown in figure D.1 below. Each of the two chambers is filled with a gas. In our experiments, P_1 is going to be filled with air and will be held at 14.7 psi (1 atmosphere) while P_4 will be varied from 100 to 4000 psi. The lower than standard atmospheric pressure in P_1 is accomplished by using a vacuum pump. The purpose of the diaphragm is to keep the gases filled in the two chambers separate till the desired pressure is reached.

The operation of the shock tube involves bursting the diaphragm at the desired pressure by pressuring the driver section till it bursts. The pressure difference at which the diaphragm bursts can be controlled by changing the thickness of the diaphragm, by using one made of a different material or by creating a scribe mark in the center of the diaphragm. The details of the diaphragm will be described later in this appendix.

When the diaphragm ruptures and a shock wave is produced, the shock tube is divided into four distinct regions as shown in figure D.2. Regions 1 and 4 retain their original properties for a while as it takes a finite amount of time for the shock wave to travel from one end of the driven section to the other with a velocity of c_s. Region 3 consists of the originally high pressure gas through which the shock wave has just passed which is the same gas as region 4 but at a different thermodynamic state. Similarly, region 2 consists of the

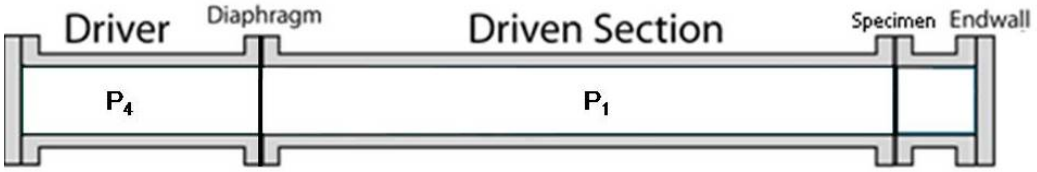

Figure D.1 State of the Shock tube when t = 0

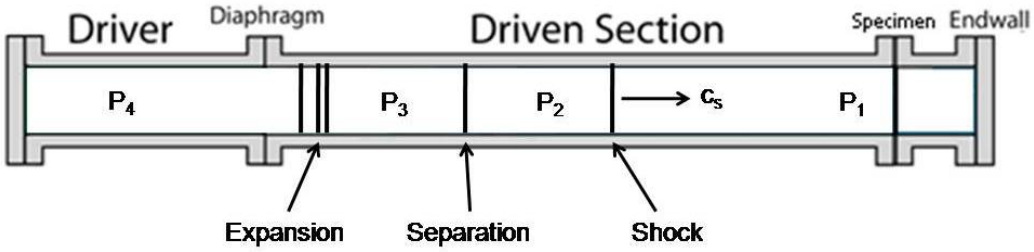

Figure D.2 State of the Shock tube when t > 0

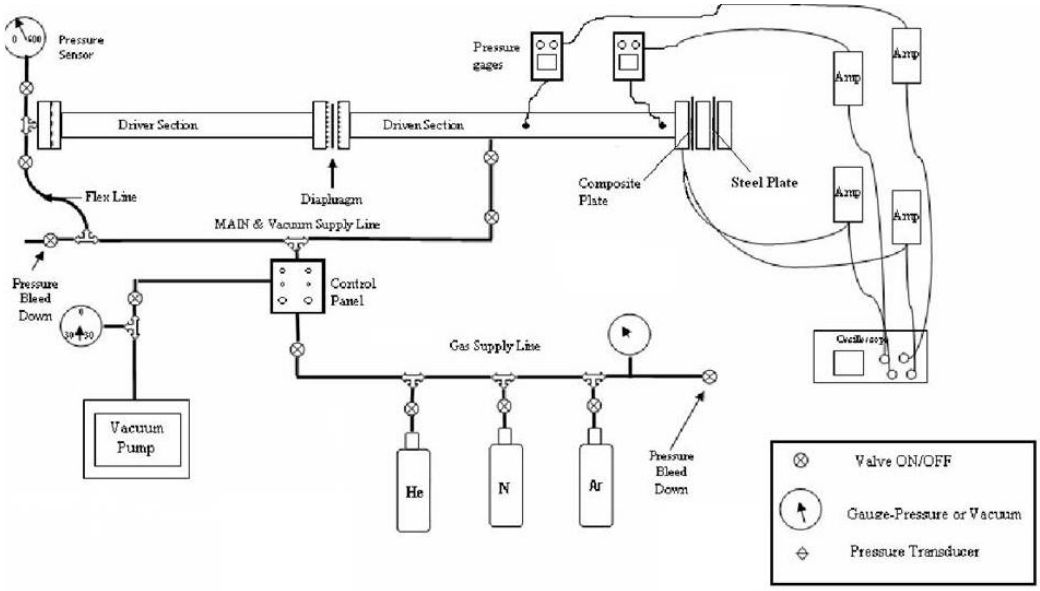

Figure D.3 Experimental setup of the Shock tube

originally low pressure gas as region 1, through which the shock has just passed. It is also at a different thermodynamic state than region 1.

Once the shock wave reaches the other end of the driven section, it gets reflected giving rise to a very high pressure in that region. It is this pressure (referred to in our calculations as P_5) that our composite specimen, which is clamped at that location, will be subjected to.

Figure D.3 shows the experimental setup for the tests. A selected gas tank is connected to the driver section through the control panel which is also connected to a vacuum pump. The panel is used to bleed the gases in the two sections after each test. The plate to be tested is tightly fastened to the mounting flange on the containment section. The tubes from the control panel are connected to the driver section through a valve and a pressure sensor (which is meant to measure P_4). Two pressure transducers are attached two meters apart in the driven section of the tube (ensuring that one of them is as close to the plate as possible). Having them positioned this way enables us to calculate the wave speed of the shock. The

readings of the pressure transducers are fed to the oscilloscope using a signal conditioner. Two high speed Photron SA.5 cameras are using to perform optical measurements in the DIC software ARAMIS.

D.1 Pressure and Mach number Calculations for the Shock Waves Produced

The following equations were used in a MATLAB code to relate the different shock tube parameters:

$$r_4 = r_2 \left[1 - \frac{(\gamma_1 - 1)(a_1/a_4)(r_2 - 1)}{\sqrt{2\gamma_1[2\gamma_1 + (\gamma_1 + 1)(r_2 - 1)]}} \right]^{\frac{-2\gamma_4}{\gamma_4 - 1}} \tag{D.1}$$

Where

$$r_i = \frac{P_i}{P_1} \tag{D.2}$$

r_4 = Pressure ratio between region 4 and region 1
r_2 = Pressure ratio between region 2 and region 1
γ_4 = ratio of specific heats for the gas in section 4
γ_1 = ratio of specific heats for the gas in section 1
a_1 = Speed of sound in gas 1
a_4 = Speed of sound in gas 4

$$a_g = \sqrt{\gamma RT} \tag{D.3}$$

R = The ideal gas constant (8314 J mol K $^{-1}$) divided by the molecular weight of the gas in grams
T = Temperature of the gas in degrees Kelvin

$$M_s = \sqrt{\frac{\gamma_1 + 1}{2\gamma_1}(r_2 - 1) + 1} \tag{D.4}$$

M_s = Mach number of the shockwave produced

Where γ_1 is used because this is the medium which the shockwave propagates into

$$A = \frac{M_s}{M_s^2 - 1}\sqrt{1 + \frac{2(\gamma_1 - 1)}{(\gamma_1 + 1)^2}\left(\gamma_1 + \frac{1}{M_s^2}\right)}(M_s^2 - 1) \tag{D.5}$$

$$M_r = \frac{1 + \sqrt{1 + 4A^2}}{2A} \tag{D.6}$$

M_r = Mach number of the reflected shockwave Assumes that the gases don't have enough time to mix, therefore it is still traveling through the air.

$$r_{52} = \frac{r_5}{r_2} = 1 = \frac{(M_r^2 - 1)2\gamma_1}{(\gamma_1 + 1)} \tag{D.7}$$

$$r_{54} = \frac{r_5}{r_4} = r_{52}\frac{r_2}{r_4} \tag{D.8}$$

$$r_5 = r_{52}r_2 \tag{D.9}$$

$$\frac{T_2}{T_1} = \frac{1 + \dfrac{\gamma_1 - 1}{\gamma_1 + 1}r_2}{1 + \dfrac{\gamma_1 - 1}{\gamma_1 + 1}\dfrac{1}{r_2}} \tag{D.10}$$

D.2 Burst Pressure for Mylar Diaphragms

It was determined that the best procedure for producing repeatable shock pressures with out the possibility of producing a projectile, mylar would be used as the diaphragm material. By layering the various different sheets of material we were able to produce very repeatable shock pressures that produced a difference of about 100 psi per sheet of mylar. The mylar was 0.07 inches thick and was all purchased from the same manufacture to ensure that we would have repeatable data. The experimental tests were tabulated in figure D.4 and it was

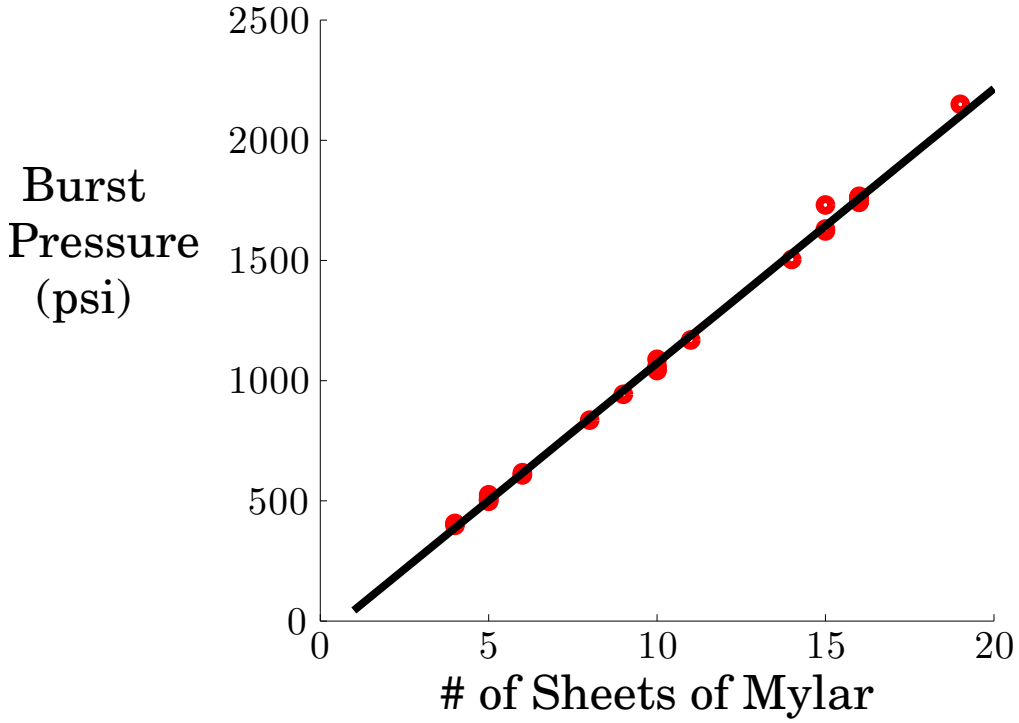

Figure D.4 Burst Pressure vs. Number of Sheets of Mylar

found that there was a linear trend to the data.

$$\text{Burst Pressure} = 114.28 psi * \text{\# of sheets} - 70.331 psi \tag{D.11}$$

Appendix E

VUSDLFD for plate failure

```
c User subroutine VUSDFLD for user-defined fields

      subroutine vusdfld(
c Read only -
     *    nblock, nstatev, nfieldv, nprops, ndir, nshr,
     *    jElemUid, kIntPt, kLayer, kSecPt,
     *    stepTime, totalTime, dt, cmname,
     *    coordMp, direct, T, charLength, props,
     *    stateOld,
c Write only -
     *    stateNew, field )

      include 'vaba_param.inc'

      dimension props(nprops),
     *          jElemUid(nblock), coordMp(nblock, *),
     *          direct(nblock, 3, 3), T(nblock,3,3),
     *          stateOld(nblock, nstatev),
     *          stateNew(nblock, nstatev),
     *          field(nblock, nfieldv)
      character*80 cmname
c Properties array
c     props(1) -> Transverse tensile strength, Yt
c     props(2) -> Matreix compressive strength, Yc
c     props(3) -> Ply shear strength, Sc
c     props(4) -> Fiber buckling strength, Xc
c     props(5) -> Initial shear modulus, G12
```

```
c      props(6) -> Nonlinear shear factor, alpha

       character*3 cData(maxblk*6)
       dimension jData(maxblk*6)
       dimension stress(maxblk*6),strain(maxblk*6)
c Read properties
       yt     = props(1)
c       yc     = props(2)
c       sc     = props(3)
c       xc     = props(4)
c       g12    = props(5)
c       alpha = props(6)
c Get stresses and strains from previous increment
c       jStatus = 1
c       call vgetvrm( 'S', stress, jData, cData, jStatus )
       jStatus = 1
       call vgetvrm( 'LE', strain, jData, cData, jStatus )

       call evaluateDamage( nblock, nstatev,
     *      nfieldv, ndir, nshr,
     *      yt,
     *      stress, strain,
     *      stateOld,
     *      stateNew, field )
c
       return
       end

       subroutine evaluateDamage ( nblock, nstatev,
     *      nfieldv, ndir, nshr,
     *      yt,
     *      stress, strain,
     *      stateOld,
     *      stateNew, field )

       include 'vaba_param.inc'
```

```
      dimension stress(nblock,ndir+nshr),
     *      strain(nblock,ndir+nshr),
     *      stateOld(nblock,nstatev),
     *      stateNew(nblock,nstatev),
     *      field(nblock,nfieldv)
c
c initialize failure flags from statev.
      do k = 1, nblock
         stateNew(k,1) = stateOld(k,1)
c          stateNew(k,2) = stateOld(k,2)
c          stateNew(k,3) = stateOld(k,3)

         em     = stateOld(k,1)
c          efs    = stateOld(k,2)
c          damage = stateOld(k,3)
c
         e11 = strain(k,1)
         e22 = strain(k,2)
*
         e12 = 2.0*strain(k,4) !e12 is engineering strain
c
c damage index: = 0 if no strain to prevent divide by zero
c
c          damage = 0.d0
c          if (e12.ne.0)
c     *         damage = (3.d0*alpha*g12*e12**2-2.d0*alpha*(e12**3)/e12
c     *                  (1.d0+3.d0*alpha*g12*s12**2)
c
C          f1 = e12**2/(2.d0*g12) + 0.75d0*alpha*e12**4
C          f2 = sc**2 /(2.d0*g12) + 0.75d0*alpha*sc**4
c
c matrix tensile/compressive failure
         if (em .lt. 1.d0) then
            if (e22 .lt. 0.d0) then
               em = (e22/yt)
```

```
            else
               em = (e22/yt)
            endif
            stateNew(k,1) = em
         endif
c
c fiber-matrix shear failure
c         if (efs .lt. 1.d0) then
c            if (e11 .lt. 0.d0) then
c               efs = sqrt((e11/xc)**2 + f1/f2)
c            else
c               efs = 0.d0
c            endif
c            stateNew(k,2) = efs
c         endif
c
c state transition diagram
c
c fv1: matrix compr/tens failure
c fv2: fiber/matrix shear failure
c fv3: material damage (shear nonlinearity)
c                            fv1  fv2  fv3       e1   e2   nu12
g12
c
c (0) no failure              0    0    0  -->  e1   e2   nu12
g12
c (1) matrix (compr/tens)     1    0    0  -->  e1    0    0
g12
c (2) fib/mtx shear           0    1    0  -->  e1   e2    0
0
c (3) matrix & f/m shear      1    1    0  -->  e1    0    0
0
c (4) pure damage             0    0    1  -->  e1   e2   nu12
0
c (5) mtrx & damage           1    0    1  -->  e1    0    0
0
```

```
c (6) f/m shear & damage       0     1     1 --> e1   e2    0
0
c (7) mtrx, f/m shr & damage   1     1     1 --> e1    0    0
0
c
c      update field variables
c
          field(k,1) = 0.d0
c          field(k,2) = 0.d0
          if (em .ge. 1.d0) then
             field(k,1) = 1.d0
          end if
c         if (efs .ge. 1.d0) then
c             field(k,2) = 1.d0
c          end if
c          field(k,3) = damage
c          stateNew(k,3) = field(k,3)
       end do

       return
       end
```

Appendix F
RUC FE Models

Steps for importing 3D cad model

1: Draw 3D model in SolidWorks

2: Save file as *.step (STEP 214 file type)

3: Open ABAQUS CAE and create a new project

4: File $\rightarrow$ Import $\rightarrow$ Part

5: Choose to Import all parts, keep topology as solid

6: Go to Assembly module

7: Build Assembly, select all parts, independent mesh on instance and don't auto offset.

8: Merge Cut instances

9: Choose to retain intersecting boundaries, supress or delete instances

10: Now you have one part with boundaries, ensure that no errors were created and use only this one part now.

11: Assign Material Properties

12: Assign sections to regions

13: Create Datum Axis by 3pt. axis selection.

14: Property $\rightarrow$ assign material orientation

15: Select Datum CYS list to pick coordinate system you just created

16: Mesh using Quad Tet Elements

17: Create sets of each constituent

18: write input file

To assign orientations to complex geometry tows

1: Write node set to .txt file

2: Create spline using ABAQUS coordinate system for tow

3: Look up which elements are used in the tow

4: Copy element definition to tow .txt file

5: If an element is not found it will be defaulted to general coordinate system.

6: Run MATLAB code output will be written to new .txt file

7: Copy data from new file into your INPUT File for coordinate orientation

8: Import INP file back into MATLAB and save again to work on in CAE.

Bibliography

[1] H.J. Huang. *In-Plane response and Mode II fracture response of Z-Pin woven laminates*. PhD thesis, University of Michigan, 2008.

[2] T.S. Chou and F.K. Ko. *Composite Materials Series: Volume 3: Textile Structural Composites*, volume 3 of *Composite Materials Series*. Elsevier, 1989.

[3] R. Kamiya, B.A. Cheeseman, P. Popper, and T.W. Chou. Some recent advances in the fabrication and design of three-dimensional textile preforms: a review. *Composites Science and Technology*, 60:33–47, 2000.

[4] M. Awais and U.N. Butt. 3d preforms in the world of composites-a review. National Textile University, Faisalabad, Pakistan.

[5] D. Stobbe and M. Mohamed. 3d woven composites: cost and performance viabiliity in comercial applications. In *48 th International SAMPE symposium*. SAMPE, 2003.

[6] A.P. Mouritz, M.K. Bannister, P.J. Falzon, and K.H. Leong. Review of applications for advanced three-dimensional fibre textile composites. *Composites: Part A*, 30:1445–1461, 1999.

[7] Susan Rush. The art of armor development. *High-Performance Composites*, pages 22–26, January 2007.

[8] C.F. Yen and A.A. Caiazzo. 3d woven composites for new and innovative impact and penetration resistant systems. Technical Report MSC TPR 1015/CD01, U.S. Army Research Office, July 2001.

[9] B. Lee, K.H. Leong, and I. Herszberg. Effect of weaving on the tensile properties of carbon fibre tows and woven composites. *Journal of Composite Materials*, 20:652–670, 2001.

[10] L. Lv, B. Sun, Y. Qiu, and B. Gu. Energy absorptions and failure modes of 3d orthogonal hybrid woven composite struck by flat-ended rod. *Polymer Composites*, pages 410–416, 2006.

[11] H. Gu and Z. Zhili. Tensile behavior of 3d woven composites by using different fabric structures. *Materials and Design*, 3:671–674, 2002.

[12] P.J. Callus, A.P. Mouritz, M.K. Bannister, and K.H. Leong. Tensile properties and failure mechanisms of 3d woven grp composites. *Composites: Part A*, 30:1277–1287, 1999.

[13] P. Tan, L. Tong, G.P. Steven, and T. Ishikawa. Behavior of 3d orthogonal woven cfrp composites part i. experimental investigation. *Composites: Part A*, 31:259–271, 2000.

[14] B.N. Cox, M.S. Dadkhah, and W.L. Morris. On the tensile failure of 3d woven composites. *Composites: Part A*, 27A:447–458, 1996.

[15] L. Lee, S. Rudov-Clark, A.P. Mouritz, M.K. Bannister, and I. Herszberg. Effect of weaving damage on the tensile properties of three-dimensional woven composites. *Composite Structures*, 57:405–413, 2002.

[16] K.H. Leong, B. Lee, I. Herszberg, and M.K. Bannister. The effect of binder path on the tensile properties and failure of multilayer woven cfrp composites. *Composites Science and Technology*, 60:149–156, 2000.

[17] J.P. Quinn, A.T. McIlhagger, and R. McIlhagger. Examination of the failure of 3d woven composites. *Composites: Part A*, 39:273–283, 2008.

[18] H. Huang and A.M. Waas. Compressive response of z-pinned woven glass fiber textile composite lamintes: Experiements. *Composites Science and Technology*, 69:2331–2337, 2009.

[19] M. Pankow, A.M. Waas, C.F. Yend, and S. Ghiorse. A new lamination theory for layered textile composites that account for manufacturing induced effects. *Composites Part A: Applied Science and Manufacturing*, 40(12):1991–2003, 2009.

[20] B.N. Cox and M.S. Dadkhah. The macroscopic elasticity of 3d woven composites. *Journal of Composite Materials*, 29:785–819, 1995.

[21] S.Z. Sheng and S. van Hoa. Modeling of 3d angle interlock woven fabric composites. *Journal of Thermoplastic Composite Materials*, 16:45–58, 2003.

[22] P. Tan, L. Tong, and G.P. Steven. Behavior of 3d orthogonal woven cfrp composites. part ii. fea and analytical modeling approaches. *Composites: Part A*, 31:273–281, 2000.

[23] J. Quinn, R. McIlhager, and A.T. McIlhagger. A modified system for design and analysis of 3d woven preforms. *Composites: Part A*, 34:503–509, 2003.

[24] B.N. Cox. Delamination and buckling in 3d composites. *Journal of Composite Materials*, 28:1114–1126, 1994.

[25] P. Tan, L. Tong, and G.P. Steven. Modelling approaches for 3d orthogonal woven composites. *Journal of Composite Materials*, 17:545–577, 1998.

[26] P. Tan and G.P. Steven. Modelling for predicting the mechanical properties of textile composites - a review. *Composites: Part A*, 28A:903–922, 1997.

[27] T. Zeng, L.Z. Wu, and L.C. Guo. Mechanical analysis of 3d braided composites: a finite element model. *Composite Structures*, 64:399–404, 2004.

[28] A. Shahkarami and R. Vaziri. A continuum shell finite element model for impact simulation of woven fabrics. *Internationl Journal of Impact Engineering*, 34:104–119, 2007.

[29] M.A. McGlockton, B.N. Cox, and R.M. McMeeking. A binary model of textile composites: Iii high failure strain and work of fracture in 3d weaves. *Journal of the Mechanics and Physics of Solids*, 51:1573–1600, 2003.

[30] L.E. Schwer and R.G. Whirley. Impact of a 3d woven textile composite thin panel: Damage and failure modeling. *Mechanics of Composite Materials and Structures*, 6:9–30, 1999.

[31] K.H. Ji and S.J. Kim. Dynamic direct numerical simulation of woven composites for low-velocity impact. *Journal of Composite Materials*, 41:175–200, 2007.

[32] S.C. Quek, A.M. Waas, K.W. Shahwan, and V. Agaram. Compressive response and failure of braided textile composites: Part 1 - experiments. *International Journal of Non-Linear Mechanics*, 39:649–663, 2004.

[33] S.C. Quek, A.M. Waas, K.W. Shahwan, and V. Agaram. Compressive response and failure of braided textile composites: Part 2 - computations. *International Journal of Non-Linear Mechanics*, 39:649–663, 2004.

[34] S.C. Quek and A.M. Waas. Micromechanical analyses of instabilities in braided glass textile composites. *AIAA Journal*, 41:2069–2076, 2003.

[35] C. Herakovich. *Mechanics of Fibrous Composites*. McGraw-Hill, New York, 2 edition, 1998.

[36] S. Song. *Compression Response of Tri-Axially Braided Textile Composites*. PhD thesis, University of Michigan, 2007.

[37] Michal Sejnoha and Jan Zeman. Micromechanical modeling of imperfect textile composites. *International Journal of Engineering Science*, 46:513–526, 2008.

[38] N.K. Naik, P. Shrirao, and B.C.K. Reddy. Ballistic impact behaviour of woven fabric composites: Formulation. *International Journal of Impact Engineering*, 32:1521–1552, 2006.

[39] B. Sun, H. Hu, and B. Gu. Compressive behavior of multi-axial multi-layer warp knitted (mmwk) fabric composite and various strain rates. *Composite Structures*, 78:84–90, 2007.

[40] J.N. Baucom, M.A. Zikry, and A.M. Rajendran. Low-velocity impact damage accumulation in woven s2-glass composite systems. *Composites Science and Technology*, 66:1229–1238, 2006.

[41] J.N. Baucom and M.A. Zikry. Low-velocity impact damage progression in woven e-glass composite systems. *Composites: Part A*, 36:658–664, 2005.

[42] T. Ogasawara, T. Ishikawa, T. Yokozeki, T. Shiraishi, and N. Watanabe. Effect of on-axis tensile loading on shear properties of an orthogonal 3d woven sic/sic composite. *Composites Science and Technology*, 65:2541–2549, 2005.

[43] J.W. Gillespie Jr., B.A. Gama, C.E. Cichanowski, and J.R. Xiao. Interlaminar shear strength of plain weave s2-glass/sc79 composites subjected to out-of-plane high strain rate compressive loadings. *Composites Science and Technology*, 65:1891–1908, 2005.

[44] Y.A. Bahei-El-Din and M.A. Zikry. Impact-induced deformation fields in 2d and 3d woven composites. *Composites Science and Technology*, 63:923–942, 2003.

[45] B. Sun and B. Gu. Shear behavior of 3d orthogonal woven fabric composites under high strain rates. *Journal of Reinforced Plastics and Composites*, 25:1833–1845, 2006.

[46] J. Grogran, S.A. Tekalur, A. Bogdanovich, and R.A. Coffelt. Ballistic resistance of 2d and 3d woven sandwich composites. *Journal of Sandwich Structures and Materials*, 9:283–302, 2007.

[47] A. Salvi and A.M. Waas. Rate-dependent compressive behavior of unidirectional carbon fiber composites. *Polymer Composites*, pages 397–406, 2004.

[48] B. Sun and B. Gu. High strain rate behavior of 4-step 3d braided composites under compressive failure. *Journal of Material Science*, 42:2463–2470, 2007.

[49] B. Sun, F. Liu, and B. Gu. Influence of the strain rate on the uniaxial tensile behavior of 4-step 3d braided composites. *Composites: Part A*, 36:1477–1485, 2005.

[50] K.V. Subramaniam, W. Nian, and Y. Andreopoulos. Blast response simulation of an elastic structure: Evaluation of the fluid-structure interaction effect. *International Journal of Impact Engineering*, 36:965–974, 2009.

[51] Xiaolan Song. *Vacuum Assisted Resin Transfer Modling (VARTM): Model Development and Verification*. Ph.d. dissertation, Virginia Polytechnic Institute and State University, April 2003.

[52] R. Chen, C. Dong, Z. Liang, C. Zhang, and B. Wang. Flow modeling and simulation for vacuum assisted resin transfer molding process with the equivalent premeability method. *Polymer Composites*, 25(2):146–164, 2004.

[53] ASTM D 2374. Standard test method for void content of reinforced plastics. *ASTM INTERNATIONAL*, 1994.

[54] ASTM D 792. Standard test method for density and specific gravity (relative density) of plastics by displacement. *ASTM INTERNATIONAL*, 1998.

[55] ASTM D 2584. Standard test method for for ignition loss of cured reinforced resings. *ASTM INTERNATIONAL*, 1994.

[56] Y. Zhou, F. Pervin, M.A. Biswas, V.K. Rangari, and S. Jeelani. Fabrication and characterization of montmorillonite clay-filled sc-15 epoxy. *Materials letters*, 60:869–873, 2006.

[57] M. Pankow, C. Attard, and A.M. Waas. Specimen size and shape effect in split hopkinson pressure bar testing. *Journal of Strain Analysis for Engineering Desing*, 44(8):689–698, 2009.

[58] AGY. Glassfiber reference guide. AGY website, 1999.

[59] S.V. Thiruppukuzhi and C.T. Sun. Models for the strain-rate dependent behavior of polymer composites. *Composites Science and Technology*, 61:1–12, 2001.

[60] ASTM D 3039. Standard test method for tensile properties of polymer matrix composites. *ASTM INTERNATIONAL*, 2002.

[61] ASTM D 2344. Standard test method for short-beam strength of polymer matrix composites amd their laminates. *ASTM INTERNATIONAL*, 2006.

[62] T.R. Walter, G. Subhash, B.V. Sankar, and C.F. Yen. Damage modes in 3d glass fiber epoxy woven composites under high rate of impact loading. *Composites: Part B*, 40:584–589, 2009.

[63] S.Deng and L. Ye. Influence of fiber-matrix adhesion of mechanical properties of graphite/epoxy composites: Ii interlaminar fracture and inplane shear behavior. *Journal of Reinforced Plastics and Composites*, 18:1041–1057, 1999.

[64] A.T. Seyhan, M. Tanoglu, and K. Schulte. Mode i and mode ii fracture toughtness of e-glass non-crimp fabric/carbon nanotube (cnt) modified polymer based composites. *Engineering Fracture Mechanics*, 75:5151–5162, 2008.

[65] P.A. Gustafson and A.M. Waas. The influence of adhesive constitutive parameters in cohesive zone finite element models of adhesively bonded joints. *Journal of Solids and Structures*, 46:2201–2215, 2009.

[66] Alaxander Forrester, Adras Sobester, and Andy Keane. *Engineering Design via Surrogate Modelling: A Practical Guide*. Wiley, 2008.

[67] P.A. Gustafson and A.M. Waas. The infulence of adhesive constitutive parameters in cohesive zone finite element models of adhesively bonded joints. *Journal of Solids and Structres*, 46(10):2201–2215, 2009.

[68] Q. Li, D. Liu, D. Templeton, and B. Raju. A shock tube-based facility for impact testing. *Experimental Techniques*, (25–28), 2007.

[69] M. Stoffel, R. Schmidt, and D. Weichert. Shock wave-loaded plates. *International Journal of Solids and Structures*, 38:7659–7680, 2001.

[70] S.A. Tekalur, K. Shivakumar, and A. Shukla. Mechanical behavior and damage evolution in e-glass vinyl ester and carbon composites subjected to static and blast loads. *Composites Part B: Engineering*, 39:57–65, 2008.

[71] J. LeBlanc, A. Shukla, C. Rousseau, and A. Bogdanovich. Shock loading of three-dimensional woven composite materials. *Composite Structures*, 79:344–355, 2007.

[72] M. Herbert, C.E. Rousseau, and A. Shukla. Shock loading and drop weight impact response of glass reinforced polymer composites. *Composite Structures*, 84:199–208, 2008.

[73] M. Stoffel. Experimental validation of anisotropic ductile damage and failure of shock wave-loaded plates. *European Journal of Mechanics A/Solids*, 26:592–610, 2007.

[74] S.A. Tekalur, A.E. Bogdanovich, and A. Shukla. Shock loading response of sandwich panels with 3-d woven e-glass composite skinds and stitched foam core. *Composite Science and Technology*, 6:736–753, 2009.

[75] S.A. Tekalur, A. Shukla, and K. Shivakumar. Blast resistance of polyurea based layered composite materials. *Composite Structures*, 84:271–281, 2008.

[76] B. Song, W. Chen, and T. Werrasooriya. Quasi-static and dynamic compressive behaviors of a s-2 glass/sc15 composite. *Journal of Composite Materials*, 37(19):1723–1743, 2003.

[77] L. Ninan, J. Tsai, and C.T. Sun. Use of split hopkinson pressure bar for testing off-axis composites. *International Journal of Impact Engineering*, 25:291–313, 2001.

[78] B.A. Gama, S. K. Lopatnikov, and J.W. Gillespie Jr. Hopkinson bar experimental technique: A critical review. *Applied Mechanics Reviews*, 57(4):223–250, 2004.

[79] S.C. Queck, A.M. Waas, K.W. Shahwan, and V. Agaram. Analysis of 2d triaxial flat braided textile composites. *International Journal of Mechanical Sciences*, 2003.

[80] I.S. Raju and J.T. Wang. Classical laminate theory models for woven fabric composites. *Journal of Composites Technology and Research*, 16(4):289–303, October 1994.

[81] N. Talbi, A. Batti, R. Ayad, and Y.Q. Guo. An analytical homogenization model for finite element modelling of corrugated cardboard. *Composite Structures*, 88:280–289, 2009.

[82] P. Tan, L. Tong, G.P. Steven, and T. Ishikawa. Behavior of 3d orthogonal woven cfrp composites part ii. fea and analytical modeling approaches. *Composites: Part A*, 31:273–281, 2000.

[83] R.L. Karkkainen and J.T. Tzeng. Micromechanical strength modeling and investigation of stitch density effects on 3d-orthogonal composites. *Journal of Composite Materials*, 43(25):3125–3142, 2009.

[84] M.P. Rao, B.V. Sankar, and G. Subhash. Effect of z-yarns on the stiffness and strength of three-dimensional woven composites. *Composites: Part B*, 40:540–551, 2009.

[85] Y.C. Fung. *Foundations of Solid Mechanics*. Prentice Hall, 1965.

[86] Shuguang Li. Boundary conditions for unit cells from periodic microstructures and their implications. *Composites Sceince and Techonology*, 68:1962–1974, 2007.

[87] SIMULIA. *ABAQUS users Manual*, 6.8 edition, 2008.

[88] G.T. Gray III. *ASM Handbooks Online*, volume 8, chapter High Strain Rate Testing. ASM International, 2004, http://www.asmmaterials.info, 1985.

[89] M.A. Kaiser. Advancements in the split hopkinson bar testing. Master's thesis, The Virginia Polytechnic Institute and State University, 1998.

[90] D.A. Gorham and X.J. Wu. An empirical method for correcting dispersion in pressure bar measurements of impact stresses. *Measurement Science and Technology*, 7(9):1227–1232, 1996.

[91] Z. Li and J. Lambros. Determination of the dynamic response of brittle composites by the use of split hopkinson pressure bar. *Composites Science and Technology*, 59:1097–1107, 1999.

[92] D. Bancroft. The velocity of longitudinal waves in cylindrical bars. *Physical Review*, 59:588–593, 1941.

[93] J. Yuan, N. Takeda, and A.M. Waas. A note on data processing in the split pressure bar tests. *Experimental Techniques*, pages 21–24, September/October 1998.

[94] B. Song and W. Chen. Dynamic sress equilibration in split hopkinson pressure bar tests on soft materials. *Journal of Experimental Mechanics*, 44:300–312, 2004.

[95] L.M. Yang and V.P.W. Shim. An analysis of stress uniformity in split hopkinson bar test specimens. *International Journal of Impact Engineering*, 31:129–150, 2005.

[96] E. Woldesenbet and J. Vinson. Specimen geometry effects on high-strain-rate testing of graphite/epoxy composites. *AIAA Journal*, 37(9):1102–1106, September 1999.